The Nature of Lubricant-Derived Ash-Related Emissions and Their Impact on Diesel Aftertreatment System Performance

by

Alexander Sappok

B.S., Mechanical Engineering
Kansas State University, 2004

S.M., Mechanical Engineering
Massachusetts Institute of Technology, 2006

Submitted to the Department of Mechanical Engineering in Partial Fulfillment of the Requirements for the Degree of

DOCTOR OF PHILOSOPHY IN MECHANICAL ENGINEERING

AT THE

MASSACHUSETTS INSTITUTE OF TECHNOLOGY

June 2009

Signature of Author: _____
Department of Mechanical Engineering
June 1, 2009

Certified by: _____
Wai K. Cheng
Professor of Mechanical Engineering
Committee Chair

Certified by: _____
Victor W. Wong
Principal Research Scientist and Lecturer in Mechanical Engineering
Thesis Supervisor

Accepted by: _____
David Hardt
Chairman, Department Committee on Graduate Students

(This page intentionally left blank)

The Nature of Lubricant-Derived Ash-Related Emissions and Their Impact on Diesel Aftertreatment System Performance

by

Alexander Sappok

Submitted to the Department of Mechanical Engineering on June 1, 2009 in Partial Fulfillment of the Requirements for the Degree of

DOCTOR OF PHILOSOPHY IN MECHANICAL ENGINEERING

ABSTRACT

Diesel particulate filters (DPF) have seen widespread use in on- and off-road applications as an effective means for meeting increasingly stringent particle emissions regulations. Over time, incombustible material or ash, primarily derived from metallic additives in the engine lubricant, accumulates in the DPF. Ash accumulation leads to increased flow restriction and an associated increase in pressure drop across the particulate filter, negatively impacting engine performance and fuel economy, and eventually requiring filter removal for ash cleaning.

While the adverse effects of ash accumulation on DPF performance are well known, the fundamental underlying mechanisms controlling these effects are not. This work explores the parameters influencing key ash properties such as porosity and permeability, and factors controlling the soot deposition - ash formation/accumulation process, which ultimately determines the magnitude of the ash effect on DPF pressure drop. In addition to the ash properties, the location of ash deposit accumulation inside the DPF channels, whether in a cake layer along the filter walls or packed in a plug at the rear of the channels, also plays a major role in influencing DPF pressure drop. Through a combined approach employing targeted experiments and theoretical models, explanations for the key factors and processes controlling ash properties and their effects on DPF pressure drop were developed.

These results, among few fundamental data of this kind, correlate changes in diesel particulate filter performance with lubricant chemistry, exhaust conditions, and ash morphological characteristics. Results are useful in optimizing the design of the combined engine-aftertreatment-lubricant system for future diesel engines, balancing the requirements of additives for adequate engine protection with the requirements for robust aftertreatment systems.

Thesis Supervisor: Victor W. Wong
Title: Principal Research Scientist and Lecturer in Mechanical Engineering

(This page intentionally left blank)

ACKNOWLEDGEMENTS

A number of people have contributed to making my time at MIT a memorable, always interesting, and extremely rewarding experience. My time at the Institute has afforded me a multitude of opportunities to grow and develop on a number of levels, and for that I am extremely grateful.

I would like to extend my sincerest thanks to my thesis advisor, Dr. Victor Wong, for encouraging me to stay on for the Ph.D., and allowing me the opportunity to spend my time here working on a project that I truly enjoy. Aside from learning to conduct scientific research, Dr. Wong has helped me to develop the ability to critically evaluate experimental results. My experience at MIT would not have been nearly as rewarding without the opportunity to work independently and publish and present my work at conferences around the world, and for that I wish to thank Dr. Wong as well. Additionally, I would also like to acknowledge Profs. Wai K. Cheng, John Heywood, and Bill Green for their advice as members of my thesis committee.

This project would not have been possible without the support of the MIT Consortium to Optimize Lubricant and Diesel Engines for Robust Emission Aftertreatment Systems. I would like to thank all of the current and past consortium members for not only funding this work, but for providing stimulating discussions and for their helpful advice during our consortium meetings. Many thanks also go to Michael Blanz and the staff at Cummins Technical Center for their technical support, and the staff of the MIT Center for Materials Science and Engineering for their contributions to the soot and ash analysis.

The contributions of Thane DeWitt and Raymond Phan to the successful completion of this project were immeasurable. Both Thane and Raymond's cheerful demeanor always brightened my day and made working in the lab that much more enjoyable. I would also like to thank all of my friends and colleagues at the Sloan Automotive Laboratory for the opportunity to develop many lasting friendships. In particular, I would like to thank Eric Senzer and Steve Przesmitzki for their help and support in preparing for my qualifying exams, and Themistocles Resvanis for his contributions to reviewing the theoretical work in this thesis. Additionally, I would like to thank RJ Scaringe, Jeff Jocsak, Devon Manz, Jim Cuseo, Ferran Ayala, Walter Hoffman, and countless others at the Sloan lab who provided many memorable moments and made the lab such an enjoyable place to work. Lastly, I am grateful for the opportunity to have supervised many undergraduate students including Tomas Vianna, Dan Beauboeuf, Yassir Hassan, Bala Mohanamurugan, and Michael Santiago whose work contributed greatly to the completion of this project.

Most of all I would like to thank my family for all of their support and the inspiration they have provided me with every step of the way. I am especially grateful to my parents for the example they set each and every day, and many thanks go to my father for his commission-free technical advice. I am also extremely blessed to have the loving support of my girlfriend, Heidi, whose patience, encouragement, and support has made my time here at MIT that much happier.

(This page intentionally left blank)

TABLE OF CONTENTS

LIST OF FIGURES

LIST OF TABLES

NOMENCLATURE

ACT	Asymmetric Cell Technology
ATS	Aftertreatment System
Ca	Calcium
CI	Compression Ignition
CO	Carbon Monoxide
CO_2	Carbon Dioxide
DPF	Diesel Particulate Filter
ECM	Engine Control Module
EDX	Energy Dispersive X-ray Spectrometry
EGR	Exhaust Gas Recirculation
HC	Hydrocarbons
HCLD	Heated Chemiluminescence Detector
HFID	Heated Flame Ionization Detector
ICP	Inductively Coupled Plasma
Kn	Knudsen Number
LNT	Lean NOx Trap
Mg	Magnesium
NAA	Neutron Activation Analysis
NDIR	Non-Dispersive Infrared
NO	Nitrogen Oxide
NO_X	Oxides of Nitrogen
P	Phosphorous
Pe	Peclet Number
PM	Particulate Matter
PPB	Parts per Billion
PPM	Parts per Million
Re	Reynolds Number
RPS	Relative Pressure Sensitivity
S	Sulfur
SCF	Stokes Cunningham Factor
SCR	Selective Catalytic Reduction
SEM	Scanning Electron Microscope
SI	Spark Ignition
SLPM	Standard Liters per Minute
SO_2	Sulfur Dioxide
SO_4	Sulfate
SOF	Soluble Organic Fraction
SOL	Insoluble Fraction
STEM	Scanning Transmission Electron Microscope
TDC	Top Dead Center
TEM	Transmission Electron Microscope
TGA	Thermo-Gravimetric Analysis
XRD	X-Ray Diffraction

ZDDP	Zinc Dialkyl-Dithio-Phosphate
Zn	Zinc
A	Area
A_f	DPF frontal area
D	Diffusion coefficient
$d_{Aggregate}$	Aggregate particle diameter
D_H	Hydraulic diameter
d_P	Pore diameter
$\overline{D}_P^2$	Surface average sphere diameter
$d_{Primary}$	Primary particle diameter
f	Fanning friction factor
k	Permeability
L	DPF length
P	Pressure
S	Channel perimeter
u	Exhaust gas channel velocity
U_w	Filtration velocity
v	Exhaust gas velocity
v_w	Exhaust gas wall velocity
w	Porous media thickness
$Z_{In/Out}$	Channel inlet/outlet friction coefficient
β	Forchheimer coefficient
ΔP_{Ash}	Ash layer pressure drop
$\Delta P_{Channel}$	Channel pressure drop
ΔP_{In}	Pressure drop due to inlet contraction
ΔP_{Out}	Pressure drop due to outlet expansion
ΔP_{Total}	Total DPF pressure drop
ΔP_{Soot}	Soot layer pressure drop
ΔP_{Wall}	Substrate wall pressure drop
ε	Porosity
μ	Dynamic viscosity
ν	Kinematic viscosity
ρ	Gas density
$\rho_{Packing}$	Packing density
$\rho_{Theoretical}$	Theoretical density
τ	Sheer stress
ξ	Contraction/expansion loss coefficient

1 INTRODUCTION

Diesel fuel is a crucial component of the world's energy supply, comprising 20% of crude oil energy consumption and providing nearly all of the energy for freight transport. The high efficiencies of diesel engines have made them the engine of choice not only in freight applications, but also in fuel price-sensitive markets, such as Europe, where diesel vehicles comprise more than 50% of the vehicle fleet. Despite these advantages, diesels emit high levels of soot, a regulated pollutant and carcinogen. Diesel-related pollution and health concerns have prompted governments to adopt strict emissions regulations.

Diesel Particulate Filters (DPF), mounted in the engine's exhaust system, trap over 99% of soot emissions and are used on nearly all 2007 and newer diesel engines in the United States and Europe. While extremely effective at reducing engine-out soot emissions, the use of DPFs presents considerable challenges to engine and exhaust aftertreatment system manufacturers, as well as lubricant formulators.

1.1 Diesel Engine Fundamentals

Today's diesel engines have advanced significantly since their development over a century ago by Rudolph Diesel. In his first patent filed in Germany in 1892, Diesel outlined the design for an innovative internal combustion engine in which combustion was initiated by injecting fuel into air heated by compression. This fundamental difference between Diesel's compression ignition (CI) engine and conventional spark ignition (SI) engines yielded an improvement in efficiency of nearly a factor of two when the engine was first introduced [1].

Despite numerous advances in diesel engine technology over the course of more than a century since Diesel introduced his first engine, the fundamental operating principles of the diesel engine have remained virtually unchanged. In its most basic form, a diesel engine is a reciprocating-piston engine employing internal mixture formation and autoignition to initiate combustion. During the engine's compression stroke, intake air is

compressed to high pressures (30 to 55 bar) with an associated increase in cylinder temperatures from 700 °C to 900 °C. Fuel is injected either directly into the cylinder or into an adjacent pre-combustion chamber late in the compression stroke, near piston top dead center (TDC), upon which the elevated temperature within the cylinder causes the fuel to autoignite [2].

Mixture formation in the diesel engine plays a critical role in diesel autoignition and subsequent combustion as well as the attainable mean effective pressure [2]. Unlike spark ignition engines that control load by restricting the intake air through the use of a throttle plate, load in a diesel engine is controlled by the amount of fuel injected per cycle. The absence of any fuel in the cylinder during compression also eliminates the possibility of uncontrolled auto-ignition or engine knock. Knock is a major problem limiting the compression ratio of conventional SI engines. The compression of only air in the diesel engine enables use of compression ratios up to twice those of a conventional SI engine, in the range of 12 to 24, depending upon engine size and aspiration [2].

1.1.1 Diesel Engine Advantages

The characteristics of the diesel combustion process, described in the previous section, provide a number of advantages over conventional spark ignition engines, the most notable of which are: improved efficiency resulting in better fuel economy, lower greenhouse gas and hydrocarbon emissions, higher torque at lower engine speeds, and extended engine life. In addition to the qualities inherent to the diesel combustion process itself, maintenance and fuel costs for diesel engines are also typically lower than the costs associated with comparable SI engines [3].

The diesel engine's higher efficiency translates into a 20-40% improvement in fuel economy for diesel-powered vehicles when compared to their gasoline-powered equivalents [4]. This significant improvement in efficiency is attributed primarily to the diesel engine's high compression ratio, low pumping losses due to its un-throttled operation, and overall lean combustion. Diesel engines also typically run at slower

engine speeds than SI engines, due in part, for the need to allow time for the heterogeneous mixture formation and autoignition to occur. The slower engine speeds contribute to a reduction in frictional losses within the power cylinder [3].

The diesel combustion process results in a large amount of heat released earlier and at a faster rate in the expansion stroke than in a gasoline engine. A direct result of the large amount of heat released early in the expansion stroke is the production of higher torque at lower engine speeds. In order to withstand the higher in-cylinder pressures and faster rate of heat release, diesel engines must be constructed in a much more robust manner than SI engines. This fact, combined with reduced friction in the power cylinder, leads to an extension of the useful life of a diesel engine three to four times that of a comparable gasoline engine. Furthermore, many of today's heavy-duty diesel engines are designed for a service life of one million miles before the first overhaul [3].

Aside from the performance advantages, the lean nature of diesel combustion also results in extremely low carbon monoxide (CO) emissions. The absence of any fuel in the cylinder during the compression stroke also reduces the formation of hydrocarbon (HC) emissions from crevice volumes [1]. The low HC and CO emissions eliminate the need for expensive aftertreatment systems (ATS) to further reduce HC and CO levels such as the three-way catalysts employed with SI engines, in most cases.

1.1.2 Diesel Engine Applications

The benefits of diesel engines, namely high efficiency and improved fuel economy, durability, and high power output have made the diesel engine the power plant of choice in a large and varied number of applications. Currently diesel engines are used in many industries including transportation, construction, agriculture, and mining, and power a wide range of vehicles from large container ships and locomotives to light-duty passenger cars and agricultural equipment. Due to these broad applications, diesel fuel accounts for 20% of crude oil energy consumption and provides nearly all of the energy for freight transport [5].

According to a 2000 study titled "Diesel Technology and the American Economy," diesel-powered vehicles transport over 95% of all freight in the United States. Furthermore, based on the fraction of fuel energy consumed by vehicle type, diesel engines power 80% of all buses (transit, intercity, and school), 100% of all freight ships, 100% of all freight trains, and 23% of all passenger trains (transit, commuter, and intercity). In addition, based on the fraction of fuel energy consumed by sector, diesel engines power 83% of all construction equipment, 66% of all agricultural equipment, and 22% of all mining equipment in the U.S. [6].

While diesel engines find widespread use in a number of heavy-duty vehicles, their acceptance in the light-duty and passenger vehicle market in the U.S. has been slow. The case for diesel engines in the automotive and passenger vehicle market in Europe and many other parts of the world is quite different from that of the United States. Based on a report by the European Automobile Manufacturer's Association, diesel vehicles accounted for slightly more than 53% of new car registrations in the EU in 2008 [7].

1.1.3 Diesel Emissions

Although the benefits presented in the previous sections make the diesel engine the most efficient internal combustion engine in mass production today, there is still considerable room for improvement in a number of key areas. The major disadvantages of diesel engines are: elevated emissions of NOx and particulate matter (PM), high weight and low specific power output, low engine speed and exhaust temperatures, and elevated engine noise levels, relative to SI engines.

The complex heterogeneous nature of diesel combustion leads to high levels of NOx and particulate matter emissions from diesel engines. Reducing both of these emissions simultaneously is, perhaps, the most difficult challenge facing diesel engine development today. Furthermore, in-cylinder means for reducing NOx generally lead to increased PM emissions and vice versa, often described as the PM-NOx trade-off.

Unlike gasoline engines which operate at stoichiometric conditions ($\varphi = 1$), the lean nature of diesel combustion poses a challenge for NOx control through the use of exhaust aftertreatment systems, as NOx reduction in an oxygen-rich environment cannot be easily achieved [3]. An additional disadvantage of lean combustion in diesel engines is its associated reduction in exhaust temperature, which complicates particle emissions reduction using diesel particulate filters, since these units require temperatures in excess of 600 °C for complete soot oxidation without the presence of a catalyst [8].

While the problem of reducing NOx and PM emissions is currently the most pressing challenge facing the diesel industry, a number of additional diesel engine design and operating characteristics are the focus of substantial improvement efforts as well. The robust engine design requirements, imposed by the high in-cylinder pressures generated in the diesel combustion process, lead to increased engine size and weight. The diesel engine's heavy weight reduces its specific power output, which is typically only 50% to 65% that of comparable gasoline engines. An additional consequence of the rapid auto-ignition event in diesel engines is elevated engine noise, especially at idle. Precision high-pressure fuel injection systems enabling multiple injection events and injection rate shaping are used to reduce engine noise and emissions in most modern diesel engines. While effective, these systems also add substantial cost to the engine [3].

1.2 Diesel Emissions Regulations

Growing concern over the contribution of diesel engines to the overall atmospheric emissions inventory, combined with increasing evidence of adverse health effects posed by diesel particulate matter emissions [9] have resulted in increasingly stringent regulations on the emissions from diesel engines. In 2009, the US EPA listed over 250 areas of the United States exceeding the allowable particulate matter air quality limits. Over one third of the US population, 100M people, lives within these particulate matter non-attainment areas. Diesel particle emissions are a recognized carcinogen and are associated with respiratory illness, heart attacks, and premature death [10]. Furthermore,

diesel engines accounted for nearly 75% of all mobile source $PM_{2.5}$ emissions in the U.S. in 2000 [11]. $PM_{2.5}$ is defined as all particulate matter smaller than 2.5 μm. The problem of particulate matter pollution from diesel sources is significantly more pronounced in Europe, due to the much larger number of diesel engines in operation. [12].

Regulations imposed by the United States Environmental Protection Agency (EPA) reduced the allowable NOx and PM emissions limits for diesel engines by an order of magnitude between 2002 and 2010. These new regulations are some of the most important factors driving diesel engine development in the United States and Europe today.

In conjunction with the tighter emissions limits, the EPA also limited the sulfur content of diesel fuel for highway engines to no more than 15 ppm effective in 2006 [13]. Aside from helping to reduce overall particle emissions, the new ultra-low sulfur diesel fuels will, more importantly, make possible the use of advanced aftertreatment devices that would otherwise be deactivated by higher fuel sulfur levels.

Both the U.S. and E.U. have implemented increasingly stringent emissions regulations, in an effort to reduce NOx and PM emission from diesel engines. In the United States, emissions of NOx and particulate matter were reduced by an order of magnitude from the 2002 levels of 2.0 g/hp-hr NOx and 0.1 g/hp-hr PM to the 2007/2010 limits of 0.2 g/hp-hr NOx and 0.01 g/hp-hr PM for heavy-duty on-highway applications. Trends in European emission regulations follow those of the U.S., however in general the E.U. regulations are slightly less stringent. As a result of these increasingly stringent emissions regulations, NOx and PM emissions will be reduced by over 98% from the 1990 levels by 2010 when the new regulations are completely phased in. Figures 1.1 and 1.2 presents historical and future trends in NOx and PM emissions reduction.

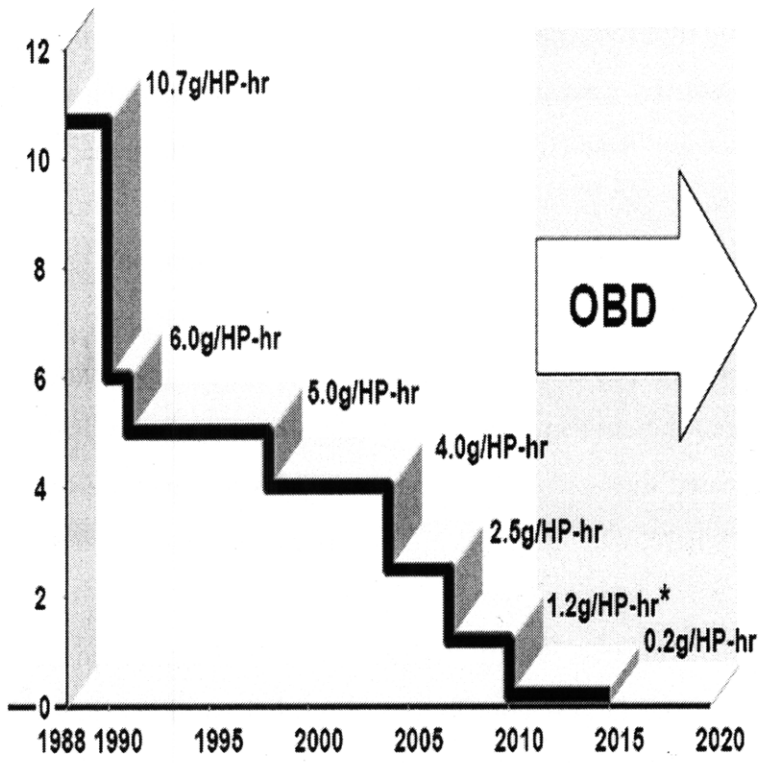

Figure 1.1. U.S. heavy-duty diesel NOx emissions limits [14]

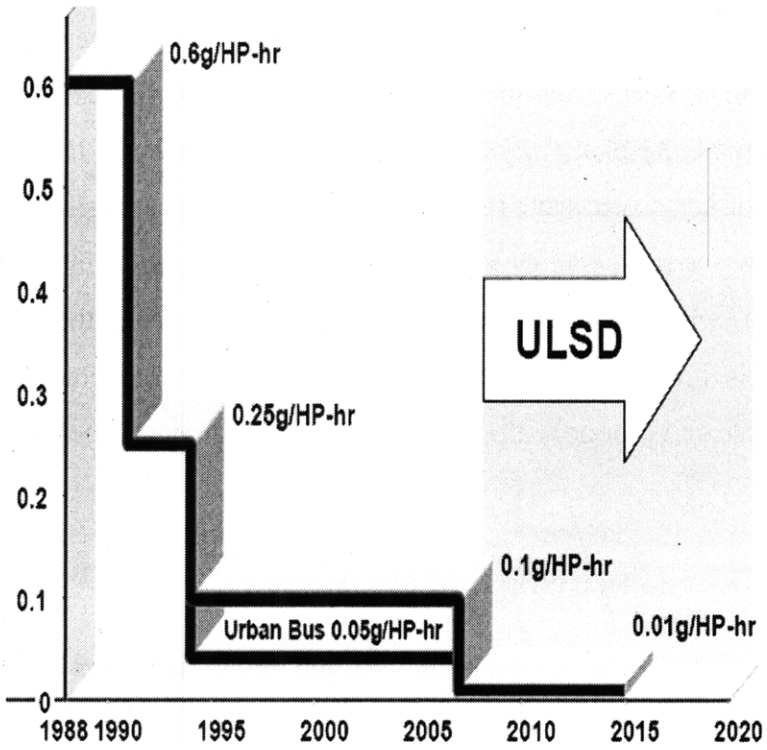

Figure 1.2. U.S. heavy-duty diesel PM emissions limits [14]

The large reduction in allowable NOx and PM emissions from heavy-duty diesel engines is motivated, in part, by growing concern over the adverse environmental and human health effects posed by these emissions. High NOx concentrations in densely populated urban areas contribute significantly to the formation of photochemical smog and ozone [1]. Additionally, many studies have demonstrated the potentially carcinogenic nature of diesel particles, which can affect humans when the particles are inhaled and become trapped in the bronchial passages and lungs [15]. Further, diesel nanoparticles (diameter $< 0.1\mu m$) have been the subject of much investigation, especially in Europe, where new studies have indicated the potential for these particles to penetrate lung tissue and enter the blood stream, whereby the particles are transported to other parts of the body [16].

In addition to health effects, recent studies have also highlighted black carbon (soot) emissions as one of the largest contributors to global warming, second only to carbon dioxide. These studies show black carbon particles have a warming effect in the atmosphere three to four times greater than previous estimates and may have up to 60% the global warming potential of CO_2. Black carbon is a strong absorber of solar radiation and one of the major components of diesel soot. While a large fraction of black carbon emissions, 25% to 35%, are due to the burning of biomass for heating and cooking in developing countries, diesel engines contribute significant amounts in developed nations. A recent study further noted that the per capita black carbon emissions from the United States and Europe are comparable to those of developing countries in south and east Asia [17]. Unlike CO_2 which may remain in the atmosphere for years, the lifetime of soot in the atmosphere is on the order of one week. Reduction of soot emissions is both technically feasible and produces almost immediate environmental benefits [18].

1.3 Diesel Emissions Reduction Measures

Emissions of unburned hydrocarbons and carbon monoxide from diesel engines are typically low and well below the regulated levels, due to the nature of the diesel combustion process. Particulate matter and NOx emissions are the two primary emissions of concern from diesel engines. Due to the large reduction in allowable

emissions levels, diesel engine manufacturers are finding it extremely difficult to meet the 2007 and 2010 PM and NOx limits through in-cylinder optimization alone. While a number of advanced engine subsystems and combustion strategies have been developed and implemented to further improve the diesel combustion process and reduce emissions, exhaust aftertreatment systems currently present the only technically feasible and economically attractive means to meet these new emissions limits.

Advances in engine technology such as the development and implementation of high-pressure common rail fuel injection systems, multiple injection strategies, variable geometry turbochargers, and cooled EGR systems have yielded significant improvements in reducing both NOx and PM emissions to the 2004 levels. In order to achieve compliance with 2007 and 2010 emissions standards, diesel particulate filters and various NOx catalysts, such as lean NOx traps and selective catalytic reduction systems, have seen increasingly widespread use. These advanced exhaust aftertreatment systems are currently the only technically feasible means for meeting the stringent emissions requirements. While effective, the use of these systems present additional challenges for engine manufacturers, and formed the motivation for this work.

(This page intentionally left blank)

2 DIESEL PARTICULATE FILTERS

Diesel particulate filters and advanced catalyzed aftertreatment systems have seen widespread use to meet increasingly stringent diesel emissions limits. Despite work on DPFs for specialty and retrofit applications since the early 1980's, the filters were first supplied as original equipment for automotive applications in 2000 by PSA in Europe [19]. Since their introduction, DPFs have quickly become the preferred means for meeting current and future particulate matter emission limits. Presently all 2007 and newer on-road diesel engines are equipped with particulate filters in the United States.

2.1 DPF Operation

While a number of filter media have been developed over the years, cellular ceramic wall-flow particulate filters have found widespread use due to their relatively low cost and high trapping efficiency. The trap consists of a ceramic honeycomb substrate with porous channel walls. The channels are alternately blocked by small ceramic plugs at each end. As particulate-laden exhaust enters the upstream open end of the channels it must pass through the porous walls before exiting the filter. As the exhaust passes through the walls, the particles are trapped inside the porous material and along the channels walls as depicted in the schematic shown in Figure 2.1. The trapped particles act as an added filtering medium in cellular ceramic traps further increasing trapping efficiency as the traps are loaded [20].

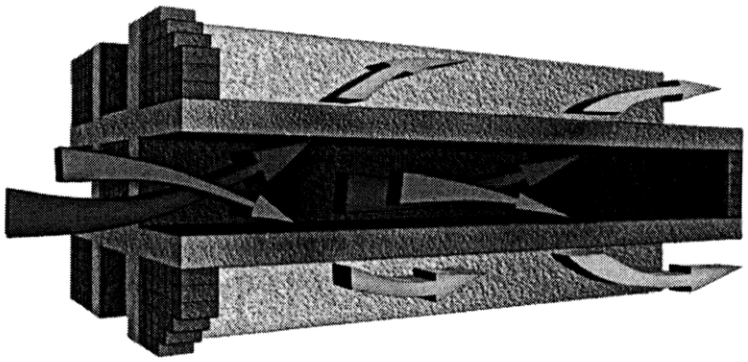

Figure 2.1. Wall-flow diesel particulate filter operation. Image from CD-Adapco.

A direct consequence of soot accumulation in the filter is increased flow restriction and a corresponding rise in exhaust backpressure, with a resulting fuel economy penalty [19]. The trapped particulate matter is removed from the trap by periodic or continuous regeneration. Trap regeneration is usually accomplished by burning off the accumulated soot [21]. Particle trapping efficiency and the pressure drop across the trap are, therefore, the two most important measures of trap performance.

Following DPF regeneration, incombustible material (ash) remains and accumulates in the filter over time. Ash accumulation eventually leads to irreversible plugging of the DPF, limiting the filter's in use service life and requiring filter removal for periodic cleaning or replacement. Current U.S. EPA regulations require manufacturers to certify diesel particulate filters for maintenance intervals of no less than 150,000 miles in heavy-duty applications [22]. Figure 2.2 depicts typical ash and soot distribution profiles in a DPF channel [23].

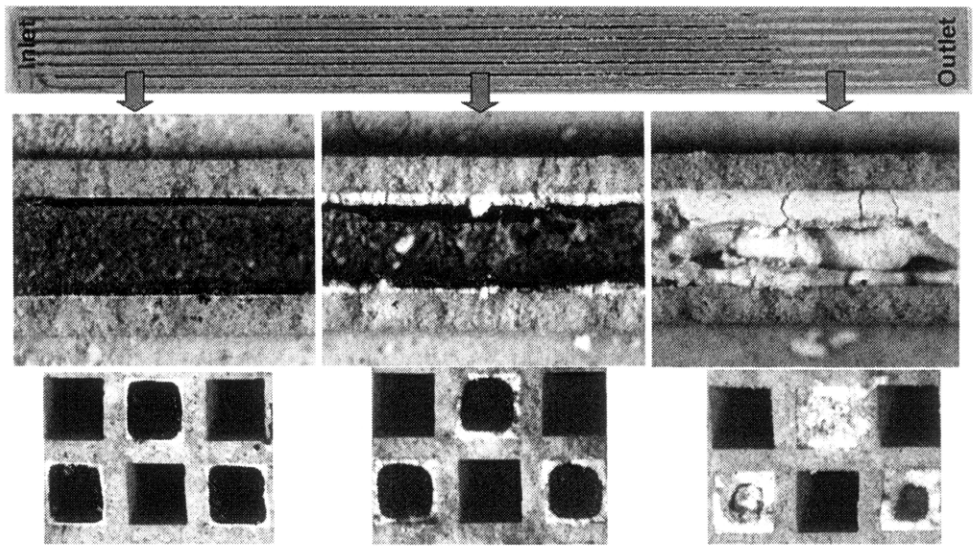

Figure 2.2. Ash and soot distribution in a DPF channel [23].

As evident in Figure 2.2, ash tends to accumulate in a thin layer along the channel walls as well as in a plug at the end of the channels. The end-plug, formed by the ash, completely fills the channels and reduces the effective length of the filter, while the ash

accumulated along the channel walls restricts the channel diameter and frontal area. Soot accumulated on top of the ash layer is also visible in the Figure 2.2.

2.2 Ash Sources

Ash accumulated in the DPF comes from a number of sources including lubricant additives, engine wear and corrosion particles, and trace metals found in diesel fuels. Typically, lubricant-derived ash comprises the majority of the ash found in diesel particulate filters in cases where fuel-borne catalysts are not used [24 - 26]. While conventional diesel engine lubricants are typically composed of 70-83% organic refinery-derived base stocks and 5-8% viscosity modifiers, it is the remaining 12-18% of the oil, consisting of a mostly inorganic additive package, that is the source of the majority of the ash emissions.

Lubricant additives perform a number of beneficial functions in the engine and are used for wear protection, deposit and corrosion control, soot dispersion, and anti-oxidant functions, among others. Calcium- and magnesium-based detergents, and zinc dialkyl-dithio-phosphates (ZDDP) for anti-wear and anti-oxidant protection are some of the most commonly used lubricant additives present in substantial amounts [22, 27].

Lubricant-derived ash is composed primarily of Ca, Zn, Mg, P, and S compounds in the form of various phosphates, sulfates, and oxides [22, 28, 29]. While these additives serve a number of beneficial functions, their accumulation in the DPF has attracted increasing attention. The CJ-4 oil specification was recently developed to minimize lubricant-derived ash impacts on aftertreatment systems by placing the following chemical limits on the lubricant:

- Maximum sulfated ash content: 1.0%
- Maximum phosphorous content: 0.12%
- Maximum sulfur content: 0.4%
- Maximum volatility: 13% [30].

Despite the introduction of the CJ-4 oil specification, the effects of specific lubricant-derived ash-related species on aftertreatment system performance are still not well understood.

From a lubricant formulation perspective, relating the impact of specific lubricant additives and oil sulfated ash levels to ash accumulation and the resulting degradation in DPF performance is not straightforward. Many of the methods used to quantify ash content in the lubricants do not accurately capture the specific mechanisms responsible for ash formation in the engine-exhaust aftertreatment system. According to the ASTM D876 specification, lubricant sulfated ash is defined as the material remaining after the oil has been treated with sulfuric acid and heated until the weight of the residual material remains constant [31]. Furthermore, variability of the test method is affected by oils formulated with magnesium-based detergents and boron-based dispersants, as well as various phosphorous compounds [32, 33].

Not all lubricant additives are consumed and emitted from the engine at the same rate. ZDDP additives, for example, decompose and form anti-wear films on engine surfaces. Differences in volatility of the specific additive components also affect their relative emission rates. These differences in additive consumption rates result in the individual additive elements accumulating in the DPF at amounts different from their proportion in the lubricant. Estimates of elemental emission rates based on bulk lubricant consumption have observed elemental capture rates in the DPF of 27% to 31% for magnesium, 37% to 42% for calcium, 37% to 86% for zinc, and 46% to 86% for phosphorous [29, 34]. The differences in additive volatility and speciated consumption rates, present a significant challenge for lubricant formulators to accurately specify lubricants to minimize ash accumulation in diesel particulate filters.

2.3 Ash Effects on DPF Performance

In recent years, much effort has been devoted to identifying the effects of lubricant additives on ash accumulation and on the performance degradation of diesel

aftertreatment systems. As a result, a considerable knowledge base has developed, leading to the following generally accepted observations:

- DPF ash increases with oil consumption and lubricant ash content [28, 29, 35, 36].
- Lubricant-derived ash is mostly composed of oxides, sulfates, and phosphates of Zn, Ca, and Mg [22, 28, 29, 37].
- The use of lubricant sulfated ash levels to predict engine-out ash over-estimates ash emissions due to lubricant volatility and differences in speciated oil consumption rates [35, 38, 39].
- Pressure drop across the particulate filter is not indicative of total ash levels [26, 29, 39].
- Specific additive elements, primarily S and P, adversely impact catalyst performance in addition to contributing to filter plugging [40 - 43].
- Ash accumulation within the DPF (plug formation versus even distribution along the channels) is affected by regeneration strategy [44, 45].

Despite considerable progress, the fundamental mechanisms responsible for many of the observations listed above are, for the most part, unknown. For example, the parameters affecting ash deposition, migration, and accumulation within the channels of the DPF (plug formation, uniform distribution, and ash bridging) are little understood. Furthermore, a number of factors are believed to affect ash packing density, which in turn impacts pressure drop; however these specific phenomena remain to be explained.

Additionally, while it is apparent that lubricant additives and the composition of their resulting ash affect ash morphology, much work is still required to correlate ash characteristics to the underlying lubricant formulation. Moreover, although Ca, Mg, and Zn are generally found in similar proportions in the DPF, as in the original lubricating oils, other elements such as boron are not [29]. These few examples highlight the need for developing a fundamental understating of the specific mechanisms and parameters responsible for the widely observed, and agreed upon, ash effects listed above.

2.3.1 DPF Pressure Drop

Ash accumulation in the DPF reduces the available filtration area, leading to flow restriction and plugging, commonly measured by an increase in the pressure differential across the filter (pressure drop). A number of studies have investigated the effect of ash accumulation in diesel particulate filters on pressure drop increase, and the compilation of these reports is presented in Figure 2.3.

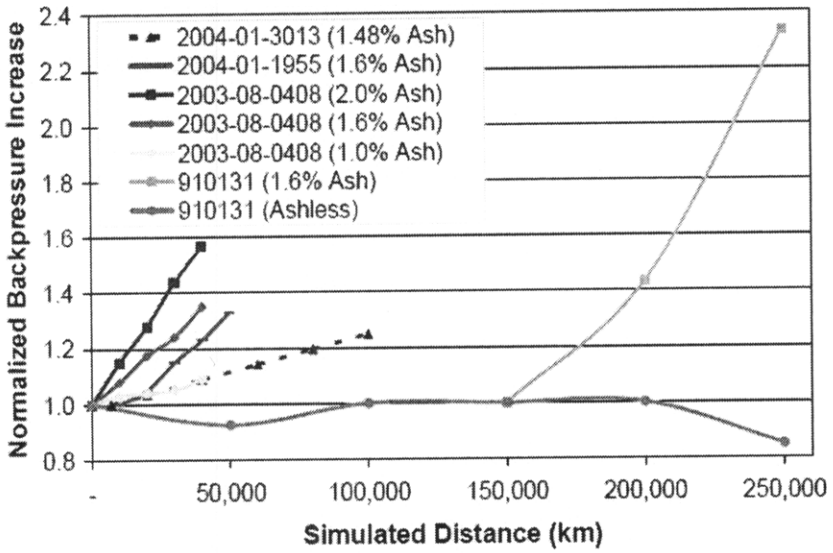

Figure 2.3. Ash contribution to measured exhaust backpressure increase as a function of simulated driving distance [25].

In general, ash accumulation is expected to lead to a doubling in pressure drop over a driving distance of 270,000 to 490,000 km with a 1.0% sulfated ash oil. At higher sulfated ash levels, a doubling in exhaust backpressure is observed over a driving distance ranging from 45,000 km to 110,000 km with a 1.6% sulfated ash oil [25].

The effect of ash accumulation on DPF pressure drop is complicated by the fact that the mass of ash in the filter is not directly correlated to the observed increase in pressure drop. Most notably, a study by Bardasz utilized ten different lubricants each formulated with various additives to a sulfated ash level of 1.8%. The authors reported no correlation between the mass of ash in the filer and measured pressure drop, and indicated that ash chemistry and morphology also play a significant role [29].

DPF pressure drop characteristics due to ash accumulation over the DPF service life also follow a non-linear trend, as reported in a 2006 study by Corning and shown in Figure 2.4. The study utilized a 1.7% sulfated ash oil and high engine load factors to mildly accelerate DPF ash loading. The laboratory tests subjected two particulate filters to 1,720 hours and 2,640 hours of ash loading on an engine dynamometer, simulating 300,000 miles and 420,000 miles of on-road use, respectively [23].

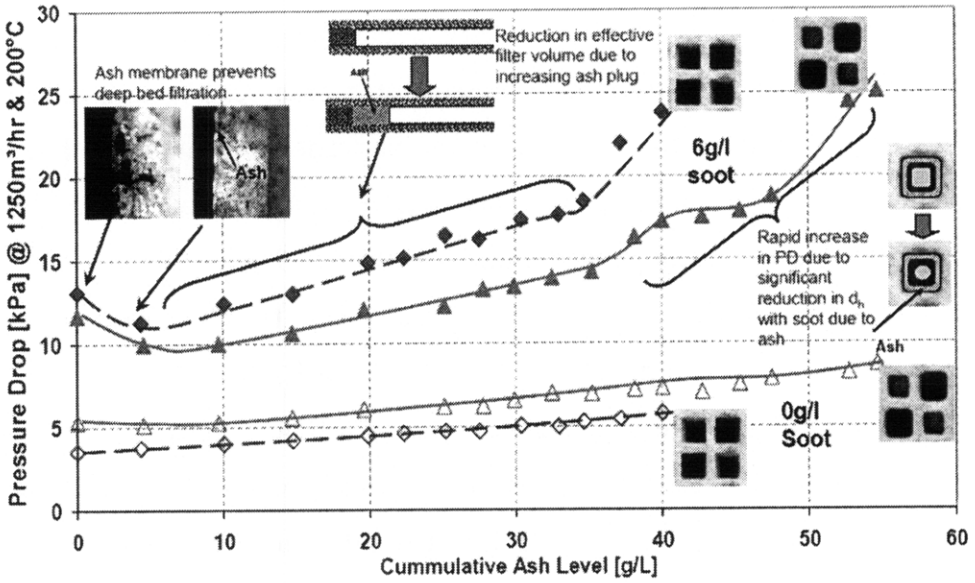

Figure 2.4. DPF pressure drop response as a function of ash loading for two DPFs containing no soot and 6g/l soot [23]. Note soot and ash loadings are typically reported in grams per nominal volume of the DPF.

In general both filters exhibited a slow and gradual linear increase in pressure drop with increasing levels of ash accumulation in the filter, ash shown in Figure 2.4 for the two cases with 0 g/l soot. However, the combined effects of soot and ash on filter pressure drop response are highly non-linear. For filters containing less than approximately 15 g/l ash and 6g/l soot, an initial reduction in pressure drop, relative to the clean filter, is observed. As ash levels increase, filter pressure drop increases significantly for the filters containing both ash and soot. Furthermore, when ash levels exceed 35 g/l, DPF pressure drop increases much more rapidly with additional soot loading. The non-linear behavior of the observed pressure drop trends was attributed to differences in ash distribution within the filter (end-plug vs. wall layer) [23]. Based on the results reported in the

literature, it is clear that not only the amount of ash in the filter, but also the composition, morphology, and distribution of the accumulated ash play a significant role in determining the DPF pressure drop response.

2.3.2 Lubricant Chemistry Effects on Pressure Drop

The studies cited in the previous section highlight the contribution of additional parameters, such as lubricant and ash chemistry, in addition to the absolute trapped mass of ash in the filter, to the increase in DPF pressure drop observed with ash accumulation. A 2003 study by Chevron utilized eight different lubricant formulations each containing different levels of boron-based dispersants, ZDDP, and calcium-based detergents. Lubricant sulfated ash content ranged from 0.42% to 1.9%. DPF ash loading was accelerated by adding 5% (by mass) of the candidate oils to the fuel. While calcium was observed to be the largest contributor to lubricant sulfated ash content, as measured by ASTM D874-06, DPF pressure drop increase, due to ash accumulation, appeared to be more closely correlated to zinc and phosphorous concentrations in the lubricant than calcium. Interestingly, no boron was found in the DPF, although it was present in the lubricants [46].

In contrast to the Chevron study, a 2005 report by Lubrizol noted that high lubricant phosphorous concentrations were not directly correlated to an increase in DPF pressure drop. This study utilized ten lubricants with various levels of calcium, magnesium, ZDDP, phosphorous, and boron. The authors further noted an interaction between the platinum levels in the DPF and phosphorous in the ash, possibly creating conditions suitable for reducing the ash particles to a sufficiently small size to pass through the DPF pores. Similar to the Chevron study, no boron was observed in the ash deposits accumulated in the particulate filter [29].

A number of studies have attempted to identify and quantify the various lubricant-derived ash components accumulated in the DPF. In general, a large fraction of the ash was found to consist of metallic sulfates and phosphates, with a much smaller contribution of

metal oxides. Calcium sulfate is observed to be the predominant lubricant-derived component found in the ash, with concentrations ranging from 59% to 75% of the total ash [24, 41, 47]. The significant differences reported in the Chevron and Lubrizol tests highlight the need for understanding, at a fundamental level, the impact of lubricant chemistry and its resulting influence on ash composition and morphology, which ultimately affects DPF pressure drop.

2.3.3 Operating Conditions and Ash Distribution Effects on Pressure Drop

Aside from ash composition and the resulting morphology of the ash layer, ash distribution within the individual DPF channels and the bulk ash distribution throughout the DPF also influence filter pressure drop. Figure 2.5 presents images of ash distribution profiles for ash generated via periodic and continuous regeneration. Ash accumulated in a DPF regenerated periodically, tended to preferentially accumulate in plugs at the end of the filter, with very little ash deposited along the channel walls. On the other hand, ash generated under continuously regenerating conditions was evenly distributed along the channel walls with very little plug formation [45].

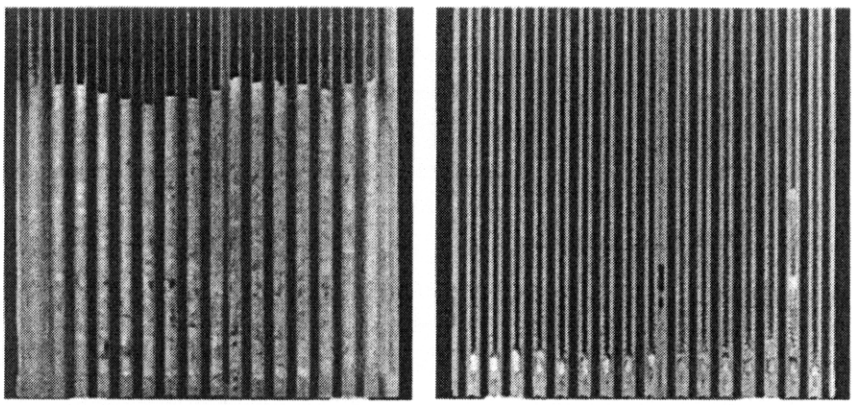

Figure 2.5. DPF ash distribution profiles for ash generated using periodic regeneration (right) and continuous regeneration (left) [44].

Ash deposited in filters regenerated periodically is initially dispersed throughout the soot cake layer that accumulates along the DPF channel walls. When the DPF is regenerated, the soot is oxidized leaving a loose network of ash agglomerates and particles. The

authors hypothesized that the ash, thus deposited, results in a highly porous and mechanically unstable structure. Over time, the ash deposits eventually collapse and break down, allowing much of the ash to accumulate in plugs toward the end of the filter.

On the other hand, in a DPF undergoing continuous regeneration, soot is continuously oxidized, and the ash is deposited directly on the DPF surface. Ash accumulated in this manner appears to adhere more strongly to the filter walls, resulting in the build-up of a fairly even ash layer along the channel length. Furthermore, particulate filters with the ash primarily packed in a plug towards the end of the DPF exhibited a smaller increase in pressure drop than filters in which the ash was distributed along the channel walls [44].

DPF ash layer profile measurements have also been reported and tend to show ash layer thickness increasing axially along the DPF channels towards the back of the filter, as shown in Figure 2.6. In general, ash deposits found near the end of the channels were almost twice as thick as the deposits measured at the front face of the filter. Studies have also compared ash layer thickness measurements for ash generated using an accelerated test method (oil addition to the fuel) to un-accelerated testing. Ash layers generated via fuel doping tended to be thicker than the layers observed in the un-accelerated tests which ranged in thickness from 100 to 300 μm [35].

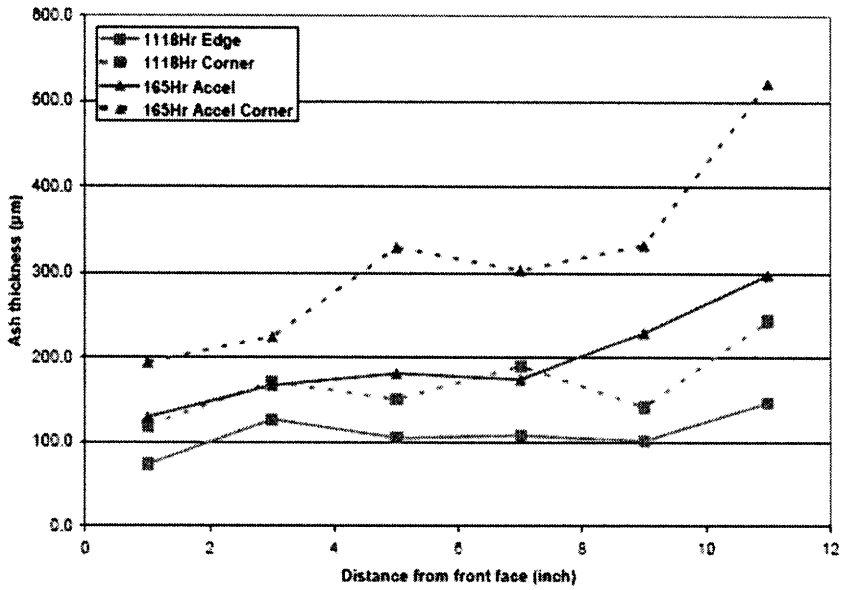

Figure 2.6. Measured ash layer thickness profiles along the DPF channels [35].

Aside from the ash distribution profiles within individual filter channels, other studies have investigated the bulk ash distribution within the DPF. A study by Lubrizol observed a non-uniform radial ash distribution with most of the ash accumulated near the center of the filter and much less ash near the DPF periphery [48]. These differences in bulk ash distribution are most likely the result of non-uniform exhaust gas flow distribution through the filter. Based on the observed differences in ash distribution and their resulting effects on DPF pressure drop, it is clear that exhaust conditions and regeneration strategy also significantly influence the manner in which ash affects DPF pressure drop.

2.4 Project Objectives

While previous studies have identified specific ash effects on DPF performance, they provide little information to describe the underlying fundamental mechanisms responsible for the observed DPF performance degradation, such as the properties of the ash entering the DPF, ash interactions with the trap medium, and the influence of exhaust conditions, among others. Further, the manner in which oil consumption and DPF ash loading is accelerated can have a significant effect on ash accumulation and DPF performance, as evidenced by the often conflicting data reported in the literature.

This investigation attempts to fill the gaps in the knowledge base by going beyond the conventional approaches listed above. Through careful control and monitoring of ash properties and feed gas composition, this work takes the first steps to investigate the fundamental characteristics of lubricant-derived ash feeding into and deposited in the DPF and the mechanisms by which DPF performance is affected. Further, comparison of the laboratory results with detailed analysis of ash loaded DPFs from the field provides not only a benchmark for comparing results obtained in the laboratory, but also additional insight into the mechanisms influencing ash properties and their effects on DPF performance.

The work in this project was conducted to systematically evaluate the effects of lubricant-derived ash on diesel aftertreatment system performance degradation via the following targeted investigations:

(1) chemical and physical characterization of engine-out ash entering the DPF, trapped in the DPF, and passing through the DPF,
(2) development and implementation of a realistic accelerated ash loading system to study ash effects on DPF pressure drop performance,
(3) correlation of lubricant composition, exhaust conditions, and the resulting ash properties to DPF performance,
(4) detailed post-mortem analysis of DPF ash properties for ash generated in the laboratory and comparison with field-aged filters,
(5) development of theoretical models to capture and aid in understanding the underlying mechanisms responsible for the manner in which ash deposits affect DPF pressure drop.

The experimental results were applied to extend the current theoretical and modeling efforts to gain a deeper understanding of the fundamental underlying mechanisms governing the effects of lubricant-derived ash on aftertreatment system plugging and pressure drop performance. Lubricant chemistry, exhaust conditional effects, and factors influencing ash deposition profiles were included in the models to more fully describe the combined ash and soot effect on DPF pressure drop and flow characteristics. Furthermore, these models provide additional insight into key system parameters, and were coupled with specific experimental studies to advance the conceptual understanding.

An enhanced understanding of these fundamental processes should prove useful to minimize the deleterious effects of lubricant-derived ash on diesel aftertreatment systems. If ash is accumulated as densely packed material in the trap, via sintering for instance, or in areas "out of the way," for example towards the channel ends, or if certain elements could be removed, such as heavy metals possibly, then means can be developed to

substantially improve the capacity and longevity of the diesel particulate filters. These results, among few fundamental data of this kind, correlate changes in diesel particulate filter pressure drop performance with ash compositional and morphological characteristics. Results will be useful in optimizing the design of the combined engine-aftertreatment-lubricant system for future diesel engines, balancing the requirements of additives for adequate engine protection with the requirements for robust aftertreatment systems.

(This page intentionally left blank)

3 FUNDAMENTAL UNDERSTANDING

A number of factors contribute to the pressure drop measured across a diesel particulate filter. These factors include exhaust gas properties, filter geometry and properties, and the characteristics of the soot and ash accumulated in the filter. While the effects of exhaust gas properties, filter characteristics, and to some extent, filter soot loading, are well understood, it is the latter factor, ash accumulation, which is the subject of this work. In order to develop a fundamental understanding of how ash accumulation affects filter pressure drop, it is instructive to first examine the various parameters influencing pressure drop and the underlying properties controlling these parameters.

3.1 DPF Pressure Drop

Pressure drop in clean diesel particulate filters has been well-studied, and the same basic principles can be applied to soot and ash loaded filters. In a very general sense, the effect of soot and ash accumulation on the DPF geometry is to reduce the total filtration area by decreasing the available channel length and reducing the hydraulic diameter of the channels. The properties of the ash and soot layers contribute to additional exhaust flow restriction. Figure 3.1 depicts the changes in filter geometry as soot and ash accumulate in the filter.

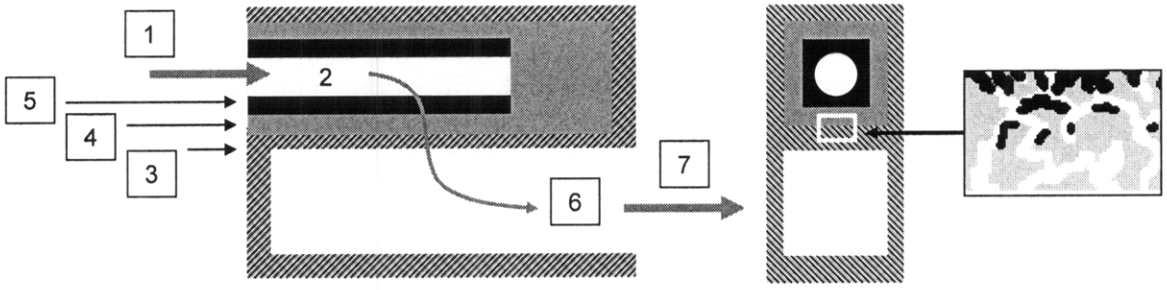

Figure 3.1. Soot and ash accumulation in a DPF channel. Inset depicts material accumulation in the DPF pores.

In general, the largest contributors to filter pressure drop are the frictional losses from flow through the substrate, and ash and soot layers, if present. Table 3.1. outlines the various parameters and controlling properties that contribute to filter pressure drop, as well as the relative magnitudes of their effects. The numbers in Table 3.1 correspond to the labels shown in Figure 3.1.

Pressure Drop Conrtibution		Key Parameters	Controling Properties	Re	Contribution to Total Pressure Drop
1	Inlet losses (Contraction)	Open frontal area	Filter geometry, ash and soot layer thickness	Transition	<3%
2	Frictional losses along inlet channel walls	Channel hydraulic diameter	Filter geometry, ash and soot layer thickness	<2,100	5%-30%
		Channel length	Filter geometry, ash end-plug formation		
3	Frictional losses from flow through wall	Wall permeability	Filter properties, amount of ash and soot depth filtration	<<1	50%-90%
		Wall thickness	Filter geometry		
		Filtration area	Filter geometry		
4	Frictional losses from flow through ash layer	Ash permeability	Ash porosity, pore size		
		Ash thickness	Ash packing density		
		Filtration area	Ash layer thickness, end-plug formation		
5	Friction losses from flow through soot layer	Soot permeability	Soot porosity, pore size		
		Soot thickness	Soot packing density		
		Filtration area	Soot layer thickness		
6	Frictional losses along outlet channel walls	Channel hydraulic diameter	Filter geometry	<2,100	~5%
		Channel length	Filter geometry		
7	Inlet losses (Expansion)	Open frontal area	Filter geometry	Transition	<3%

Table 3.1. Key parameters and controlling properties contributing to DPF pressure drop. Adapted from [23].

When ash and soot first begin to accumulate in a clean filter, the ash and soot preferentially occupy the filter pores (depth filtration). Material accumulation in the filter pores is shown in the inset in Figure 3.1. Depth filtration is undesirable, from a pressure drop perspective, as the material accumulation in the filter pores significantly restricts the pore diameters, leading to a rapid increase in pressure drop.

Following depth filtration, additional material accumulates along the filter walls (cake filtration). The filter cake builds up over time and provides an additional layer of filtrate (soot or ash) with its own associated flow restriction and increase in pressure drop. In general, the pressure drop associated with filter cake buildup is less acute than the pressure drop increase due to material deposition in the filter pores. Figure 3.2. presents

a schematic of a typical DPF pressure drop curve as soot accumulates in the filter. The depth filtration regime is identified as the initial loading phase in the figure.

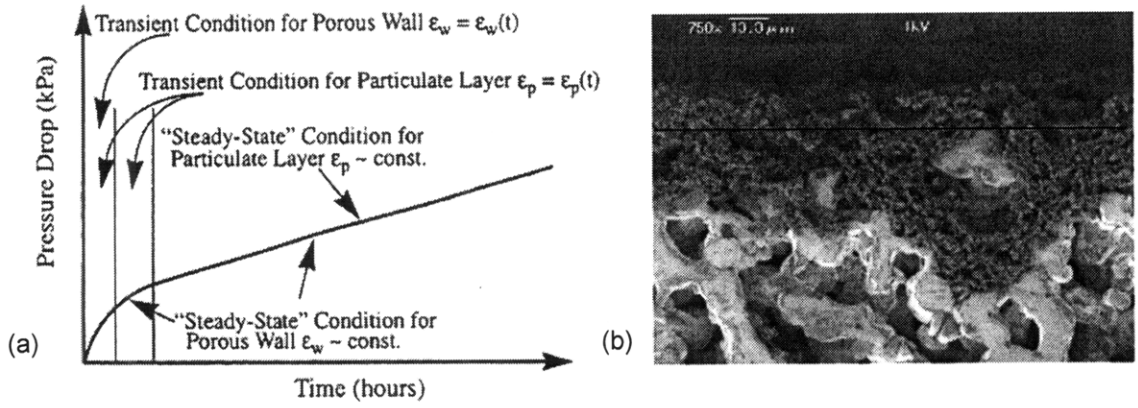

Figure 3.2. Typical DPF pressure drop characteristics as a function of material accumulation, (a) [49] and image of soot depth and cake filtration (b) [50].

DPF depth filtration further presents a challenge for the monitoring of soot loading and the control of filter regeneration. Filter soot loading is currently estimated using a combination of pressure drop measurements and predictive models. The non-linear effects of depth filtration on DPF pressure drop complicate filter soot load measurements.

3.1.1 Zero-Dimnesional DPF Pressure Drop Models

Zero-dimensional models capture many of the key factors contributing to DPF pressure drop, and are instructive to highlight the controlling parameters and properties which require further investigation through experiments and more sophisticated modeling efforts. The total pressure drop through the DPF is the sum of the various effects shown in Figure 3.1 and described in Table 3.1. Mathematically, the total DPF pressure drop can be described as follows:

$$\Delta P_{Total} = \Delta P_{In} + \Delta P_{Out} + \Delta P_{Channel} + \Delta P_{Wall} + \Delta P_{Ash} + \Delta P_{Soot} \tag{3.1}$$

where $\Delta P_{In/Out}$ is the pressure drop associated with the contraction and expansion of the exhaust gases at the filter inlet and outlet, $\Delta P_{Channel}$ is the pressure drop due to frictional

losses for gas flow along the length of the channel, and $\Delta P_{Wall/Ash/Soot}$ are the pressure losses associated with flow through the porous media including the filter wall, soot layer, and ash layer.

The pressure drop associated with the filter inlet and outlet losses, due to gas expansion and contraction can be described as:

$$\Delta P_{In/Out} = Z_{In/Ou}\left(\frac{\rho v^2}{2}\right) \tag{3.2}$$

where ρ is the exhaust gas density, v is the exhaust gas velocity, and $Z_{In/Ou}$ defines the friction coefficients for the inlet channel gas contraction as:

$$Z_{In} = -0.415\left(\frac{A_f}{A}\right) + 1.08 \tag{3.3}$$

and the outlet channel gas expansion as:

$$Z_{Out} = \left(1 - \frac{A_f}{A}\right)^2 \tag{3.4}.$$

The area terms in Equations 3.3 and 3.4 relate the filter frontal area, A_f, to the total surface area, A. As listed in Table 3.1, the pressure drop due to inlet gas expansion and outlet contraction is generally small compared with the total filter pressure drop. The equations described above assume laminar flow at the filter inlet and exit. Where this is not the case, the appropriate friction coefficients for turbulent or transition flows must be used [51].

Pressure drop due to frictional losses in the exhaust gas flows along the channels can be estimated from the following equation:

$$\Delta P_{Channel} = 4f\left(\frac{L}{D_H}\right)\left(\frac{\rho v^2}{2}\right) \tag{3.5}$$

where f is the Fanning friction factor, L is the length of the channel, D_H is the channel hydraulic diameter, ρ is the exhaust gas density, and v is the exhaust gas velocity in the channel. The friction factor may be estimated from:

$$f = \frac{K}{\mathrm{Re}} \tag{3.6}$$

where Re is the Reynolds number and K is equal to 14.23 for DPF channels with a square cross section and 16.00 for channels with a round cross section [51]. It is important to note that the profile of the channel cross section may change as the channel becomes loaded with ash or soot, thus affecting both the cross-sectional area and the value of the friction factor. The exhaust gas flow in DPF channels is typically laminar. The pressure drop due to flow along the DPF channels is generally a fraction of the pressure drop due to flow through the porous media, however it can become significant, particularly at high soot and ash loads, where the channel hydraulic diameter is considerably reduced.

The pressure losses associated with flow through the porous filter walls, and soot and ash layers, provide the largest contribution to filter pressure drop. The flow through a porous media can be described using Darcy's Law. However, the Forchheimer-Extended Darcy Equation provides a more accurate estimate of pressure drop through the porous layers by accounting for inertial effects as well:

$$\Delta P_{Wall\,/\,Ash\,/\,Soot} = \left(\frac{\mu}{K_P}\right) \cdot v_w \cdot w + \beta \cdot \rho \cdot v^2 \tag{3.7}$$

where μ is the exhaust gas dynamic viscosity, K_p is the permeability of the porous media, v_w is the gas wall velocity, w is the layer thickness, and β describes the inertial resistance. In most practical applications of diesel particulate filters, the Reynolds number for flows through the porous layers is much less than one, and inertial terms can be neglected as a first-order approximation. Neglecting the inertial term results in the well-known form of Darcy's Law:

$$\Delta P_{Wall\,/\,Ash\,/\,Soot} = \left(\frac{\mu}{K_P}\right) \cdot v_w \cdot w \tag{3.8}.$$

Ash and soot accumulation in the DPF increases the material layer thickness, w, and introduces additional flow resistance through the porous layer, reflected in the layer permeability, K_p [52]. The effect of material accumulated in the pores, as opposed to the cake layer, is more complicated; however it can be accounted for in Equation 3.8 by modifying the filter's wall permeability to reflect the amount of material occupying the pores, i.e. reduction in pore diameter.

3.1.2 Controlling Properties and Parameters

Although, the basic zero-dimensional description of filter pressure drop outlined in the previous section does not describe all of the details and parameters affecting filter pressure drop, it is useful to highlight the key parameters and material characteristics warranting further investigation. The thickness and permeability of the accumulated material layers are two of the most important parameters used to characterize flow through porous media and are reflected in Darcy's Law in Equation 3.8.

Permeability is related to an average pore diameter, shape, and length, and as such, has dimensions of [L^2]. It is an intensive property of the porous medium and thus does not depend on the sample size for a homogenous medium [53]. The permeability of a porous material is directly related to the porosity and pore diameter of the material. For the DPF substrate, characterizing these properties is fairly straightforward, and the DPF permeability can be estimated as follows:

$$K_w = \frac{1}{5.6}\varepsilon^{5.5} d_p^2 \tag{3.9}$$

where ε is the porosity and d_P is the pore diameter [52]. The porosity describes the void volume of the porous material. While the porosity of the clean cellular ceramic substrates is often specified by the manufacturer, it can be computed for the soot or ash layers accumulated in the DPF as:

$$\varepsilon = 1 - \frac{\rho_{Packing}}{\rho_{Theoretical}} \qquad (3.10).$$

The packing density, $\rho_{Packing}$, is the measured density of the porous material or powder and the theoretical density, $\rho_{Theoretical}$, is the true density of that material. The packing density has a direct effect on the volume (layer thickness) of the accumulated material in the DPF as well. While measurements of substrate permeability, porosity, packing density, and mean pore size are fairly straightforward, the same measurements are significantly more challenging when applied to the ash and soot layers. Further, soot and ash also accumulate in the pores of the DPF during the initial filter loading phase, altering the properties of the substrate as well.

Soot packing density and the resulting soot layer permeability is significantly affected by soot particle size, deposition angle, and velocity, among others. Furthermore, lubricant-derived ash is deposited on the filter along with the soot. The ash layer forms following soot oxidation, whereby the ash particles agglomerate and form various porous structures. While considerable efforts have been devoted to better understand soot layer properties and characteristics, little is known about the governing processes controlling ash layer formation and packing in the DPF. In general, however, the permeability of the ash layer is expected to be directly related to the porosity and mean pore size.

3.2 Material Properties

Before examining the details of the various parameters controlling DPF pressure drop, it is useful to understand the length scales at which these processes take place. In many cases, the length scales are directly related to the material properties of the DPF, and the ash and soot accumulated therein. The following is a brief discussion of theses properties and their impact on filter pressure drop.

3.2.1 DPF Properties

The DPF properties directly affect both the filter trapping efficiency as well as the filter's pressure drop characteristics. While the filter's pore geometry and pore characteristics are initially determined by the manufacturer, these parameters quickly change for a filter in use, due to soot and ash accumulation in the pores, as well as on the filter surface. Table 3.2 presents typical properties for two commonly used DPF substrates, cordierite and silicon carbide [52].

It is instructive to compare the DPF properties listed in Table 3.2, with the soot and ash properties presented in Sections 3.2.2 and 3.2.3, particularly ash particle sizes, layer thickness, and permeability with the typical pore sizes, dimensions, and permeability values for the DPF substrates. A 2004 study using mercury porosimetery with ash loaded cordierite filters measured the combined porosity of the ash and substrate between 35% and 40% and average pore sizes of 15 to 16 μm [35].

Property		Cordierite	SiC
Channel Width	[mm]	1.3 - 2.1	1.0 - 1.6
Wall Thickness	[mm]	0.3 - 0.5	0.3 - 0.8
Mean Pore Size	[μm]	13 - 34	8 -17
Porosity	[%]	45 - 50	42 - 58
Permeability	[m^2]	0.5×10^{-12}	$1.2 - 1.3 \times 10^{-12}$
Melting/Sublimation Temperature	[° C]	1,450	1,800 - 2,400

Table 3.2. Compilation of typical properties of cordierite and silicon carbide DPFs.

As listed in Table 3.2, the porosity for typical cordierite and SiC DPFs ranges from 45% to almost 60% depending on the filter material and geometry. In most cases, over half of the DPF wall volume consists of void space, which is composed of a network of pores. The electron micrographs in Figure 3.3 depict the wall structures for polished samples from cordierite particulate filters.

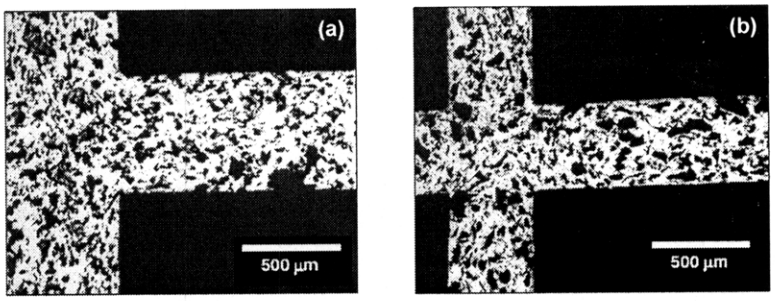

Figure 3.3. Micrographs of polished cordierite samples from (a) RC 200/19 and (b) EX-80 100/17 diesel particulate filters [54].

3.2.2 Ash Properties

The first step in understanding ash effects on DPF performance is to quantify key ash properties and understand how those properties affect filter performance characteristics. The second step, and currently the largest knowledge gap, is understanding how certain parameters such as lubricant chemistries, exhaust conditions, and regeneration strategy affect the ash properties that, in turn, affect DPF performance.

A number of studies in the literature have measured ash properties such as packing density, porosity, and permeability which are known to affect filter pressure drop. Table 3.3 presents a summary of ash property values reported in the literature along with their respective sources [24, 26, 55 - 57].

Source (SAE)	Packing Density [g/cm^3]	Theoretical Density [g/cm^3]	Porosity [%]	Permeability [m^2]
2000-01-1016[i]	0.4 - 1.0			2.8 - 7.4 x 10^{-14}
2001-01-0190	0.54	3.13	83	
2004-01-0948[ii]	0.4	2.5	85	~ 5 x 10^{-12}
2005-01-3716		2.85		
2006-01-3257	0.32 - 0.52			
2008-01-0331[iii]	0.45			

i. Permeability estimated by the authors.
ii. Permeability listed as 10X more permeable than cordierite
iii. Study used fuel-borne catalyst for regeneration.

Table 3.3. Compilation of select ash properties. Except where otherwise noted, data is from field-aged DPFs.

In many cases, the wide range of values reported for the ash properties listed in Table 3.3 is due to differences in specific test parameters and measurement techniques. Ash theoretical density is based on the true density of an assumed, or in some cases, measured ash composition. Ash packing density has also been reported to vary in both the radial and axial directions in some DPFs [26].

Ash particle size plays a strong role in influencing the properties listed in Table 3.3, and the geometry of the ash layer significantly influences DPF performance as well. Table 3.4 presents a summary of ash particle sizes and layer deposit thicknesses reported in the literature, along with their respective sources [22, 24, 38, 55, 58, 59]. Ash deposits are believed to be composed of micron-sized structures formed by agglomerates of smaller sub-micron-sized ash particles.

Once again, different test parameters and measurement techniques may be partly responsible for the large range of values reported in Table 3.4. A 2006 study of field ash samples indicated low sulfated ash oils may lead to the formation of ash with larger particle structures as compared to higher sulfated ash oils [26].

Source	Particle Size [μm]	Deposit Thickness [μm]
SAE 2000-01-1016	d_{eff} ~ 0.5 - 2.0 range ~ (1-10)	
SAE 2001-01-0190	$d_{primary}$ ~ 0.1 -0.5	
SAE 2004-01-0948	2.4 - 37.6	
SAE 2004-01-3013[i]		73 - 298
MECA 2005	5 - 50	
SAE 2005-01-3716	0.4 - 8	
SAE 2006-01-0874[ii]	1	
SAE 2006-01-3416[ii]		44 - 94
i. Data from accelerated and un-accelerated testing. ii. Data from accelerated testing.		

Table 3.4. Compilation of ash particle size and layer thickness from the literature. Except where otherwise noted, data is from field-aged DPFs.

Aside from deposit thickness, the location and distribution of the ash deposited in the DPF may also significantly affect filter pressure drop. Experimental and computational studies have shown that ash generated under periodic regeneration tends to accumulate in ash plugs at the back of the DPF, whereas ash accumulated under continuously regenerating conditions is evenly distributed along the channel walls with little plug formation. These differences in the bulk ash distribution may appreciably affect the magnitude of the ash effect on DPF pressure drop [44, 45]. The factors controlling the location of ash deposition, mobility, and accumulation in the DPF are not well understood.

Based on the ash property measurements reported in the literature, it is clear that lubricant chemistries play an important role in influencing ash physical and chemical properties. However, equally important are the exhaust conditions (temperature and flow) that affect ash deposition, packing characteristics, and mobility within the DPF. Knowledge of the effects of each of these parameters is critical to understanding the underlying mechanisms responsible for the observed ash effects on DPF performance.

3.2.3 Soot Properties

In contrast to the factors affecting ash properties, soot layer properties and the controlling parameters affecting these properties are much better understood. Soot layer packing density and permeability have been reported as a function of the Peclet number (Pe), which provides a measure of inertial and diffusional deposition. In a 2002 study by Konstandopoulos et al., the following relationships were defined relating soot properties to the Peclet number:

$$Pe = \frac{U_w \cdot d_{Primary}}{D} \tag{3.11}$$

where U_w is the filtration velocity, $d_{Primary}$ is the primary soot particle diameter (typically ~25-40 nm), and D is the diffusion coefficient. A high value for the Pe number results in more inertial deposition and a more densely packed soot layer, whereas a low value for

the Pe number results in a more loosely packed soot layer due primarily to diffusional deposition [60].

The diffusion coefficient, D, can further be estimated from the known exhaust gas properties and soot aggregate geometry as:

$$D = \frac{K_B \cdot T}{3\pi \cdot \mu \cdot d_{agg}} \cdot SCF \tag{3.12}$$

where K_B is Boltzmann's constant, T is the exhaust temperature, μ is the exhaust gas dynamic viscosity, and d_{agg} is the aggregate soot particle diameter, generally on the order of 100 nm. SCF is the Stokes-Cunningham Factor to account for non-continuum conditions due to the small size of the soot particles. The SCF can be expressed as a function of the Knudsen number, Kn, as follows:

$$SCF = 1 + Kn\left(1.257 + 0.4e^{-1.1/Kn}\right) \tag{3.13}$$

where the Knudsen number relates the gas mean free path to the particle length scale:

$$Kn = \frac{2\lambda}{d_{agg}} \tag{3.14}.$$

The Knudsen number is generally in the range of 1 to 5 for soot particles in diesel exhaust. The gas mean free path, on which the Knudsen number is based, is computed from the exhaust gas conditions as:

$$\lambda = \nu\sqrt{\frac{\pi MW}{2RT}} \tag{3.15}$$

where ν is the exhaust gas kinematic viscosity, MW is the exhaust gas molecular weight, R is the universal gas constant, and T is the exhaust gas temperature. The Peclet number

defined in equation 3.11 is therefore a direct function of the exhaust conditions and soot particle size [60]. Figure 3.4 presents the variation of soot layer properties as a function of the Peclet number.

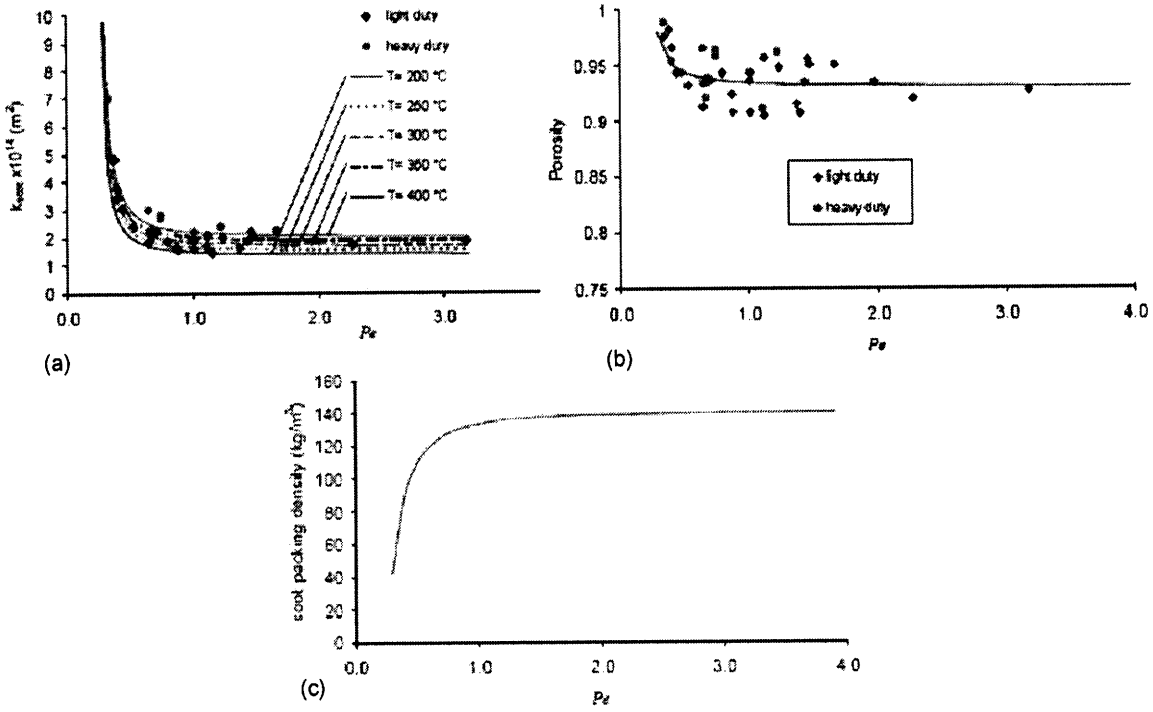

Figure 3.4. Variation of soot (a) permeability, (b) porosity, and (c) packing density as a function of Pe number [60].

The soot permeability may also be expressed as a direct function of the exhaust gas conditions and soot particle geometry. The soot layer permeability is defined as:

$$K_{Soot} = f(\varepsilon) \cdot d^2_{\text{Primary}} \cdot SCF \qquad (3.16).$$

The soot layer permeability is, thus, a direct function of the soot layer porosity and particle size. The porosity function, f(ε) is computed from the measured soot layer porosity:

$$f(\varepsilon) = \frac{2}{9} \cdot \frac{\left[2 - (9/5)(1-\varepsilon)^{1/3} - \varepsilon - 1/5 \cdot (1-\varepsilon)^2\right]}{(1-\varepsilon)} \qquad (3.17).$$

As evident in Figure 3.4, the experimentally determined soot properties exhibit a fairly good correlation with the Pe number [60]. For cases in which the Pe number is greater than 1 and inertial deposition dominates, soot properties are relatively constant. These conditional arise when soot particles are fairly large, or when filtration velocities are relatively high, as is most often the case.

Packing densities for soot particles on the order of 0.1 g/cm^3 and PM layer permeability values in the range of $1.5x10^{-14}$ m^2 to $3.3x10^{-14}$ m^2 are reported in the literature [58, 61]. Based on the ash property data in Table 3.3, ash packing densities are roughly four times greater than PM packing densities. Due to the large variation in ash permeability values, differences in ash and soot permeability may vary between a factor of two and one-hundred.

While soot properties appear to be fairly well correlated to Pe number, accurate determination of the Peclet number is oftentimes difficult due to the challenges associated with determining soot particle size. Diesel particles exhibit a bimodal size distribution with primary particles in the 10 nm to 40 nm range and PM agglomerate sizes on the order of 100 nm [62, 63]. Ash particle sizes listed in Table 3.4 are on the order of 1,000 nm. Given the difficulties associated with accurately estimating the Pe number for actual engine-out soot and exhaust conditions, other studies have attempted to correlate the soot layer properties directly to filtration velocity, soot mass loading, and filter pressure drop.

Figure 3.5 presents the variation in measured soot packing density as a function of DPF wall velocity and total soot load. The experimental data presented in Figure 3.5 was based on measured soot layer properties for soot layers generated in a single channel DPF sample under carefully-controlled conditions. The authors further noticed some effect of DPF pressure drop on soot layer packing density; however the specific impact of filter pressure drop was unclear. Pressure drop is not expected to considerably affect soot packing given the exhaust conditions generally observed for normal engine operation.

The authors further estimated soot layer permeability based on the experimental data, and the summary of the results is presented in Table A-1 of the Appendix [64].

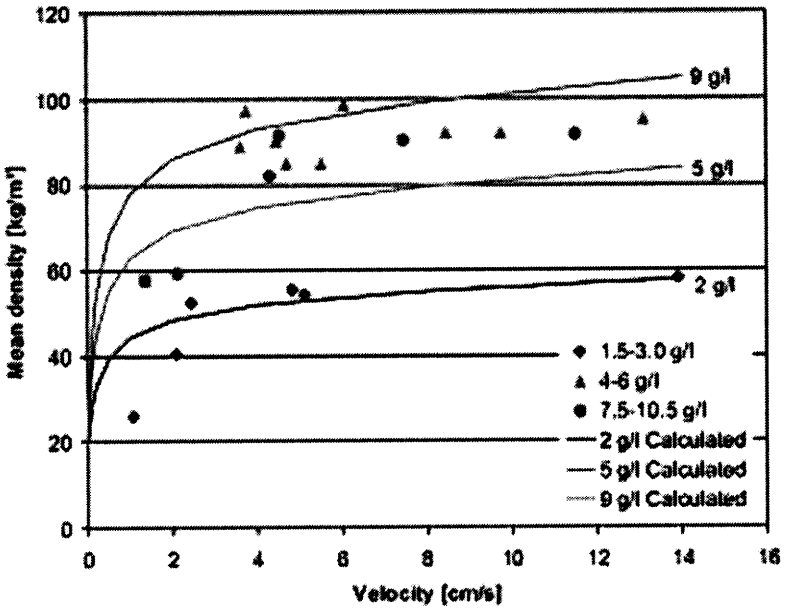

Figure 3.5. Soot layer packing density as a function of filtration velocity for three levels of DPF soot loading [64].

Based on the data available in the literature and summarized above, the variation of soot properties with exhaust conditions and soot particle size is fairly well understood. Studies investigating lubricant-derived ash distribution on the particulate matter entering the DPF indicated the ash constituents to be finely distributed on the PM agglomerates. No lubricant-derived ash compounds were found to exist separately from the carbonaceous PM in the exhaust [65]. Given the large difference in reported in ash and soot particle sizes, it appears that the ash compounds and precursors, initially finely distributed on the PM, fuse together and agglomerate once deposited in the DPF. The parameters controlling ash formation and accumulation within the DPF are not nearly as well understood as those controlling PM deposition, much less the resulting ash layer properties. This study aims to investigate the factors controlling these processes, and ultimately correlate changes in the factors affecting ash properties to DPF performance.

3.3 DPF Pressure Drop Performance Characteristics

Using the zero-dimensional models and the soot and ash properties described above, a series of calculations were performed to evaluate the effect of individual parameters on DPF pressure drop. These initial calculations are useful to frame the expected experimental results as well as to identify key areas requiring further experimental and more sophisticated modeling efforts.

Figure 3.6 presents the results of the filter pressure drop calculations as a function of channel area restriction for a DPF containing various ash levels. The calculations assume all of the ash is deposited in a layer along the channel walls with a packing density of 0.25 g/cm^3, a permeability of 3.0x10^{-14} m^2, and a DPF space velocity of 20,000 hr^{-1}.

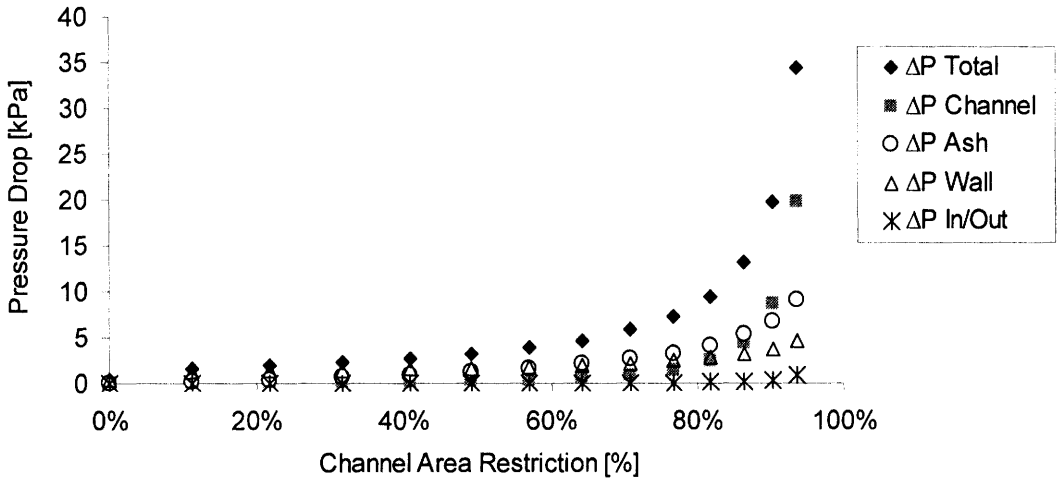

Figure 3.6. Effect of channel area restriction on individual components of DPF pressure drop for a DPF containing only ash, with 100% of ash accumulation on the channel walls.

The results of the calculations show a significant effect on pressure drop for channel area restrictions above 65%. In general, these high levels of channel area restriction are not expected to occur in on-engine applications. Typical field-aged DPFs may contain 30 g/l to 40 g/l ash before cleaning, which corresponds to 30% - 40% reduction in channel area.

Initially, for channel area restrictions below 50%, the pressure drop through the ash and soot layers accumulated along the filter walls provides the most significant contribution to the total filter pressure drop. However, as the channel area is further restricted, the pressure drop for the flow through the channel becomes the dominant parameter. For typical ash levels expected in the experiments conducted as part of this study, the effect of channel area restriction due to ash accumulation is expected to be between 1 – 3 kPa.

The same calculations were performed to compute DPF channel and wall velocities as a function of channel area restriction due to ash accumulation. The results of these calculations are shown in Figure 3.7. Similar to the pressure drop data in Figure 3.6, reducing the channel area restriction beyond 65% gives rise to a large increase in both the channel and filter wall velocities. For typical ash loading cases with channel area restrictions less than 40%, the increase in wall and filtrations velocities is much less drastic and fairly linear.

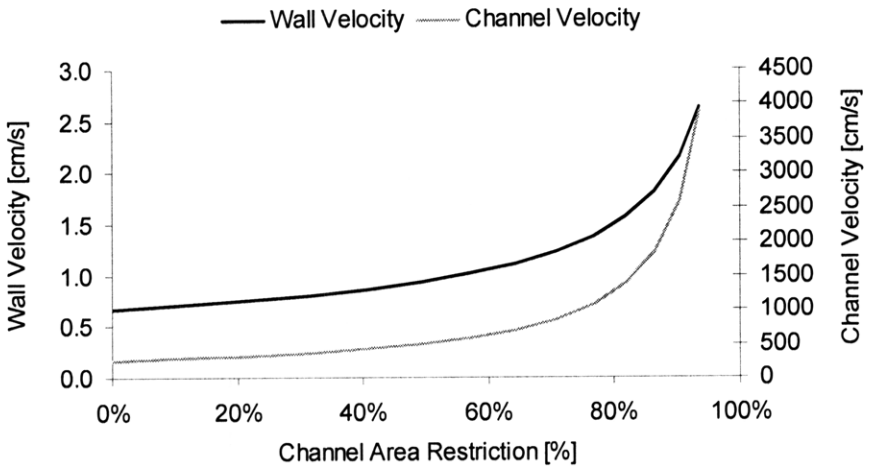

Figure 3.7. Effect of channel area restriction on individual wall and channel velocities for a DPF containing only ash, with 100% of ash accumulation on the channel walls.

The change in filter pressure drop as a function of channel length reduction was also computed and the results are shown in Figure 3.8. The calculations assume all of the ash is deposited in a plug at the end of the channel with a packing density of 0.25 g/cm^3, a permeability of 3.0×10^{-14} m^2, and a DPF space velocity of 20,000 hr^{-1}. Since all of the

ash was assumed to accumulate at the back of the channel in end-plugs, no ash was accumulated along the channel walls. The most significant contribution to the total filter pressure drop is attributed to the pressure drop through the DPF substrate.

In contrast to the results presented in Figure 3.6 for the case in which all of the ash was deposited along the channel walls, the channel pressure drop is only a minor contributor to the total filter pressure drop when all of the ash is accumulated in the channel end-plug. The overall magnitude of the effect of channel length reduction (ash accumulation in the end-plug) on filter pressure drop is less than the pressure drop predicted for similar amounts of ash accumulated along the channel walls, by approximately a factor of two.

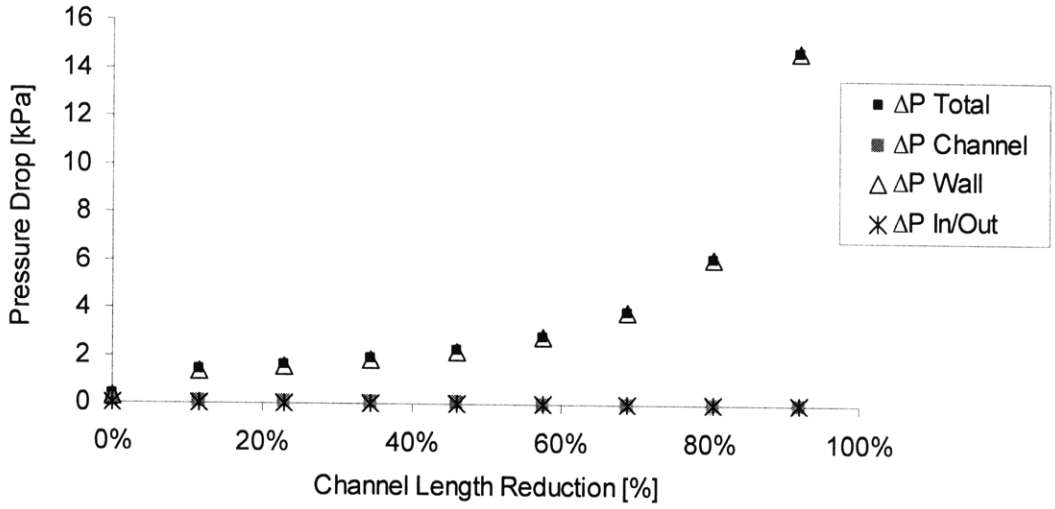

Figure 3.8. Effect of channel length reduction on individual components of DPF pressure drop for a DPF containing only ash, with 100% of ash accumulation in end-plugs.

Figure 3.9 presents the estimated wall velocities and channel velocities as a function of channel length reduction with all of the ash accumulated in the end-plug.

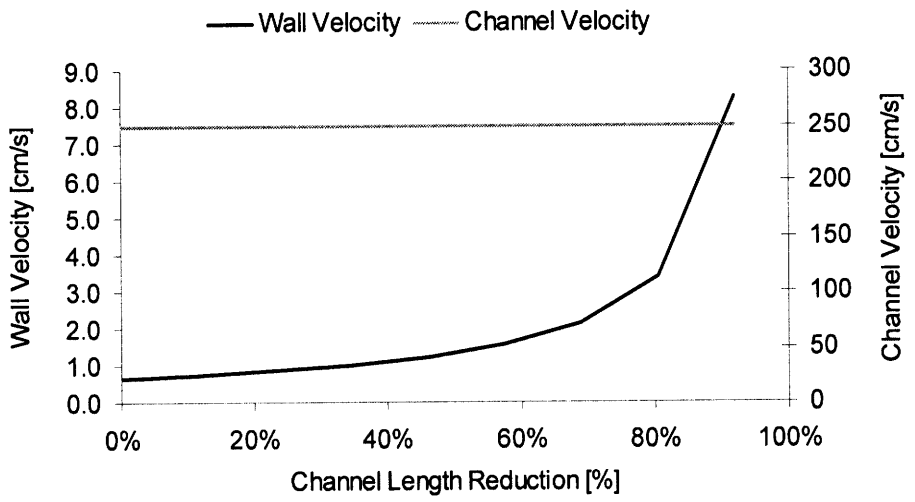

Figure 3.9. Effect of channel length reduction on individual wall and channel velocities for a DPF containing only ash, with 100% of ash accumulation in the channel end-plugs.

As no ash is accumulated along the channel walls, the channel hydraulic diameter and channel velocity remains constant. On the other hand, as the channel length is reduced, the wall velocities increase quite significantly. The increase in channel wall velocities as ash is accumulated in the end-plugs and the effective filter length is reduced, is responsible for the observed increase in pressure drop shown in Figure 3.8. Furthermore, the increase in wall velocity for the case in which all of the ash is accumulated in the channel end-plug is approximately twice as large as the case in which all of the ash is deposited along the channel walls, shown in Figure 3.7.

Figure 3.10 shows the reduction in channel area and length for the two hypothetical ash accumulation scenarios. When all of the ash is assumed to accumulate in the end-plug at the back of the channel, the channel length is reduced. At an ash level of 40 g/l, a 46% reduction in channel length is observed. On the other hand, for the case in which all of the ash is assumed to accumulate along the channel walls, the channel area is reduced by approximately 41%. For real cases in which ash is accumulated along the channel walls and in end-plugs at the back of the channel, the reductions in channel length and area will be proportional to the amount of ash accumulated in those regions.

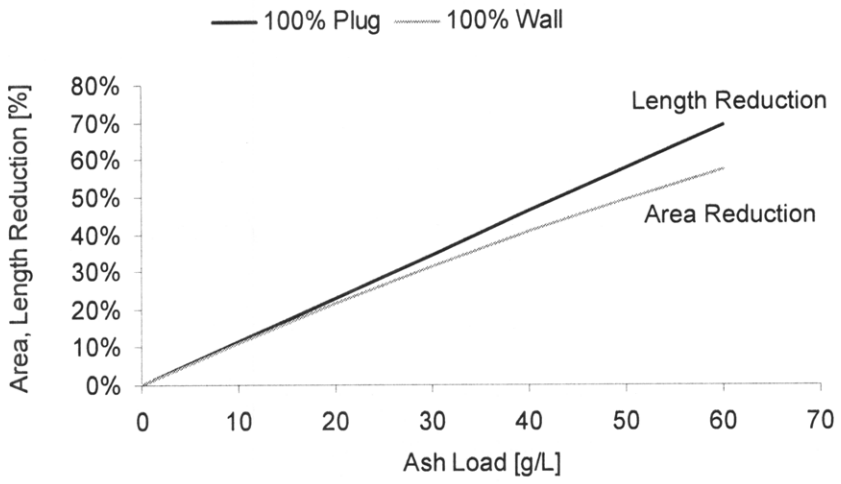

Figure 3.10. Reduction in channel area and length as a function of ash accumulation for 100% of ash accumulated on channel walls and 100% of ash accumulated in the end-plug.

In reality, both ash and soot accumulate in the DPF. Figure 3.11 presents the changes in filter geometries for the two ash distribution scenarios as a function of soot load for a DPF containing 33 g/l ash. For both cases, the soot was assumed to distribute evenly along the available filter length, and the soot density was held constant at a value of 0.1 g/cm^3.

For the case in which all of the ash is accumulated on the channel walls, additional soot accumulation on the walls further reduces the available cross-sectional area of the channels. On the other hand, for cases in which all of the ash is packed in the end-plug at the back of the channel, the channel length is already reduced by nearly 40% for a DPF containing 33 g/l ash. Further, soot accumulates directly on the filter walls, but the soot layer thickness increases much more rapidly due to the reduced filter length. These large differences in the bulk soot and ash distribution are expected to have significant effects on total filter pressure drop.

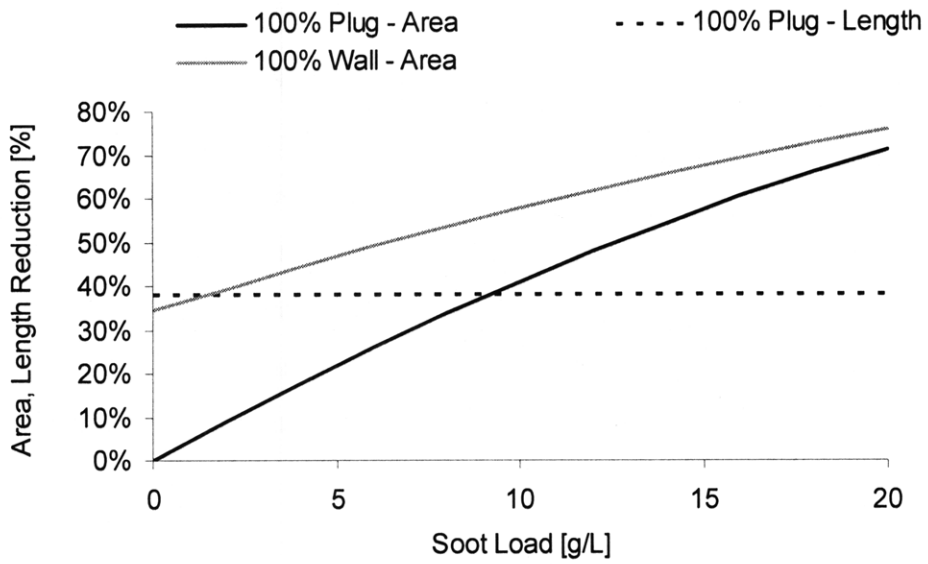

Figure 3.11. Reduction in channel area and length as a function of soot load for 100% of ash accumulated on channel walls and 100% of ash accumulated in end-plug for a DPF containing 33 g/l ash.

The results of the zero-dimensional calculations presented in this section highlight the large-scale effects of soot and ash distribution in the filter on DPF pressure drop. The specific details and parameters controlling the various effects, soot and ash properties, and ash packing and distribution, are the subject of the targeted experiments and detailed modeling efforts undertaken as part of this study. While approximate, these calculations serve to frame the expected experimental results and the also highlight the detailed effects requiring further investigation.

3.4 Cake Filtration Theory

While the information presented in Section 3.2 identified many of the parameters influencing DPF pressure drop performance, it fails to accurately describe the underlying physical processes and many of the subtleties which can have a significant effect on how the accumulated ash and soot affect filter pressure drop. Unlike diesel particulate filters which have only recently been the subject of significant research efforts, cake filtration theory has been studied for over a century.

Houi et al. applied a statistical model to describe the physical mechanisms governing particle deposition and cake layer growth observed in experiments. The simulations described particle motion in terms of a random, diffusive component (Brownian motion), and a ballistic component driven by drag forces on the particle due to fluid flow. The authors utilized two simulations: Type A to explore the details of the deposit structures using only a small number of particles (1,000), and Type B using a much large number of particles to describe the macroscopic structure of the cake layer. The simulation results are depicted in Figure 3.12.

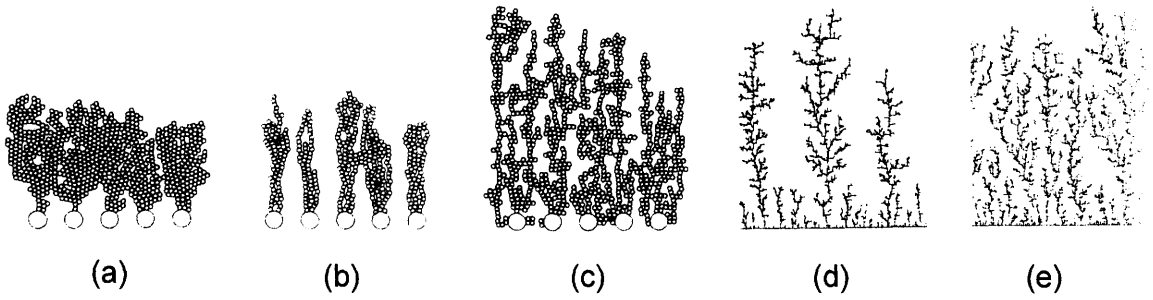

Figure 3.12. Simulation results for (a-c) 1,000 particle simulation where the particles are deposited on individual collectors, and (d, e) macroscopic structure and evolution of the cake layers [66].

The results presented in Figure 3.12 (a-c) show the details of particle deposit evolution for particles having a much smaller diameter than the filter pores. The filter surface is represented by collectors depicted as outlined circles. Soot and ash accumulation in diesel particulate filters occurs on similar length scales. Figure 3.12 (d, e) depicts the evolution and growth of the particle structures over time. Furthermore, the simulation also accounted for a "sticking" probability, i.e. a parameter based on the angle of incidence of the particle, to determine whether or not the particle sticks to the structure or simply bounces away. The authors observed that the density of the particle layers increased as the sticking probably decreased; that is the particles do not initially stick to the structure but may bounce off multiple structures before finally settling and forming a deposit. Furthermore, the authors noted that the structures depicted in Figure 3.12 are obviously unstable and will eventually collapse to form bridges [66].

Tassopoulos et al., observed similar effects related to deposit structure formation. The authors noted that as the Peclet number decreases (ie. Brownian motion becomes more important) the resulting deposit structures become more open, the average height of the deposit increases, and tree-like patterns begin to appear. Further, particles deposited under these conditions exhibit a fractal structure in which the average height of the deposit increases with the number of particles in a non-linear manner. For particles deposited with $Pe<0.4$, the resulting structures are very open. On the other hand, particles deposited under ballistic conditions tend to be more densely packed and exhibit porosity independent of any particle length scales [67].

Tassopoulos, in his dissertation, provides additional details regarding the relationship between particle deposition mechanisms, the resulting deposit microstructure, and particle transport processes. This study utilized computer simulations to account for particle impact velocity, incident angle (measured from the normal to the target), and the number of particle "rolling events," and resulted in the following main conclusions:

(1) Increasing the angle of incidence of the arriving particle results in more open and fingerlike deposits.
(2) For any given incident angle, increasing the velocity of the incoming particle results in more dense deposits. This compacting effect becomes more pronounced as the angle of incidence increases.
(3) Particles arriving normal to the surface result in deposits having solid fractions approaching the random-loose-packing level, and thus cannot easily become denser. Furthermore, the deposit solid fraction for particles arriving normal to the surface was reported at 52%, independent of the initial particle velocity.
(4) As the particle incident angle increases, the effect of impact velocity is more pronounced. For large incident angles, increasing the impact velocity always has a compacting effect.
(5) Increasing the number of rolling events generally results in more densely packed deposits. Simulations allowing for many rolling events lead to deposit structures

exhibiting a porosity in close agreement with experimentally-derived porosity values for packed beds.

(6) The predicted surface roughness for deposits formed by particles arriving normal to the surface was almost flat. On the other hand, strong fluctuations in surface roughness were reported for particles arriving with at an incident angle of 65°, indicating the formation of very large void regions until some later point where these regions are blocked by newly-arriving particles.

(7) The size, shape, and orientation of the arriving particles can significantly affect the microstructure of the deposits. Large particle mean-free-paths (mean-free-path larger than the actual particle size, Kn<1) generally result in more compact deposits [68].

Figure 3.13 presents several schematics depicting cake layer morphology for deposits generated under varying conditions.

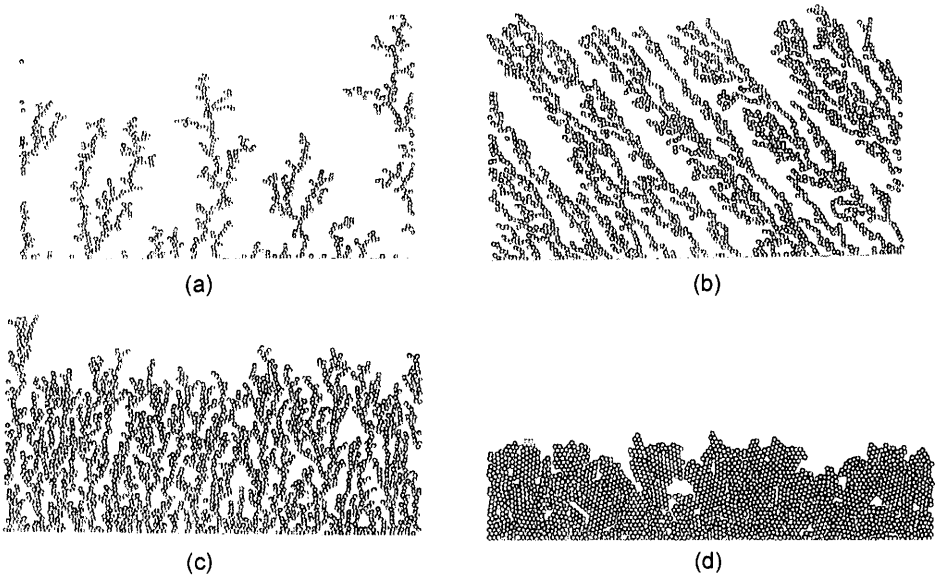

Figure 3.13. Particle deposition and filter cake layer growth for (a) pure diffusional deposition, (b) ballistic deposition at 60° incident angle, (c) ballistic deposition normal to the filter surface, and (d) ballistic deposition with particle restructuring, i.e. multiple rolling events [68].

Similar results were reported in a computational study by Konstandopoulos in 2000. Figure A-1 in the Appendix presents a summary of the results along with schematics depicting the deposit microstructures for a range of particle incident angles and impact velocities [87]. Further, the models were extended and applied to soot accumulation in diesel particulate filters. Figure 3.14 shows a simulated soot deposit generated at high Peclet numbers on the surface of a wall-flow diesel particulate filter.

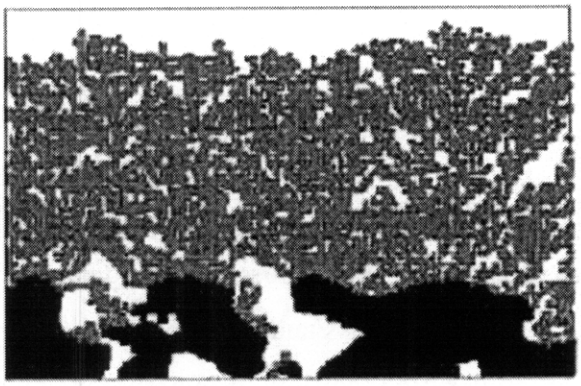

Figure 3.14. Simulated soot deposits generated at a high Pe number on the DPF surface [60].

Based on the physical description of particulate matter deposition and accumulation in the cake layer on a diesel particulate filter, the resulting deposit microstructure can be expected to more closely resemble a loose network of interconnected pores, the boundaries of which are defined by finger- or tree-like structures, as opposed to a bed of packed spheres. Furthermore, the dependence of the deposit morphology on particle incidence angle and velocity may be affected by the presence of ash in the filter channels.

Ash accumulation reduces the available filter area, resulting in increased gas velocities through the filter walls, thereby increasing the velocity of the particles entrained in the gas stream. Furthermore, the restriction of the channel hydraulic diameter with ash accumulation may also serve to increase the incident angle of the arriving particles. The experiments and accompanying models, developed as part of this work, aim to explore these effects in greater detail.

3.5 DPF Pressure Drop Models

A number of DPF pressure drop models have been developed over the last thirty years. While the complexity of these models has increased to account for a number of additional details, the underlying theory remains the same, based largely on mass and momentum balance and considering Darcy pressure drop through the porous media. While many of these models have focused on predicting pressure drop in clean and soot-loaded filters, very few have accounted for ash accumulation.

3.5.1 Clean DPF and Soot Models

A basic pressure drop model describing the performance of clean DPFs was developed by Konstandopoulos and Johnson in the late 1980s. This model applied the one-dimensional form of the governing equations for mass and momentum transport of the exhaust gasses and utilized Darcy's Law to describe the flow through porous media. The mass balance of exhaust flow through the channels is:

$$\text{Inlet Channel: } \frac{d}{dx}\left(\rho u_1\right) = -\frac{4}{a}\rho u_w \tag{3.18}$$

$$\text{Outlet Channel: } \frac{d}{dx}\left(\rho u_2\right) = -\frac{4}{a}\rho u_w \tag{3.19}$$

where ρ is the exhaust gas density, $u_i(x)$ is the exhaust gas channel velocity, a is the channel width, u_w is the gas wall velocity, and the factor of 4 accounts for gas flows through all four sides of the channel. Similarly, the momentum balance for the flow through the channels is described as:

$$\text{Inlet Channel: } \frac{d}{dx}\left(\rho u_1^2\right) = -\frac{dP_1}{dx} - \frac{S}{A}\tau_1 \tag{3.20}$$

$$\text{Outlet Channel: } \frac{d}{dx}\left(\rho u_2^2\right) = -\frac{dP_2}{dx} - \frac{S}{A}\tau_2 \tag{3.21}$$

where $P_i(x)$ is the channel pressure, S is the channel perimeter, A is the channel area, and τ is the shear stress. Further, Darcy's Law to describe the flow the porous media is:

$$-\nabla P = \frac{\mu}{k}\mathbf{u} \tag{3.22}$$

where k is the permeability of the porous media. Darcy's Law, applied to describe the pressure drop across the porous DPF wall, or soot/ash layer can be written as:

$$P_1 - P_2 = \frac{\mu}{k} u_w \cdot w_s \tag{3.23}$$

where w_s is the wall/layer thickness. Applying the appropriate boundary conditions, sufficient parameters are described to solve the system of equations and compute the filter pressure drop. The boundary conditions are listed as:

$$u_1(0) = U \tag{3.24}$$

$$u_2(0) = 0 \tag{3.25}$$

$$P_2(L) = P_{atm} \tag{3.26}.$$

It should be noted that the above-derivation neglected to account for the DPF inlet and outlet pressure losses, which the authors described as minimal for typical exhaust conditions. The model further neglected inertial effects in the formulation on Darcy's Law to describe the exhaust gas flow though the filter substrate. Nonetheless, the model described above was in good agreement with experimental data for pressure drop over clean filters [69].

More advanced models have since been developed, building on the basic framework outlined above. Most notably, these models have included additional parameters to account for inlet and outlet losses, inertial effects, and soot deposition. Johnson in 2000

expanded upon the previous work, noted above, and presented the results along with experimental data for two different particulate filter cell geometries of 100 and 200 cpsi. The most notable addition in the Johnson model over the previous work was the addition of a term to account for losses at the inlet and outlet regions of the DPF channel:

$$\Delta P_{In/Out} = \xi \rho_{Exh} v^2 \tag{3.27}$$

where ξ is the contraction/expansion inertial loss coefficient, which depends upon the filter open cross-sectional area and the Reynolds number. Furthermore, this model also included the effect of soot accumulation in the DPF pores and in the cake layer on the filter substrate. The authors estimated the soot layer permeability from the well-known correlation of Rumpf and Gupte:

$$k_P(t) = \frac{\varepsilon(t)^{5.5} \cdot D_P^2}{5.6} \tag{3.28}$$

where D_P is the particle diameter and ε is the porosity, which varies a function of time. The value of D_P was adjusted in the models to describe the change in permeability due to soot accumulation in the DPF pores during the initial soot loading phase [70].

Subsequent models have evolved to include inertial effects in the Darcy term, which can become significant at high filtration velocities or for high porosity filters. The pressure drop through the porous media is thus described as:

$$\Delta P_{Wall} = \frac{\mu}{k} u_w w_s + \beta \rho u_w^2 w_s \tag{3.29}$$

where β is the Forchheimer coefficient and represents a length scale related to the pore "roughness." Both k and β depend on the pore size and can be related as:

$$\beta = \frac{const.}{\varepsilon^{1.5}\sqrt{k}} \tag{3.30}.$$

The value of the constant in Equation 3.30 ranges from 0.134 to 0.298 as determined from data for smooth particles and rough particles, respectively, in packed beds [71].

More advanced models have since been developed that further include additional sub-models to more accurately describe particle filtration processes as well as regeneration and DPF thermal histories. While the physics describing DPF pressure drop behavior are well understood, as evidenced in the evolution of the pressure drop models listed above, the accuracy of the models is strongly dependent upon the input parameters, specifically the properties of the porous media, such as the porosity and permeability.

Recent modeling efforts have focused on more accurately describing the properties of the porous media by including specific filtration sub-models. Initial work developing the filtration sub-models accounted for PM accumulation by diffusion and direct interception, and the estimated soot permeability was used to describe soot accumulation in the DPF pores and in the filter cake. These models computed soot permeability as a function the soot porosity and average pore diameters which were estimated based on the known soot particle size distribution and deposition mechanisms as influenced by the Peclet number [61].

Still other models have extended the one-dimensional approach to solve the full two-dimensional flow fields in the filter, and accounted for particle deposition via diffusion, inertia, and interception. These time-dependent filtration models have shown good agreement, with experiments (within 1%) for estimating filter trapping efficiencies based on the initial measured particle size distribution [49].

While much effort has been devoted to developing models to accurately predict DPF pressure drop response for clean and soot-loaded particulate filters, only a small handful of studies have applied the same methodology to account for ash accumulation in the

filter. Furthermore, even less is known about the ash properties and interaction between the ash, substrate, and soot layers, key input parameters which exert significant influence on the overall filter pressure drop.

3.5.2 Ash Models

It is surprising that relatively few DPF pressure drop models reported in the literature account for ash effects, despite the fact that filter plugging due to ash accumulation has been reported as one of the most significant problems facing engine manufacturers [58]. The DPF pressure drop models that do account for ash effects utilize the same basic formulation and follow the same approach as the clean and soot-loaded DPF models described in the previous section.

Early work incorporating ash accumulation effects in existing filter models was described by Konstandopoulos in 2000. This work extended the Darcy models for pressure drop through porous media to account for the additional contribution of the ash layer by incorporating estimated ash property measurements from laboratory and bench experiments [58]. Additional work in 2003 by the same authors refined the model to describe ash transport and distribution within the DPF channels to more accurately account for variations in ash deposition along the DPF channel walls and in end-plugs toward the back of the filter.

The ash transport model, proposed by Konstandopoulos, described ash re-entrainment in the DPF channel flow as a function of the flow shear stress along the channel walls (i.e. when the flow shear stress exceeded the local critical shear stress of the ash deposits). The critical shear stress of the ash was estimated as a function of the ash properties and thermal history to compute a relative ash "stickiness" factor. Figure 3.15 presents the simulation results for varying degrees of ash stickiness. While these models provide some conceptual description of ash transport, the authors noted that additional efforts are required to more accurately determine ash properties, particularly those which impact the critical shear stress of the ash [72].

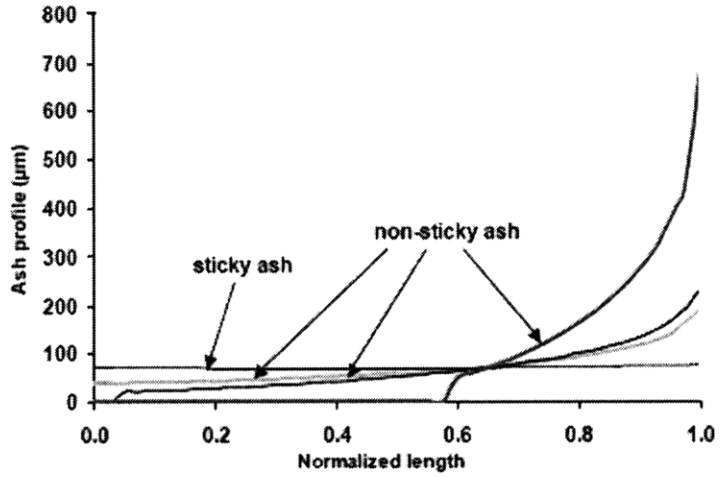

Figure 3.15. Simulated ash deposition profiles along the DPF length for varying levels of ash stickiness [72].

Information regarding the ash deposition profiles in the DPF was applied to simulations investigating the optimum DPF cell density accounting for both soot and ash accumulation in the filter. These models assumed constant values, from the literature, for ash packing density and permeability of 500 kg/m^3 and 5.2x10^{-14} m^2, respectively, and as such can only be expected to yield approximate results [73].

Perhaps the most detailed model to account for ash effects was developed by Gaiser and Mucha in 2004. The model formulation accounted for differences in soot and ash distribution along the DPF channels (wall layer vs. end-plug) as well as material accumulation in the filter pores. Figure 3.16 presents a schematic of the relevant channel geometry. The effect of ash on the pressure drop for exhaust flow through the accumulated material was expressed as:

$$P_1 - P_2 = \mu \cdot u_w \cdot \left(\frac{w_W}{k_W} + \frac{w_S}{k_S} + \frac{w_A}{k_A} \right) + \rho \cdot u_W^2 \cdot \left(\beta_W \cdot w_W + \beta_S \cdot w_S + \beta_A \cdot w_A \right) \qquad (3.31).$$

following the conventional Darcy-Forchheimer equation to also account for inertial effects. It is important to point out that accurate determination of the soot and ash layer

thickness terms, w_i, and ash and soot layer permeabilities, k_i, is critical to the application of the model, and knowledge of the parameters controlling these properties is not well-developed.

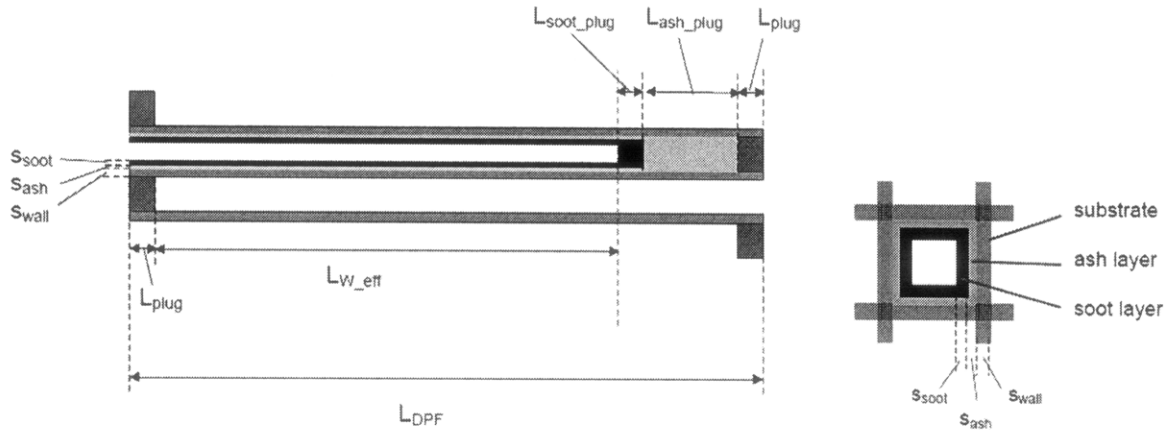

Figure 3.16. DPF channel geometry showing ash and soot distribution along the channel walls and in end-plugs at the back of the filter [44].

The results based on the model formulation described above, showed a reduction in DPF pressure drop when ash was accumulated as a plug in the back of the DPF compared with the same amount of ash accumulated along the channel walls. The additional flow resistance, due to the ash layer along the filter was cited as the reason for the observed difference in pressure drop. Interestingly, when both soot and ash were accumulated in the filter, the filter pressure drop response displayed the opposite effect [44].

While some progress has been made in extending the existing DPF models to account for ash deposition in the filter, the models are only as good as the values and parameters serving as the inputs, and much work remains. Specifically, the particular areas requiring further investigation include accounting for: (1) ash transport and distribution, (2) ash properties such as permeability, porosity, and mean pore sizes, and (3) thermal and exhaust conditional effects on the resulting ash properties. Given the well-developed state of current DPF pressure drop models, the emphasis in the this work is not so much on developing additional models, but in better defining the fundamental mechanisms controlling ash properties, which, in turn, directly affect the inputs to these models.

4 MODEL DEVELOPMENT

The model developed as part of this work, follows the framework previously developed and described in the Chapter 3. The distinguishing features of the present model include specific emphasis placed on accurately defining the ash and soot distribution within the DPF channels as well as their associated properties. The model development proceeded in parallel with the experimental work, which provided valuable inputs and served to validate the theoretical predictions. However, perhaps more importantly, application of the model provided considerable insight into the details and physical processes not readily transparent from the experimental data.

4.1 Pressure Drop Model: DPF-PERFROM

The pressure drop model developed and utilized in this study followed the same methodology and approach described by Johnson, Konstandopoulos, and Gaiser outlined in Chapter 3. The model further accounts for the actual soot and ash distribution in the filters, as observed in the experiments. Figure 4.1 presents a schematic of the DPF channel geometry, including soot and ash deposits, as well as the relevant model parameters.

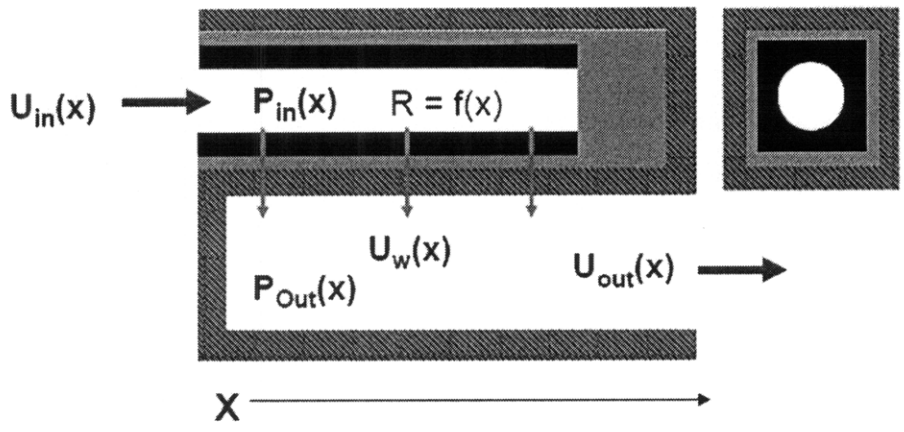

Figure 4.1. DPF channel geometry showing soot and ash distribution and relevant model parameters.

The major components of the DPF pressure drop model are summarized as follows:

(a) Axial Channel Flow: The governing equations are given by the mass and momentum balance to account for frictional losses of the flow along the filter channels. The governing equations were listed in Equations 3.18 – 3.21.

(b) Flow through Porous Media: The flow through the DPF substrate, ash layers, and soot layers is modeled using the Darcy-Forchheimer equations. Although the inertial effects are expected to be small, additional flexibility exists within the model to extend the simulations and cover a wide range of flow conditions. The formulation of the Darcy-Forchheimer equation used in this model is given in Equation 3.29.

(c) Inlet and Outlet Sections: Losses due to exhaust gas contraction at the DPF inlet and expansion at the channel outlet are accounted for using the relevant loss coefficients as outlined in Equation 3.27.

The model, described above, solves the full-coupled non-linear differential equations for the channel inlet and exit velocities for the given boundary conditions (Equations 3.24-3.26). The velocity profiles are then used to compute the pressure drop through the filter following Darcy's Law.

It should be noted that Darcy's Law is valid specifically for viscous flow through porous media, which can be defined by the porous medium Reynolds number, Re*:

$$\mathrm{Re}^* = \frac{U_i \sqrt{k}}{\nu} << 1 \tag{4.1}$$

where U_i is the pore velocity, k is the permeability of the porous media, and ν is the exhaust gas kinematic viscosity. The relationship given by Equation 4.1 typically holds true for the flow conditions and DPF channel configurations found in most real applications and the inertial contribution is expected to be small [69]. However, the

critical Reynolds number above which Darcy's law may no longer be valid has been found to vary from 0.1 to 75 depending upon the specific properties of the porous media including pore structure and "surface roughness" [74]. The Forchheimer term is, thus, included in the pressure drop model to account for these effects.

4.2 Composite Permeability Model

Soot and ash initially accumulate in the pores of a clean filter, giving rise to a rapid increase in pressure drop. The deposition of material in the DPF pores changes the effective porosity and permeability of the substrate. In-situ investigations have shown that the material which accumulates in the DPF pores does not penetrate deep into the filter, but rather accumulates in the pores near the filter surface. Figure 4.2 presents an image and associated measurements showing soot depth filtration and penetration into the filter wall [50].

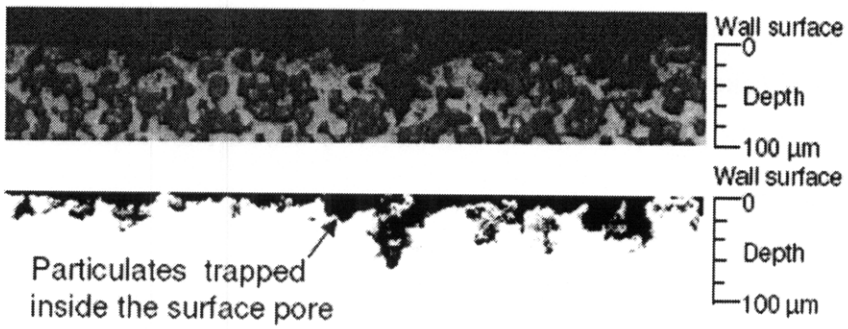

Figure 4.2. Soot trapped in surface pores of a SiC DPF [50].

Due to the large effect of depth filtration on the overall filter pressure drop, as shown in Figure 3.2, a composite permeability sub-model was developed to account for material accumulation in the filter pores. The approach taken to estimate the composite permeability of the filter walls, accounting for soot and ash trapped in the pores, is analogous to the sum of resistors in series. The total wall permeability is, therefore, computed as:

$$\frac{1}{K_{Composite}} = \frac{1}{K_{Wall}} + (AWF)\frac{1}{K_{Ash}} + (SWF)\frac{1}{K_{Soot}} \tag{4.2}$$

where $k_{composite}$ is the composite permeability of the wall layer including material trapped in the DPF pores, k_{wall} is the permeability of the clean filter wall, k_{ash} is the permeability of the ash, and k_{soot} is the permeability of the soot. Further, a weight fraction term is defined to describe the amount of ash and/or soot accumulated in the pores relative to the available pore volume. The composite permeability is therefore, based on the relative weight fractions or amount of material deposited in the filter pores. The weight fraction to account for soot or ash depth filtration is defined as follows:

$$WeightFraction = \frac{Vol.Deep.Bed}{Void.Volume} \tag{4.3}$$

which is simply the ratio of the volume of material deposited in the DPF pores to the total pore volume of the filter.

As shown in Figure 4.2, only a small fraction of the total pore volume is occupied by the trapped material, which primarily accumulates in the pores near the filter surface before building the filter cake. A further parameter, the deep-bed space fraction, is defined to determine the pore volume realistically available for ash or soot deposition. The deep-bed space fraction is:

$$D_B Fraction = \frac{Avail.Deep.Bed.Vol.}{TotalVoid.Volume} \tag{4.4}.$$

Experimental data has shown the amount of material accumulated in the filter pores generally occupies only a small fraction of the available volume, less than 10%, for most wall-flow filter designs. Once the deep-bed space fraction is defined, the model initially allows material to accumulate in the available pore volume within the filter walls. After the pores are filled, additional material accumulation in the filters is deposited in the cake layer on top of the filter walls or in the channel end-plug.

4.3 Ash and Soot Distribution Model

The manner in which ash and soot is distributed within the DPF channels plays an important role in determining how the accumulated material affects DPF pressure drop. Furthermore, the distribution of this material is often non-uniform, not only within individual DPF channels, but also within the overall filter itself. In general, ash accumulates in a layer along the channel walls and in a plug at the back of the channels near the filter outlet. A detailed description of ash accumulation and distribution in the DPF was presented in Chapter 2. Aside from contributing to additional flow resistance, ash deposition in the channels significantly alters the filter geometry. In effect, the filter and, specifically, the channel geometries are a function of the amount of ash accumulated in the filter and vary with time. Figure 4.3 depicts ash accumulation along the channel walls and as plugs toward the back of the filter.

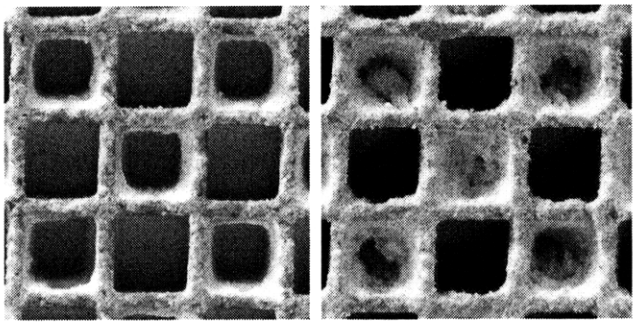

Figure 4.3. Typical ash deposits found within individual DPF channels.

Experimental observations obtained as part of this work, further show ash deposition as a dynamic process, i.e. the relative proportion of the ash deposited in the filter walls, as a layer along the filter walls, and in the plug at the back of the filter, varies depending on the loading state of the filter. The schematic in Figure 4.4 depicts the ash build-up process in the DPF and its overall effects on channel geometries.

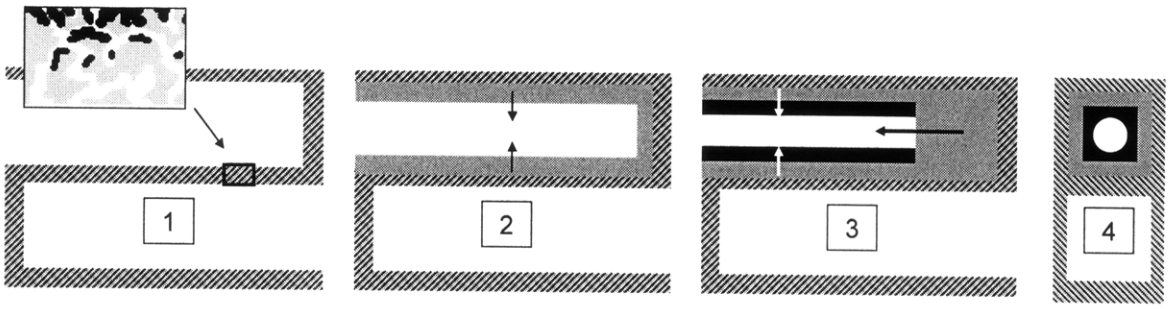

Figure 4.4. Evolution of ash deposition and build-up in DPF channels with time.

In a clean DPF, ash initially accumulates primarily in the surface pores of the filter. Following accumulation in the pores, a cake layer is formed along the channel walls. This cake layer typically grows as additional material is deposited in the filter. The evolution of the cake layer decreases the channel hydraulic diameter and introduces an additional flow resistance for gas flows through the cake layer and filter wall. The height of the cake layer is a function of the ash packing density as well as the local critical shear stress of the ash deposits, as described in Chapter 3.

The studies conducted as part of this work show that ash primarily accumulates in the cake layer until the layer reaches some critical thickness after which the local critical shear stress of the ash deposits is exceeded and material is transported to the back of the DPF resulting in plug formation. Ash plug formation generally only becomes significant in filters containing a large amount of ash, in excess of 20 g/l, and the effect of the ash plug is to reduce the available length of the DPF channel. The reduction in channel length leads to a decrease in filtration area and higher local soot loadings toward the front of the DPF. Unlike ash, soot is generally deposited in the filter as a fairly even layer along the channel walls with little end-plug formation.

Ash deposition along the filter inlet channels significantly alters the channel geometry and affects the manner in which additional material, soot and ash, is distributed within the filter. As all of this material is trapped in the filter inlet channels, the filter outlet channels remain clean and their geometries are unaffected. These differences in channel geometries, as a result of material accumulation, affect the accuracy of the zero-

dimensional models described in Chapter 3. The one-dimensional model developed, as part of this work, accounts for these differences in inlet and outlet channel geometries. Furthermore, sufficient geometric parameters are defined so as to accurately describe material accumulation within the filter pores, along the channel walls in the cake layer, and in the plug at the end of the channel.

For both soot and ash, a plug volume fraction is used to describe the relative amount of material accumulated along the channel walls and in the end-plug at the back of the filter. The end-plug fraction is defined as:

$$End_P Fraction = \frac{Vol.End.Plug}{Total.Volume} \tag{4.5}$$

which is simply the ratio of the volume of ash or soot accumulated in the end-plug, to the total volume of ash or soot deposited in the filter. As ash accumulates in the filter over time, the end-plug fraction is varied to account for the dynamic nature of the observed ash distribution. The total volume occupied by the material in the filter (ash or soot) is dependent on its packing density, which must also be input into the model. Experiments have further shown that the packing density may vary for material accumulated in the end-plugs and material trapped along the channel walls. The ash and soot-distribution sub-models, outlined above, accurately describe the dynamic behavior of material accumulation and distribution in the filter, and serve as inputs to the pressure drop calculations.

4.4 Ash Properties

Ash packing density, porosity, and permeability were identified in Chapter 3, as they key ash properties affecting filter pressure drop. In fact, permeability is a direct function of ash porosity and the mean pore size. Unfortunately, not all of these properties are easily measured. Furthermore, the specific mechanisms controlling ash particle size and packing in the DPF, which ultimately control these key properties, are not well-known.

The experiments conducted as part of this study, focused specifically on enhancing understanding of the parameters (lubricant chemistry, exhaust conditions) that control the ash properties.

Measurement of ash packing density is relatively straightforward, and serves as one of the key inputs to the model. Knowledge of ash packing density enables calculation of ash porosity as outlined in Chapter 3. Determination of ash layer permeability, however, is not as straightforward. A number of relations describing the permeability of porous media as a function of porosity and mean pore size have been developed over the past century, the most relevant of which are described below.

One of the most widely used relationships to describe the permeability of the DPF as well as the ash and soot layers in the DPF is that of Rumpf and Gupte. It should be noted however, that this relationship was determined from experiments utilizing uniformly random packs of spherical particles over a porosity range from $0.35 \leq \varepsilon \leq 0.7$, with Reynolds numbers from $10^{-2} \leq Re_P \leq 10^2$, and a range of particle diameters with $D_{P,max} / D_{P,min} \sim 7$. The Reynolds number, Re_P was defined as:

$$\mathrm{Re}_P = \frac{\upsilon \overline{D}_{P2}}{\nu} \tag{4.6}$$

where, $\overline{D}_{P2}$, is the surface average sphere diameter. The Rumpf and Gupte relationship is thus defined as:

$$k = \frac{\varepsilon^{5.5}}{5.6} \overline{D}_{P2}^2 \tag{4.7}.$$

For porous layers with higher porosities ($\varepsilon > 0.8$) the Carman-Kozeny equation has been proposed:

$$k = \frac{\varepsilon^3}{180(1-\varepsilon)^2} \overline{D}_{P2}^2 \tag{4.8}$$

and has been successfully applied to describe the properties of some powders. In cases where the layer is highly porous, or the particle geometry deviates significantly from a spherical shape, the relationship described above may break down. Further, the permeabilities computed from Equations 4.7 and 4.8 are highly dependent upon the particle size distribution, porosity, particle shape, and packing structure [74].

In the case of highly porous structures ($\varepsilon > 0.95$), the flow is better described by approaches used for "flows around submerged structures" rather than "flow through porous media." In general, at high porosities the most significant contribution to flow resistance is due to friction drag mechanisms as opposed to viscous shear, which dominates in conduit-type flow [74]. A number of empirical correlations have been proposed for fibrous beds, which often exhibit extremely high porosities, however these were not utilized in this work due to the complexity in defining the geometries. Equations 4.7 and 4.8 have also been defined as a function of the average pore diameter instead of the average particle size in DPF modeling studies [49].

Unlike general cake filtration theories which describe the deposition of particles having some known size distribution on a filter surface as a function of the Peclet number, ash accumulation in the DPF follows a different physical mechanism. Ash-related species may be distributed within the particulate matter in a solid or liquid phase and are deposited with the carbonaceous soot on the DPF surface. Following repeated regenerations, ash particles begin to agglomerate and form a porous layer along the channel walls. In effect, the ash particles and the ash layer properties are formed directly in the DPF, and are much less a function of the soot deposition mechanisms. While the various relationships, described above, relating permeability to the porous layer properties serve as a starting point for the modeling work, significant effort was devoted to better define the specific form of the relationship between ash layer morphology and its resulting permeability.

(This page intentionally left blank)

5 EXPERIMENTAL SET-UP AND APPROACH

The general experimental approach utilized in this study focused on the following specific areas: (1) quantifying and characterizing engine-out ash-related species, (2) determining the effects of ash accumulation on DPF pressure drop performance, and (3) measuring ash distribution, morphology, and key properties of the ash deposited in the filter. The experiments utilized a Cummins ISB 300 and a specially designed accelerated ash loading system coupled to the exhaust of the engine. The ash loading system was designed to simulate engine-out ash in a realistic manner and allow for careful control and monitoring of exhaust conditions.

5.1 Approach

The lack of fundamental understanding of ash effects on DPF performance degradation is due in large part to the slow, cumulative nature of ash accumulation. Field and laboratory tests show on the order of 100,000 miles or several thousand hours of testing are required to observe and quantify specific ash effects [26, 39, 75, 76]. As a result, un-accelerated testing is both costly and time consuming. While field trials provide arguably the most realistic conditions for ash accumulation, the inherent variability of these tests makes identifying the underlying fundamental mechanisms all the more difficult. On the other hand, laboratory tests, well-suited to conducting carefully-controlled experiments, are nearly impossible to conduct given the extremely long run times required. Before describing the approach taken in this work, it is instructive to examine the various approaches reported in the literature.

5.1.1 Accelerated Ash Loading

In response to the long run-time requirements, researchers have developed many new and innovative test procedures for accelerating the ash exposure of diesel aftertreatment systems. A 2003 study by Lubrizol accelerated ash loading by doping oil in the fuel up to 0.2% in order to simulate 100,000 km of ash exposure over the total test duration. Four

different oils were investigated, with sulfated ash levels between 0.63% and 2.26%. Similar to field-aged filters, the majority of the ash was found near the back of the filter. The use of high sulfated ash oils in the fuel doping experiments yielded ash that was denser and more evenly distributed along the filter channels as compared to lower sulfated ash oils [48]. A similar Chevron study utilized eight oils with different sulfated ash levels ranging from 0.43% to 1.97%, doped in the fuel at the 5% level. Interestingly, while boron was found to contribute to sulfated ash in the lubricants, little boron was found in the ash accumulated in the particulate filters [46].

In addition to fuel doping, researchers have also injected oil into the intake manifold to accelerate oil consumption and DPF ash loading. A Lubrizol study in 2004 injected oil at a rate of 1.5 ml/min using an SAE 15W-40 1.5% sulfated ash oil. A 165 hour DPF ash loading test was conducted and the results compared to a 1,118 hour un-accelerated test. While both cases showed the ash deposited in a similar manner, the ash generated by intake oil injection appeared thicker and less porous [35]. More recent studies have utilized intake manifold oil injection with a slightly undersized DPF (DPF to engine volume ration of 0.88) to further accelerate ash loading. These experiments increased oil consumption by 20 g/hr over the average stock engine oil consumption rate for a test duration of 120 hours. Based on these tests, the authors observed a non-linear effect of ash loading on backpressure, with little backpressure increase until high levels of ash loading were reached [38, 76].

Still other researchers have avoided such drastic acceleration methods as fuel doping and intake manifold misting. They have, instead, utilized high oil consumption engine operating conditions (high speed and load) in order to somewhat accelerate DPF ash loading. This technique was employed by Exxon in a 2003 study with a 200 hr dynamometer test simulating 20,000 to 30,000 km, a 1,200 hr dynamometer test simulating 120,000 km, and a 120,000 km vehicle test for comparison [28]. A similar study was conducted by Lubrizol in 2005 in which 10 oils were evaluated, each with the same 1.8% level of sulfated ash but different additive packages. The test duration for each oil was 270 hours, simulating 27,000 km. Once again, little correlation was

observed between DPF pressure drop and ash accumulation [29]. Most recently, a 2007 paper by Corning described a test procedure with relatively high engine load factors to simulate 300,000 miles and 420,000 miles over test durations of 1,720 hours and 2,640 hours, respectively. These experiments provided further evidence of the non-linear response of DPF pressure drop to both soot and ash loading [39].

While all of the studies described above utilized a wide range of techniques to accelerate DPF ash loading, differences in acceleration methods, lubricant properties, test cycles, and temperature and flow histories all affect exhaust and ash characteristics and their resulting impact on aftertreatment system performance. These differences bring into question the relevance of accelerated methods to accurately simulate actual DPF ash loading. Only a small number of studies have made some comparison between the ATS ash effects observed using accelerated techniques and un-accelerated loading methods and field tests. Further, very few, if any, studies have explored the effects of acceleration method on exhaust and ash properties and applied this understanding to interpret differences in results obtained using accelerated methods and actual vehicle field tests.

Perhaps one of the more thorough investigations into the effect of acceleration method on exhaust and particle properties was conducted by Oak Ridge National Laboratory in 2005. This study compared the effects of fuel doping and intake and exhaust manifold oil injection to accelerate the phosphorous poisoning of diesel oxidation catalysts. For oil doped in the fuel or injected into the intake manifold, P, S, Zn, and O were found in small particles on the soot, whereas exhaust manifold injection coated the PM in a glaze of P, Zn, S, and O. The method of oil introduction was observed to have a significant effect on both exhaust PM composition as well as DOC poisoning [42]. Clearly, additional fundamental studies investigating the effects of acceleration techniques on PM and ash properties and ATS impact are warranted.

5.1.2 Field Studies

In addition to gaining a better understanding of the fundamental differences between accelerated and un-accelerated ash loading methods, field trials provide valuable information and serve as benchmark for the validation of accelerated testing procedures. One of the most extensive field trials, reported in 2006, utilized 9 fuel delivery trucks retrofitted with passive DPF systems each run over 180,000 miles. This study observed differences in ash morphology and structure for vehicles using different lubricants, with lower sulfated ash oils yielding larger ash particles. Additionally, older and high mileage engines showed increased ash levels in the DPF as compared with newer engines. Similar to previous studies, exhaust backpressure was not observed to be a direct function of ash accumulation [26].

5.1.3 MIT Approach

A review of the current knowledge base clearly demonstrates the need to gain a fundamental understanding of the key parameters and mechanisms responsible for the observed effects of lubricant-derived ash on diesel ATS performance. The approach utilized in this study developed and validated an accelerated ash loading system through a methodical analysis of exhaust and ash characteristics, and comparison with actual engine-out conditions. While no accelerated ash loading method will simulate all of the effects observed in the field perfectly, well-developed and validated techniques can capture the underlying fundamental processes. Furthermore, differences in PM and ash characteristics between accelerated and non-accelerated methods need to be investigated in order to better understand and quantify differences in observed ATS performance. Lastly, carefully-controlled laboratory experiments are required if progress related to uncovering the underlying fundamental mechanisms influencing ash effects on ATS is to be made.

DPF ash loading can be accelerated using the following methods: (1) increase total oil consumption rate, (2) increase ash level in the oil, (3) decrease DPF size. In order to utilize lubricants with conventional additive packages, the use of high sulfated ash oils

was not considered in the initial system design, and the acceleration methods focused on using a combination of an undersized DPF and elevated oil consumption rates. In order to realistically accelerate lubricant-derived ash loading of diesel aftertreatment systems, it is instructive to understand the major oil consumption mechanisms in a heavy-duty diesel engine:

1. Transport through the piston ring pack leading to combusted and volatile losses.
2. Valve and turbocharger seal leakage leading to liquid oil losses.
3. Blowby and loss through the PCV system, if used [77].

The experimental approach taken in this work focused on three key aspects. First, the effects of specific acceleration methods on PM and ash characteristics were investigated, so that differences between accelerated and non-accelerated techniques could be accounted for. Second, investigations into the effects of specific oil consumption mechanisms (combusted lubricant, and volatile and liquid losses) on engine-out PM and ash characteristics were utilized to more accurately accelerate lubricant consumption. As the combustion of lubricant in the power cylinder is the single largest source of diesel engine oil consumption, development of the accelerated ash loading system focused on how lubricant combustion affected ash properties. Lastly, ATS performance and ash characteristics evaluated using the accelerated methodology were compared with field-aged units in order to understand and minimize any significant differences.

5.2 Accelerated Ash Loading System

Figure 5.1 presents the required oil consumption rates for a 1.0% sulfated ash oil to achieve a DPF ash level of 40 g/l over a test duration of 100, 50, and 10 hours for various DPF sizes. The volume of the full-sized DPF system utilized on the Cummins ISB in this study was 17.8 liters in order to accommodate the full engine exhaust flow while maintaining acceptable exhaust backpressure levels. Reducing DPF size presents one means of accelerating DPF ash loading. The DPF volume selected for the accelerated ash

loading studies was 2.47 liters, and accommodated only a portion of the engine's total exhaust flow.

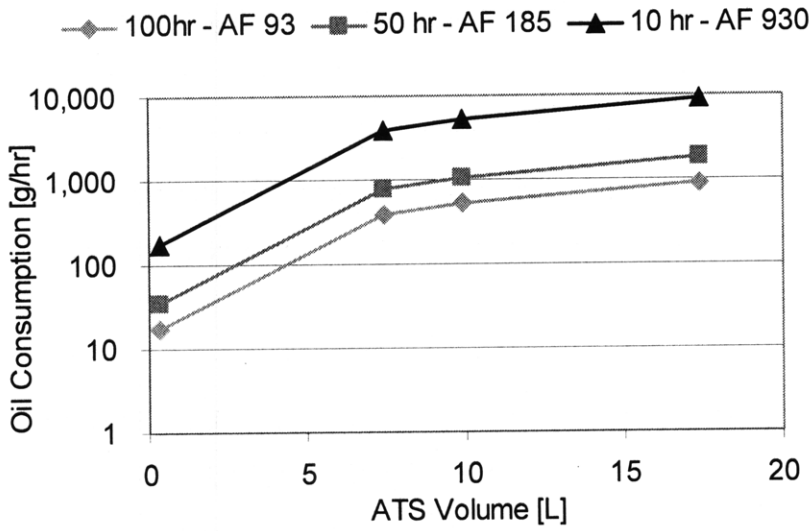

Figure 5.1. DPF ash loading acceleration rates and oil consumption requirements.

The accelerated ash loading and aftertreatment aging system was designed to load a conventional D5.66" (14.38 cm) X 6" (15.24 cm) DPF to 40 g/l of ash in slightly under 100 hours. Using a CJ-4, 1.0% sulfated ash oil requires an oil consumption rate of approximately 4 ml/min, as a considerable amount of the ash generated in the system is deposited along the exhaust pipes and combustion chamber. Ash levels of 40 g/l have been reported to correspond to roughly 300,000 miles of on-road use [39].

A schematic of the accelerated ash loading system is shown in Figure 5.2. Use of the accelerated loading system in conjunction with the Cummins ISB allows the feed-gas particle and ash characteristics to be carefully controlled and monitored. Further, the system provides considerable flexibility to vary a number of parameters including ash : PM ratio, total ash emissions rate, ash chemical composition, volatile and combusted lubricant fraction, exhaust gas composition, and DPF inlet temperatures and flow rates, among others.

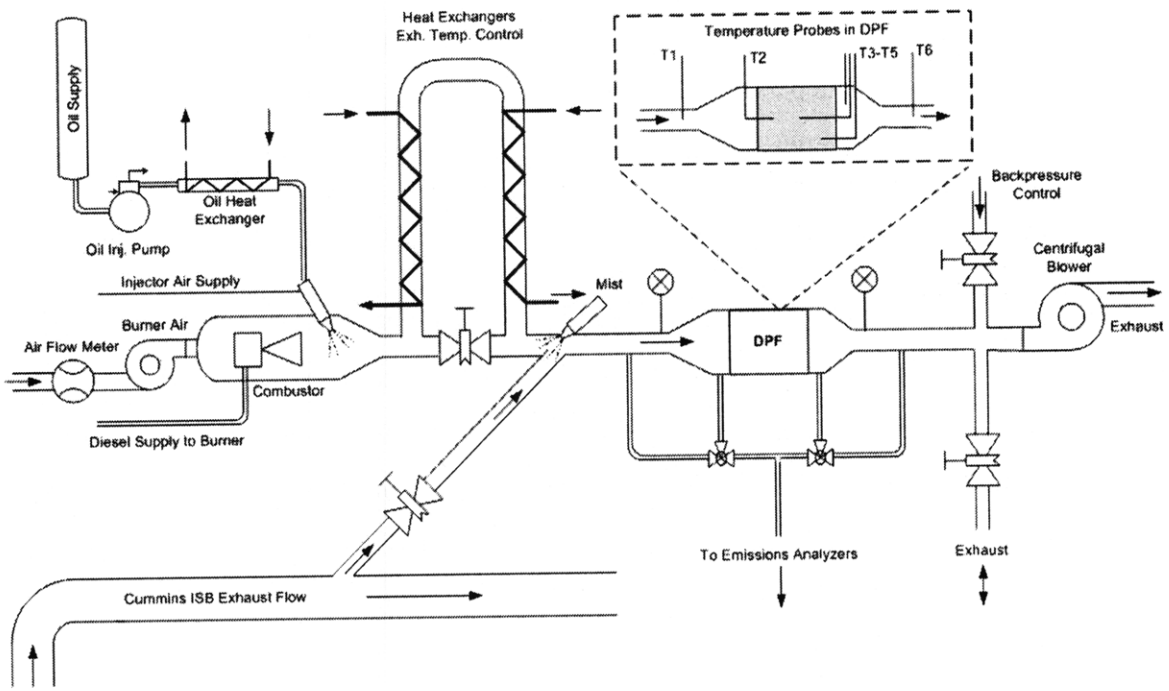

Figure 5.2. Configuration of accelerated ash loading and aftertreatment aging system.

The accelerated ash loading system consists of an industrial diesel burner and custom combustion chamber. A secondary air-assisted oil injector mounted on top of the combustion chamber allows for precise control of lubricant introduction into the combustor. Oil flow to the injector is supplied by a computer controlled constant volume pump. Fully-formulated lubricants, base oils, and individual additives can be introduced into the combustor using this system. Further, variation of injection parameters and combustor air flow offer some control over combustion quality and the characteristics of the combustion products. Table 5.1 presents the system's operating specifications and provides additional details.

System Paramater	Description
Fuel Consumption	1.5 - 7.6 l/h
Oil Consumption	0.94 - 9.4 ml/min
Injection Pressure	700 - 1400 kPa
Air Flow	266 - 1130 slpm
DPF Inlet Temperature	200 - 800 ° C

Table 5.1. Accelerated ash loading system specifications.

A heat exchanger mounted downstream of the combustor provides additional control of exhaust temperature, independent of the burner settings, allowing for online DPF regeneration. In this manner DPF inlet temperatures can easily be controlled between 200 °C and 800 °C.

A junction between the combustor outlet and heat exchanger inlet connects the Cummins exhaust system to the accelerated ash loading rig. A portion of the ISB's exhaust can be routed to the ash loading system, providing a realistic exhaust composition (gaseous and PM) that is mixed with the ash and soot generated by the combustor. Following the heat exchanger, the exhaust and combustion products are fed into the aftertreatment test section.

The purpose of the accelerated ash loading system, shown in Figure 5.2, is to allow for careful control and acceleration of specific oil consumption mechanisms, enabling the simulation of engine-out ash and PM as closely as possible. The supplementary injector (mist) located downstream of the heat exchanger allows for the injection of lubricant and additive components directly into the hot exhaust stream. This injection system was not used in this study, but provides flexibility to control the amount and phases (solid, liquid, vapor) of lubricant/ash introduced in the exhaust.

A centrifugal blower mounted downstream of the DPF test section provides additional control over exhaust gas flow rates through the particulate filter during the accelerated ash loading cycle. With the burner switched off, the test set-up functions as a flow bench with airflow through the DPF varied using the blower to evaluate the pressure drop behavior of the DPF as well. Airflow measurements through the accelerated ash loading system are provided by an Eldridge Series 8732 thermal mass flow meter. Temperature probe locations within the DPF are also shown in the inset in Figure 5.2.

The significant length of the exhaust pipes and heat exchanger system connecting the combustion chamber to the DPF test section provide ample surface area for particle and ash deposition. The oil consumption rate of 4 ml/min, accounts for this deposition along

the exhaust system. As all of the DPFs were tested on the same system, following the same test procedures, and the final ash-loaded DPF weights are known, particle deposition along the exhaust system is not expected to affect the results. Figure A-2 of the Appendix shows the accelerated ash loading system installed on the test bed.

5.3 Engine and Instrumentation

The engine used in this study was a Cummins pre-production development engine based on the 2002 ISB 300 engine platform. The ISB 300 is a 6 cylinder, 5.9 liter, four-stroke, turbocharged, direct injection diesel engine. The engine is rated at 224 kW (300 hp) at 2500 rpm and 890 N-m (660 ft-lb) at 1600 rpm. In order to meet 2002 EPA emissions standards, the engine employs a number of advanced subsystems such as a Bosch high-pressure common rail fuel injection system, Holset variable geometry turbocharger, and cooled exhaust gas recirculation (EGR). The engine and its associated subsystems are all electronically controlled, and access to Cummins control and calibration software allows for real-time monitoring and modification of engine control parameters. In this study, the stock 300-horsepower calibration was uploaded into the ECM and only slight modifications to the engine control parameters were made. Table 5.2 contains additional details regarding engine specifications and geometry.

Model	ISB 300
Maximum Torque	890 N-m @ 1600 rpm
Maximum Power	224 kW @ 2500 rpm
Number of Cylinders	6, in-line
Combustion System	4 stroke, direct injection
Injection System	Common Rail
Aspiration	Variable geomoetry turbocharger and intercooler
Displaced Volume	5.9 liters
Compression Ratio	17.2:1
Cylineder Head Layout	4 valves/cylinder
Injection Nozzle	O.D. = 158 μm
	L = 1.00 mm
	8 sac-less nozzles per injector
Injection Pressure	800-1600 bar

Table 5.2. Cummins ISB 300 engine specifications.

In addition to the stock electronic controls, the engine was heavily instrumented and all measurements were recorded using National Instruments data acquisition hardware and software. Slow-speed data was acquired using three 32-chanel thermocouple modules (SCXI-1102B) with fixed 200 Hz low-pass filters, while a general 32-channel module (SCXI-1100) containing a fixed 10 kHz low-pass filter was used to acquire both high- and slow-speed signals. The various modules were connected to a SCXI-1100 multiplexing chassis routed to a high-speed PCI-6024E data acquisition board. The slow-speed measurements consisted mainly of data from various thermocouples, pressure transducers, and flow meters, while high-speed data consisted of crank angle and in-cylinder pressure measurements.

5.3.1 Particulate Matter Emissions Sampling

Bulk particulate matter emissions were collected on conventional glass fiber and Teflon filters in order to determine PM emission rates by gravimetric analysis as well as to analyze bulk PM composition and ash content. Individual PM samples were also collected on small metallic grids for morphological and compositional analysis using electron microscopy.

5.3.1.1 Gravimetric Sampling

Particulate samples were collected simultaneously before and after the DPF to allow for accurate determination of trapping efficiency. All particle emissions were sampled from the raw and undiluted exhaust to preserve particulate matter composition. Bulk PM samples were collected on 47 mm Pallflex glass fiber filters, and the amount of particles collected was determined gravimetrically.

Following the gravimetric analysis, bulk composition of the particulate aggregates collected on the filter papers was characterized using Horiba's MEXA 1370 PM analyzer. Total particulate mass (TPM) is generally sub-divided into three major components: soluble organic fraction (SOF), sulfate fraction (SO_4), and an insoluble fraction (SOL). The SOF consists of organic material originating in the lubricating oil and fuel, while the

SOL is primarily composed of elemental carbon and most inorganic ash-related compounds. The sulfate fraction consists of sulfuric acid and water, with the sulfur originating in both the engine lubricant and fuel [15]. A detailed description of the measurement principles employed by the MEXA 1370 PM analyzer can be found in [78].

5.3.1.2 Individual Particle Sampling

Aside from bulk PM sampling, individual particulate samples were also collected at the entrance and exit of the DPF on small 3 mm (0.12 inch) diameter grids for subsequent analysis by both transmission electron microscopy (TEM) and scanning transmission electron microscopy (STEM). The sample grids were composed of a copper substrate covered with a pure carbon film, and were fixed to a 6 mm (0.24 inch) sample probe. Figure 5.3 shows the sample grids. In order to collect a PM sample, the probe was inserted directly into the exhaust for a duration of 5 - 30 s depending upon the sampling location (pre- or post-DPF). Individual particulate samples were then collected directly on the sample grid. The use of this sampling technique allowed for the collection of particles frozen in both composition and structure, and provided an ideal means for the subsequent analysis of particle composition and morphology via electron microscopy. A similar automated sampling system has been extensively used at Argonne National Laboratory for the past several years, and a more detailed description of the technique can be found in [62, 63, 79].

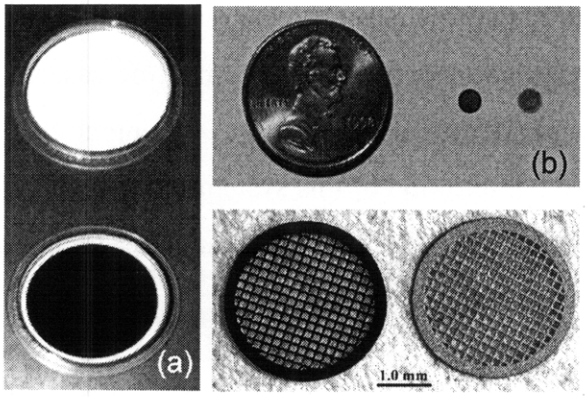

Figure 5.3. Conventional 47mm glass fiber filter for bulk PM collection (a) and 3mm TEM sample grid for individual PM collection (b).

5.3.2 Gaseous Emissions Sampling

Exhaust concentrations of HC, CO_2, CO, O_2, NO, NOx, and SO_2 were measured both upstream and downstream of the DPF. Hydrocarbon emissions were measured using a flame ionization detector (FID), and a heated chemiluminescence analyzer was used to determine NOx and NO emissions. The CO, CO_2, and O_2 measurements were carried out using a non-dispersive infrared analyzer, with the CO_2 measurements used to verify EGR fraction in the intake manifold.

Sulfur dioxide emissions were measured using an API 100E UV fluorescence analyzer with a lower detectable limit of 0.4 ppb_v. In addition to the gaseous SO_2 measurements, total sulfur in the exhaust was also measured with an Antek 6000SE SO_2 analyzer. The Antek utilizes two pyro furnaces each at 1,000 °C to convert any sulfur on the particles and in the exhaust stream to SO_2 for measurement via a UV fluorescence detector. Accurate determination of low-level SO_2 emissions is complicated by the presence of interference gasses such as poly-aromatic hydrocarbons (PAH) and NO present in diesel exhaust. In order to minimize these effects, the API analyzer employs a hydrocarbon scrubber as well as a NO optical filter, whereas the Antek utilizes an ozone generator to minimize NO interference. Nonetheless, NO emissions were always measured along with SO_2 to ensure that any changes in SO_2 levels were indeed accurate and not influenced by changes in NO levels as well.

An exhaust gas conditioning and analyzer system was constructed at the Sloan Automotive Laboratory to allow for the measurement of gaseous emissions in the raw exhaust stream before and after the DPF, as well as the engine's intake manifold to verify EGR fraction. A detailed description of this system is presented in [80]. A schematic of the experimental setup as well as the emissions sampling points and analyzer system is shown in Figure 5.4.

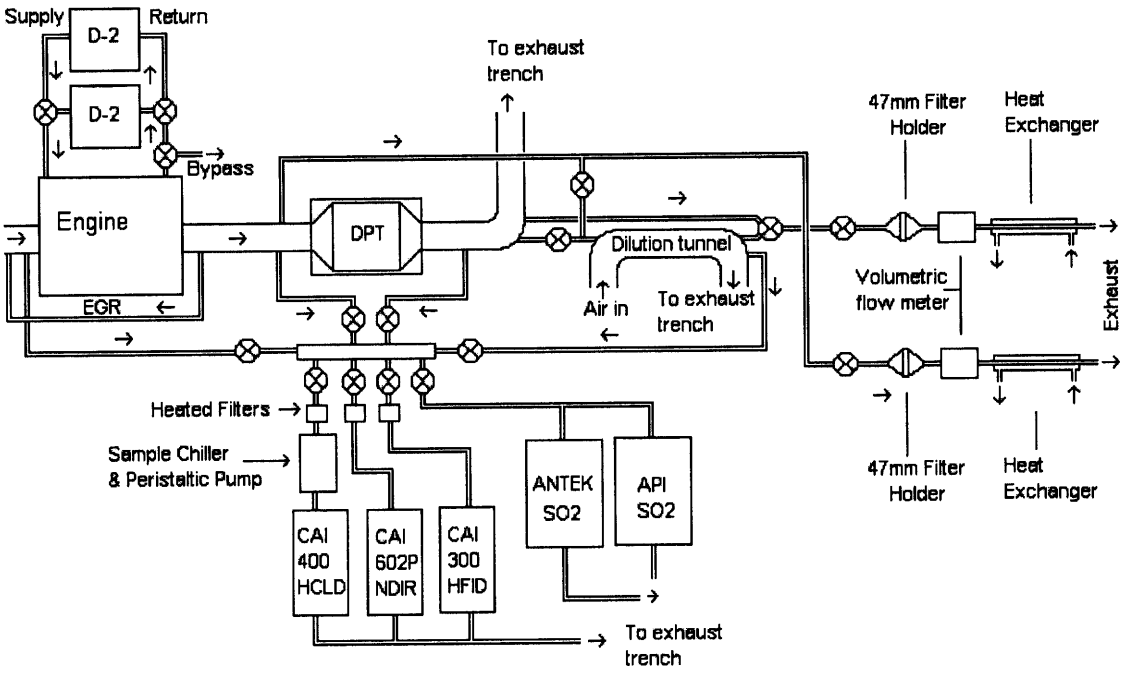

Figure 5.4. Experimental configuration showing test-bed, exhaust aftertreatment system, and emissions sampling points and associated hardware.

In this study, all gaseous emissions comparisons were based on measurements sampled from the raw exhaust using heated sample lines and filters to prevent any water from condensing out of the exhaust stream. The HC, NO, NOx, and total sulfur emissions were sampled wet, while the CO, CO_2, and O_2 emissions were sampled dry after first passing through a sample chiller and condenser.

5.4 Analytical Techniques

A number of analytical techniques were employed to characterize the chemical and physical nature of the ash- related compounds collected in the bulk particulate matter and as individual particles directly on the sample grids.

5.4.1 Electron Microscopy

Electron microscopy techniques were used to characterize PM and ash morphology, as well as elemental composition. All of the electron microscopy analysis was carried out at the MIT Center for Materials Science and Engineering (CMSE). Scanning electron microscopy (SEM) and transmission electron microscopy (TEM) were applied to obtain high quality images of the ash and particulate samples. SEM is capable of providing resolution near one nanometer, whereas image resolution to a fraction of a nanometer can be obtained with TEM. Further post-processing of the images using commercially available image processing software allowed for the determination of average particle and agglomerate sizes, relative number concentrations, and related information.

5.4.1.1 Scanning Electron Microscopy

Scanning electron microscopy was used to characterize ash morphology and composition for ash in the exhaust entering the DPF, as well as ash deposited in the lab- and field-aged filters. In contrast to TEM, SEM provides high resolution, three-dimensional images of the ash. In addition to imaging, energy dispersive x-ray analysis (EDX), used in conjunction with the SEM, allowed for the identification of specific elements in the ash particles. This technique, thus, provides qualitative information on ash composition and distribution of lubricant elements in the ash samples.

5.4.1.2 Transmission Electron Microscopy

Transmission electron microscopy was used to characterize ash morphology in the exhaust entering the DPF. TEM provides high resolution two-dimensional images of ash and soot particles and agglomerates to a fraction of a nanometer. The use of commercial image processing software enabled the determination of average primary particle and agglomerate sizes and additional morphological information.

5.4.1.3 Scanning Transmission Electron Microscopy

Concurrent with the physical characterization of the ash and PM samples, information regarding the distribution of specific ash-related elements in the bulk PM and in the ash samples was collected via scanning transmission electron microscopy (STEM). STEM utilizes a highly-focused 1.0 nm diameter beam of electrons scanned across the surface of the specimen in a raster. An x-ray detector collects x-rays excited in the irradiated sample, producing a spectrum characteristic of the various elements of which the sample is composed. This technique, therefore, allows not only the identification of the composition of various individual ash particles, but also the distribution of ash-related elements in the bulk particulate matter entering the DPF. Under ideal conditions, STEM can provide information on chemical composition with a sensitivity of a few atoms and spatial resolution of 0.5 nm. This technique, thus, provides qualitative information on ash composition and distribution of the ash particles in the carbonaceous particulate matter entering the aftertreatment system.

5.4.2 Thermal Analysis

A number of thermal analysis techniques were employed to measure the ash content of the engine-out particulate matter, as well as to characterize the specific properties of the ash deposited in the DPF.

5.4.2.1 Thermogravimetric Analysis

Thermo-Gravimetric analysis (TGA) was used to provide information on bulk particulate composition, total ash content, and ash properties. TGA is a conventional thermal analysis technique, which measures changes in sample weight as a function of temperature in a controlled atmosphere. All of the TGA analysis was carried out at the MIT CMSE utilizing a Perkin Elmer TGA 7. The PE TGA 7 is capable of attaining a maximum temperature of approximately 1,000 °C with a sensitivity of + 1 μg. A detailed description of TGA analysis as applied to the determination of total ash content in

particulate matter was presented in [65]. The ash generated as a result of the TGA analysis was further subjected to a detailed microscopy investigation as well.

5.4.2.2 Thermogravimetric – Mass Spectrometry Analysis

In some cases a mass spectrometer was used in conjunction with the TGA to monitor the species evolved from the sample. The mass spectrometer uses an electron beam to generate ions from the sample. The ions are then classified according to their mass-to-charge ratio, resulting in the mass spectra. The resulting spectrum generally shows the relative intensity of the various ions detected in the sample, listed by their mass [81]. As the sample of soot or ash is heated in the TGA, the gasses flowing through the TGA, including any evolved species from the sample, are fed through the mass spectrometer for analysis. TGA combined with mass spectrometry provides information on sample decomposition as a function of temperature, which is useful to study the effects of temperature on ash composition.

5.4.2.3 Dilatometry

Dilatometry was utilized to determine the change in length of an ash sample as a function of temperature. This is a widely used technique to measure material expansion or contraction due to temperature changes. The dilatometer consists of a sample holder, generally a cylinder, contained inside a furnace, into which the powder sample is placed. A push-rod is inserted in one end of the cylinder and the sample is placed under a small, generally negligible load. As the sample is heated, a linear displacement transducer accurately monitors push-rod position. The Netzsch dilatometer used in this study was capable of achieving a maximum temperature of 2,000 °C with a resolution to measure the change in length of 1.25 nm. The output of the instrument is change in sample length (volume) as a function of temperature and can be used to determine sintering onset, and sample expansion or contraction [82]. The data obtained from the dilatometer measurements can be combined with the TGA data to compute the change in sample density as a function of temperature as well.

5.4.3 Compositional Analysis

A number of techniques were employed to measure the bulk composition of the ash samples. The techniques ranged from elemental analysis to compound identification and were useful to compare ash composition for the ash generated in the laboratory with ash obtained from field-aged filters, as well as to relate ash composition to lubricant chemistry and ash properties.

5.4.3.1 Inductively Coupled Plasma

Inductively coupled plasma (ICP) provides a convenient means of simultaneously determining the elemental composition of a sample. In ICP atomic emission spectroscopy (ICP-AES), the sample is ionized by means of high-energy plasma and the photon emissions from the ions are detected to produce the spectrum. Analysis of the spectral lines and their corresponding intensities provides information related to the elemental composition of the sample. Detection limits for ICP-AES generally range from 1 to 100 ppm depending on the specific element analyzed. For solid samples, such as ash, a digestion technique must be utilized prior to analyzing the sample with ICP. Most of the ICP data reported in this work utilized a combined approach of acid and microwave digestion. It is also possible to couple ICP with a mass spectrometer (ICP-MS) to obtain detection limits on the order of parts per billion (ppb), however ICP-AES was used for the analysis of the ash samples [83]. In addition to measuring elemental composition of ash samples accumulated in the particulate filter, ICP was also employed to monitor levels of ash-related elements in the particulate matter emitted by the engine.

5.4.3.2 Neutron Activation Analysis

Aside from ICP, neutron activation analysis (NAA) was used to obtain a quantitative assessment of speciated ash emission rates in the particulate matter. NAA is a non-destructive measurement technique allowing the simultaneous quantification of multiple elements. Minimum detectable levels (MDL) for neutron activation analysis depend

upon the elements of interest, but are typically in the sub-ppm range, making the technique ideally suited for quantifying trace metals and ash-related elements in the PM.

In neutron activation analysis, the PM samples collected on 47mm quartz filters are irradiated for a specified amount of time at the MIT Nuclear Reactor Laboratory. While in the reactor, the PM sample is bombarded by neutrons causing the elements present to form various isotopes. Following irradiation, the sample is placed in a radiation detector to measure the emissions generated by the decay of the isotopes. By comparing the decay characteristics and spectra of the PM and ash samples to that of a known standard, the specific trace ash elements in the PM can be quantified.

5.4.3.3 X-Ray Diffraction Analysis

X-Ray Diffraction (XRD) is a powerful technique used to identify and quantify the chemical compounds present in a sample. In XRD the diffraction pattern measured from the incident x-ray beam contains information related to the atomic spacing of the crystal lattice according to Bragg's Law. The position and intensities of the peaks in the spectra are used to determine the type, crystallographic phase, and quantity of material present [84]. A Rigaku Powder Diffractometer at the MIT CMSE was used extensively in this work to identify the lubricant-derived compounds present in the DPF ash samples.

6 EXPERIMENTAL TEST MATRIX AND PROCEDURES

The experimental parameters, test matrices, and general procedures are outlined in this section. Engine-out ash emissions and the effect of ash accumulation on DPF pressure drop were investigated using the Cummins ISB and accelerated ash loading system for a number of operating conditions and lubricant formulations.

6.1 Lubricants

The lubricants used in this study consisted of commercial formulations and specially formulated blends with specific additive chemistries. A fully-formulated commercial CJ-4 oil was used to form the upper bound in terms of ash accumulation in the DPF. Experiments conducted with this oil were expected to yield results comparable to those obtained with other CJ-4 oils currently in use. The lower bound was obtained by using a group II base oil. This oil did not contain any additives, and represents the best case scenario for reducing ash emissions in the case where all of the additives are removed from the lubricant.

The CJ-4 oil and base stock were used in the baseline testing to identify the upper- and lower-bounds in terms of ash accumulation and effects on DPF pressure drop. Two additional specially-formulated lubricant blends were also used to investigate the effect of individual additives on ash morphology and pressure drop. Table 6.1 presents the measured additive levels in each of the lubricants tested.

	ASTM D5185							
Lubricant	B [ppm]	Ca [ppm]	Fe [ppm]	Mg [ppm]	P [ppm]	Zn [ppm]	S [ppm]	Mo [ppm]
CJ-4	586	1388	2	355	985	1226	3200*	77
Base Oil	1	<1	<1	<1	8	<1	60	<1
Base Oil + Ca	3	2928	1	5	2	<1	609	<1
Base Oil + ZDDP	1	<1	<1	<1	2530	2612	6901	<1
Base Oil + Ashless	1	5	<1	<1	2	<1	19	<1

Table 6.1. Lubricant elemental composition for the oils used in the experiments.

The specially formulated lubricant blends consisted of base oil containing only a calcium-based detergent, and base oil containing only ZDDP. Both oils were formulated to a sulfated ash level of 1.0%, the same sulfated ash level as the commercial CJ-4 oil. A third lubricant formulation consisted of the same base oil with an ashless additive package; however the results of those tests are not included in this work.

6.2 Fuels

A conventional ultra-low sulfur diesel fuel (ULSD) was used in both the Cummins ISB and accelerated ash loading system. The ULSD contains no more than 15 ppm sulfur. In order to rule out significant contributions to ash emissions from the fuel, samples of the ULSD were periodically subjected to a detailed elemental analysis, and the results are shown in Table 6.2.

ASTM D5185						
Element	Ca	Mg	P	Na	K	Zn
ULSD [ppb]	<97	<56	<1180	<2010	<2690	<155

Table 6.2. Elemental analysis of the test fuel.

In all cases, trace elements measured in the fuel were always below the minimum detectable limits (MDL) of the analyzer. Depending on the element, the MDL ranged from approximately 100 to 1,000 ppb.

6.3 Particulate Filters

Conventional cordierite particulate filters were utilized in all of the ash loading tests. The filter cell geometry was 200/12 (200 cells per square inch, 0.012 inch wall thickness). All of the ash loading tests were conducted using catalyzed filters containing either a vanadium- or platinum-based catalyst. While both the vanadium and platinum catalyzed filters were used for baseline performance studies, only the platinum catalyzed filters

were utilized in the subsequent ash loading tests. Table 6.3 presents the details for the filter specifications and geometries.

Substrate	Catalyst	Dimensions	Cell Density	Wall Thickness	Filter Volume
Cordierite	Pt	D5.66" x 6" (D14.38 x 15.24 cm)	200 cpsi (31 cells/cm)	0.12" (0.3mm)	2.47 L
Cordierite	V				

Table 6.3. Properties of the diesel particulate filters used in this work.

While D5.66" (14.38 cm) x 6" (15.24 cm) filters were used in all of the accelerated ash loading tests, larger sized filters 7.5" (19.05 cm) x 12" (30.48 cm) were used in parallel in preliminary engine tests with the Cummins ISB. The larger filter size was required to accommodate the full exhaust flow from the ISB while maintaining engine backpressure within acceptable limits.

6.4 Engine Testing

Tests conducted on the Cummins ISB were used to evaluate DPF performance and characterize the engine-out soot and ash emissions. The specific engine tests consisted of the following:

- Studies to quantify total ash emission rates, lubricant-derived elemental emissions rates, and ash composition and distribution in the exhaust entering the DPF.
- Calculations of total and speciated ash trapping efficiency in the full-sized DPF for a range of engine and DPF operating conditions (loading and regeneration).
- Baseline DPF performance testing for the full-sized DPFs, consisting of soot loading tests and measurements of PM trapping efficiency, pressure drop response, and gaseous emissions.
- DPF performance characterization for clean and ash loaded DPFs. Targeted experiments were conducted to investigate the effects of soot and ash loading on filter pressure drop.

The engine provided both a standard of comparison for the soot and ash generated by the accelerated ash loading system, as well as the means to test the ash loaded filters using real engine exhaust and particulate matter. Furthermore, the engine-out ash characterization studies provided valuable information to describe the various forms of the ash in the exhaust, and the manner in which this ash is transported and deposited in the DPF.

6.4.1 Particulate Matter and Ash Measurements

PM samples were collected from the Cummins ISB as well as the accelerated ash loading system. All particulate samples were collected from the raw exhaust upstream of the aftertreatment system. This allowed for the characterization of the particles and ash as they exist in the raw undiluted exhaust entering the particulate filter. Bulk PM samples were collected on 47 mm glass fiber filters and particulate emission rates were determined gravimetrically. Following gravimetric analysis, the composition of the particles was characterized using Horiba's MEXA 1370 PM analyzer. The MEXA 1370 measures PM sulfate fraction (SO_4), soluble organic fraction (SOF), and insoluble fraction (SOL).

Ash content in the bulk particulate matter was determined using thermogravimetric analysis. In order to conduct the TGA measurements, the PM samples were carefully removed from the glass fiber filters and deposited in the TGA pan. Typical TGA sample sizes were approximately 5 mg.

In addition to bulk PM sampling and analysis, individual particulate samples were also collected from the raw exhaust. The particles were collected directly on 3 mm (0.12 inch) diameter grids, fixed to a sample probe and inserted through a sample port on the exhaust system upstream and downstream of the DPF. The individual PM samples, thus collected, were subsequently analyzed via electron microscopy.

The PM size measurements from the images obtained via TEM were processed using commercially available image processing software. Two dimensions were measured for each agglomerate and primary particle as shown in Figure 6.1. Previous work measuring primary particle size at two different viewing angles of 0° and 50° showed primary particles to be nearly spherical [63]. On the other hand, agglomerate particles, as shown in Figure 6.1, generally do not fit a simple geometric description.

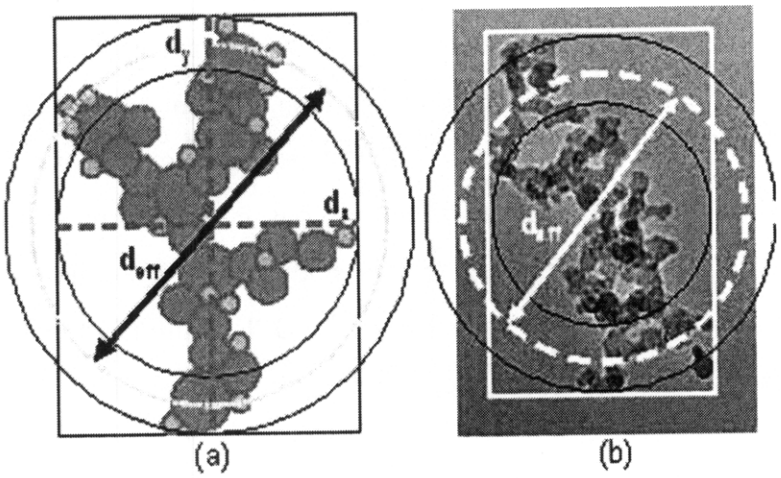

Figure 6.1. Measurement methodology for determination of agglomerate effective diameter (a) conceptual representation and (b) PM agglomerate at 27,000X.

The two dimensions measured for each agglomerate, d_y and d_x, were used to compute an effective diameter, d_{eff}, as follows:

$$d_{eff} = \frac{d_x + d_y}{2} \tag{6.1}$$

Additionally, the geometry of the agglomerate can be described by the following modified aspect ratio:

$$1 \leq \frac{\max(d_x, d_y)}{d_{eff}} < 2 \tag{6.2}$$

where perfectly spherical particles exhibit a ratio of 1 and long chain-like agglomerates approach 2. While measurements of radii of gyration and fractal geometries are often used to describe agglomerate dimensions in the literature, the limitations of the image

processing software used in this study required the use of the simple measurements described above. Nonetheless, the measurements appear adequate for the comparative purposes of this work.

6.4.2 Gaseous Emissions Measurements

A wide range of regulated and unregulated gaseous emissions were measured before and after the DPF. The gaseous emissions measurements, particularly CO and HC, provide a direct indication of catalyst effectiveness. While significant experimental efforts were devoted to characterizing ash effects on catalyst performance, the work is outside the scope of this thesis, and thus most of the gaseous emissions measurements are not reported here. Of significant interest to this study are sulfur emissions, since sulfur compounds are also present in ash deposited in the DPF. Sulfur in the exhaust can exist in various forms including sulfur dioxide, or in the particulate matter sulfate fraction.

Sulfur dioxide was measured upstream and downstream of the DPF using an API SO_2 analyzer. The sulfur dioxide measurements are useful to quantify sulfate production and storage over the platinum catalysts, as well as DPF sulfur emissions during high temperature regeneration (desulfation). Particle-phase sulfur emissions were measured from the particulate samples using the Horiba MEXA 1370, and the ANTEK total sulfur analyzer was also used to quantify total sulfur emissions before and after the DPF. Use of these three measurement methods provided some level of redundancy helpful to confirm the sulfur emissions measurements.

6.4.3 Full-Size DPF Testing

The full-size DPF testing on the Cummins ISB was primarily conducted to characterize pre- and post-DPF PM and ash emissions, as well as to quantify baseline DPF performance. The DPF system used for the full-sized filter testing consisted of two filters in parallel, each filter having dimensions of 190.5 mm (7.5 inches) in diameter and 304.8 mm (12.0 inches) in length. With both filters installed in the exhaust system in parallel,

the total DPF volume was 17.4 liters. A schematic of the parallel DPF configuration is shown in Figure 6.2.

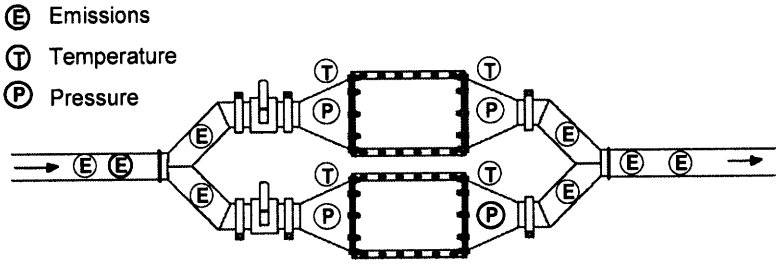

Figure 6.2. Parallel flow particulate filter configuration.

Pressure transducers were installed at the inlet and outlet of each DPF to allow for the measurement of exhaust backpressure as well as pressure drop across the filter. In addition, exhaust inlet and outlet temperatures were also measured. The locations of the pressure, temperature, and emissions taps on the DPF are shown in Figure 6.2.

Besides the parameters mentioned above, the temperatures within various regions inside the DPF were monitored throughout the course of this study. Seven thermocouples were placed inside each filter at depths of 5.8 cm (2.0 inches), 15.2 cm (6.0 inches), and 25.4 cm (10.0 inches) from the filter inlet and exit. All thermocouples were inserted into the DPF through the inlet and exit channels, and no modifications to the substrate were made. Figure 6.3 depicts the locations of the thermocouples within the DPF.

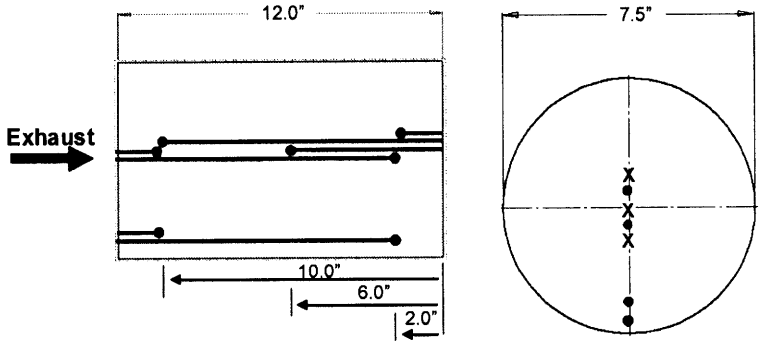

Figure 6.3. Thermocouple locations within each DPF.

The fully-instrumented DPF system is shown installed on the test bed in the photograph in Figure A-3 of the Appendix. Trap 1 is located on the right-hand side of the picture nearest to the exhaust system and engine, while trap 2 is located farthest to the left near the outside of the test bed.

6.4.4 Small-Scale DPF Testing

In contrast to the full-sized on-engine DPF testing, smaller filters (D5.66" x 6", 2.47 liters) were used with the accelerated ash loading system to reduce the total ash loading duration. The design of the accelerated ash loading system and DPF test section allows for the same DPF to be loaded with exhaust (partial flow) from the Cummins ISB, the accelerated loading system, or both. The system lay-out, including DPF instrumentation was shown in Figure 5.2, and described in Chapter 5.

The pressure drop characteristics for the 2.47 L DPFs were evaluated using the flow bench for the clean and loaded filters. Due to the small size of the filters, only the partial exhaust flow from the Cummins ISB was utilized to load these filters with soot. Ash loading was carried out using the accelerated ash loading system, with no supplemental engine exhaust. The filters were also periodically removed and weighed hot to accurately measure soot and ash levels. An Acculab VA-12KG balance used to weigh the filters. The balance has a 12 kg maximum capacity with a 0.2 g resolution. By alternating between the ash loading system and the Cummins ISB, the filter pressure drop response to soot and ash loading was evaluated using the flow bench for a range of DPF space velocities and ash and soot loading levels.

6.5 Accelerated Ash Loading

Development of the accelerated ash loading system required significant tuning and validation efforts to accurately simulate engine-out soot and ash emissions as closely as possible. The effect of specific acceleration techniques and oil consumption methods on ash and soot morphology was assessed and compared to the ash and soot generated on the Cummins ISB. Tuning of the oil consumption rate, injection method, and combustion

air:fuel ratio allowed for reasonable simulation of the engine-out PM and ash characteristics. The accelerated ash loading system that resulted following these development and validation efforts was used to load the DPFs with ash.

6.5.1 System Validation: PM and Ash Emissions

Particle emissions were sampled from the Cummins ISB and accelerated ash loading system at a number of operating conditions. PM sampled from the ISB was collected at a low speed and load condition (1682 rpm, 25% rated load) designated A25 and representative of DPF loading conditions, and a low speed and high load condition (1682 rpm, 75% rated load) designated A75 and representative of DPF regeneration conditions. Particles generated by the accelerated ash loading system were collected from the diesel burner alone, the diesel burner with 20% (vol.) oil doped in the fuel, and the diesel burner with the same amount of oil supplied using a separate injection system. Table 6.4 shows the experimental test matrix.

	Condition	Oil	Temperature
			[C]
Cummins ISB, A25	1682 rpm, 25% Load DPF Loading	None	300
Cummins ISB, A75	1682 rpm, 75% Load DPF Regeneration	None	620
Burner	DPF Loading	None	300
Burner + Oil Injection	DPF Loading	20% of Fuel	300
Burner + Fuel Doping	DPF Loading	20% of Fuel	300

Table 6.4. Experimental test matrix.

All particles were sampled at the DPF inlet, both on the engine and for the accelerated ash loading system. The corresponding DPF inlet temperatures for each operating condition are shown in Table 6.4. The characteristics of the particulate samples collected from the Cummins engine and accelerated ash loading system were evaluated and compared using the techniques described above. Following PM analysis, the particles were subjected to TGA in which the combustible PM fraction was oxidized, leaving the ash behind. These ash samples were further characterized using SEM.

Figure 6.4 presents a comparison of total PM emissions, normalized to DPF volume, for both the Cummins ISB and accelerated loading system. The DPF used on the accelerated ash loading system has a volume of approximately 2.47 liters. The two engine test conditions shown in the figure form upper and lower bounds on engine-out PM. The volume of the DPF currently installed on the test engine is 17.8 liters; however a maximum upper bound was obtained by assuming the use of an 8 liter DPF, giving an acceptable DPF to engine volume ratio of 1.35.

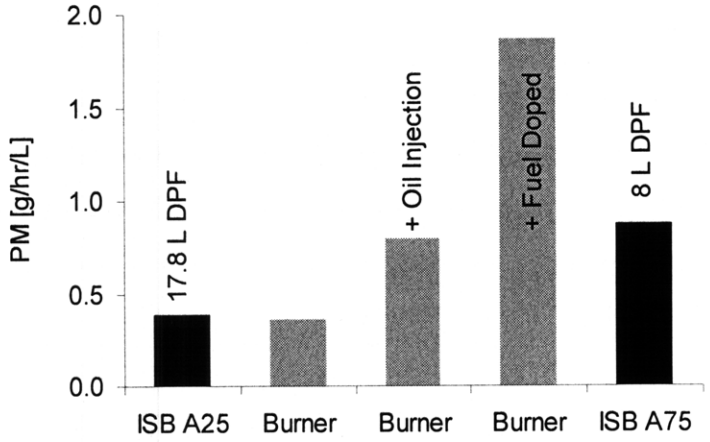

Figure 6.4. Comparison of PM emissions for oil introduction method normalized to DPF volume.

A large contributor to the high PM emissions relative to DPF size observed for the accelerated ash loading system is the small size of the DPF relative to the PM output of the diesel/oil burner. Additionally, Figure 6.4 shows roughly a doubling in PM emissions over the diesel burner alone when oil is injected into the combustion chamber using the air assisted injector. Interestingly, the addition of the same quantity of lubricant via fuel doping showed an increase in PM emissions by more than a factor of four over the case of the burner alone. Clearly the method of lubricant introduction impacts particulate matter emissions.

An analysis of particle composition revealed differences between the accelerated and non-accelerated tests, as shown in Figure 6.5. The technique used to measure PM composition (Horiba MEXA 1370) does not directly measure ash as part of the insoluble

fraction. Therefore, ash measurements, determined via TGA, were used to account for the ash fractions, and only the carbon content of the PM samples is shown in Figure 6.5. Once again, the results of the analysis for the accelerated cases are bounded by those of the Cummins ISB.

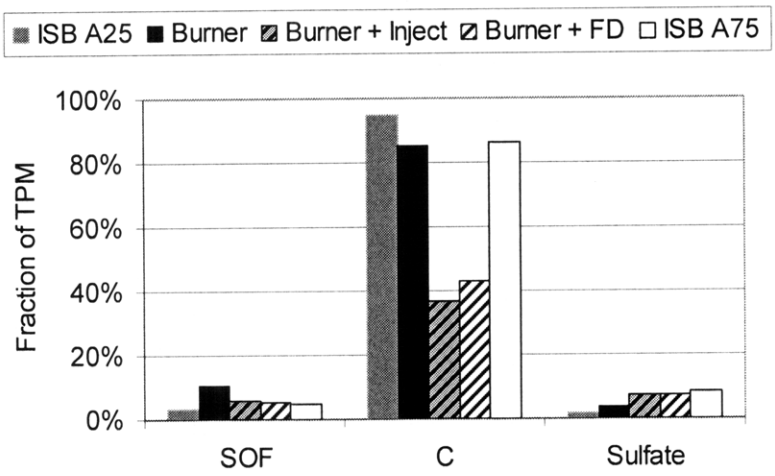

Figure 6.5. Composition of PM generated by the accelerated ash loading system and Cummins ISB.

The most significant difference in particle composition for the accelerated and non-accelerated cases is a large reduction in insoluble carbonaceous fraction, attributed to the increase in ash fraction in the accelerated tests. Due to the large increase in ash fraction in the PM generated by the accelerated ash loading system, the insoluble carbonaceous fraction ranged from 37%-43%, compared with 87% to 95% for particles sampled from the Cummins ISB.

In general, soluble organic fraction increased for the accelerated loading system without additional oil introduction, and is therefore primarily attributed to the diesel burner itself. On the other hand, as expected, the sulfate fraction increased significantly for the two accelerated cases in which additional oil was consumed in the combustor.

Based on the sulfate measurements presented in Figure 6.5, the contribution of the fuel and lubricant to total particle-phase sulfur emissions was computed. Figure 6.6 shows

the relative contribution of the fuel and lubricant to particle-phase sulfur emissions for the accelerated ash loading system, by oil introduction method. For the case of the burner alone, all of the particle-phase sulfur can be attributed to the fuel. The additional particle-phase sulfur measured for the two methods of oil introduction can, thus, be attributed to the lubricant. In the case where oil was doped in the fuel, the reduced fuel consumption rate was accounted for.

From Figure 6.6 it is evident that doping the fuel with lubricant leads to elevated PM-phase sulfur emissions by nearly a factor of two, as compared with injecting the lubricant directly into the combustion chamber, for the same rate of oil consumption. Approximately 7% of the lubricant sulfur is emitted in the particle-phase (sulfates) for the case in which oil is doped into the fuel, compared to only 3% for oil injection. Once again, the method of oil introduction and combustion is seen to affect PM emissions characteristics.

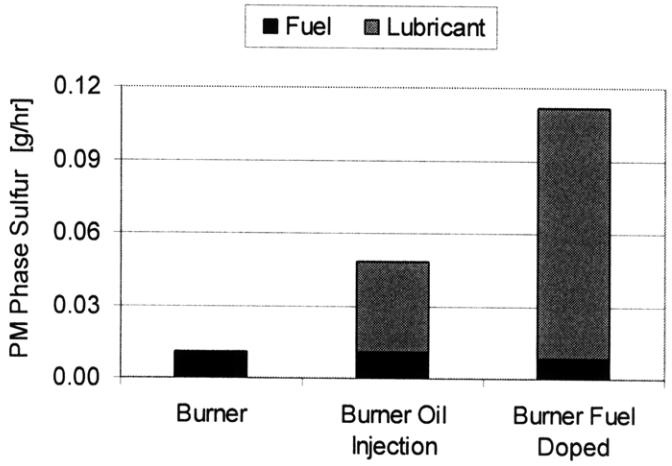

Figure 6.6. Total PM-phase sulfur emissions for the accelerated ash loading system by oil consumption method.

Figures 6.7 and 6.8 show the fractions of sulfur emitted in both the gas and particle-phases for the Cummins ISB and accelerated loading methods.

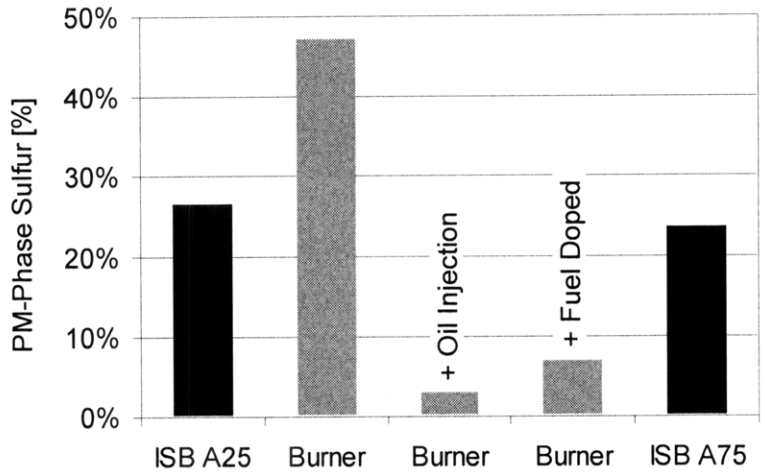

Figure 6.7. Fraction of total sulfur emitted in particle-phase for the accelerated ash loading system and Cummins ISB.

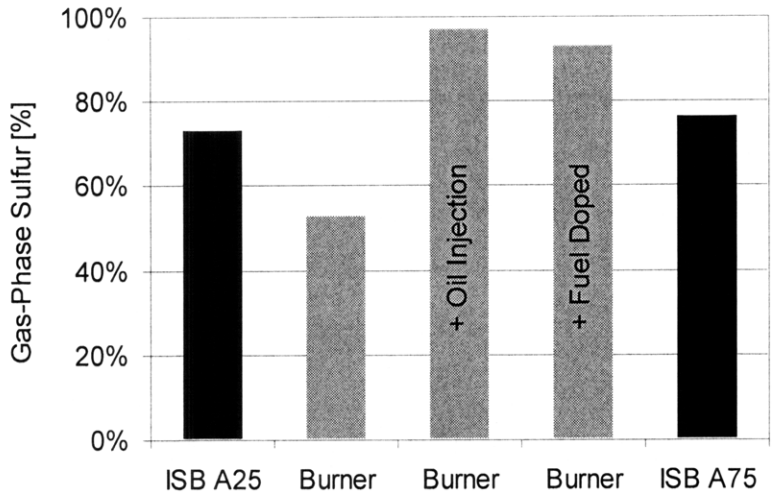

Figure 6.8. Fraction of total sulfur emitted in gas-phase for the accelerated ash loading system and Cummins ISB.

The fraction of total sulfur emitted in the gas-phase is slightly higher for the two cases in which oil consumption was accelerated in the diesel burner as compared to the results obtained for the Cummins ISB and diesel burner alone. Correspondingly, the fraction of sulfur emitted in the particle-phase is lower for these two conditions as well. Since it is well known that different forms of sulfur (SO_2 or SO_4) affect ash composition and catalyst performance in different ways, it is important to understand how the method of oil introduction affects the overall SO_2 to SO_4 ratio in the exhaust.

Total ash emissions were determined for each operating condition by TGA analysis. The PM sampled from the Cummins ISB at the low speed and load DPF loading condition was composed of approximately 0.5% ash. These measurements are in good agreement with the findings of a previous study on this engine reporting 0.5% to 1.0% ash as a fraction of total PM mass depending on engine operating condition [85].

The results of the TGA analysis were used to compute the ash-to-particle ratios for the two Cummins test conditions, as well as the two methods of oil combustion using the accelerated ash loading system. The results of this analysis are shown in Figure 6.9. Both accelerated methods yield ash/PM ratios that are nearly two orders of magnitude greater than those observed in the exhaust of the Cummins engine. While great efforts have been made to ensure as many parameters as possible remain constant between actual engine exhaust conditions and the exhaust produced by the accelerated loading system, the ash-to-particle ratio is the exception. By accelerating the ash loading process, the amount of ash in the exhaust inevitably increases.

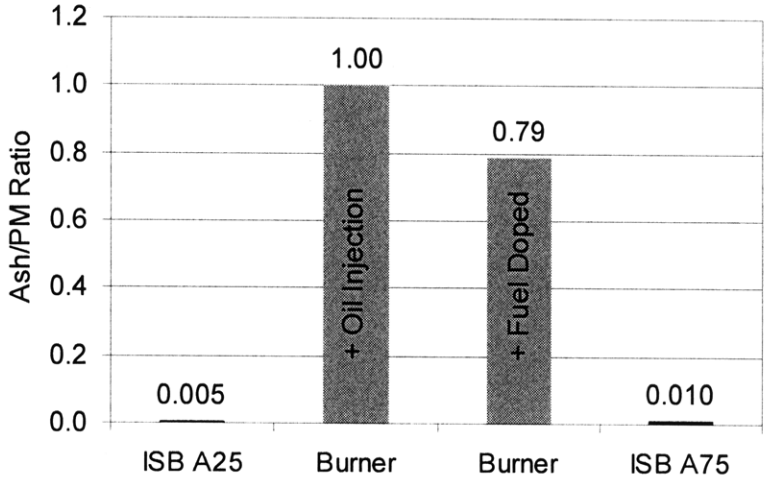

Figure 6.9. Ash-to-particulate matter ratios for the accelerated ash loading system and Cummins ISB.

Aside from differences in the overall ash fraction, the properties of the ash generated by injecting oil in the combustor and doping oil in the fuel appear to be significantly different. Figure 6.10(b) shows the ash generated from particles produced by doping the fuel with oil, which appear as small clumps spread about the TGA pan. In contrast, ash generated from PM produced by injecting oil into the combustion chamber, Figure 6.10(c and d), produced clearly defined pellets following soot oxidation in the TGA.

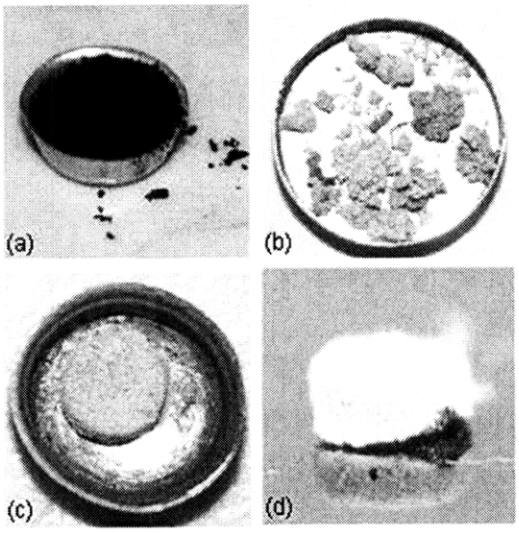

Figure 6.10. TGA samples of (a) PM prior to TGA, (b) ash generated by fuel doping, (c) and (d) ash created using oil injection.

Images of the ash particles following TGA analysis show significant differences in bulk ash morphology for the two oil introduction methods. The ash generated from direct oil injection into the combustion chamber appears to have a much greater affinity for sticking to itself than the ash generated by doping the same amount of oil into the fuel.

6.5.2 System Validation: PM and Ash Morphology

In addition to quantifying ash emission rates and differences in bulk ash and PM properties, a detailed analysis of particle morphology was undertaken. It is expected that particulate agglomerate and primary particle sizes affect the manner in which the PM is collected and distributed along the channel walls of the DPF. TEM image analysis and

size measurements were used to quantify size and structural differences between PM generated by the accelerated ash loading system and engine.

Figure 6.11 compares mean primary particle diameters for each operating condition. The error bars in the figure represent the range of one standard deviation above and below the mean. The diameters of approximately two-hundred primary particles were measured for each operating condition.

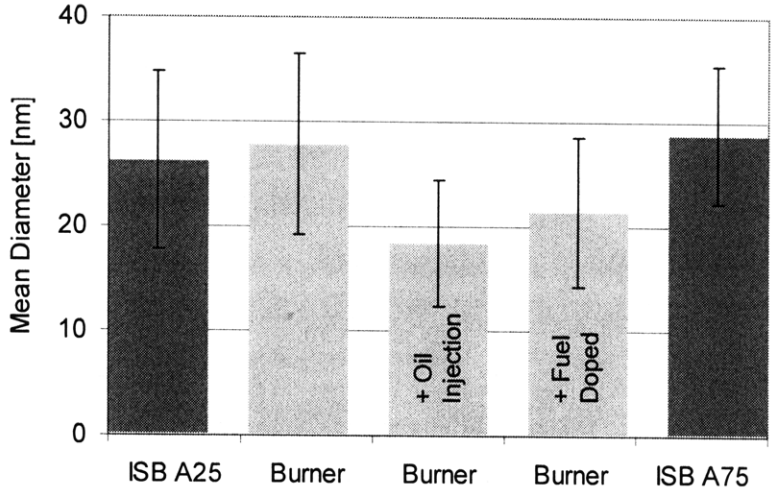

Figure 6.11. Mean primary particle diameters for the accelerated ash loading system and Cummins ISB.

In general, the diameters of primary particles generated by both accelerated oil consumption methods were approximately 8 nm smaller than the primary particles generated by the Cummins ISB. Interestingly, primary particle diameters measured for the diesel burner alone were nearly identical to those measured for the engine tests. In all cases, measured primary particle diameters were well within the range reported in the literature of 15 nm to 35 nm [62, 63]. The primary particle size distributions for all of the operating conditions are shown in Figure A-4 of the Appendix.

A collection of PM agglomerate images representative of each operating condition for the accelerated and un-accelerated loading tests is shown in Figure 6.12. The agglomerates

generated by the accelerated ash loading system appeared slightly more clustered, than the longer chain-like agglomerates generated by both engine operating conditions.

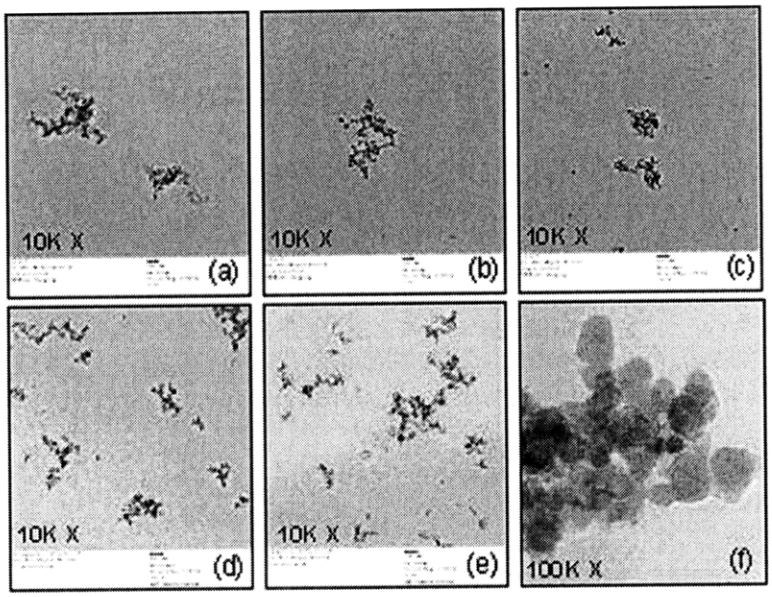

Figure 6.12. TEM images of particulate agglomerates from the accelerated ash loading system (a) diesel burner, (b) diesel burner with oil injection, and (c) diesel burner with fuel doping and Cummins ISB at (d) 1682 rpm, 75% rated load, (e) and (f) 1682 rpm, 25% rated load.

Figure 6.13 shows the effective diameters measured for the agglomerates. Slightly more than one-hundred agglomerates were measured for each condition. Particles and small agglomerates below 50 nm in size were not included in the computation of mean effective diameters shown in Figure 6.13. The agglomerate size distributions for all of the operating conditions are presented in Figure A-5 of the Appendix, and show a more uniform size distribution over a larger size range for the PM generated by the diesel burner relative to the engine-out PM.

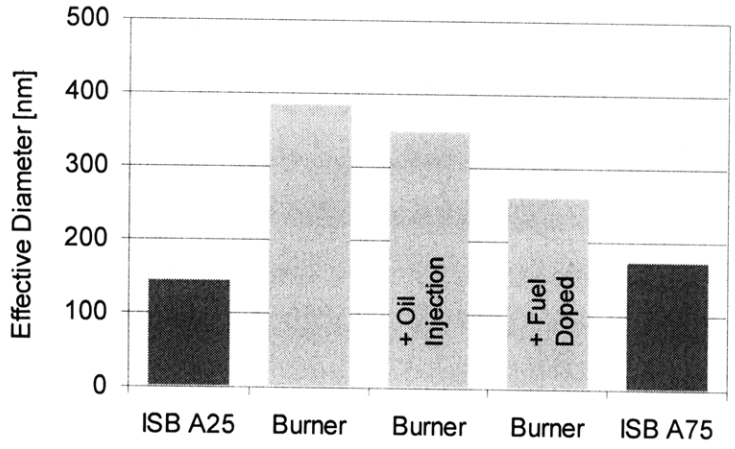

Figure 6.13. Mean agglomerate effective diameters for the accelerated ash loading system and Cummins ISB.

The agglomerates generated by the diesel burner alone and the diesel burner with oil injection were, on average, twice as large as the agglomerates generated by the engine. On the other hand, the size of the agglomerates generated by the burner with oil doped in the fuel more closely matched the size of typical engine-out particles. Agglomerate geometry (extent of cluster formation versus long-chain structures) can be quantified using the modified aspect ratio defined in Equation (6.2). Figure 6.14 presents the average ratios for each operating condition.

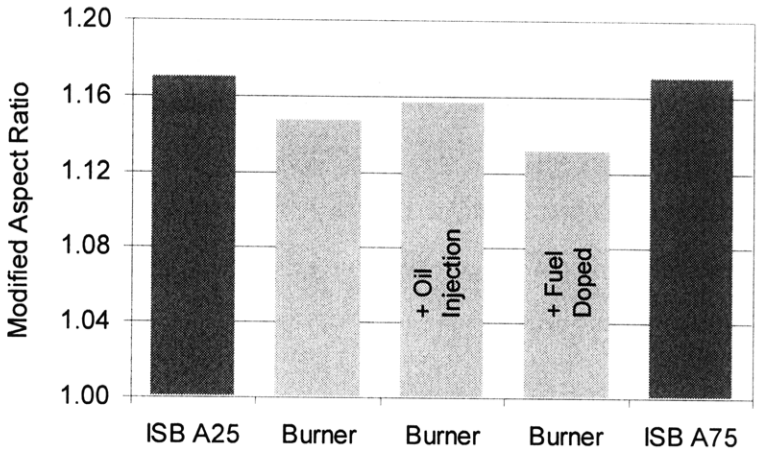

Figure 6.14. Modified aspect ratios for particles sampled from the Cummins ISB and accelerated system.

As evidenced in Figure 6.14 and observed in the images presented in Figure 6.12, the agglomerates generated using both accelerated oil consumption methods, as well as the diesel burner alone, are slightly more clustered with modified aspect ratios ranging from 1.13 to 1.16. In contrast, the modified aspect ratio computed for particles generated by the Cummins ISB was 1.17 for both engine operating conditions. The agglomerate measurements indicate only slight differences in particle geometries between the engine and accelerated ash loading system.

The ash samples obtained from the accelerated loading system following the TGA analysis were compared with ash from field-aged DPFs. Due to differences in temperature histories, flow conditions, and specific lubricant composition between the ash generated by the accelerated loading system and the ash generated in the field, the results provide only a qualitative comparison of the most significant differences between the two cases.

Inspection of a cross section taken from the rear of the field-aged DPF provides some insight into the manner in which soot and ash are deposited along the channel walls over time. Figure 6.15 depicts two regions on the same cross section, one with little ash accumulation, shown in Figure 6.15(a), and the other with a significant amount of ash accumulation, shown in Figure 6.15(b). From the images it is clear that the ash and soot initially accumulate together, i.e. the ash and soot particles are fairly well mixed. However, it appears that over successive regeneration cycles, the ash slowly begins to agglomerate and separate itself from the soot, as shown in Figure 6.15(b).

It is interesting to note that the ash does not immediately settle down to coat the channel walls but rather appears to stick to itself, as opposed to the surrounding cordierite. This same phenomenon was observed in the ash generated by injecting oil directly into the combustion chamber of the accelerated ash loading system, shown in Figure 6.10. While this is one possible explanation for the observed distribution of ash and soot along the channels of the DPF, ash migration and the potential for incomplete regenerations in the field-aged DPF may also influence the ash/soot distribution. As the channels begin to

accumulate higher levels of ash, shown in Figure 6.15(b) and 6.15(d), the ash and soot clearly form distinctly separate layers with no intermixing.

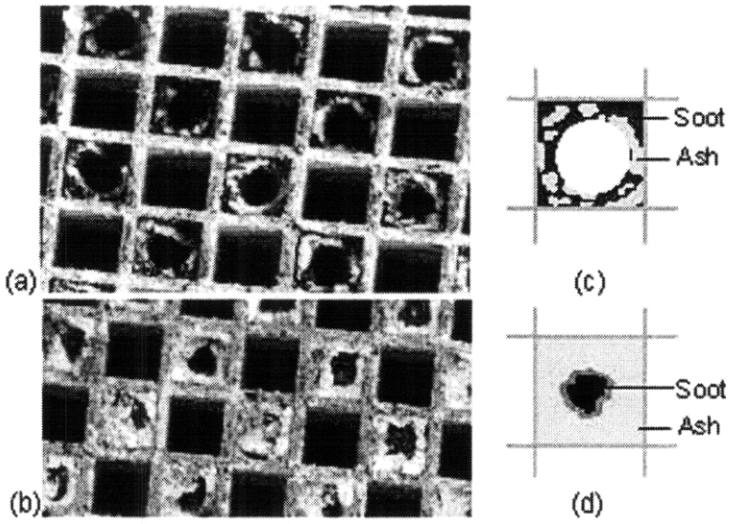

Figure 6.15. Ash and soot deposition within a DPF channel wall for: (a) and (b) field observations, and (c) and (d) conceptual description.

Ash samples from the field-aged filters shown above were removed and analyzed via SEM. Figure 6.16 shows a comparison between ash samples generated by the two accelerated methods and ash from the field.

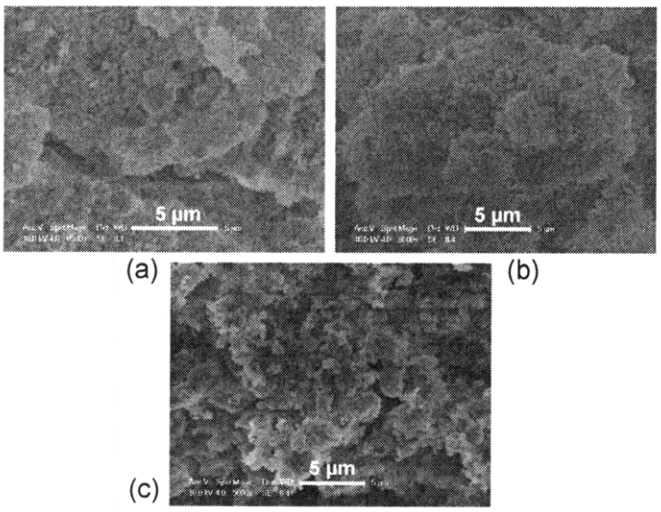

Figure 6.16. Ash (a) generated by oil doping, (b) generated by oil injection, and (c) from field-aged DPF.

Based on initial analysis of the images, the field-aged ash appears to be slightly less dense than the ash generated by the accelerated ash loading system, following TGA analysis. Furthermore, the ash primary particles appear slightly larger in the field ash samples. This difference has been observed in other accelerated ash loading studies in the literature as well [48]. However, it is unclear whether the observed variation in ash morphology is due to inherent differences between the accelerated ash loading test and field tests, or differences in temperature and flow histories.

Figure 6.17 presents the results of the elemental analysis via EDX for the three ash samples described above. No large differences were observed between the two accelerated ash loading methods. Differences in elemental composition between the accelerated tests and field ash are due to differences in lubricant composition. The field ash compositional analysis is included in the chart to illustrate the absence of sulfur in the ash generated by the accelerated system following TGA analysis. Previous studies have confirmed the loss of sulfur during the high temperature exposure of the sample in the TGA [65].

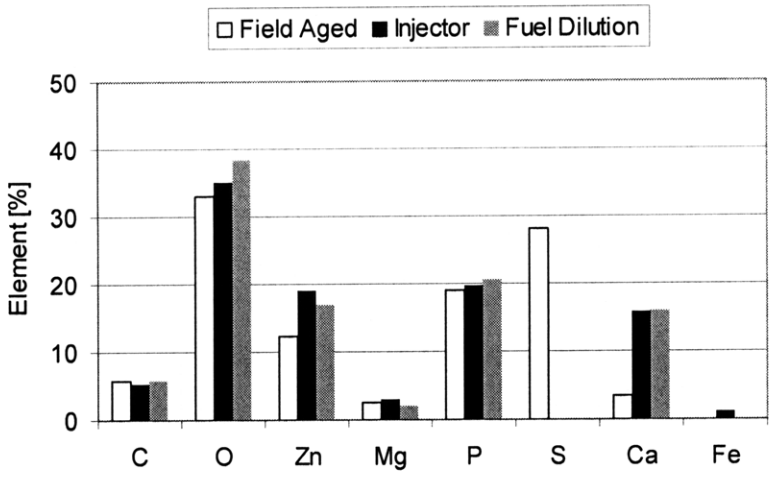

Figure 6.17. Composition of ash from field-aged DPFs and accelerated ash loading system.

6.5.3 System Validation: Ash Properties

Field-aged DPF samples were obtained from select diesel engine manufacturers. The ash samples were collected from catalyzed particulate filters used on heavy-duty diesel engines running CJ-4 oils. Ash samples removed from the DPFs were analyzed using the same techniques applied to the ash generated by the accelerated loading system. A comparison of the field-aged ash samples with the ash generated using the accelerated ash loading system highlights differences and similarities between the two samples. More importantly, this comparison serves as the basis for identifying the mechanisms responsible for the observed differences.

Following DPF performance evaluation, a detailed analysis of key ash physical and chemical characteristics was undertaken. Ash property measurements provide valuable information to aid in explaining the observed differences in DPF performance. Ash packing density and porosity are two fundamental parameters which determine the magnitude of the ash effect on DPF pressure drop. Figure 6.18 presents a comparison of measured average ash packing densities for three field-aged and one laboratory-aged DPF.

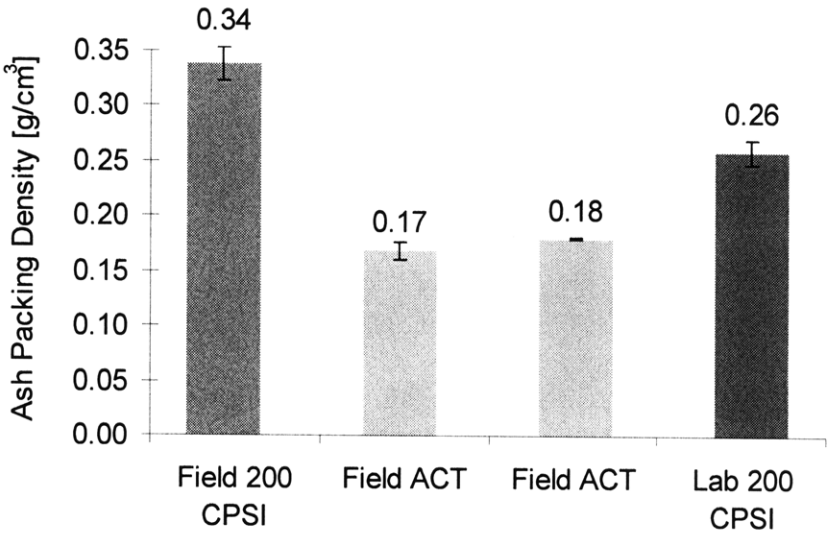

Figure 6.18. Average measured packing densities for ash plugs in field- and laboratory-aged DPFs.

All filters (field and lab) were subjected to periodic regeneration using CJ-4 oils. Packing densities are measured for the ash accumulated in plugs at the rear of the filter channels. Typical packing densities for the field ash range from 0.17 to 0.34 g/cm^3. The packing density for the ash accumulated in the laboratory ash loaded DPF of 0.26 g/cm^3 is well within the range of packing densities measured for the field ash. Similar packing densities were also measured for filter samples loaded with ash at MIT and sent to Oak Ridge National Laboratory for x-ray analysis. The results of the x-ray analysis are shown in Figure 6.19.

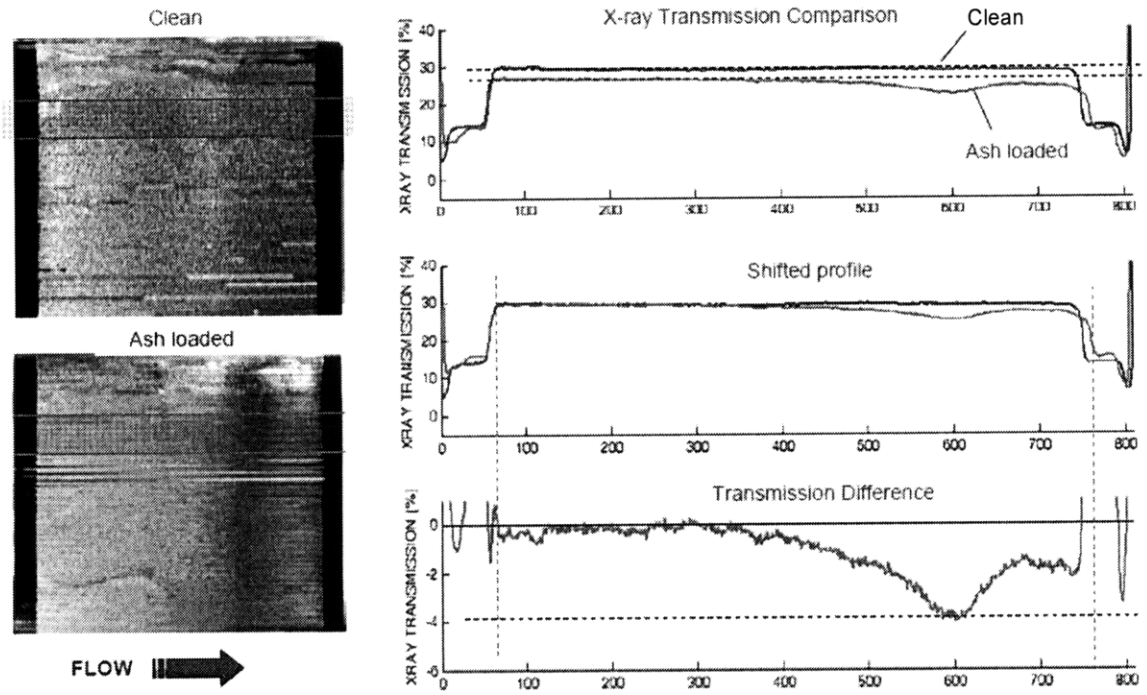

Figure 6.19. X-ray ash distribution profiles and packing density measurements for DPF loaded with ash in the laboratory.

The packing density variation along the length of the ash plugs for the two field-aged DPFs was measured as well. The ash plug length in each filter measured approximately 6 inches (15.24 cm) from the back of the filter. Both of these field-aged filters had accumulated slightly more than 180,000 miles with CJ-4 oils and periodic regeneration. The ash plug was divided into three regions as indicated in Figure 6.20. Each region of

the ash plug was 2 inches (5.08 cm) long and packing density was measured for each of these samples.

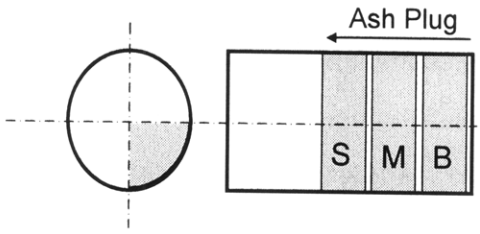

Figure 6.20. Location of DPF ash samples for packing density measurements. Shaded area indicates start (S), middle (M), and back (B) of ash plug.

The results of the axial ash plug packing density measurements for both field-aged DPFs are shown in Figure 6.21. In general little variation in packing density was observed along the length of the ash plug for both of the ACT field-aged particulate filters.

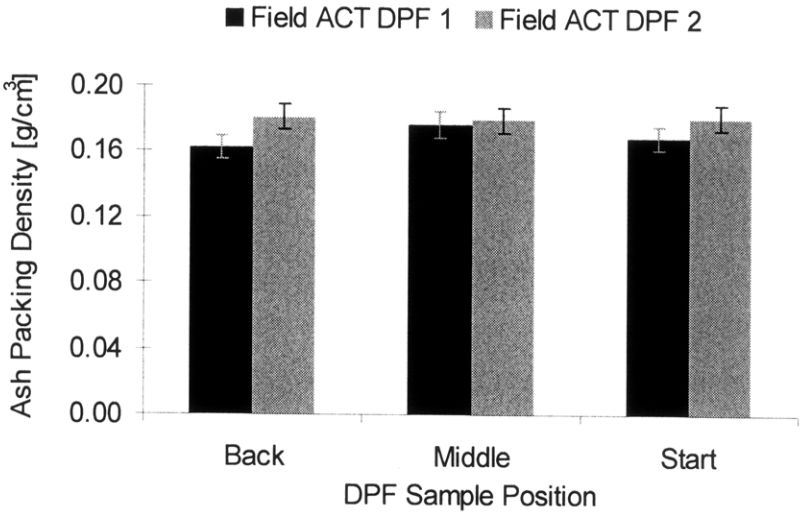

Figure 6.21. Ash packing density comparison for ash located at the back, middle, and start of the ash plug in two field-aged DPFs.

ICP was used to measure the average elemental composition of the field and laboratory ash samples. The results of the ICP analysis are shown in Figure 6.22, and show Ca and Zn as the most abundant lubricant-derived elements in the ash. While ICP provides average values of bulk ash composition, SEM-EDX was used to investigate the localized

distribution of lubricant-derived elements within individual DPF channels. The results of this analysis are presented in Figure 6.23.

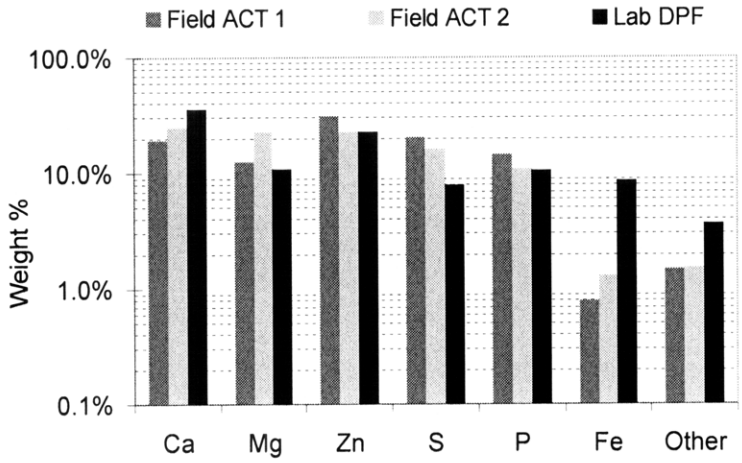

Figure 6.22. Ash elemental composition measured via ICP for field and laboratory ash samples.

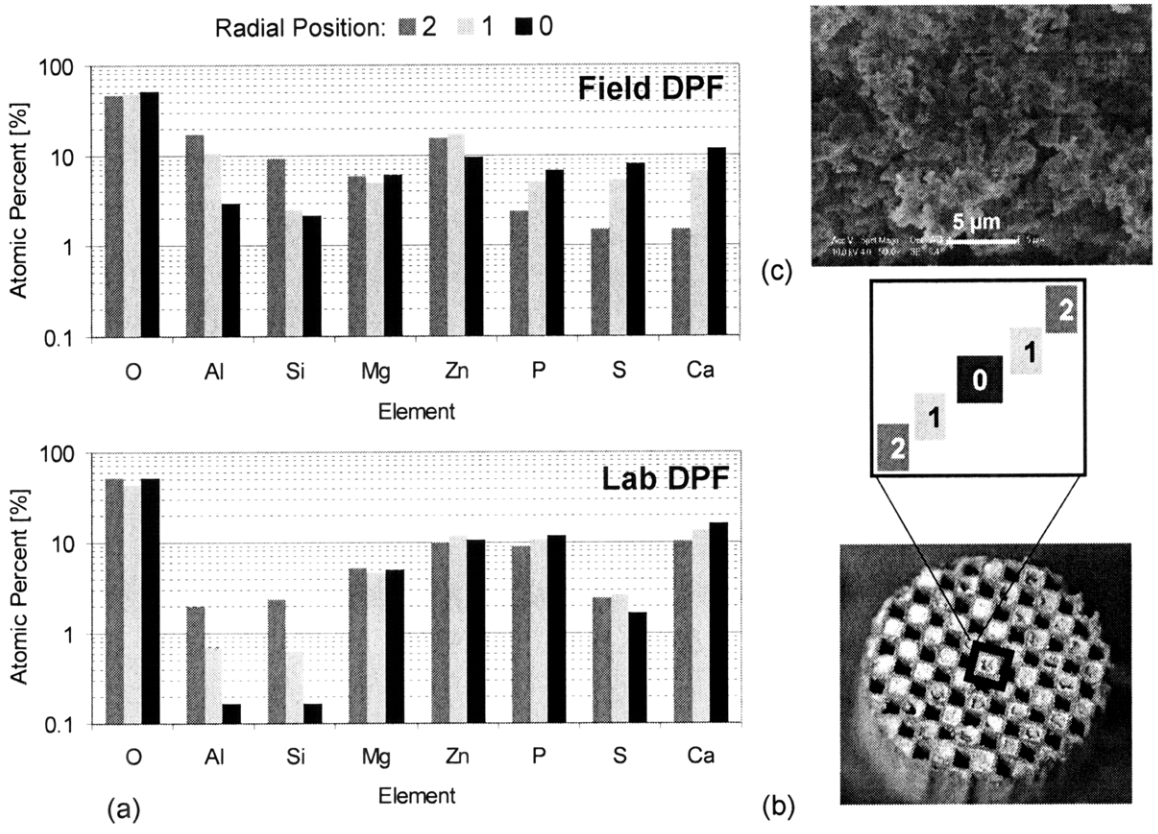

Figure 6.23. Elemental distribution (a) measured across ash plugged DPF channels via SEM EDX (b), (c) for laboratory and field-aged diesel particulate filters.

In the case of both field and laboratory ash samples, Ca, S, and P were found in higher levels near the center of the ash plug, whereas Mg and Zn tended to be evenly distributed (in the radial direction) across the face of the channel. As expected, levels of Al and Si are observed to decrease with increasing distance from the channel walls. The mechanisms governing ash transport to the rear of the channel, resulting in plug formation under periodic regeneration, and the observed elemental distribution in the ash plug are still not well understood. This study addresses these specific processes in more detail.

While some differences in ash morphology were observed between the ash generated from the accelerated ash loading system and ash generated in the field, many similarities were observed as well. Distinctly spherical ash particles were clearly visible in both the field and laboratory ash samples, shown in Figure 6.24.

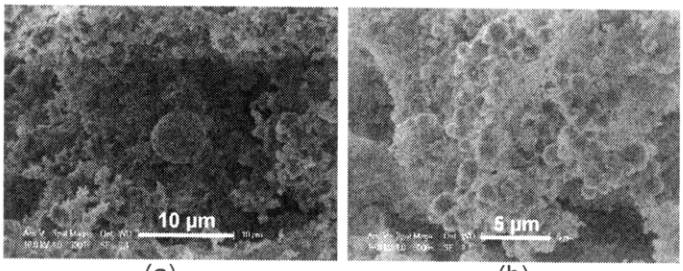

Figure 6.24. Spherical ash particles observed in (a) field-aged and (b) synthetic ash generated by the accelerated ash loading system.

Preliminary elemental analysis of the spherical particles revealed them as primarily composed of calcium, in either a phosphate or oxide, as evidenced in the spectra shown in Figure 6.25. A large number of these calcium particles were observed in the ash generated by the accelerated system, shown by the large clusters in Figure 6.24 (b) and the higher levels of calcium in the ash generated by the accelerated loading system shown in Figure 6.22. Additionally, the spherical calcium particles found in the field ash samples are significantly larger than the calcium particles found in the ash generated by the accelerated loading system, by approximately 4 µm.

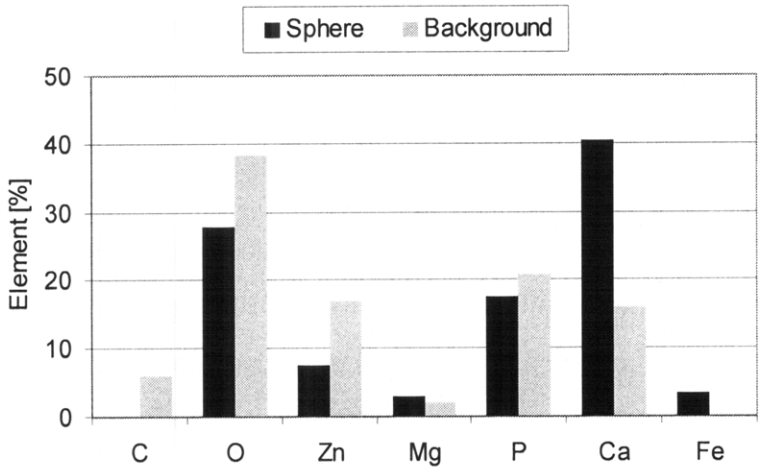

Figure 6.25. Elemental spectra of ash spheres and background ash composition.

The identification of spherical calcium ash particles indicates that specific lubricant additives may form ash particles, each having a distinct morphology specific to their elemental composition. Iron particles with a clearly defined morphology have also been identified in ash samples in the literature [38]. Further, the larger size of the primary ash particles and spherical calcium particles in the field ash samples suggests that additional factors, such as temperature histories, may contribute to ash particle sintering and agglomeration over time.

6.5.4 DPF Ash Loading

The DPFs in this study were typically loaded to 33 g/l of ash (2.47 liter DPF) using the accelerated loading system, with various measurements and evaluations performed at different stages of ash loading as described above. To achieve this level of ash load with the CJ-4 oil required 75 hours of loading on the accelerated system consuming 18 liters of oil. Details regarding DPF geometry and cell density were listed in Table 6.3.

It is estimated that the accelerated ash loading procedure is equivalent to roughly 188,000 miles or 4,680 hours of DPF operation. This estimate is based on the following assumptions for a typical medium heavy-duty diesel engine: 15 g/hr average oil

consumption [86], 40 mi/hr average speed, and a full sized particulate filter volume of 12 liters. In some cases different levels of ash loading were desired, with correspondingly different on-road equivalent miles/hours.

All of the DPF ash loading was carried out on the accelerated ash loading system. The system was used for both continuous and periodic DPF regeneration. Figures 6.26 and 6.27 present typical DPF inlet temperature and pressure drop profiles over the duration of the accelerated ash loading cycle for a DPF undergoing periodic regeneration.

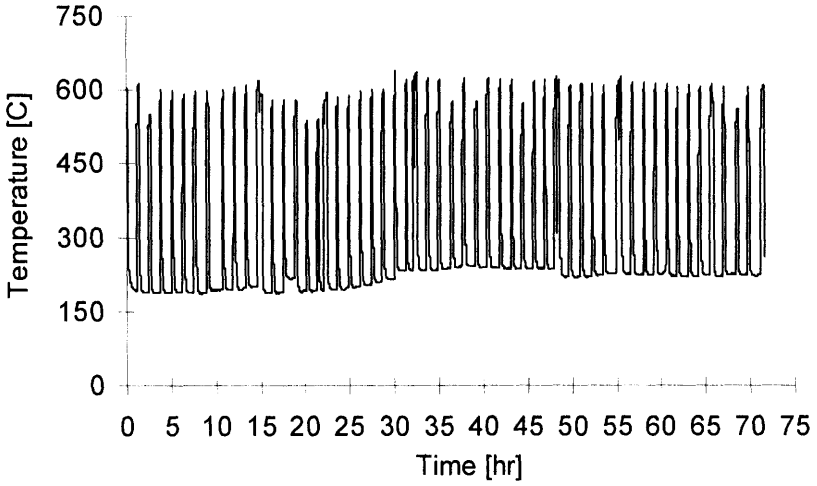

Figure 6.26. Typical DPF inlet temperature profiles for periodic loading and regeneration cycles.

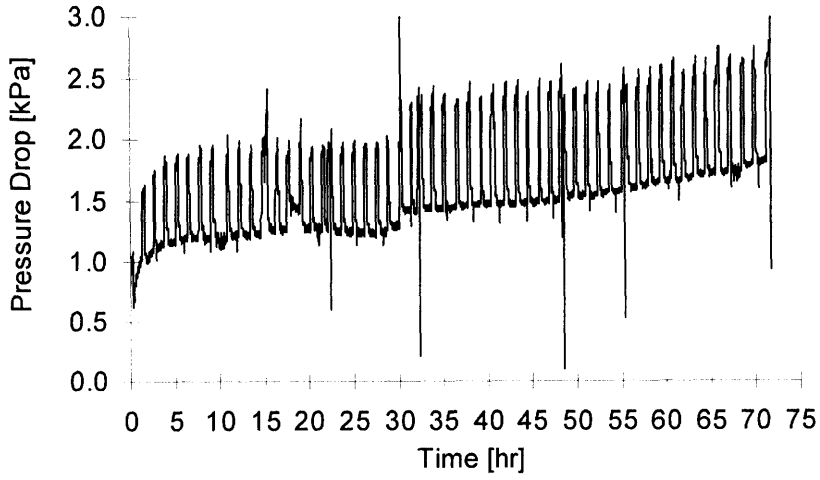

Figure 6.27. Typical DPF pressure drop trends for periodic loading and regeneration cycles.

As shown in Figure 6.26, DPF inlet temperatures during the loading portion of the cycle range from 200 °C to 250°C, with inlet temperatures during regeneration around 600 °C. Figure 6.27 shows a gradual increase in pressure drop over the course of the ash loading cycle due to ash accumulation in the DPF. It is also interesting to note the sharp increase in pressure drop over the first several hours of the test, indicative of ash depth filtration.

Ash loading tests under continuously regenerating conditions were also carried out. In these tests the DPF inlet temperature was maintained between 620 °C and 650 °C for the duration of the test cycle.

6.5.5 DPF Performance Evaluation and Test Procedure

The test procedure was designed to minimize test variability and allow for careful control and monitoring of ash composition and exhaust conditions. All DPF performance evaluation was conducted using either the Cummins ISB or the flow bench. The accelerated ash loading system was only used to load the particulate filters with ash. Due to the small filter volume, only a portion of the exhaust from the Cummins engine was diverted to flow through the DPF when the engine was used.

Initially all of the DPFs were subjected to a degreening cycle using the burner with no oil injection to expose the filters to a series of high temperature cycles. Supplementary exhaust from the Cummins ISB was also used to load the filter with soot. Following complete DPF regeneration using the burner, the filter was weighed hot to determine its clean weight. The balance used to weigh the DPF has a 12 kg maximum capacity with 0.2 g resolution. All DPF ash and soot loading reported in this paper was determined by weighing the DPF hot to eliminate error due to condensed water in the filter. DPF internal temperatures at the time of weighing were around 200 °C.

Following filter degreening, the basic test procedure is as follows:

1. Performance characterization using the Cummins ISB for soot loading to 6 g/l. Monitor gaseous emissions conversion (CO, HC, NO) and pressure drop. Soot loading determined gravimetrically by weighing the filter hot.
2. Flow bench tests to measure pressure drop over a range of space velocities at various stage of DPF soot loading.
3. Balance point / light off test using diesel burner with no oil injection. Complete filter regeneration, verified by weighing the filter hot.
4. Ash loading using the accelerated loading system with either periodic or continuous DPF regeneration. Monitor exhaust flow, pressure drop, and emissions. Ash loading determined gravimetrically by weighing the filter hot.
5. Flow bench tests to measure pressure drop over a range of space velocities at various stage of DPF ash loading.

The test procedure described above was repeated a number of times (steps 1-5) with each filter and oil to evaluate the effect of ash and soot loading on DPF pressure drop for various soot and ash levels. Unless otherwise noted, all of the pressure drop data presented in this thesis for the accelerated ash loading tests was acquired from the flow bench measurements using air at ambient conditions. Use of the flow bench provided more repeatable flow conditions for each test. While catalyst performance was also evaluated, a detailed discussion of the catalyst effects is beyond the scope of this work. Following ash loading and performance evaluation, all of the filters were subjected to a detailed post-mortem analysis.

6.6 DPF Post-Mortem Analysis

The post-mortem analysis allowed for the measurement and characterization of ash morphology, properties, and distribution in the DPF channels. Both the laboratory- and field-aged filters were subjected to the post-mortem analysis. The results of the analysis provide valuable information to correlate lubricant chemistry, exhaust conditions, and

filter thermal history to the measure ash properties. These ash properties ultimately control the magnitude of the ash effect on filter pressure drop.

6.6.1 Field-Aged Filters

A number of field-aged DPFs were subject to the post-mortem analysis to provide a benchmark for comparison with the results obtained in the laboratory. All of the field-aged filters were installed on medium- and heavy-duty trucks and used CJ-4 oils. The filter details and specifications are as follows:

- **Field DPF 1** – Robust cordierite, asymmetric cells
  - Mileage: 185,656 miles with 6 inch ash plug from rear
- **Field DPF 2** – Robust cordierite, asymmetric cells
  - Mileage: 185,886 miles with 6.5 inch ash plug from rear
- **Field DPF 3** – Robust cordierite

Both field-aged DPFs (1 and 2) experienced slightly more over 180,000 miles of on-road use, which is the same mileage exposure the accelerated ash loading system is designed to simulate. These two filters serve as an ideal standard for comparison with the filters loaded with ash in the laboratory. Unfortunately, less information is known about the third field-aged DPF, however the ash morphological information was useful, nonetheless.

6.6.2 Laboratory-Aged Filters

All of the filters loaded with ash in the laboratory were subjected to the post-mortem analysis. Table 6.5 presents the various filters, lubricants, and loading conditions, along with the estimated on-road equivalent aging.

Test Parameters		DPF Configuration	
		CDPF-V	CDPF-Pt
Oils	CJ-4 @ 1% Ash	180k mi.	68k, 180k, 230k mi.
	Base Oil (No Ash)	180k mi.	
Additive	Base Oil + ZDDP @ 1% Ash		180k mi.
	Base Oil + Ca Detergent @ 1% Ash		180k mi.
DPF Regen	Periodic (250 - 620C)	180k mi.	68k, 180k, 230k mi.
	Continuous (620-650C)		180k mi.

Table 6.5. Laboratory-aged filters subjected to post-mortem analysis. Mileage shown is the estimated on-road equivalent aging.

6.6.3 Ash Measurements

Post-mortem analysis for all of the particulate filters followed the same procedure. Each DPF was axially sectioned into two equal and symmetric halves. One half of the filter was preserved for future testing and analysis, while the other half was further sectioned into a number of smaller samples for analysis. Figure 6.28 depicts the locations of the DPF samples.

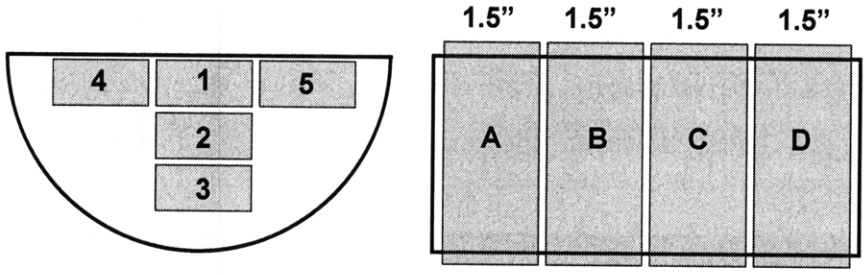

Figure 6.28. DPF sections and samples prepared for post-mortem analysis.

Each filter half section was subdivided into four 1.5 inch long sections axially. The axial sections were further subdivided into five samples corresponding to the different radial positions labeled in Figure 6.28. Each DPF sample consisted of approximately 140 to 180 individual cells of 1.5 inches in length. In this manner, twenty core samples were obtained from each filter, allowing for determination of ash properties' variation in both

the axial and radial directions in the DPF. The following measurements were taken for each DPF core sample:

- Ash layer thickness or plug dimensions depending on the ash distribution in the sample. This information was used to compute ash volume.
- Ash mass used in combination with the ash volume measurements to compute ash packing density.

The measurements listed above provide ash layer thickness profiles, ash packing density profiles, and ash distributional information for the ash accumulated in the DPF. Select ash samples from each filter were further subjected to compositional analysis via XRD as well as microscopy analysis via SEM-EDX.

Ash volume and packing density measurements for each individual ash core sample followed a set procedure developed in-house. Figure 6.29 depicts a typical filter core sample at each stage of the analysis.

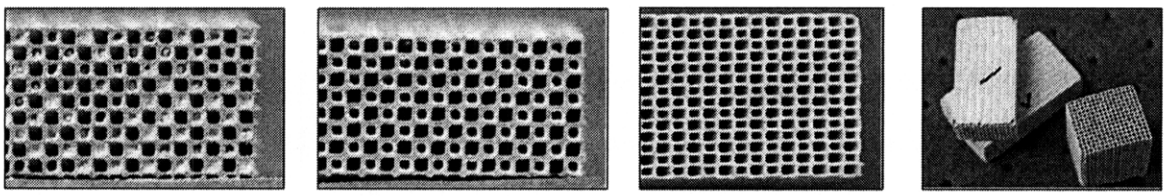

Figure 6.29. DPF core samples at each stage of the ash volume and packing density measurements.

For ash samples originating near the front or middle section of the DPF, the ash was mostly distributed in a thin layer along the channel walls. The front and back of each 1.5 inch long ash sample was imaged, and the ash layer thickness measured directly from the images using commercially available image processing software. Two ash layer thickness measurements were made per channel on each side of the filter sample. Figure 6.30 depicts a close-up view of a typical filter sample and the ash layer thickness measurement.

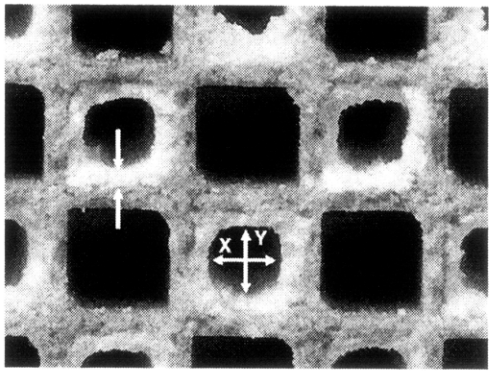

Figure 6.30. Close-up view of ash thickness measurements for the ash deposited along the DPF channel walls.

By measuring ash layer thickness at the front and back of each sample, the thickness profile over the 1.5 inch sample length was readily determined. For DPF samples originating at the back of the DPF, the ash tended to be primarily accumulated in plugs completely filling the channel. In these cases, the ash volume was readily computed from the known channel dimensions and sample length. The ash layer thickness and end-plug measurements for each sample were then combined to reconstruct the ash distribution profiles inside the entire filter.

Aside from determining the ash distribution profiles, ash packing density was also computed. The packing density determination utilized the ash layer and plug volume measurements and was carried out using the following procedure:

1. Front and back face of sample imaged for measurement (Figure 6.29-a)
2. Ash plugged filter sections weighed
3. Ash tapped out (~5 min)
4. Samples imaged and reweighed (Figure 6.29-b)
5. Ash blown out using compressed air
6. Clean filter sections weighed (Figure 6.29-c)
7. Packing density computed from known ash volume and ash weights.

Similar to the determination of the ash distribution profiles, the packing density measurements obtained as a result of this procedure were utilized to reconstruct the ash packing density profiles for the entire DPF.

The ash removed from the filter samples as part of the packing density measurement procedure was collected and subjected to analysis via XRD and ICP. While ICP only provides information related to ash elemental composition, it was extremely valuable in comparing ash composition (elemental ratios) for the ash samples obtained from the field, and the ash generated in the laboratory. XRD was used to identify the specific form of the ash compounds. This information was used to compute ash porosity based on the theoretical densities for the ash compounds and the measured ash packing density as:

$$\varepsilon = 1 - \frac{\rho_{Packing}}{\rho_{Theoretical}} \tag{6.3}$$

It should be noted that the primary ash particles comprising the structures and agglomerates deposited in the DPF may themselves be porous or hollow, giving rise to fairly high computed porosity values. While physically correct, the high porosity values do not accurately reflect the ash layer geometry experienced by the gas flows through that layer. Accurate determination of ash porosity for use in the DPF pressure drop calculations is difficult without a detailed knowledge of the primary particle morphology and structure. In general, the porosity value determined in Equation 6.3 should be corrected to account for porous and/or hollow ash particle structures before being applied to compute ash layer permeability for purposes of pressure drop calculations.

Lastly, select DPF core samples were also subjected to the microscopy investigation using SEM – EDX. SEM images are useful to understand the manner in which the ash is distributed in the DPF pores, as well as the structure of the cake layer. Further, ash particle size, pore geometries, and related morphological information are also provided by the SEM images, however extracting quantitative data from the images is often quite

challenging. EDX provides additional capabilities to measure elemental composition and elemental distribution at the microscopic level.

The post-mortem analysis conducted following DPF ash loading and performance evaluation provided a host of information describing ash distribution within the DPF, in addition to quantifying key ash properties. This information, among the first of its kind, is useful to correlate specific lubricant chemistries and exhaust conditions to the observed ash properties, and enhance understanding of the underlying mechanisms controlling the manner in which ash accumulation affects DPF pressure drop.

7 ASH TRANSPORT – ENGINE TO DPF

Before understanding how ash accumulation in the DPF affects filter pressure drop, it is instructive to investigate the mechanisms responsible for lubricant-derived ash transport to the exhaust and accumulation in the DPF. In order to better understand the ash transport and deposition processes, as series of experiments were performed using the Cummins ISB to characterize engine-out ash emissions and determine speciated DPF trapping efficiencies. This information is useful to describe ash accumulation in the DPF, and also to compare the characteristics and properties of the ash generated using the accelerated ash loading system with engine-out ash and PM.

7.1 Ash Distribution on Soot Particles

The distribution of specific ash-related elements in the particulate aggregates was investigated using electron microscopy. A portion of the PM from the exhaust of the Cummins ISB was collected on 47 mm glass fiber filters and transferred to small 3 mm carbon coated copper grids for analysis using STEM. Figure 7.1 depicts a typical STEM spectrum of the PM composition upstream of the DPF during the soot loading cycle.

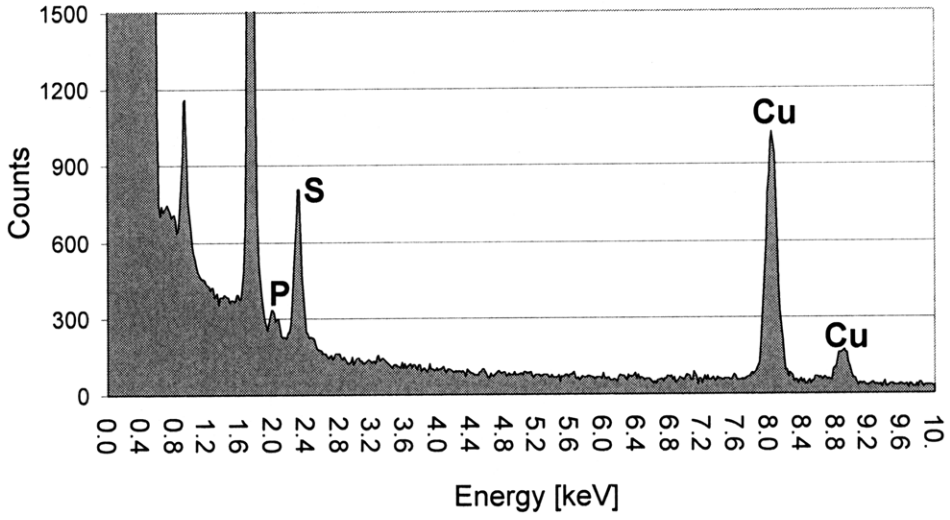

Figure 7.1. Typical STEM spectrum of PM entering the DPF during soot loading at 1682 rpm, 25% load on the Cummins ISB.

The large peaks on the far left of the spectrum are primarily due to the high carbon content of the soot, whereas the two copper peaks on the far right are the result of the background from the copper grids used to prepare the sample. As evident in Figure 7.1, the most significant ash-related elements in the PM appear to be sulfur and phosphorous. While the sulfur is due to the sulfur present in both the engine lubricant and fuel, the phosphorous originates in the lubricant additives alone. Due to the high concentration of carbon and relatively low concentration of ash-related metals in the PM, no other significant peaks were observed in the majority of the bulk PM samples.

In order to determine whether or not significant variations in localized concentrations of ash-related elements existed in the PM, specific regions of the sample were scanned, and spectra representative of the elemental distribution of each region were acquired. Figure 7.2 shows a TEM image of the bulk PM sample, as well as the localized regions subjected to the elemental analysis.

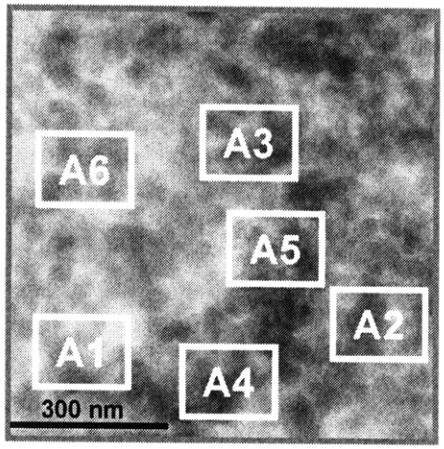

Figure 7.2. Localized STEM scan regions on the bulk PM sample for PM generated at 1682 rpm, 25% load.

The elemental spectra corresponding to each of the localized regions of the soot samples scanned in Figure 7.2 are shown in Figure 7.3.

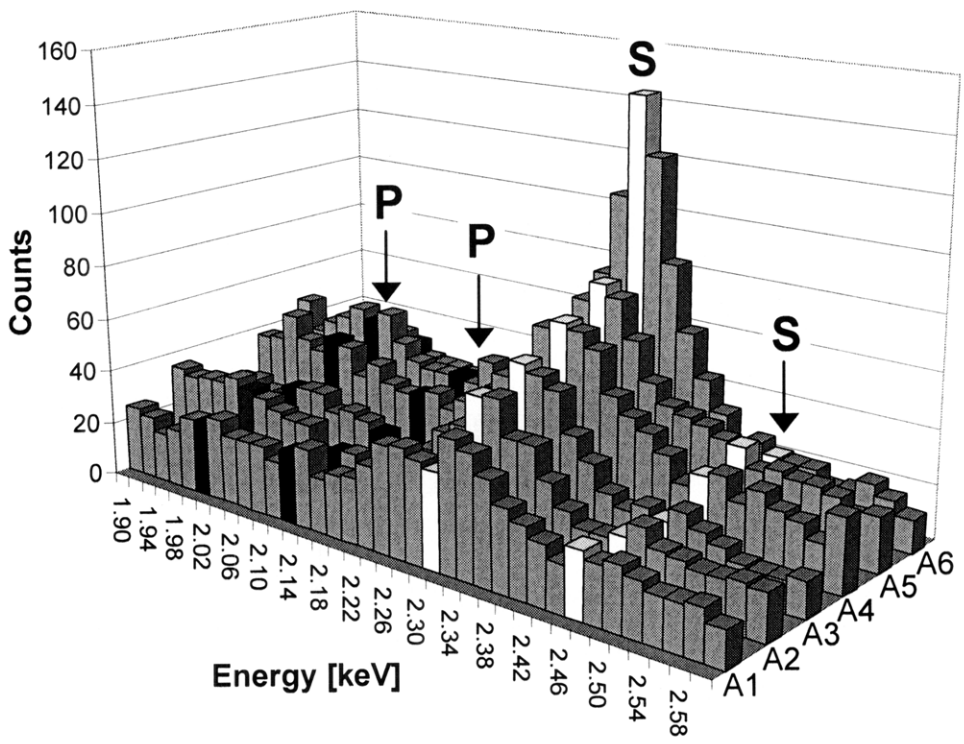

Figure 7.3. Localized variations in sulfur and phosphorous distribution in the bulk particulate matter samples.

In Figure 7.3 the light lines correspond to the spectral lines for sulfur, whereas the dark lines correspond to those of phosphorous. From Figure 7.3 it is clear that localized regions of high sulfur and phosphorous concentrations exist, implying a heterogeneous distribution of ash-related elements in the individual particulate agglomerates.

Figure 7.4 presents a comparison of the entire spectra for two separate regions of a small (200 nm) soot agglomerate. The size of the agglomerate is characteristic of the typical PM agglomerate sizes which enter and are collected in the DPF. Similar to the bulk particulate matter analysis, significant variations in Zn, S, and P distribution are evident between the two local areas of investigation on the individual soot agglomerate.

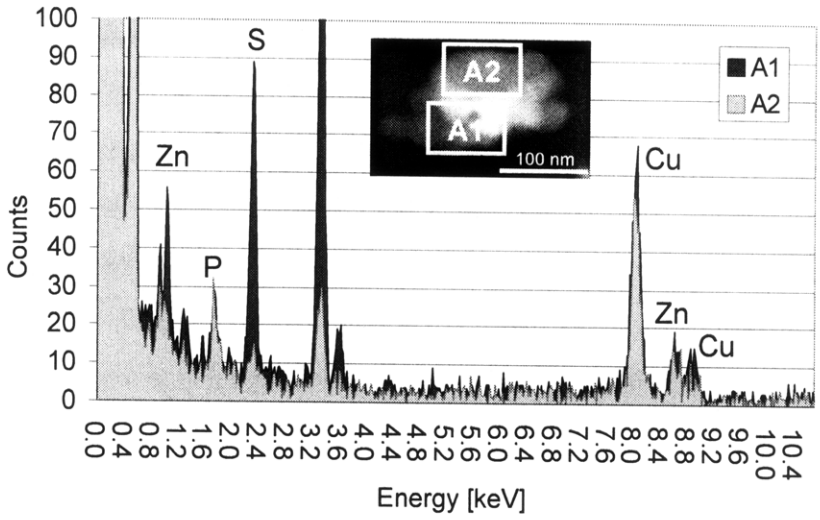

Figure 7.4. Localized variations of Zn, S, and P for two regions of a particulate agglomerate generated at 1682 rpm, 25% load.

Aside from the bulk PM sampling and analysis, individual particle samples were collected directly on the TEM grids by inserting a probe to which the grids were fixed into the exhaust stream of the Cummins engine at the entrance and exit of the DPF. This system was utilized in addition to the bulk sampling methods to collect individual particles frozen in composition and structure, with the primary objective of determining whether or not the ash-related compounds exist as separate particles or are bound to the carbonaceous PM agglomerates in the exhaust. Figures 7.5 and 7.6 depict representative TEM images of particles sampled directly before and after the DPF.

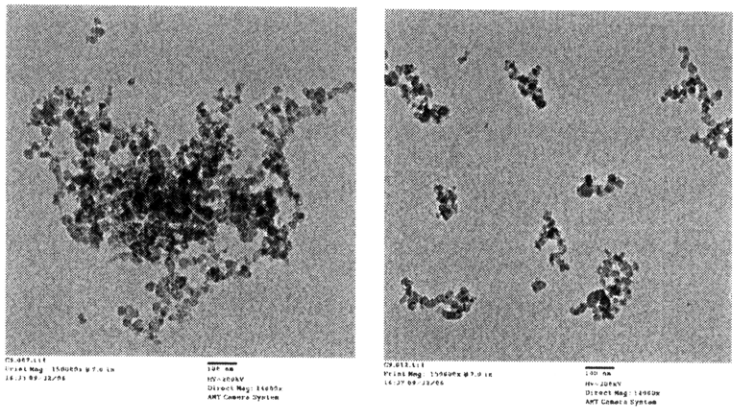

Figure 7.5. TEM images of particles sampled near the entrance to the DPF at 1682 rpm, 25% load (150,000x).

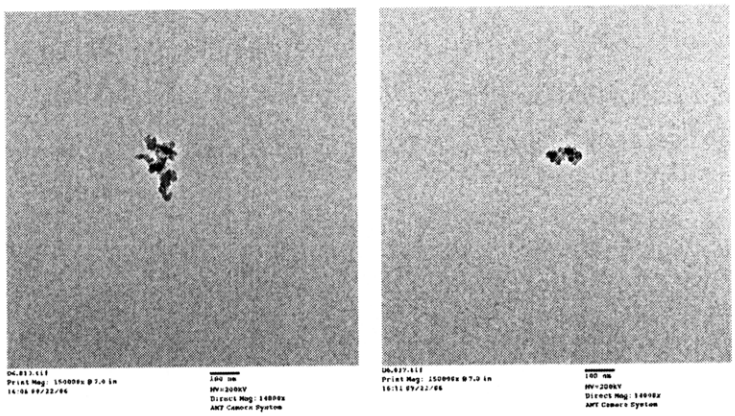

Figure 7.6. TEM images of particles sampled near the exit of the DPF at 1682 rpm, 25% load (150,000x).

The images in Figures 7.5 and 7.6 were taken at the same magnification to allow for direct comparison of particle size and number concentrations between the two cases (pre- and post-DPF). While the high trapping efficiency of the DPF does capture most of the particles present in the exhaust, smaller nuclei-mode and some agglomerate particles were observed in the exhaust, downstream from the DPF.

In addition to analyzing the physical characteristics of the particles collected before and after the particulate filter, the elemental composition of each particle was determined using STEM. Similar to the bulk PM analysis, trace amounts of lubricant-derived ash-related elements were found in the individual soot agglomerates. However, individual wear metal and corrosion particles were observed to be clearly separate particles from the carbonaceous PM. An example of such a particle and its associate spectra is shown in Figure 7.7.

The results of the individual soot particle microscopy analysis showed most lubricant-derived elements to be intimately bound to the carbonaceous soot agglomerates. No lubricant-derived elements were observed to exist as separate particles in the exhaust. These observations imply that lubricant-derived ash-related elements are deposited in the DPF along with the PM agglomerates forming a soot layer along the DPF channel walls, throughout which the lubricant-derived ash is dispersed. On the other hand, engine wear

and corrosion particles were observed to exist as separate particles, independent of the carbonaceous PM, as depicted in Figure 7.7.

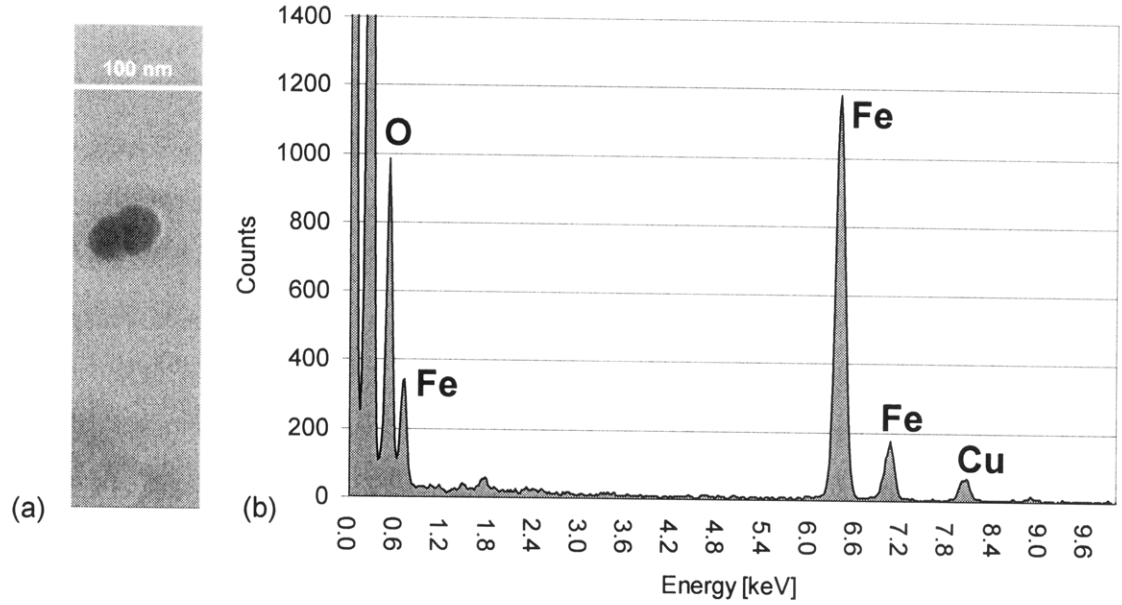

Figure 7.7. TEM image (a) and associated spectra (b) for a separate FeO particle originating from engine wear or exhaust system corrosion.

Following soot oxidation, the incombustible ash material remains, and forms ash agglomerates in the channel pores and along the filter walls. The resulting ash properties are much more a function of the ash elemental distribution in the PM and the soot oxidation processes, than the actual PM deposition mechanisms. Further, while not conclusive, the fact that all lubricant-derived ash-related elements were found bound to the carbonaceous PM, and not as separate particles in the exhaust, implies that the ash particle size entering the DPF is on the order of the soot agglomerate size (~ 100nm). This provides further evidence for the strong influence of the ash formation/sintering mechanisms during DPF regeneration which are responsible for the increase in ash particle size to on the order of 1 micron, which is typically observed for the ash accumulated in DPFs.

7.2 Ash Emissions Rate

The total ash fraction of the engine-out PM was determined via TGA analysis. The PM sample size for the analysis ranged from 5 to 6 mg, and was obtained from the soot collected on the 47 mm glass fiber filters. A typical TGA profile for a PM sample collected upstream of the DPF during the soot loading cycle is shown in Figure 7.8.

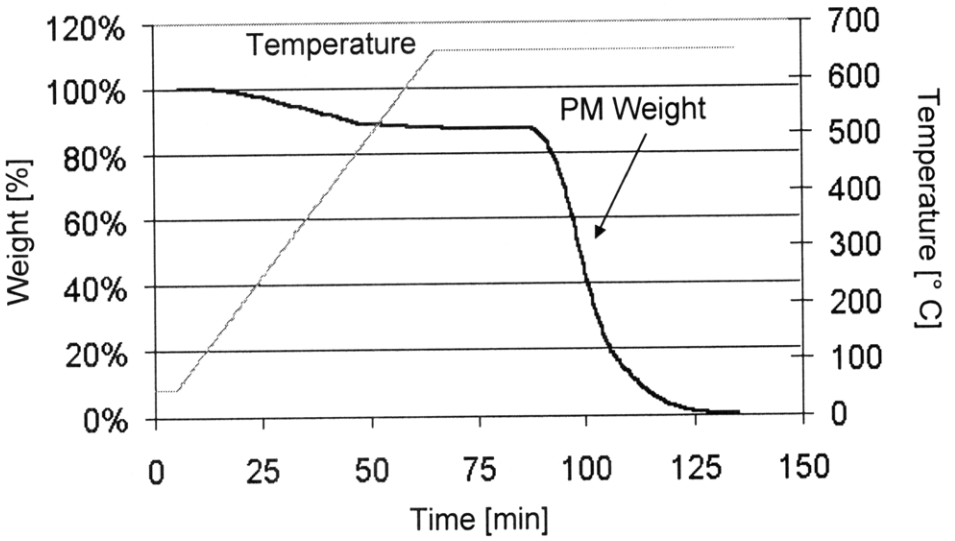

Figure 7.8. TGA profile for typical PM sample collected upstream of the DPF at 1682 rpm, 25% load on the Cummins ISB.

For the first 85 minutes of the analysis, the sample was heated to 650 °C and then maintained at that temperature in a nitrogen atmosphere. Following this time period, air was introduced and the remaining PM was oxidized. The following compositional regimes for the PM were defined based on the amount of mass lost between specified temperature intervals:

- High volatile fraction: mass lost up to 160 °C in N_2
- Medium volatile fraction: mass loss from 160 °C to 650 °C in N_2
- Combustible fraction: mass lost at 650 °C upon the introduction of air
- Ash: remaining un-oxidized material following the analysis.

The composition of the PM entering the DPF during the soot loading phase as determined by TGA is depicted in Figure 7.9.

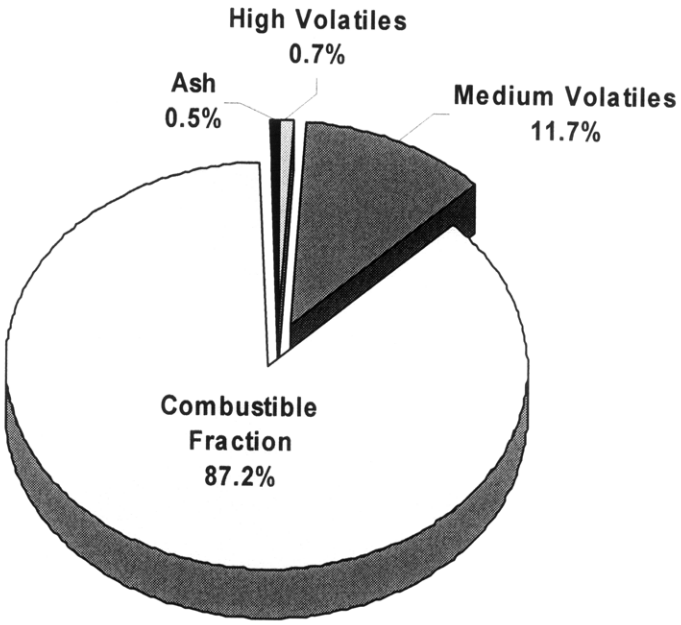

Figure 7.9. PM composition as determined by TGA for PM sampled upstream of the DPF at 1682 rpm, 25% load on the Cummins ISB.

From Figure 7.9 it is clear that the ash comprises a very small fraction of the PM generated at this condition. The high- and medium- volatile fractions correspond roughly to the soluble organic fraction, whereas the combustible fraction consists primarily of carbon and is roughly equivalent to the insoluble carbonaceous fraction.

Figure 7.10 presents the ash fraction of the total particulate matter emissions from the Cummins ISB as a function of the engine's rated load at 1682 rpm. The measured ash fraction varied between slightly less than 0.5% to 1.0% of the total particulate matter. These measurements correspond to ash emissions in the range of 0.007 to 0.00035 g/hp-hr (0.21 to 0.11 g/hr at rated conditions), and are consistent with ash levels measured in diesel particulate filters following extended on-road use, prior to ash cleaning.

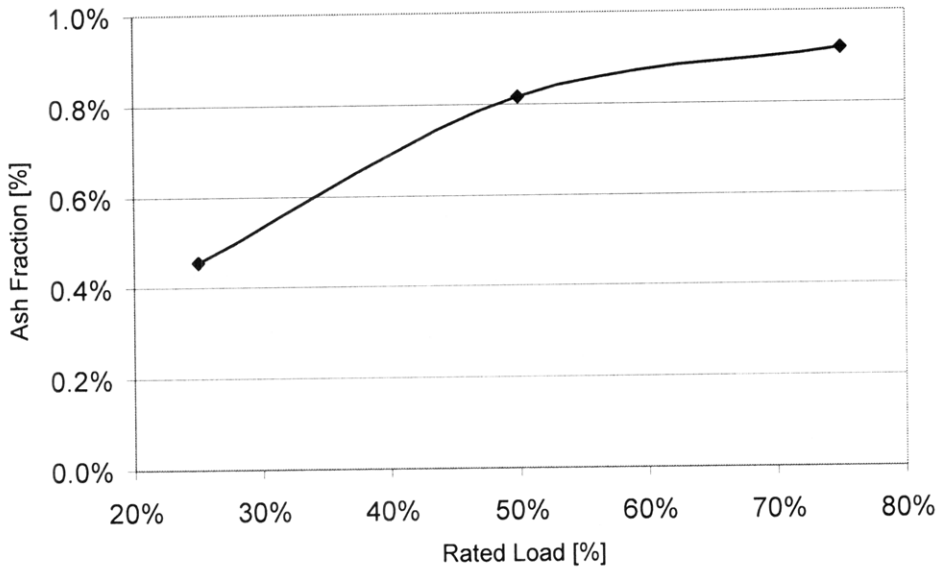

Figure 7.10. PM ash fraction as a function of engine rated load determined by TGA for PM sampled upstream of the DPF at 1682 rpm on the Cummins ISB.

7.3 Ash Formation and Composition

A SEM image of the ash that resulted from the TGA analysis is shown in Figure 7.11. The average particle sizes for the ash generated using TGA ranged between 1μm to 8μm, which is in good agreement with results reported in the literature for agglomerated ash particles generated in DPF systems in the field.

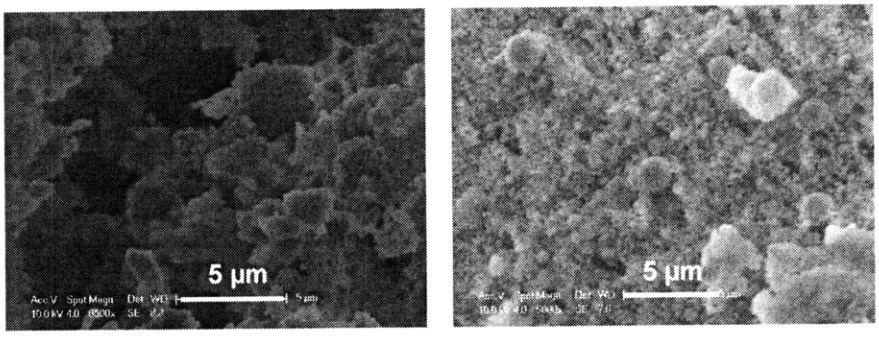

Figure 7.11. SEM images representative of ash particles generated during TGA with soot collected from the Cummins ISB .

The ash generated from the PM as a result of the TGA was then subjected to the same STEM analysis as the original particle samples. Once again, the ash samples were prepared in much the same manner as the previous PM samples using 3 mm carbon coated copper sample girds. A typical STEM spectrum of the ash composition generated from the PM collected upstream of the DPF during the soot loading cycle is shown in Figure 7.12.

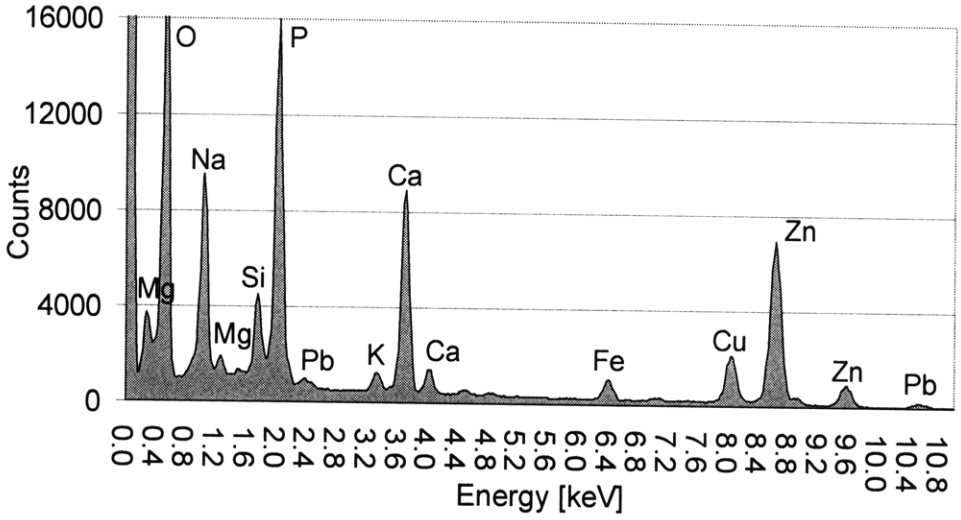

Figure 7.12. Typical STEM spectrum of ash generated from PM entering the DPF at 1682 rpm, 25% load on the Cummins ISB.

From Figure 7.12 it is evident that the ash is composed of a number of lubricant-derived elements including Ca, Mg, Zn, and P. Interestingly, no significant amounts of sulfur were observed in any of the ash samples. Additional metallic elements found in the ash included Fe and Pb, believed to be the result of engine component wear and/or exhaust system corrosion. The absence of any sulfur in the ash is attributed to the manner in which the ash was generated from the PM using TGA, and may not be completely representative of the ash generated in the DPF. Specifically, the apparent desulfation of the ash is attributed to the long residence time at 650 °C to which the PM and subsequently generated ash was subjected in the TGA.

Figures 7.13 and 7.14 depict maps showing the elemental distribution of various lubricant- and engine wear-derived metals as well as P and O overlaid on the TEM images of individual ash particles.

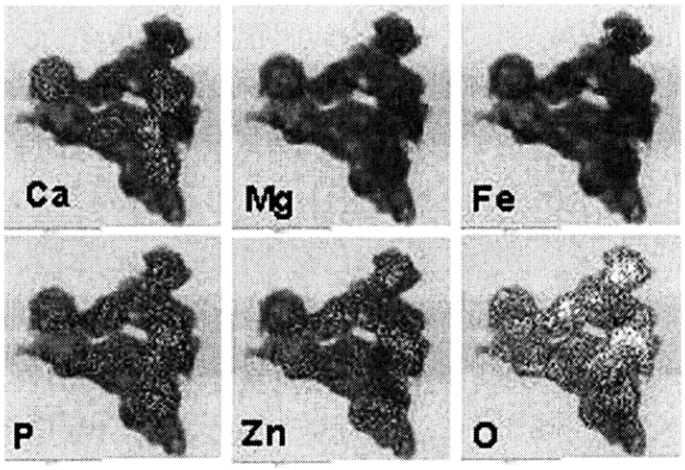

Figure 7.13. Elemental distribution of Ca, Mg, Fe, P, Zn, and O on a TEM image of an ash particle generated in the TGA with soot collected from the Cummins ISB.

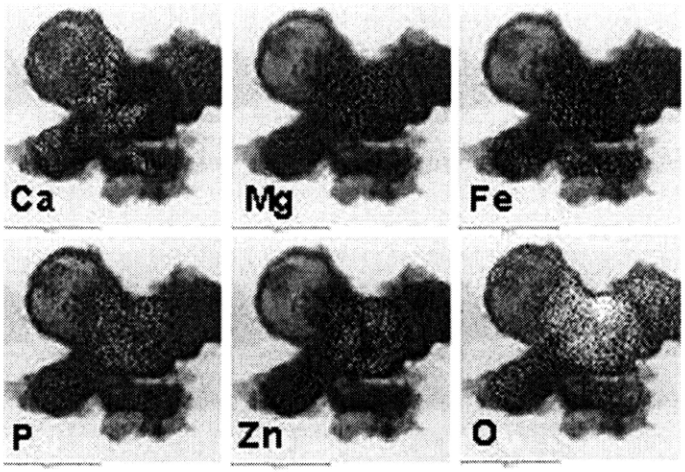

Figure 7.14. Elemental distribution of Ca, Mg, Fe, P, Zn, and O on a TEM image of an ash particle generated in the TGA with soot collected from the Cummins ISB.

Figures 7.13 and 7.14 show localized variations in the distribution of Ca, P, and Zn. The variations in the distribution of these elements in the ash particles, combined with the

oxygen distribution, offers some qualitative insight into the form of the ash compounds in each of these locations. From the elemental maps, regions containing high calcium phosphate, zinc phosphate, and calcium and zinc oxide concentrations are apparent. Furthermore, only small traces of magnesium can be seen sparsely distributed across the ash particle. In addition, Figure 7.13 shows a highly localized distribution of Fe present only in the upper right-hand corner of the ash. The elemental analysis of the ash further show the ash agglomerates are composed of various ash compounds, indicating the agglomerates form when individual ash particles sinter or fuse together.

In addition to compositional information, Figure 7.14 provides some information regarding ash morphology. The upper left-hand corner of the TEM images show the presence of what appears to be a large hollow sphere, the walls of which are composed primarily of calcium and phosphorous compounds. The TEM images indicate the ash agglomerates are composed of primary ash particles which may themselves be porous or hollow. While these properties of the particles do not directly affect the exhaust gas flow, it is important to account for these characteristics when computing ash packing density and porosity for use in estimating ash contribution to the DPF pressure drop. The hollow primary particles will occupy a significantly greater volume than solid structures. Further evidence supporting these experimental observations is provided in Figure 7.15 from the literature. The figure shows an individual ash particle, which is clearly hollow.

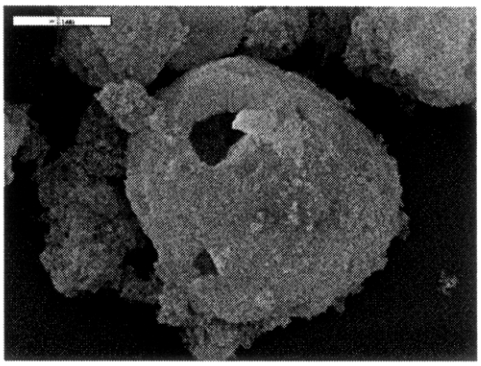

Figure 7.15. SEM image depicting hollow spherical ash particle [58].

7.4 Ash Elemental Emissions and Trapping Rates

Measurements and analysis of the soot emissions at the DPF inlet and outlet allowed for determination of the speciated and elemental DPF trapping efficiencies. Specifically, analysis of the soot samples using the Horiba Mexa 1370 and analytical chemistry techniques allowed for determination of the amounts of insoluble materials, soluble organics, and sulfates trapped in the DPF. Figure 7.16 shows the measured pre- and post-DPF emission rates of insoluble (primarily carbonaceous and ash) material. Both the catalyzed and un-catalyzed DPFs averaged a 99% trapping efficiency for the insoluble fraction over both the steady-state loading and regeneration cycles.

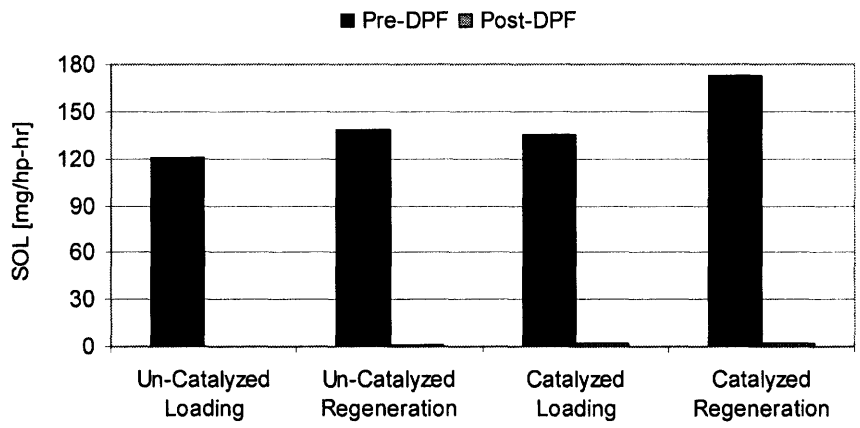

Figure 7.16. Pre- and post-DPF emissions of insoluble PM fraction measured during DPF loading and regeneration cycles.

The speciated emission rates computed for the soluble organic fraction are shown in Figure 7.17. The speciated trapping efficiency for the soluble organic fraction averaged 95% for the un-catalyzed DPFs over both the loading and regeneration cycles. The trapping efficiency for the SOF over the catalyzed DPFs averaged approximately 85% during the steady-state loading cycle and 97% during the regeneration cycle.

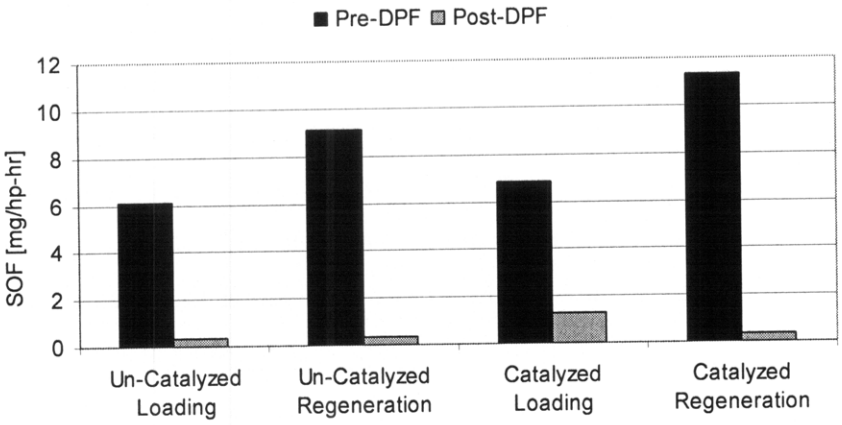

Figure 7.17. Pre- and post-DPF emissions of soluble organic PM fraction measured during DPF loading and regeneration cycles.

Figure 7.18 presents the speciated emission rates for the sulfate fraction. The speciated trapping efficiency of the sulfate fraction in the un-catalyzed DPFs ranged from 35% during the loading cycle to 55% during DPF regeneration. On the other hand, the speciated emission rates for sulfates with the catalyzed DPFs remained nearly constant over the DPF loading cycle and then decreased significantly with an 87% trapping efficiency during DPF regeneration.

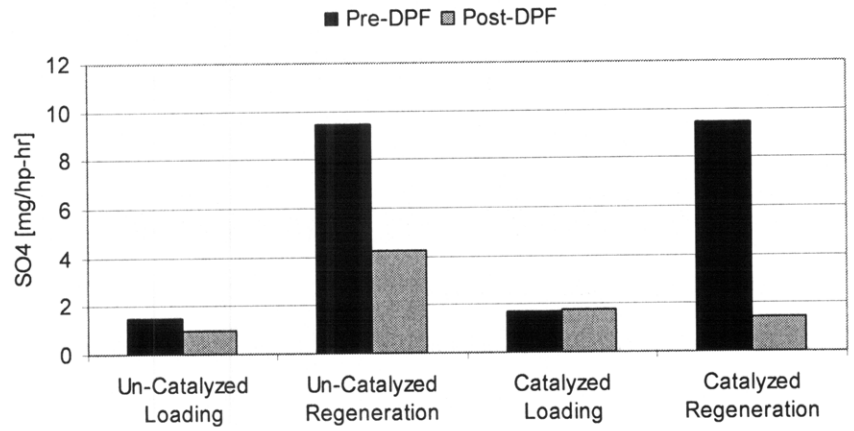

Figure 7.18. Pre- and post-DPF emissions of sulfate PM fraction measured during DPF loading and regeneration cycles.

The difference in speciated trapping efficiencies for the sulfates is circumstantial indication that the trapping mechanisms for particulate matter depend on both the

physical and chemical characteristics of the material being trapped. In the case of the un-catalyzed DPFs, the significant differences in the trapping efficiencies for the sulfates are attributed to differences in the physical trapping mechanisms. The majority of the sulfate PM exists in either liquid/vapor form and may, thus, pass through the DPF more easily than the insoluble fraction that exists primarily in the solid phase.

The explanation for the differences in trapping efficiencies for the sulfate fraction observed with the catalyzed DPFs is complicated by the potential interactions of the sulfur species in the exhaust with the platinum catalyst. The observed reduction in SO_2 emissions and strong affinity of the sulfur species to the Pt catalyst may lead to the conversion of gaseous SO_2 to particle-phase sulfates within the DPF, which may contribute to the elevated post-DPF sulfate emission rates measured during the steady-state loading cycle. On the other hand, during the high temperature regeneration cycle, the amount of sulfates entering the DPF increased significantly, while sulfate emission rates from the DPF remained virtually unchanged, thus leading to the increase in observed trapping efficiency.

In addition to determining the speciated PM trapping rates, the lubricant-derived elemental emissions were also measured upstream and downstream of the DPF. The levels of trace elements in the bulk particulate matter samples were determined using ICP analysis. The entire filter, along with the accumulated soot, was subjected to an acid and microwave digestion technique, prior to analysis via ICP. Clean filter samples, were processed in the same manner, to account for the presence of any trace elements on the filters themselves, which may affect the results. Similar measurements were repeated using neutron activation analysis. As the NAA experiments focused primarily on elemental emission rates of biodiesel fuels, the detailed results are not presented here. In general the NAA measurements with ULSD were in good agreement with the ICP data.

Figure 7.19 presents the measured elemental emission rates for lubricant- and fuel-derived trace elements entering the DPF, and Figure 7.20 shows a direct comparison of

pre- and post-DPF elemental emissions. In both cases, the elemental emission rates were determined via ICP analysis of the PM samples.

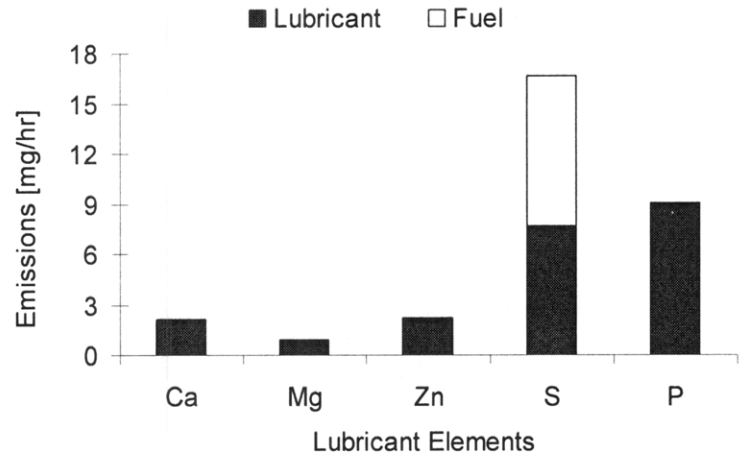

Figure 7.19. Lubricant- and fuel-derived elemental emission rates measured at 1682 rpm and 25% rated load at the DPF inlet on the Cummins ISB.

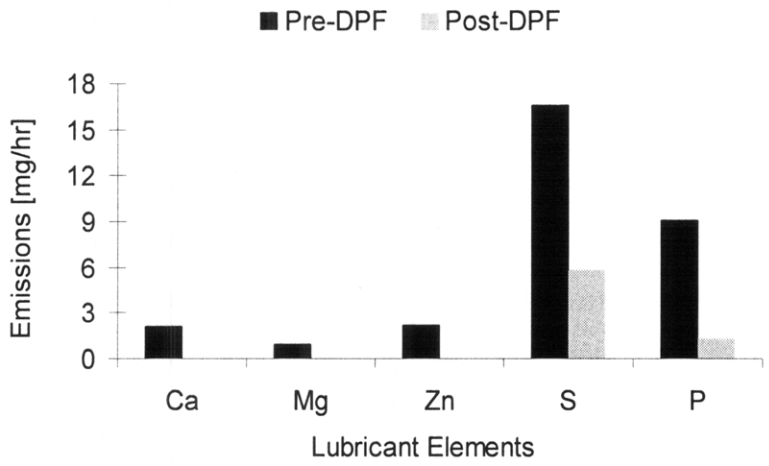

Figure 7.20 Lubricant-derived elemental emission rates and DPF trapping rates measured at 1682 rpm and 25% rated load on the Cummins ISB.

From Figure 7.19, elemental emissions of lubricant-derived trace metals ranged from approximately 1 mg/hr to 3 mg/hr at these engine operating conditions, however phosphorous and sulfur emissions were significantly higher. The high sulfur emissions measured in the PM samples are due to the sulfur present in the fuel as well as the lubricant. Based on PM sulfur measurements with a zero sulfur Fischer-Tropsch diesel fuel, the relative fuel and lubricant contributions to the PM-phase sulfur were estimated

and are shown in Figure 7.19. With a conventional ultra-low sulfur diesel fuel, a significant amount of the fuel sulfur is emitted as sulfur dioxide as well.

The elemental trapping efficiencies were computed based on the pre- and post-DPF elemental emissions measurements shown in Figure 7.20. The trapping efficiencies are shown in Table 7.1 below. In general, nearly all of the trace metals (Ca, Zn, Mg) were trapped in the DPF at a high rate, in excess of 98%. The trapping efficiencies for sulfur and phosphorous compounds were slightly lower and ranged from 65% to 85% respectively.

	Ca	Fe	Mg	P	S	Zn
Trapping Efficiency	99.9%	92.4%	98.0%	85.1%	64.9%	99.7%

Table 7.1. Lubricant elemental DPF trapping efficiencies measured at 1682 rpm and 25% rated load.

The reduction in sulfur trapping efficiency can be attributed to the different phases of the sulfur species in the exhaust (primarily gaseous and liquid phase) which may pass through the DPF. Sulfate particles generally contribute to PM primary particle emissions and exist in the liquid phase in the exhaust. Additionally, sulfate production over the DPF catalyst can also contribute to post-DPF particle-phase sulfur emissions, complicating the trapping efficiency measurements. The slight reduction in trapping efficiency for phosphorous may also be due to certain phosphorous species passing through the DPF, however at 85% the phosphorus trapping efficiency is still quite high.

7.5 Exhaust Ash Transport Theory

The experimental observations of exhaust ash characteristics, morphology, and composition provide considerable insight into ash transport through the exhaust system and deposition in the DPF. The results of the TGA measurements have shown ash to comprise only 0.5% to 1% of the total particulate matter emissions from a modern diesel engine. Additionally, the microscopy studies provide evidence to indicate that lubricant-

derived ash is intimately bound to the carbonaceous particulate matter in the exhaust. These observations are further supported by the fact that the soluble organic PM fraction is generally associated with condensed hydrocarbons originating in the engine lubricant. No separate lubricant-derived ash particles were observed in the microscopy studies, however elements resulting from engine-wear and corrosion were observed to exist as distinctly separate particles in the exhaust.

STEM analysis of elemental distributions on the PM found variation in sulfur, phosphorous, and zinc levels in the PM agglomerates. This circumstantial evidence indicates that the lubricant-derived elements transported and accumulated in the DPF are closely bound to the soot particles. Therefore, the relative size of the lubricant-derived species in the exhaust must be equal to or less than the size of the PM agglomerates (typically on the order of 100 nm). These experimental observations are depicted in the schematic shown in Figure 7.21.

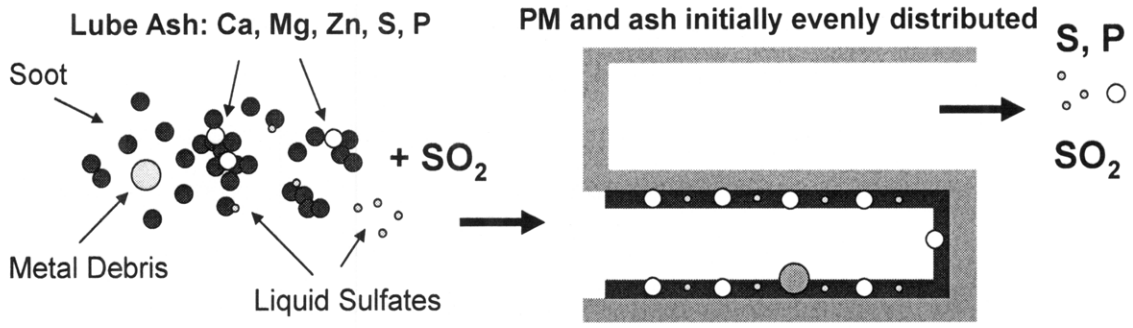

Figure 7.21 Schematic depicting ash transport in the exhaust and accumulation in the DPF.

Figure 7.21 shows lubricant derived elements emitted from the engine, dispersed on the carbonaceous particulate matter, and engine wear-related elements existing as separate particles in the exhaust. Lubricant- and fuel-derived sulfur may exist in particle-phase sulfates or in the gaseous phase as SO_2. The lubricant-derived ash, which comprises only a small fraction of the particulate matter, is then deposited along with the carbonaceous soot on the walls of the DPF. Over time, soot and ash accumulate in the pores and in the cake layer of the DPF. During filter regeneration, the soot is oxidized

leaving the ash behind. Further, the sub-micron sized ash primary particles sinter and agglomerate to form the micron-sized ash deposits commonly found in DPFs following extended aging and ash accumulation. Since the ash comprises less than 1% of the total particulate matter, soot oxidation during filter regeneration leaves behind an extremely porous and mechanically unstable ash structure. Over time these structures grow with additional ash accumulation in the DPF to form an ash layer along the filter walls. Depending on the shear stress imposed by the exhaust flow through the channels and the local critical shear stress of the ash deposits, the ash may become re-entrained in the gas flow and deposited elsewhere in the DPF. The ash accumulation and transport theory proposed above, is revisited in Chapter 8, following a review of the DPF post-mortem analysis and experimentally determined ash properties and distribution profiles.

(This page intentionally left blank)

8 ASH EFFECTS ON DPF PRESSURE DROP

The results presented in this section correspond to experiments conducted using the fully-formulated commercial CJ-4 oil and ashless base oil. All of the DPF ash loading was conducted on the accelerated ash loading system, and the filters were regenerated periodically. The experimental results are representative of the ash deposition and increase in filter pressure drop observed after extended on-road aging of approximately 180,000 miles.

8.1 Initial Ash Accumulation Phases

Similar to soot accumulation in a clean DPF, ash accumulation tends to show both depth and cake filtration regimes, as depicted in Figure 8.1. The data presented in the figure was obtained by measuring pressure drop on a flow bench at various stages of filter ash loading, following complete regeneration.

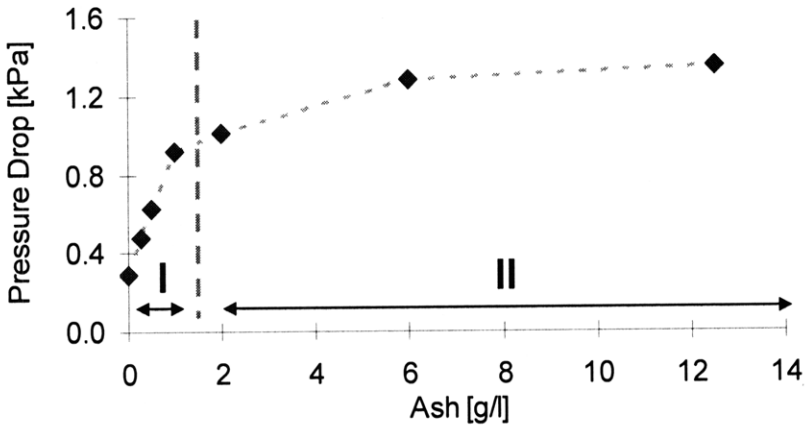

Figure 8.1. Depth (I) and cake (II) filtration regimes at 20,000 hr^{-1} space velocity for ash accumulation in a DPF undergoing periodic regeneration.

The amount of ash trapped in the filter walls is expected to be around 2 g/l based on the pressure drop profile. Despite the small amount of ash trapped in the filter walls (only 5% to 10% of the total DPF ash loading in this study), ash accumulated in the walls contributes significantly to the total pressure drop due to ash loading.

Figure 8.2 presents a schematic showing the evolution of ash accumulation in the DPF pores and the build-up of the ash cake layer. The regions of the DPF pressure drop curves corresponding to the location of the various ash deposits are clearly labeled in Figure 8.3. The experimental data shown in Figure 8.3 is the result of two separate experiments with two different DPFs. Variation of approximately 0.2 kPa was observed between the two tests. The first set of test data depicted in Figure 8.3 contains a larger number of data points (higher resolution) for the initial ash accumulation process (0-12.5 g/l ash), whereas the second set of data lacks resolution during the initial ash loading stages, but shows the filter pressure drop response at much higher ash loads (up to 42 g/l).

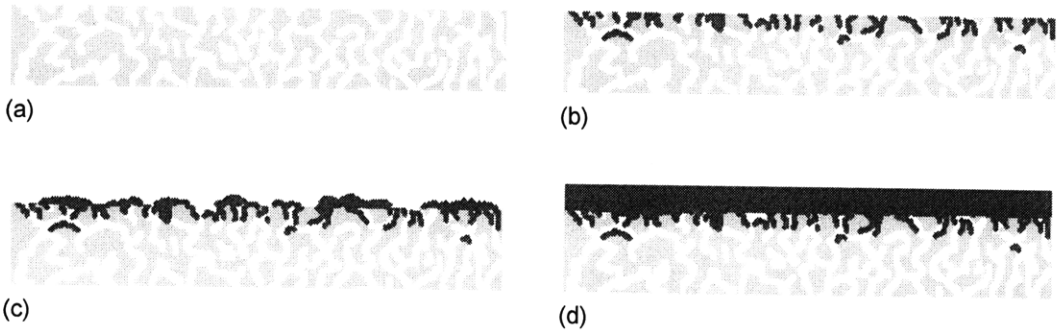

Figure 8.2. Stages of ash accumulation on (a) clean porous ceramic filter, (b) ash accumulation in filter pores, (c) transitional ash accumulation in pores and on filter surface, and (d) ash build-up on filter cake layer.

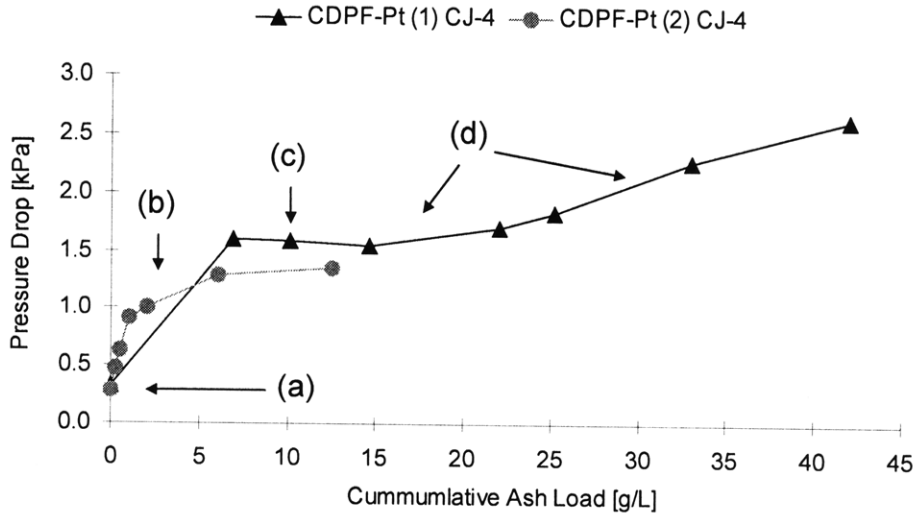

Figure 8.3. DPF pressure drop curves showing each stage of ash accumulation.

In a clean DPF the ash initially accumulates primarily in the DPF pores, resulting in a rapid increase in filter pressure drop as shown by the region (b) in Figure 8.3. Additional ash deposition in the DPF results in a transitional filter loading state, where the ash continues to accumulate in some of the DPF pores and also along the filter walls as depicted in region (c) of Figure 8.3. As ash continues to collect in the DPF, it primarily builds a filter cake layer, giving rise to the gradual increase in pressure drop shown by region (d) in Figure 8.3.

8.2 Ash-Impact Over DPF Service Life

A comparison between the pressure drop trends for DPFs undergoing periodic regeneration using the base oil and conventional CJ-4 oil is shown in Figure 8.4. The data presented in the figure corresponds to the pressure drop measured following each complete regeneration cycle, ensuring that only ash (no soot) was present in the DPF. The dimensionless pressure drop is computed as the pressure drop over the loaded DPF divided by the pressure drop of the initially clean DPF (after 1.5 hours on the accelerated loading system) at the same exhaust temperature and flow conditions. A dimensionless pressure drop value of unity is indicative of a clean filter with no material accumulation.

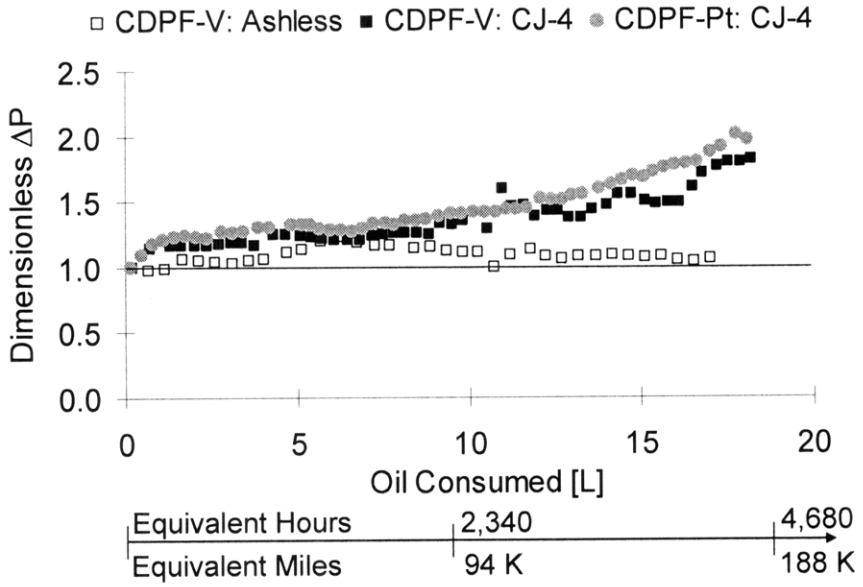

Figure 8.4. Dimensionless pressure drop comparison for the base oil and CJ-4 oil.

The secondary horizontal axis in Figure 8.4 presents the estimated equivalent hours and mileage for the accelerated test procedure, which is roughly equivalent to 4,680 hours or 188,000 miles of on-road use. Both DPFs tested using CJ-4 oils accumulated approximately 33 g/l of ash and exhibited an increase in pressure drop 1.8 to 1.9 times greater than the clean case. On the other hand, no ash was detected in the DPF exposed to the base oil alone and there was little discernable difference in pressure drop.

Figure 8.5 compares pressure drop as a function of space velocity for DPFs tested with the ashless base oil and conventional CJ-4 oil on the accelerated ash loading system. The pressure drop data was obtained using a flow bench with air at ambient conditions. The DPFs were aged on the accelerated loading system for the same duration consuming equivalent amounts of oil. Both of the clean filters exhibited nearly the same pressure drop characteristics at the start of the test. No real difference was observed between the clean and aged (loaded) case with the base oil, while a significant increase in pressure drop over the clean case is observed with the ash-loaded DPF (33 g/l) using the CJ-4 oil.

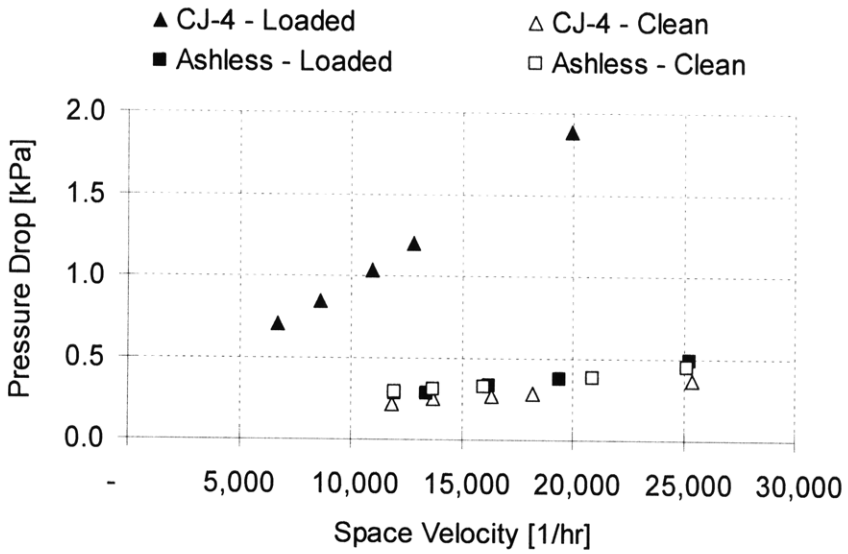

Figure 8.5. Pressure drop variation with space velocity for the vanadium catalyzed DPF using conventional CJ-4 and ashless base oil.

8.3 Ash-Properties and Ash Distribution

The DPF post-mortem analysis provided information on the distribution and properties of the ash trapped in the filter. Figure 8.6 shows two filter samples from different axial positions of the same DPF. The DPF sample shown in Figure 8.6(a) was removed 57mm from the front face of the filter, and shows ash accumulated in a thin layer along the channel walls. Figure 8.6(b) is from a DPF sample towards the back of the filter and clearly shows the ash plugging nearly all of the channels.

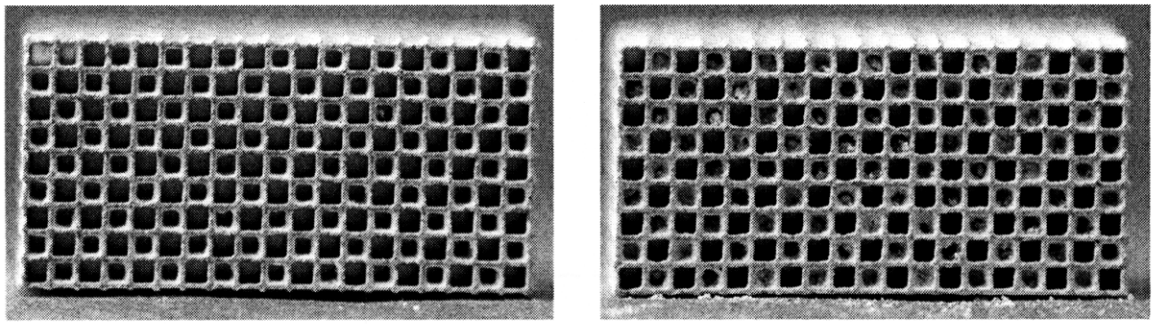

(a) (b)

Figure 8.6. DPF samples containing 42 g/l ash generated in the laboratory using CJ-4 oil and periodic regeneration along center of filter (a) 57 mm from front face and (b) 133 mm from front face.

The ash distribution shown in Figure 8.6 is representative of the ash distribution profiles generally found in most field-aged filters, however the relative amount of ash collected along the channel walls versus at the back of the filter in the plugs may vary. The DPF measurements presented in the following sections attempt to quantify differences in ash distribution along the channel walls and in the ash plugs.

8.3.1 Ash Layer Thickness: High Ash Loads

Figures 8.7 and 8.8 show the measured ash distribution profiles for a filter containing 42 g/l ash generated with a CJ-4 oil and periodic regeneration. Figure 8.7 depicts the measured ash layer thickness profiles along the length of the DPF for three different radial positions. The scale on the horizontal axis of Figure 8.7 corresponds to the total

DPF channel length. Furthermore, the length of ash accumulated in the end-plug is also clearly visible in the figure. The amount of ash accumulated in the end-plugs tended to decrease with increasing distance from the center of the DPF. The abrupt changes in ash layer thickness, particularly near the start of the end-plug, are due to the lack of measurement resolution, i.e. the specific size of the DPF samples. Depending on the radial location, ash layer thickness values of 0.12 mm to 0.18 mm were measured for the ash accumulated along the DPF channel walls.

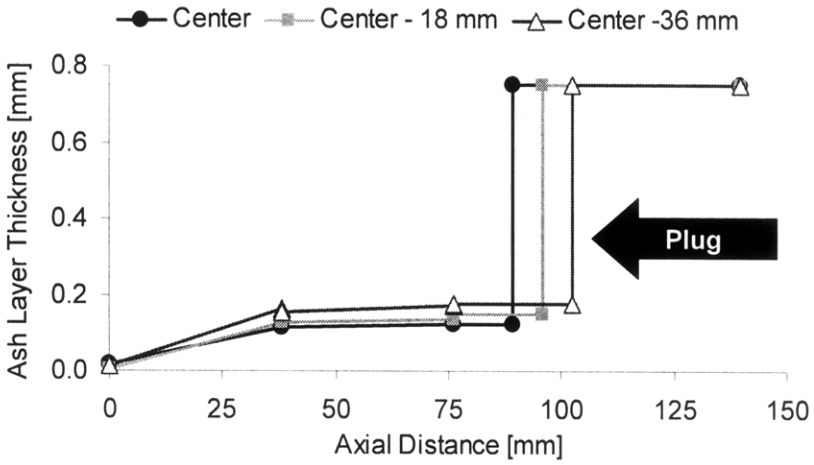

Figure 8.7. Ash layer thickness profiles for a DPF containing 42 g/l ash generated in the laboratory using CJ-4 oil and periodic regeneration.

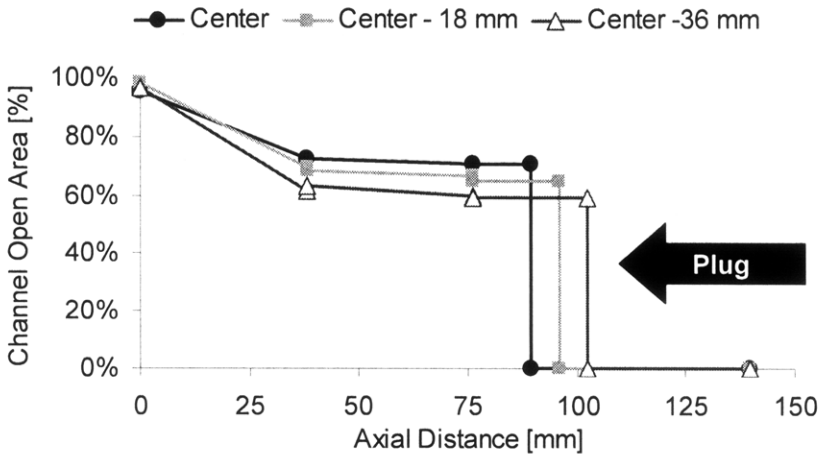

Figure 8.8. Channel open area profiles for a DPF containing 42 g/l ash generated in the laboratory using CJ-4 oil and periodic regeneration.

The channel open areas were also computed from measured ash distribution profiles and are shown in Figure 8.8. Ash levels of 42 g/l lead to a reduction in the channel open areas by 41% to 30%. The ash plug in the DPF further reduces the effective channel length and available filtration area.

8.3.2 Ash Layer Thickness: Low Ash Loads

The same ash distribution measurements were made for the filter loaded to 12.5 g/l of ash with the CJ-4 oil undergoing periodic regeneration. Figure 8.9 presents the measured ash distribution profiles along the length of the filter for three different radial positions. The average ash layer thickness ranged from 0.06 mm to 0.08 mm along the channel walls. Almost no ash was found accumulated at the back of the channels in these filters.

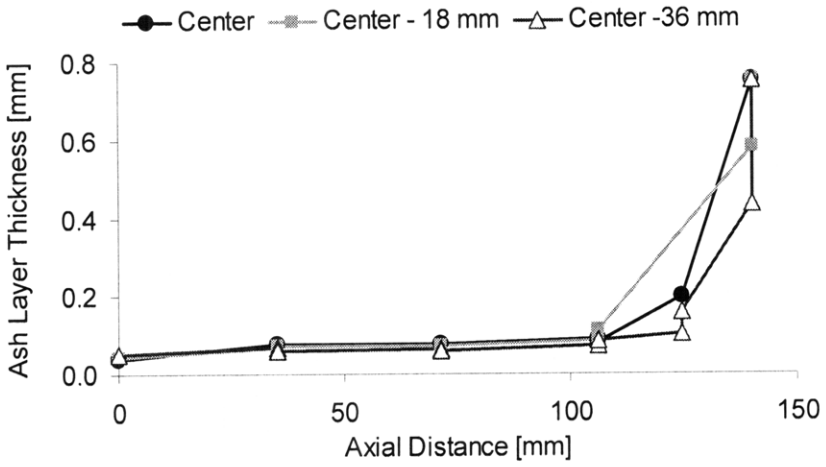

Figure 8.9. Ash layer thickness profiles for a DPF containing 12.5 g/l ash generated in the laboratory using CJ-4 oil and periodic regeneration.

The measured ash distribution profiles shown in Figure 8.9 and the absence of any significant amount of ash accumulated in plugs at back of the DPF indicate that ash primarily accumulates along the DPF walls during the initial stages of ash loading. Furthermore, the pressure drop trends presented in Figure 8.1 clearly show ash depth filtration, corresponding to approximately 2 g/l ash trapped in the DPF pores. Ash plugs do not appear to form during the early stages of ash loading in the filters analyzed in this work. The plugs, clearly visible in the filter loaded to 42 g/l ash, appear to form only

after a sufficient amount of ash has been deposited in the filter walls and accumulated in the filter cake layer. The height of the ash deposits in the layer along the filter walls may affect the critical shear stress above which ash particles are removed from the walls, re-entrained in the flow, and deposited near the back of the channels.

The channel open areas for the filter loaded to 12.5 g/l ash are shown in Figure 8.10. At this ash loading level, the channel frontal areas are reduced by 15% to 20% due to build-up of the ash cake layer along the channel walls. Little radial variation is observed in the ash deposition profiles along the length of this filter.

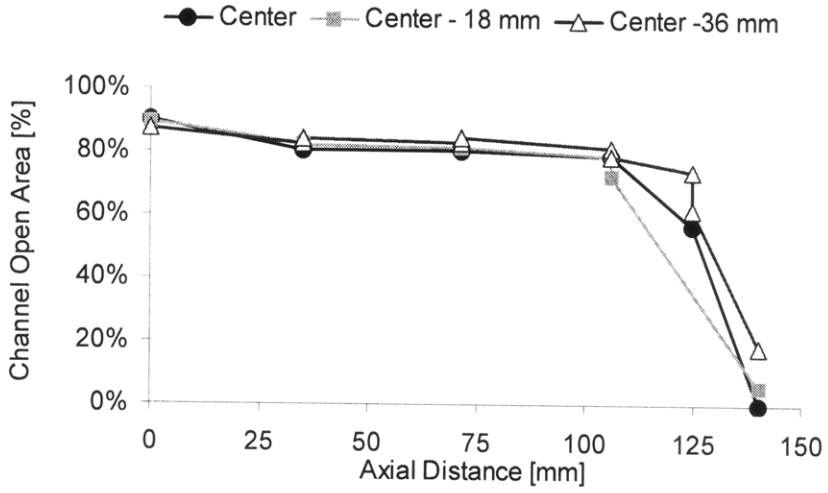

Figure 8.10. Channel open area profiles for DPF containing 12.5 g/l ash generated in the laboratory using CJ-4 oil and periodic regeneration.

8.3.3 Ash Layer and End-Plug Formation

Figure 8.11 further illustrates the evolution of the ash deposits in the DPF and compares the measured ash deposition profiles along the centerline of the filters for the DPFs loaded with 12.5 g/l ash and 42 g/l ash with the CJ-4 oils. This direct comparison of the ash thickness profiles provides further evidence that ash plug formation occurs primarily during the later stages of ash accumulation, after a substantial ash cake layer has already formed. Furthermore, little difference in the ash layer profiles is observed near the face of the DPF, along the first 30 mm of the filter channel. Based on the ash layer thickness

profiles for a DPF containing 42 g/l ash, 60% of the ash layer thickness along the channel walls is established during the first 30% of ash loading on a mass basis. Following this initial loading phase, proportionally more ash is accumulated in the ash plug, than is deposited on the channel walls. The ash distribution in the DPF is a dynamic process which varies with time and the amount of ash accumulated in the filter. The channel open area profiles corresponding to the ash layer thickness measurements are shown in Figure 8.12.

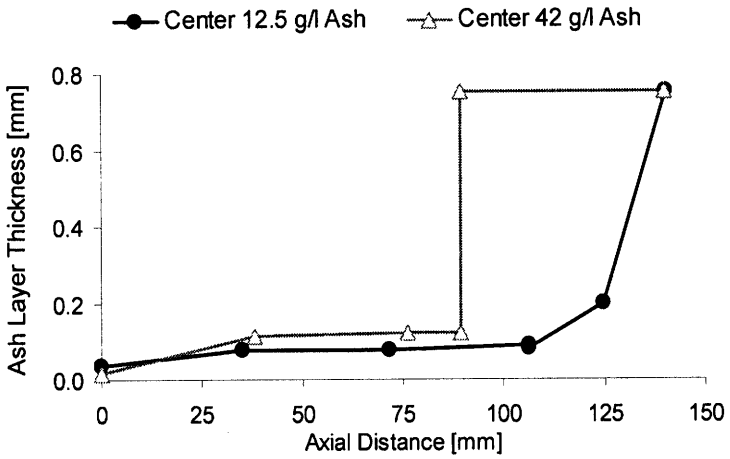

Figure 8.11. Comparison of ash layer thickness profiles along the filter centerline for DPFs containing 12.5 g/l ash and 42 g/l ash generated in the laboratory using CJ-4 oil and periodic regeneration.

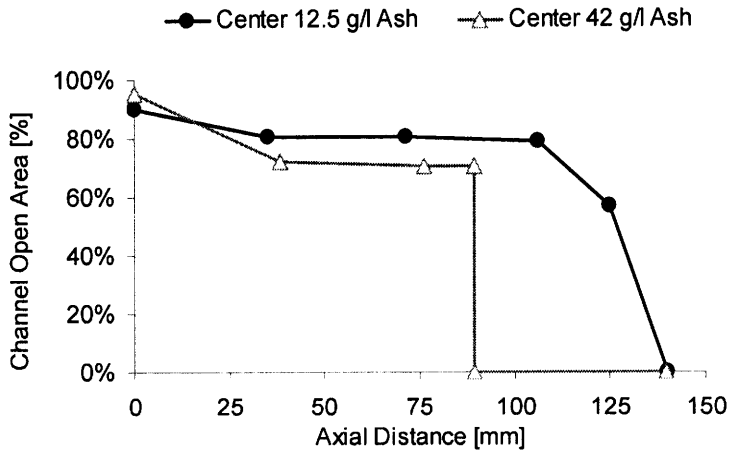

Figure 8.12. Comparison of channel open area profiles along the filter centerline for DPFs containing 12.5 g/l ash and 42 g/l ash generated in the laboratory using CJ-4 oil and periodic regeneration.

Figures 8.13 and 8.14 present the ash distribution measured within a single DPF channel for three different radial locations in the DPFs loaded to 12.5 g/l ash and 42 g/l ash, respectively. The differences in ash plug formation and wall cake layers are clearly visible for the low- and high-ash loaded filters.

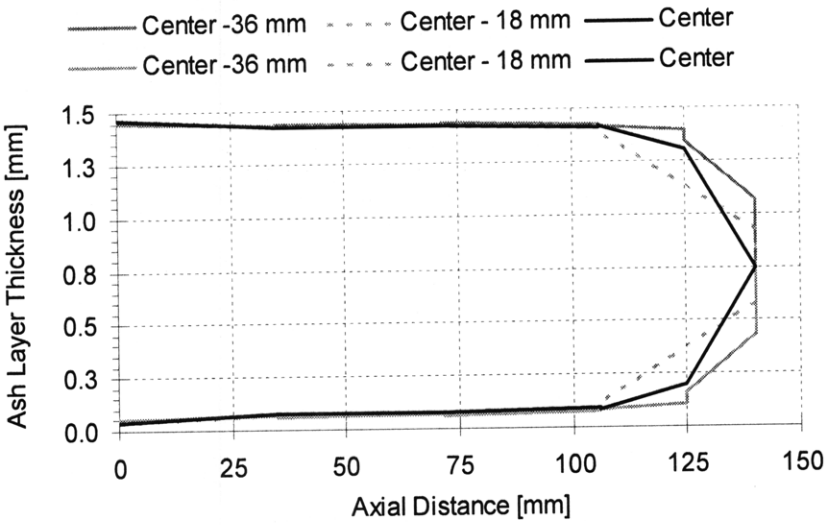

Figure 8.13. Ash distribution in a single channel for a DPF containing 12.5 g/l ash generated in the laboratory using CJ-4 oil and periodic regeneration.

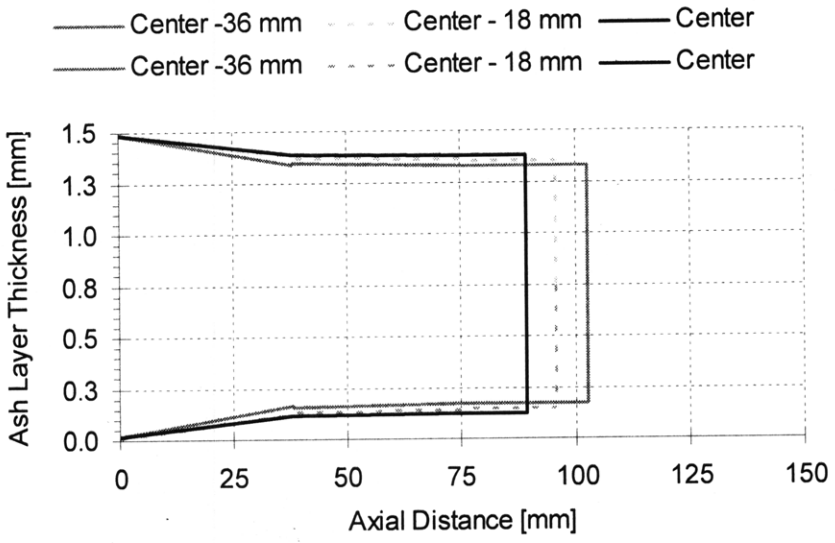

Figure 8.14. Ash distribution in a single channel for a DPF containing 42g/l ash generated in the laboratory using CJ-4 oil and periodic regeneration.

The scale of the horizontal axis in Figures 8.13 and 8.14 correspond to the DPF channel length. Once again, the DPF containing the high ash load of 42 g/l exhibits a significantly reduced channel length and decrease in cross-sectional area. A series of images presented in Figure 8.15 provides a side-by-side comparison of samples from the same regions in the low- and high-ash loaded filters.

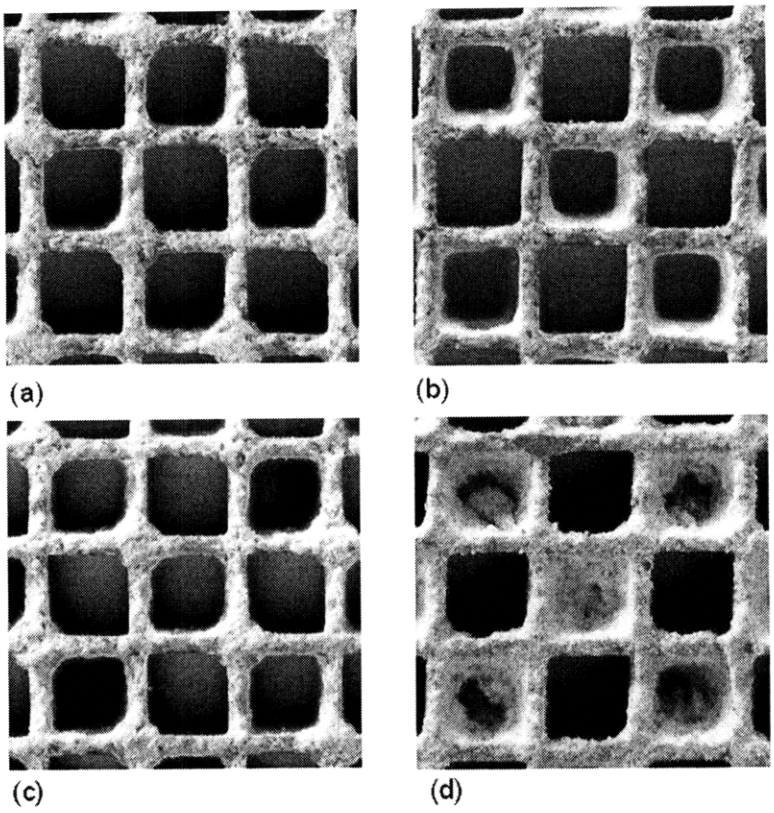

Figure 8.15. Comparison of channel ash accumulation 57 mm from the DPF face for (a) DPF containing 12.5 g/l ash, (b) DPF containing 42 g/l ash, and 133 mm from the DPF face for (c) DPF containing 12.5 g/l ash, (d) DPF containing 42 g/l ash.

For ash accumulated near the back of the filter, the DPF containing 42 g/l ash shows significant channel plugging, whereas no plugging is observed in the filter containing 12.5 g/l ash. Furthermore, the ash layer deposited along the channel walls is clearly thicker in the filter containing the higher ash load. It is also interesting to note the apparent indentations in the center of the ash plugs shown in Figure 8.15(d). Based on the images, the ash deposited in the center of the plug appears much more loosely packed than the ash in the plug close to the channel walls.

Based on the results of the post-mortem analysis for the filters containing 12.5 g/l and 42 g/l of ash, the evolution of the ash distribution is shown in Figure 8.16. The figure shows an increasing proportion of ash deposited toward the back of the filter in the end-plug as the total ash level is increased.

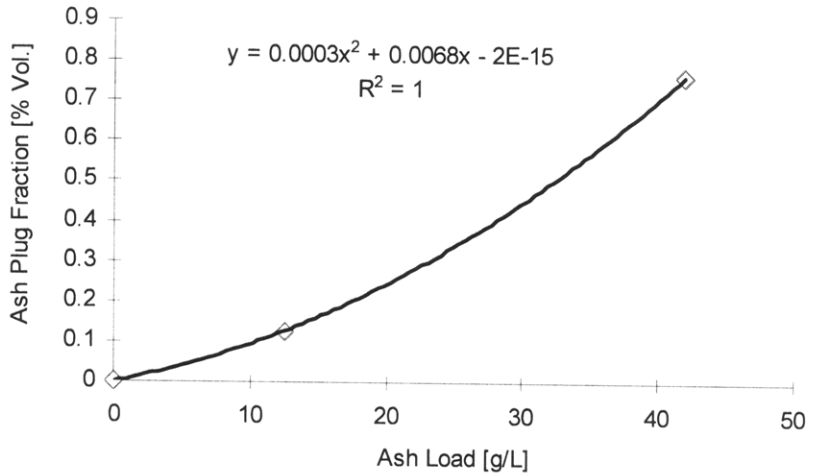

Figure 8.16. Evolution of ash accumulation in DPF end-plug.

Ash packing density measurements for the ash accumulated in the channel end-plugs for the DPF containing 42 g/l ash are shown in Figure 8.17. Lightly tapping the DPF samples containing the ash plugs caused the ash deposited in the center of the plug to fall out. Each DPF sample was tapped until no more ash could be removed. Measurements of the ash remaining in the layer along the channel walls allowed for determination of ash packing density in the center and edges of the plug.

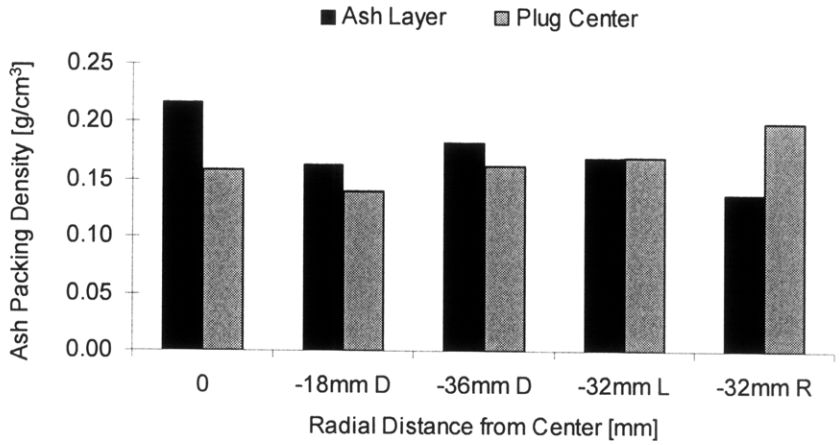

Figure 8.17. Comparison of radial packing density variation within ash end-plugs for a DPF containing 42 g/l ash from a CJ-4 oil undergoing periodic regeneration.

The ash plug packing density measurements show a distinct density gradient within the ash plug. Ash accumulated in the plug near the channel walls appears more densely packed than the ash found in the center of the plug. The density gradient appears most pronounced for the ash plugs formed near the DPF centerline, and less so for the ash plugs accumulated near the DPF periphery. The far radial locations (-32mm L and -32 mm R) do not show the same trends in density gradient, however.

The apparent density gradient measured in the ash plugs is consistent with the previous observations and ash profile measurements, showing the ash initially accumulating as a layer along the filter walls. Exhaust flow through these porous layers affects the characteristics and packing densities of these layers. As the average ash layer thickness along the DPF channels increases, and the shear stress imposed by the exhaust flow exceeds the critical shear stress of the ash deposits residing near the surface of the ash layer, ash particles are re-entrained in the flow. These particles are transported to the back of the DPF where they accumulate on top of the already formed ash layers in the center of the ash plug. The material accumulated near the center of the ash plug experiences little to no exhaust flow, thereby resulting in a less densely packed deposit, as observed by the density gradients in Figure 8.17.

8.3.4 Ash Packing Density and Porosity

The ash distribution measurements, described above, provide information related to the DPF volume occupied by the ash deposits. The same measurements were combined with weight data from the individual ash samples before and after ash removal, to compute the packing density of the ash accumulated in the DPF channels. Figure 8.18 presents the packing density profile along the length of the filter for the DPF loaded to 42 g/l ash with CJ-4 oil and periodic regeneration.

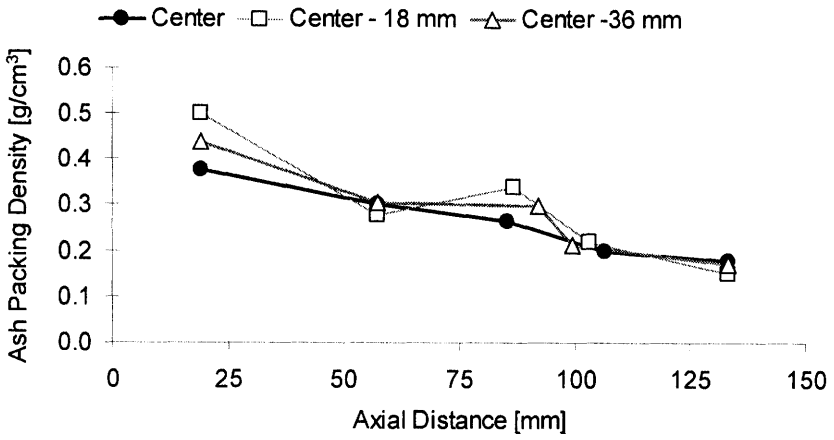

Figure 8.18. Ash packing density profiles for a DPF containing 42 g/l ash generated in the laboratory using CJ-4 oil and undergoing periodic regeneration.

Due to the size of the DPF samples, there was some difficulty in determining the exact beginning of the ash plug, as well as the ash layer profile in the channels close to the ash plug. Therefore, the packing density measurements corresponding to the sample at 133 mm from the front of the filter are believed to be more representative of the true packing density in this region of the filter, as opposed to the measurements at 80 mm to 90 mm from the front face of the DPF. Similarly, ash layer thickness measurements at the face of the filter were complicated by the very small amount of ash present at the filter face. For this reason, the ash packing density measurements for the ash layer 57 mm from the face of the DPF are expected to be more accurate than the measurements taken at 20 mm from the DPF inlet face.

Similar ash packing density profiles are shown for the DPF containing 12.5 g/l ash in Figure 8.19. The ash packing density profiles for the DPF containing 12.5 g/l ash appeared fairly constant along the length of the filter. In contrast, a large difference in ash packing densities between the front and back of the DPF loaded to 42 g/l ash was observed, as shown in Figure 8.18.

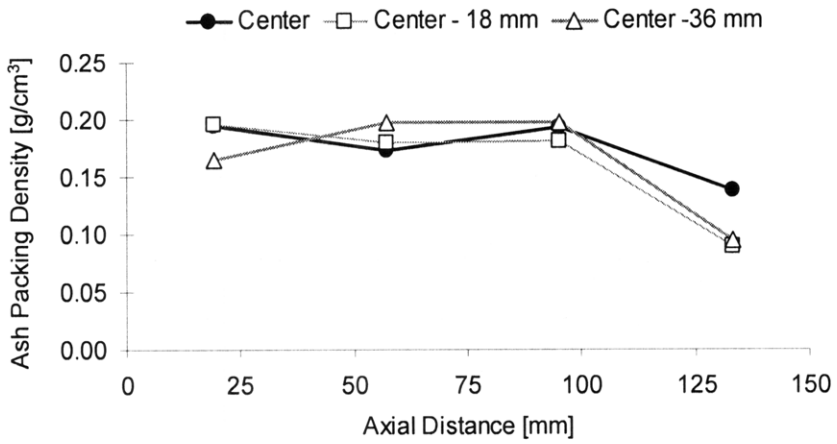

Figure 8.19. Ash packing density profiles for a DPF containing 12.5 g/l ash generated in the laboratory using CJ-4 oil and undergoing periodic regeneration.

In both the high- and low-ash loaded filters, ash packing density decreases near the back of the filter, which corresponds to the region of ash plug formation and lowest filtration velocities. The apparent high ash layer packing densities for the ash near the front face of the DPF containing 42 g/l ash is attributed to difficulties in determining the ash layer thickness profiles in this region of the filter. The resolution of the measurement is a direct function of sample size (in this case sample length). For filter samples in which the ash layer thickness changes significantly over the sample length (such as at the filter inlet), additional error may be introduced in the measurement.

In order to minimize error in the measurements, only the samples for which the ash distribution profiles were known to a relatively high degree of certainty were selected for direct comparison of the packing density measurements for the high- and low-ash loaded filters. These filter samples correspond to positions within the DPF of 57 mm and 133 mm from the inlet face of the filter. Figure 8.20 presents the results of the packing density comparison.

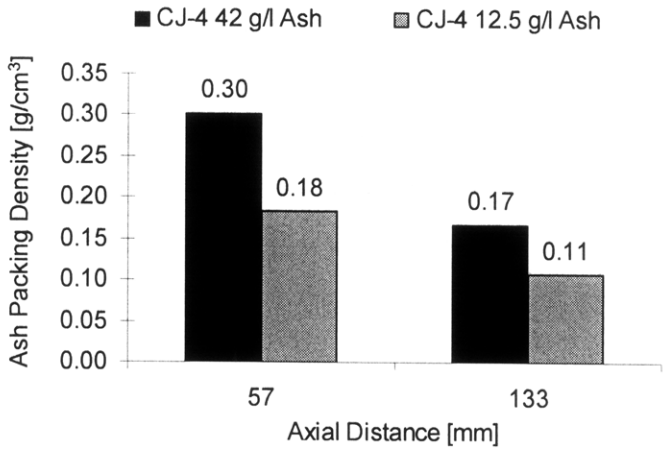

Figure 8.20. Comparison of ash packing density for DPFs containing 12.5 g/l ash and 42 g/l ash generated in the laboratory using CJ-4 oil and periodic regeneration.

For both filters, ash accumulated along the channel walls near the front and center regions of the filter was more densely packed than the ash found at the back of the filter. In the DPF containing 42 g/l ash, the sample position at 133 mm from the filter's inlet face was completely plugged with ash. On the other hand, for the DPF containing only 12.5 g/l ash, there was little ash plug formation observed. These differences in measured ash packing density may be attributed to reduced filtration velocities near the back of the DPF.

Additionally, the difference in ash layer packing density for the two samples at the 57mm location may indicate some dependence of ash packing density on the amount of ash present (layer thickness) as well. The direct relationship between increasing ash accumulation in the DPF and increasing filtration velocity makes the latter process the most likely physical mechanism responsible for the increase in layer packing density in the 42 g/l ash loaded filter. It is important to note, however, that the DPF containing 42 g/l ash has also experienced a proportionally larger number of regeneration events. The specific thermal histories may also affect ash packing density and particle sintering.

8.3.5 Ash Composition

The composition of the ash generated from the CJ-4 oil and accumulated in the DPF following periodic regeneration was analyzed using x-ray diffraction. The spectrum is shown in Figure 8.21. While a number of minor constituents were identified in the ash sample, the two predominant ash compounds were calcium sulfate and zinc magnesium phosphate. The main peaks corresponding to these compounds are also identified in the spectra.

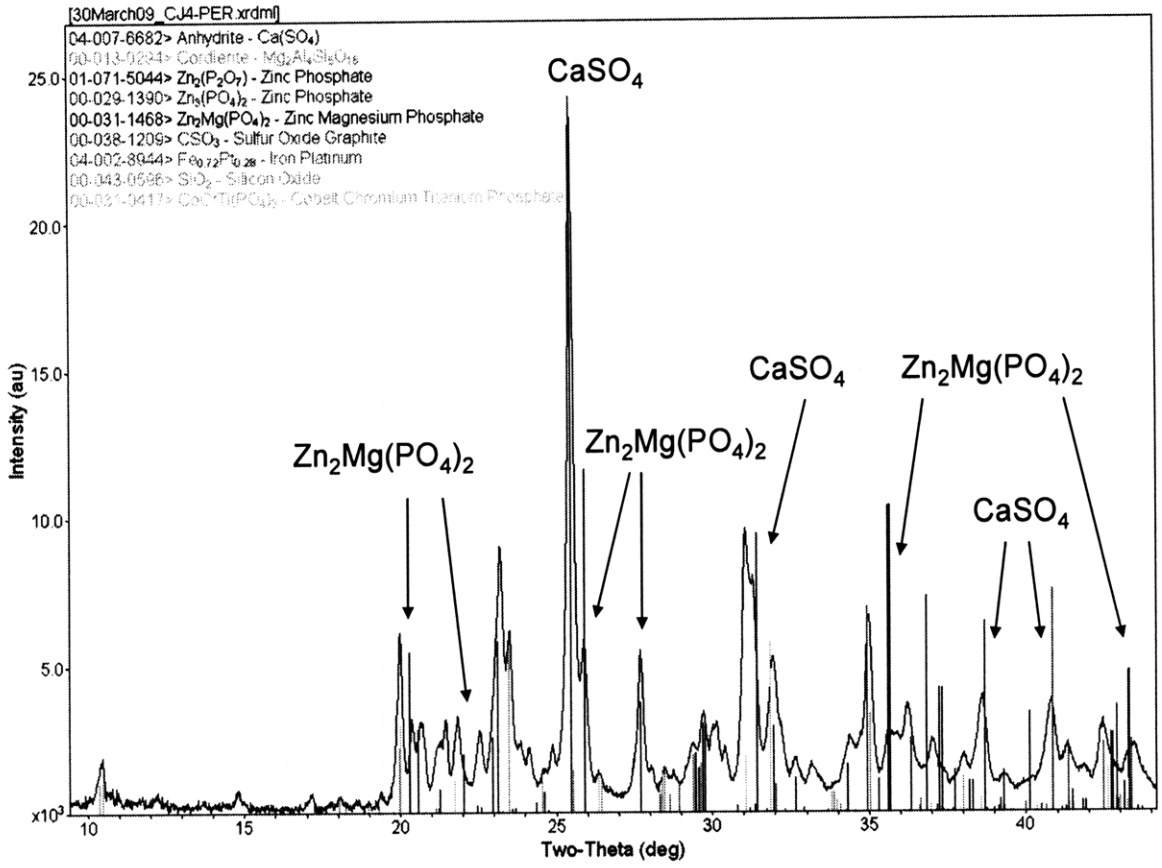

Figure 8.21. Ash compositional analysis via XRD for ash generated from CJ-4 oil in a DPF undergoing periodic regeneration.

The theoretical density of calcium sulfate, $CaSO_4$, is 2.96 g/cm^3, whereas the theoretical density of zinc magnesium phosphate, $Zn_2Mg(PO_4)_2$ is 3.60 g/cm^3. Assuming a theoretical ash composition consisting of calcium sulfate and zinc magnesium phosphate in a ratio of 1 : 2, respectively, gives a theoretical ash density of approximately 3.4 g/cm^3.

The theoretical ash density values are useful to compute ash porosity using the measured packing densities from the post-mortem analysis listed in Section 8.3.4.

8.3.6 Ash Accumulation and Transport Processes

To better understand the ash morphology, accumulation, and ash layer properties measured and described in the previous sections, ash deposits were also imaged using a scanning electron microscope. The images presented in Figure 8.22 show ash accumulated on the DPF surface. The DPF pores and surface structure are clearly visible in the figure. While the ash deposits clearly block many of the surface pores, very little ash is observed to be deposited within the DPF pores. Figure 8.23 presents a series of electron micrographs showing details of the individual ash structures, and Figure 8.24 presents additional images showing the ash layer accumulated on the DPF surface.

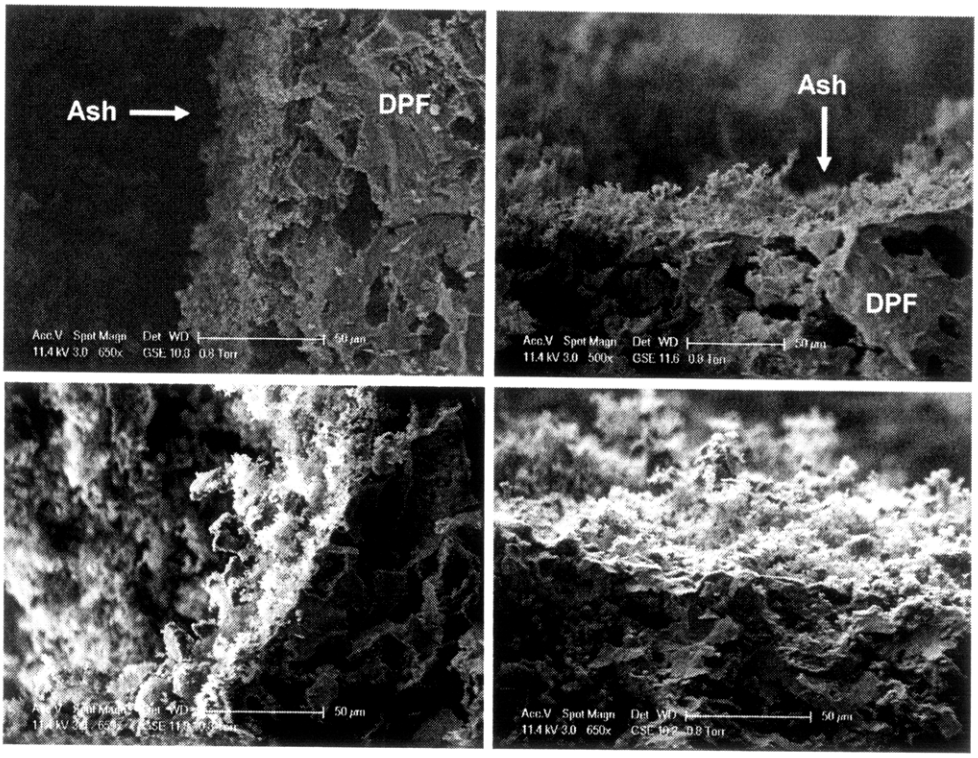

Figure 8.22. SEM images showing the ash layer formed along DPF walls. Ash does not penetrate deep into the DPF pores.

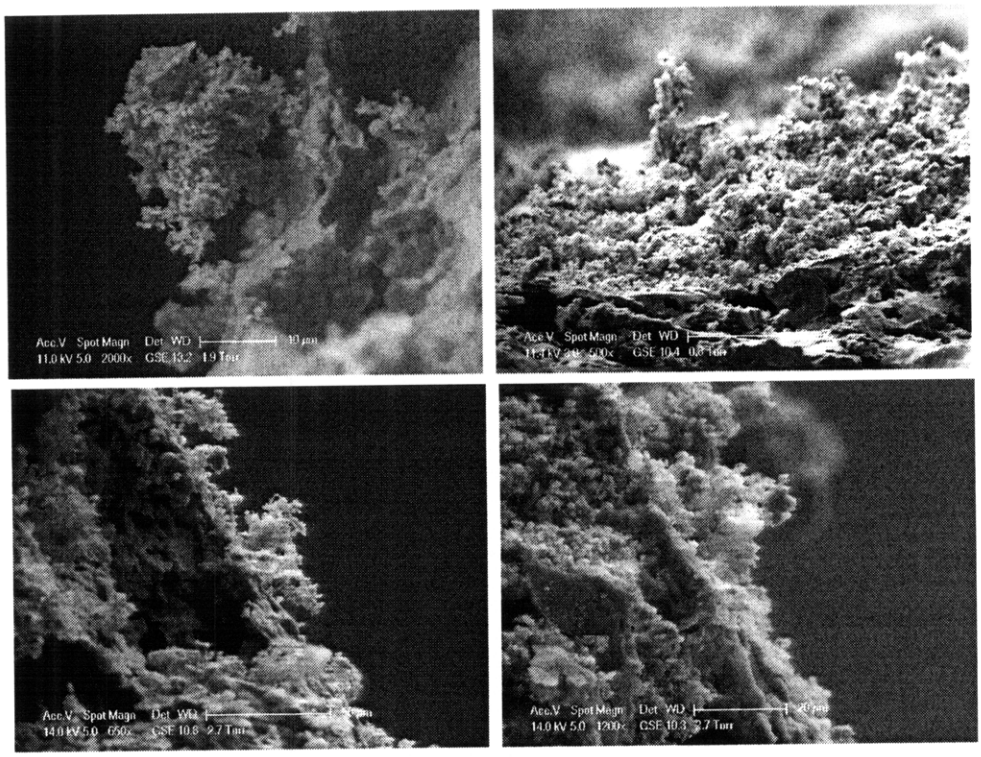

Figure 8.23. SEM images showing ash structure formation on the DPF walls.

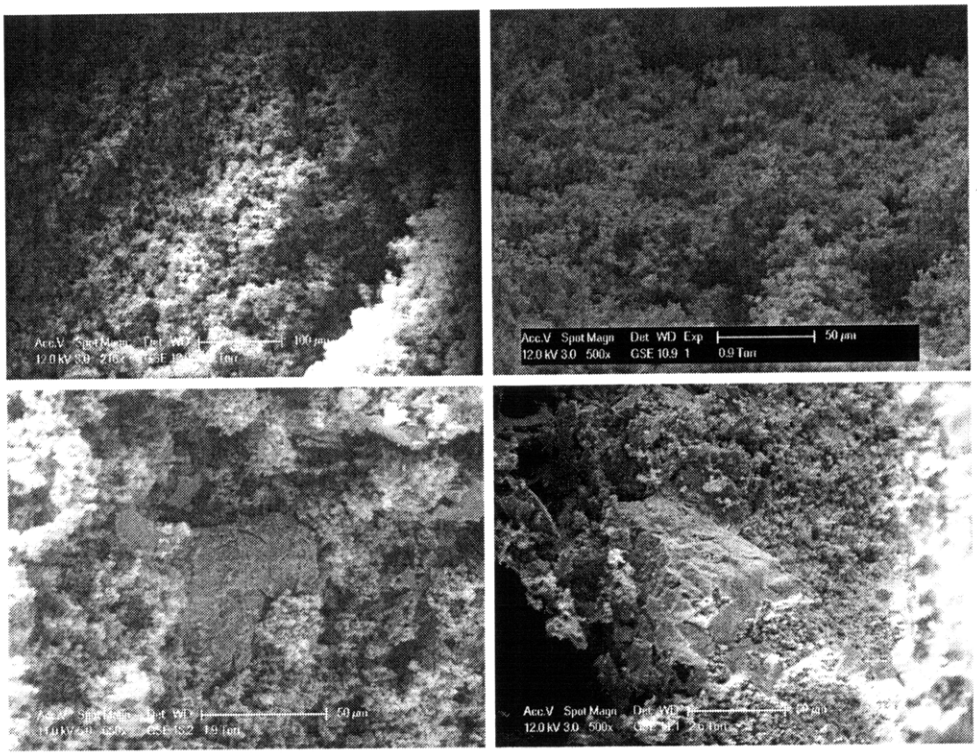

Figure 8.24. SEM images showing ash deposits on DPF surface. Top two images show thick ash layer. Bottom images show initial stages of ash accumulation.

The micrographs in Figure 8.23 show ash particle structures on the order of 10 μm deposited on the filter surface. It is expected that pieces of these structures eventually break off due to the shear stress imposed by the exhaust flow, and are then transported to the back of the DPF. Figure 8.24 presents additional images showing the ash layer, at various stages of ash loading, covering the filter surface. The highly-porous and irregular shape of the ash structures is clearly visible in the top two images.

8.4 Measured and Computed Ash Properties

A summary of the measured ash properties from the post-mortem analysis is presented in Table 8.1 below. Based on the measured ash packing density values and ash composition determined via XRD, the ash porosity for the DPF containing 12.5 g/l ash was 94.6% and the ash layer in the DFP containing 42 g/l ash was 91.1% porous. These measured ash properties provide additional evidence of some ash settling or compaction during filter loading following repeated thermal cycling.

Lubricant	Regeneration	Ash	Ash Layer Thickness	Wall Density	Plug Density	Theoretical Density	Ash Porosity
		[g/l]	[cm]	[g/cm^3]	[g/cm^3]	[g/cm^3]	[%]
CJ-4	Periodic	42.0	0.013	0.30	0.17	3.4	91.1
CJ-4	Periodic	12.5	0.007	0.18	0.00	3.4	94.6

Table 8.1. Summary of measured ash properties for ash generated using CJ-4 oil and periodic regeneration.

Table 8.2 provides additional parameters related to the changes in DPF geometry computed from the ash distribution measurements and properties listed in Table 8.1 above. At an ash load of 42 g/l, the DPF channel area is reduced almost 48% and the length is reduced by slightly more than 40%. Furthermore, over 75% of the ash was found to be accumulated in the channel end-plugs, by volume. On the other hand, the DPF containing only 12.5 g/l ash, showed almost no ash accumulated in the channel end-plugs with a much smaller reduction in channel area and length due to ash accumulation.

Lubricant	Regeneration	Ash	Channel Filtration Area	Change in Filtration Area	Change in Frontal Area	Change in Length	Ash End Plug Volume Fraction
		[g/l]	[cm^2]	[%]	[%]	[%]	[%]
CJ-4	Periodic	42.0	4.7	-47.9%	-27.0%	-40.5%	76.3%
CJ-4	Periodic	12.5	7.0	-22.4%	-20.2%	-6.8%	12.7%

Table 8.2. Summary of calculated ash effects on filter geometry for ash generated using CJ-4 oil and periodic regeneration.

8.5 Ash Distribution Effects on Pressure Drop

The ash properties and effects on DPF geometry are useful to better interpret the experimental DPF pressure drop data. The pressure drop trends for both the DPFs loaded to 12.5 g/l ash and 42 g/l ash, using CJ-4 oil, as a function of space velocity are shown in Figure 8.25. The pressure drop characteristics of the clean filters are also provided for comparison.

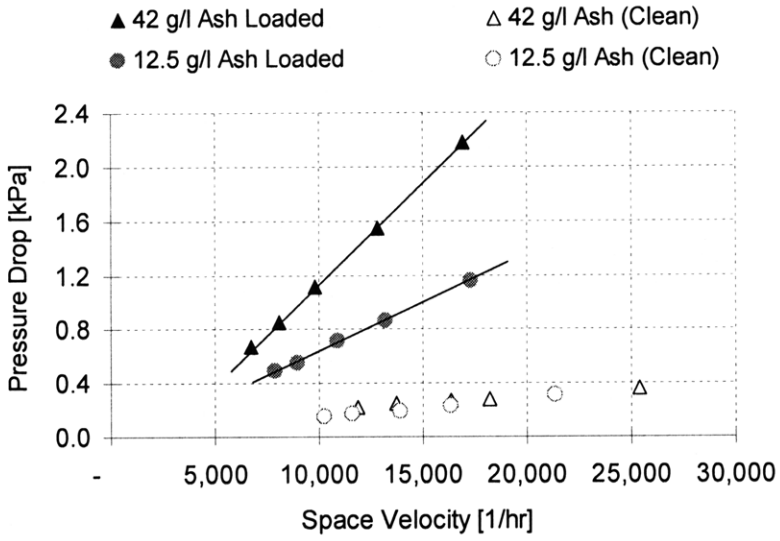

Figure 8.25. DPF pressure drop profiles as a function of space velocity for the clean and ash loaded filters using CJ-4 oil.

The large effect of the initial filter loading phase (depth filtration) on pressure drop is clearly shown in the Figure 8.25, as is the increase in filter pressure drop with increasing ash levels. The pressure drop data presented above was collected on the flow bench using air at ambient conditions.

The ash distribution measurements obtained from the post-mortem filter analysis were used to compute the average filter wall velocity, which is dependent on the exhaust gas flow rate and available filtration area. Figure 8.26 shows the filter pressure drop contribution due to flow through the ash layer and DPF substrate (porous media) as a function of wall velocity for the DPFs loaded with 42 g/l and 12.5 g/l of ash.

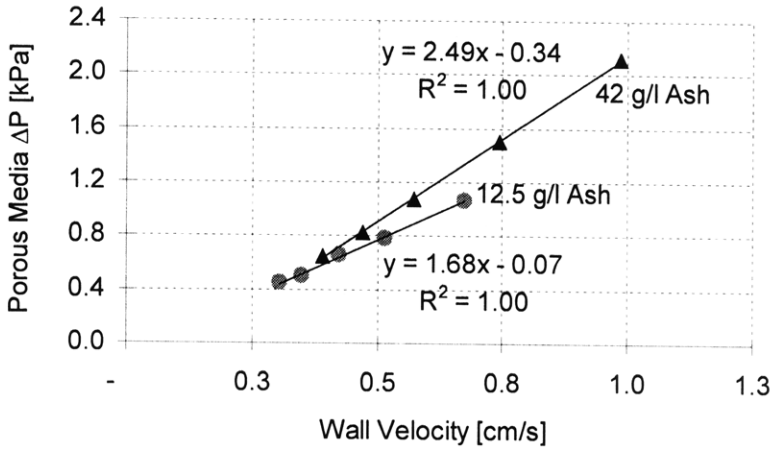

Figure 8.26. DPF pressure drop due to flow through ash layer and substrate as a function of wall velocity, computed from the measured ash deposition profiles, for the clean and ash loaded cases.

The pressure drop due the flow through the ash and substrate was determined by subtracting the pressure drop due to DPF inlet and outlet contraction/expansion, as well as channel flow, from the total measured DPF pressure drop. The pressure drop contributions from the DPF inlet, outlet, and channel losses were estimated from Equations 3.2 and 3.5. Plotting the porous media pressure drop as a function of wall velocity, therefore, accounts for the changes in DPF channel geometry due to ash accumulation.

Following the general form of Darcy's law describing flow through porous media (Equation 3.23), the slope of the pressure drop curve in Figure 8.26 is directly proportional to the quantity (w/k). This term is related to the flow resistance of the porous media (layer thickness divided by permeability), as all of the test were carried out on the same filter substrate at the same temperature and gas viscosity using the flow bench with air at ambient conditions.

The average ash wall layer thickness measured as part of the post mortem analysis for the DPF containing 12.5 g/l ash was 0.07 mm, whereas the average ash wall layer thickness for the DPF containing 42 g/l ash was 0.13 mm. The ash layer in the DPF containing 42 g/l ash was, therefore, approximately 1.8 times thicker than the ash layer in the DPF containing 12.5 g/l ash. The slopes of the pressure drop curves, representative of the flow resistance through the ash layer and DPF substrate are also shown in Figure 8.26. The slope of the pressure drop curve for the DPF containing 42 g/l ash is approximately 1.5 times greater than the of pressure drop slope for the DPF containing 12.5 g/l ash. The fact that the ratio of ash layer thicknesses and pressure drop slopes for the two cases are nearly the same indicates the difference in ash layer thickness is primarily responsible for the increase in pressure drop observed in the DPF containing 42 g/l ash relative to the filter containing only 12.5 g/l ash.

The slight difference in the ash layer thickness and flow resistance ratios may be attributed to the fact that average ash layer thickness and flow velocity values were used in the calculations. Additionally, slight differences in the ash layer permeabilities may also account for the differences in the layer thickness and flow resistance ratios noted above. This may be due to changes in the ash layer porosity and/or mean pore size as ash accumulates in the cake layer. Further, differences in filter wall velocities and thermal histories for the DPFs loaded to 12.5 g/l and 42 g/l ash over the ash loading cycle may also affect the resulting ash layer permeability.

8.6 Comparison of Ash and Soot Effects on Pressure Drop

The experimental data presented in the previous sections focused primarily on the manner in which ash affects filter pressure drop. It is instructive to directly compare the effect of ash and soot on DPF pressure drop for the same material mass loading in the filter. Figure 8.27 shows the individual effects of soot and ash on DPF pressure drop.

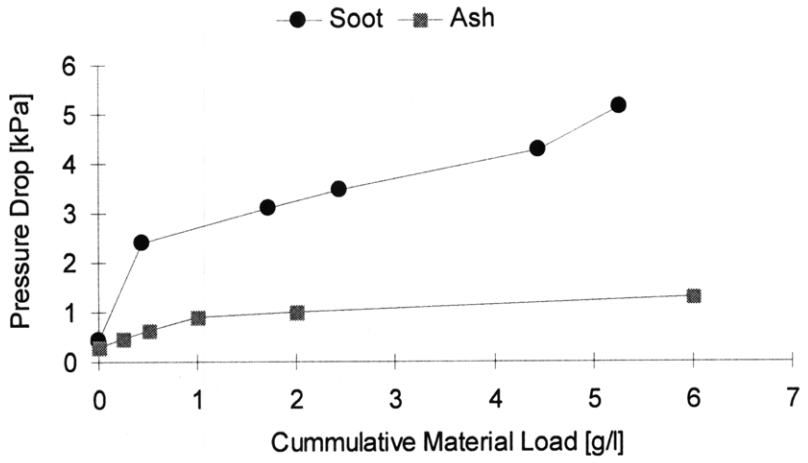

Figure 8.27. Comparison of individual soot and ash effects on DPF pressure drop as a function of material loading.

The data presented in Figure 8.27 was collected at various stages of filter ash or soot loading, determined by weighing the filter at specific intervals during the loading process. Filter pressure drop was measured using a flow bench with ambient air at a space velocity of 20,000 hr^{-1}. The pressure drop curves show a much larger increase in pressure drop for the soot loaded filters relative to the ash loaded filters, with the same level of material loading.

During the initial stages of filter loading (depth filtration) approximately 0.5 g/l soot is trapped in the DPF pores compared with around 1 g/l for the ash, based on the pressure drop curves. Despite more ash being trapped in the pores, the rapid increase in pressure drop due to depth filtration of the soot, was much greater than in the ash loaded filter. This difference is primarily attributed to the low packing density of the soot, which occupies a significantly larger volume of the DPF pores, as compared with the ash, for

the same mass loading. The increase in pressure drop associated with the cake layer build-up is also larger in the soot-loaded filter. On average, soot accumulation in the DPF leads to an increase in filter pressure drop two to four times greater than ash, for the same filter mass loading. Accurate understanding of key soot and ash properties is critical to explaining these differences.

8.7 Combined Ash and Soot Effects on Pressure Drop

In real on-engine applications, both soot and ash accumulate in the particulate filter. DPFs containing known levels of ash were also loaded with soot using the Cummins ISB, allowing for the evaluation of the combined effects of soot and ash on DPF performance.

8.7.1 DPF Pressure Drop Regimes

Figure 8.28 presents a summary of ash and soot effects on pressure drop as a function of soot accumulation for various levels of ash loading. The pressure drop profile for a DPF with no ash accumulation is provided for comparison. In all cases, DPFs containing ash show higher levels of pressure drop with no soot accumulation relative to the clean case. This initial increase in filter pressure drop with no soot, is due to the ash deposits alone. Further, the presence of the ash layer along the channel walls provides a physical barrier preventing depth filtration of the soot.

Soot depth filtration is clearly visible in the filter with no ash, characterized by the steep pressure rise during the initial soot loading period. On the other hand, the ash pre-loaded filters do not exhibit the characteristic rapid increase in pressure drop associated with soot depth filtration, during the initial soot loading phase. For all of the ash pre-loaded filters (12.5 g/l to 42 g/l) the soot begins to accumulate on the ash cake layer immediately, building a second soot cake layer, and does not accumulate in the filter pores.

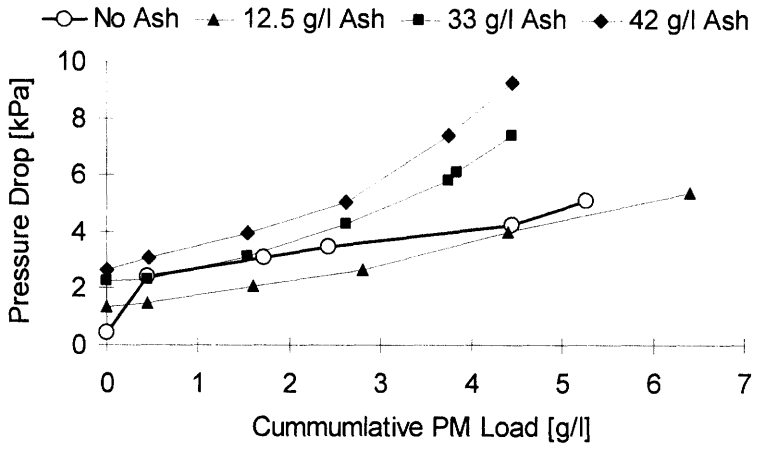

Figure 8.28. Pressure drop as a function of soot accumulation on a Pt-catalyzed DPF at various stages of ash loading measured at 20,000 hr^{-1} space velocity with CJ-4 oil and periodic regeneration.

For a given soot load, DPFs with low ash loads (below 12.5 g/l) exhibit a reduction in pressure drop relative to the filter with no ash, as shown in Figure 8.28. These low ash loads may actually provide a benefit to filter performance. Similar results have been reported in computational studies [59]. Additionally, ash and soot accumulation in the DPF show two effects on filter pressure drop: (1) low pressure drop sensitivity to soot loads below 3 g/l soot, and (2) increased pressure drop sensitivity to soot loads above 3 g/l. Interestingly, even for a DPF with soot loads in the range of 0.5 g/l to 1.5 g/l there is almost no difference in pressure drop between the filter with 33 g/l ash and no ash. The following analysis attempts to explore these differences in pressure drop sensitivity in more detail.

Figures 8.29 and 8.30 show pressure drop trends as a function of DPF soot load for DPFs with and without ash. In both cases, two distinct pressure drop regimes are observed and labeled (I) and (II). The presence of two similar pressure drop regimes has also been observed from data published in the literature and plotted in a similar fashion [23]. These results are included in Figure A-6 of the Appendix.

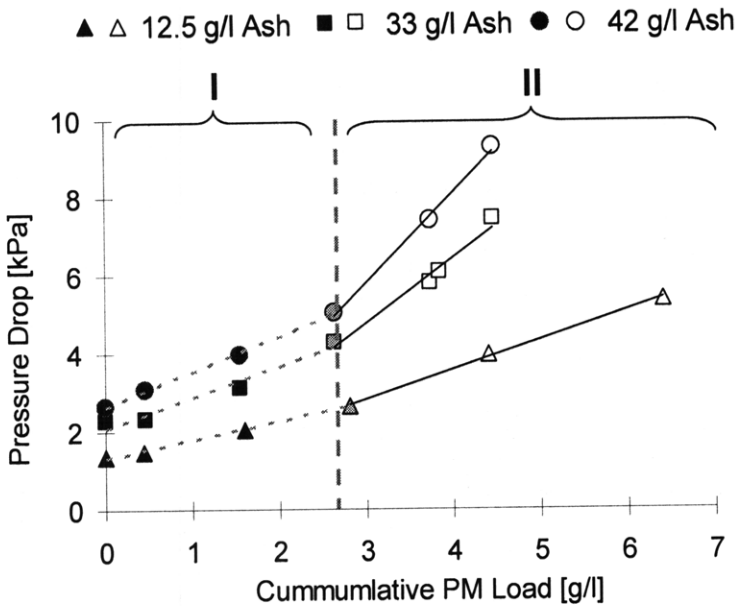

Figure 8.29. Definition of pressure drop regimes (I) and (II) observed with soot accumulation on ash loaded DPFs at 20,000 hr^{-1} space velocity.

In the case of the ash loaded filters, shown in Figure 8.29, a distinct change in slope is observed near a cumulative soot load of 3 g/l for all levels of ash loading ranging from 12.5 to 42 g/l ash. The change in slope is used to delineate the two pressure drop regimes. On the other hand, the filter with no ash exhibits the typical depth and cake filtration regimes shown in Figure 8.30.

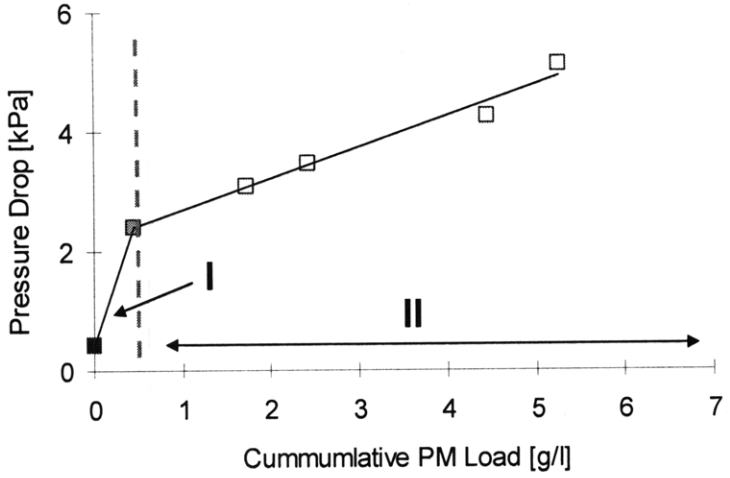

Figure 8.30. Typical depth (I) and cake (II) filtration regimes for soot accumulation in a DPF with no ash at 20,000 hr^{-1} space velocity.

The reader will note that the two pressure drop regimes for the filters with and without ash overlap. It is thus possible to define three pressure drop regimes when comparing the pressure drop response of the ash loaded DPFs to that of the filters with no ash, as a function of soot load. The three pressure drop regimes are defined as follows:

- Response to soot loading up to 0.4 g/l
- Response to soot loading from 0.4 to 2.6 g/l
- Response to soot loading in excess of 2.6 g/l

Figure A-7 of the Appendix clearly depicts the pressure drop regimes described above. Further, the DPF pressure drop response as a function of soot load can be described by a simple linear fit for each pressure drop regime defined in Figures 8.29 and 8.30. The linear regression is also shown in Figure A-7.

8.7.2 Pressure Drop Sensitivity

The slopes of the pressure drop curves define the sensitivity of the pressure drop measurement to additional soot accumulation in the DPF. In this manner, the relative pressure drop sensitivity (RPS) is defined as:

$$\text{RPS} = \left(\frac{\partial \Delta P}{\partial PM}\right)_{Ash,i} \div \left(\frac{\partial \Delta P}{\partial PM}\right)_{Clean,i} \tag{8.1}$$

which is simply the slope of the pressure drop curve for the ash loaded DPF divided by the slope of the pressure drop curve for the DPF with no ash (clean) as a function of soot load. Here ΔP is the pressure drop, PM is the soot load, and i defines the pressure drop regime. An RPS value of unity indicates no change from the performance of the filter with no ash, whereas values greater than one indicate an increase in pressure drop sensitivity and values less than one indicate a decrease. The relative pressure drop sensitivity is plotted as a function of ash load for each of the three soot loading regimes and is shown in Figure 8.31.

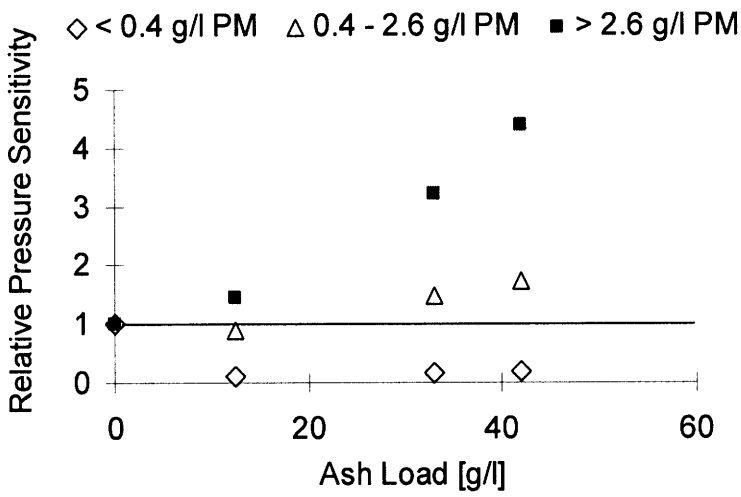

Figure 8.31. Pressure drop sensitivity to soot accumulation as a function of DPF ash load for periodically regenerated DPFs using CJ-4 oils.

From Figure 8.31 it is clear that increasing ash levels in the DPF increase the pressure drop sensitivity to additional soot accumulation quite significantly, relative to the filter with no ash, for soot loads greater than 2.6 g/l. Conversely, ash loaded filters with low soot loads (below 0.4 g/l) show a large decrease in pressure drop sensitivity to incremental soot accumulation. Further, the decrease in pressure drop sensitivity is most pronounced at low ash loads, and increases slightly for elevated ash loads above 12.5 g/l ash. Although the pressure drop sensitivity for soot loads above 2.6 g/l in the DPF containing only 12.5 g/l ash is slightly greater than one, the total filter pressure drop was still lower compared to a DPF with no ash, at this particular level of ash loading.

Separately, the effects of soot and ash accumulation on DPF pressure drop follow predictable and well-behaved trends. However, the combined effect of soot and ash on filter pressure drop significantly alters the pressure drop response of the DPF to additional material (soot and ash) accumulation. The large differences in pressure drop sensitivity shown in Figure 8.31 present a significant challenge to DPF regeneration control schemes based on filter pressure drop.

In order to explore the observed changes in DPF pressure drop sensitivity in more detail, the experiments were repeated with a clean DPF, with much higher levels of soot loading than those shown in Figure 8.30. The pressure drop trends for the clean DPF (no ash) as a function of soot load are shown in Figure 8.32.

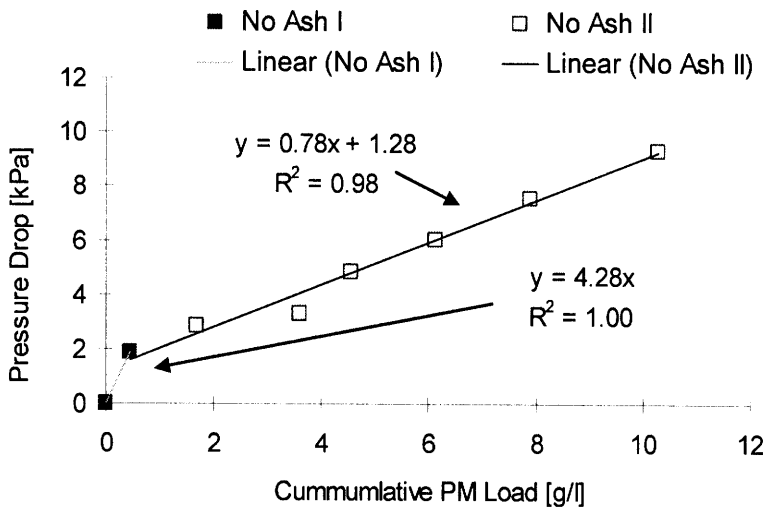

Figure 8.32. Pressure drop as a function of soot load for a DPF containing no ash.

Following initial soot depth filtration, pressure drop measured over the soot loaded DPF remained fairly linear, even for high levels of soot loading, up to 10 g/l. These results indicate that for a DPF containing no ash, even with high soot levels, no change in pressure drop sensitivity is observed. Further, ash accumulated in the DPF reduces the effective filter volume, resulting in higher local soot loads in the regions of the DPF not blocked by the ash and encountered by the exhaust flows. In essence, the ash reduces the DPF size, and this size reduction must be accounted for when comparing DPF pressure drop measurements for DPFs containing different levels of ash.

Figure 8.33 presents a subset of the pressure drop data shown in Figure 8.28, however the specific soot load (mass per DPF volume) has been adjusted, based on the results of the post-mortem analysis, to account for the DPF volume reduction due to ash accumulation. Comparing DPF pressure drop measurements relative to the actual available DPF volume, shifts the curves and reduces the apparent increase in pressure drop sensitivity.

The results presented in Figure 8.33 correspond to the most extreme case, in which the DPF contains 42 g/l of ash. Similar results are observed for the filters containing less ash.

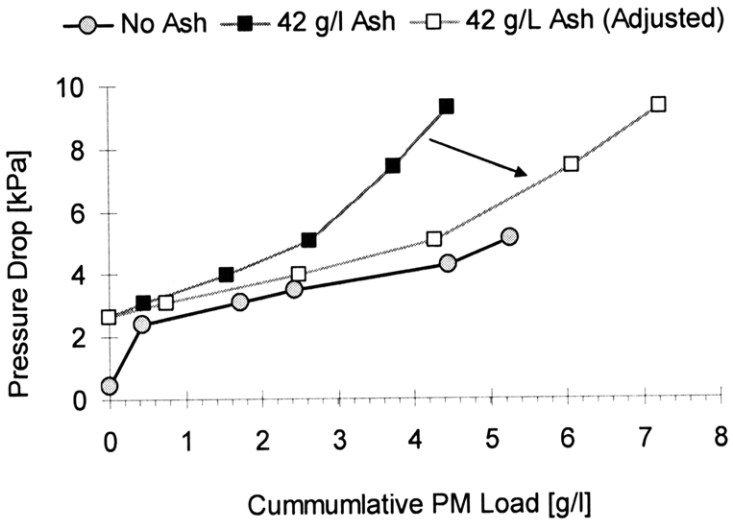

Figure 8.33. Shift in pressure drop curves adjusted for ash accumulation in DPF channels.

After correcting for the DPF volume occupied by the ash, the summary of the ash effects on pressure drop sensitivity is presented in Figure 8.34. Compared with the unadjusted data, shown in Figure 8.31, correcting for the reduction in DPF volume results in a marked decrease in filter pressure drop sensitivity. For low soot levels below 0.4 g/l, ash loaded DPFs still exhibit a significant decrease in pressure drop sensitivity, as the ash prevents soot depth filtration and accumulation in the pores. However, for soot loads between 0.4 g/l and 2.6 g/l there is little observable difference in pressure drop sensitivity between the ash loaded filters, and the reference case of a filter that does not contain any ash.

For high DPF soot loads, above 2.6 g/l, an increase in pressure drop sensitivity is still observed with the ash-loaded filters, despite the volume correction. While the pressure drop sensitivity is significantly reduced, compared to the case in which the volume was not corrected (Figure 8.31), the pressure drop sensitivity of an ash loaded filter is still greater than that of a filter containing no ash by a factor of two to three.

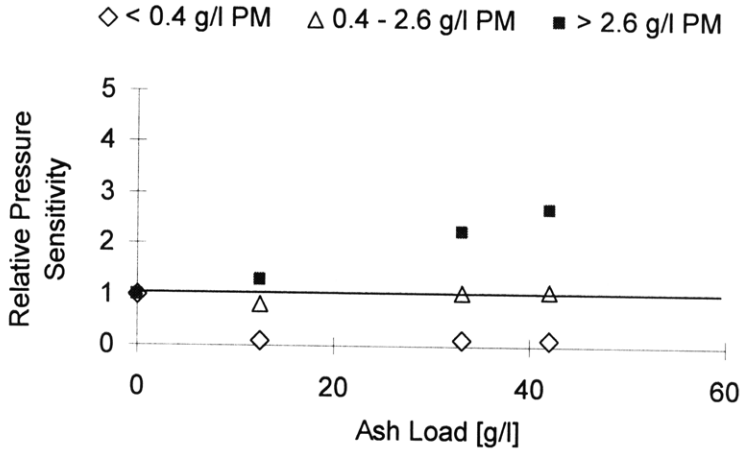

Figure 8.34. Pressure drop sensitivity adjusted to account for DPF volume occupied by ash.

Figure 8.35 presents the reduction in pressure drop sensitivity due to the decrease in DPF volume with ash accumulation. Accounting for the DPF volume occupied by the ash explains nearly 90% of the difference in the pressure drop sensitivity between the ash loaded filters and the DPFs that do not contain any ash, for soot loads between 0.4 g/l and 2.6 g/l. At elevated DPF soot loads, above 2.6 g/l, correcting for the reduction in DPF volume with ash accumulation accounts for only 50% of the difference in pressure drop sensitivity. Additional modeling studies were undertaken and reported in Chapter 11 to further explore these effects.

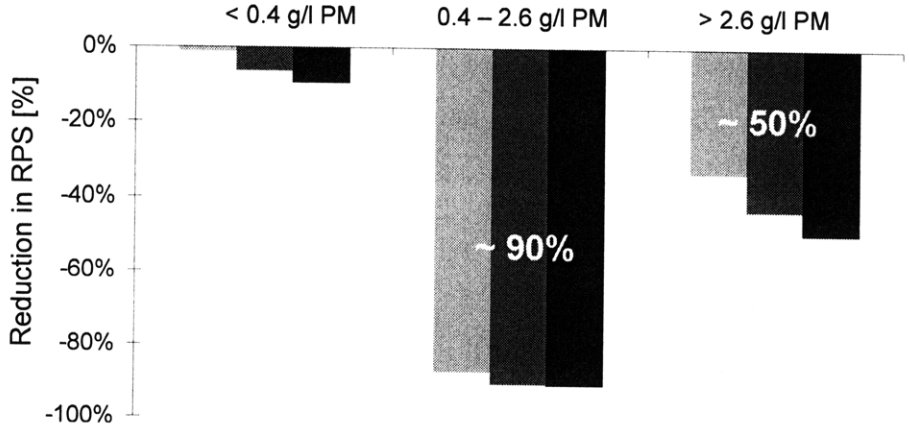

Figure 8.35. Reduction in pressure drop sensitivity due to decrease in DPF volume accounting for ash accumulation.

9 LUBRICANT EFFECTS ON DPF PRESSURE DROP

The effects of individual additives, including calcium-based detergents and ZDDP, on ash morphology and filter pressure drop were also investigated. This section presents the results of the studies with the individual additives.

9.1 Ash Accumulation and Impact Over DPF Service Life

The effect of lubricant chemistry on DPF pressure drop is shown in Figure 9.1. The figure shows the pressure drop trends for three DPFs loaded with 28 g/l to 33 g/l of ash, determined by weighing the filters, using three different lubricant formulations. All of the lubricants were formulated to a 1.0% sulfated ash level; however the specific lubricant additive packages varied considerably and were listed in Table 6.1.

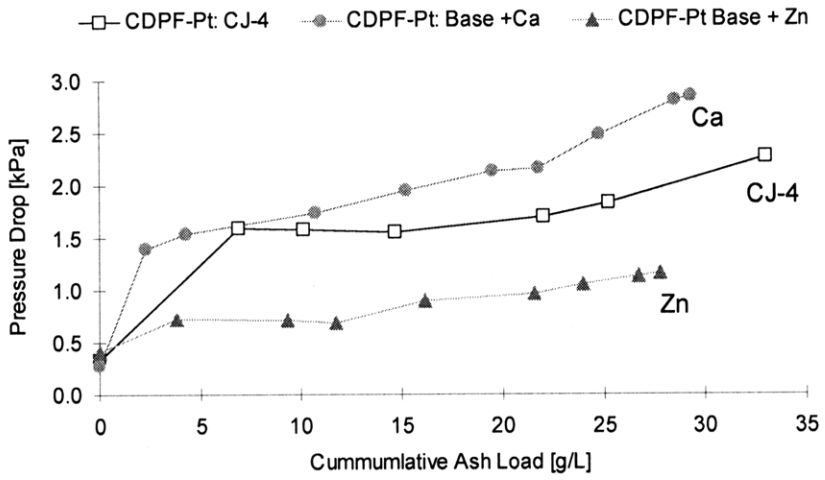

Figure 9.1. Pressure drop trends as a function of ash load for a conventional CJ-4 oil and oils formulated to 1% sulfated ash and only containing a calcium detergent or ZDDP additive.

Figure 9.1 shows the DPF loaded with the base oil containing only a calcium detergent exhibiting the largest increase in filter pressure drop. On the other hand, the filter loaded with a base oil containing only ZDDP resulted in the lowest increase in pressure drop.

The pressure drop trend for the fully-formulated CJ-4 oil was between that of the Zn and Ca lubricant formulations.

Both the calcium and CJ-4 oils exhibit a similar response to ash depth filtration and accumulation in the filter pores. The effect on pressure drop of ash deposition in the DPF pores for the zinc-based oil was much less pronounced. Based on the pressure drop trends, however, it appears that all three lubricants result in roughly the same amount of material trapped in the DPF pores by mass, as indicated by the initial rapid rise in the measured pressure drop. Despite having approximately the same amount of material accumulated in the pores, the zinc-based ash still exhibits a significant reduction in overall pressure drop. It is expected that differences in the ash properties, specifically ash packing density and permeability, are responsible for these observed differences.

Figure 9.2 shows DPF pressure drop as a function of space velocity for the filters loaded with ash from each of the three oils. The pressure drop trends for the clean filters are also shown for comparison, and exhibited nearly the same clean pressure drop response. Consistent with the data presented in Figure 9.1, the calcium-based lubricant results in the greatest increase in DPF pressure drop, whereas the zinc-based oil shows the lowest increase. All of the pressure drop data in Figure 9.2 was obtained from tests using the flow bench and air at ambient conditions.

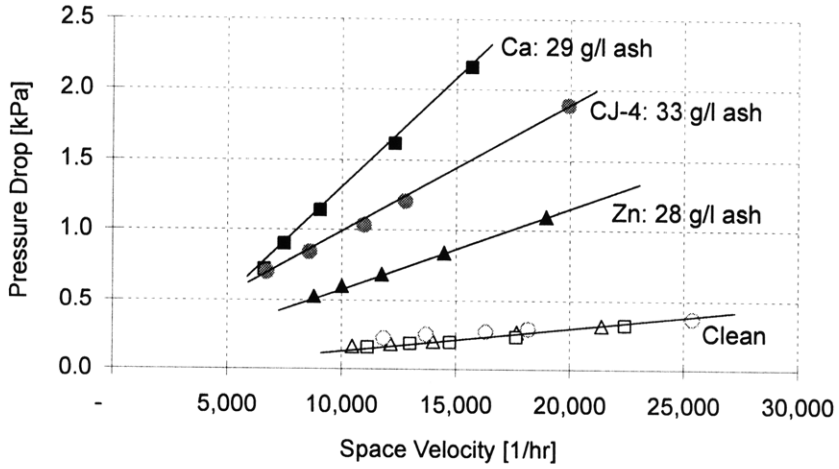

Figure 9.2. Pressure drop variation with space velocity for the platinum catalyzed DPF using conventional CJ-4 oil and oils formulated to 1% sulfated ash and only containing a calcium detergent or ZDDP additive.

The same data presented in Figure 9.1 can be divided into two pressure drop regimes corresponding ash depth filtration and cake filtration. Further, the pressure drop response within each of these regimes can be described with a linear fit. Figure 9.3 shows the linear regression used to describe DPF pressure drop for the cake filtration regime. The linear regression analysis was used to predict filter pressure drop for the cake filtration regime, and the results are shown in Figure 9.4.

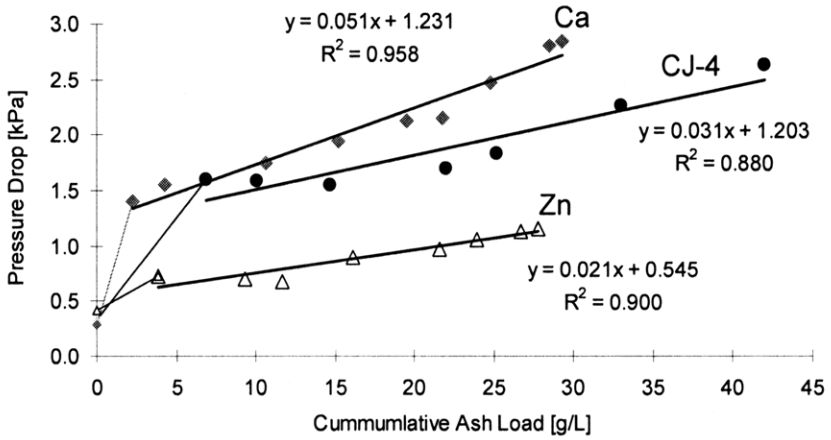

Figure 9.3. Approximation of filter pressure drop for the ash depth and cake filtration regimes.

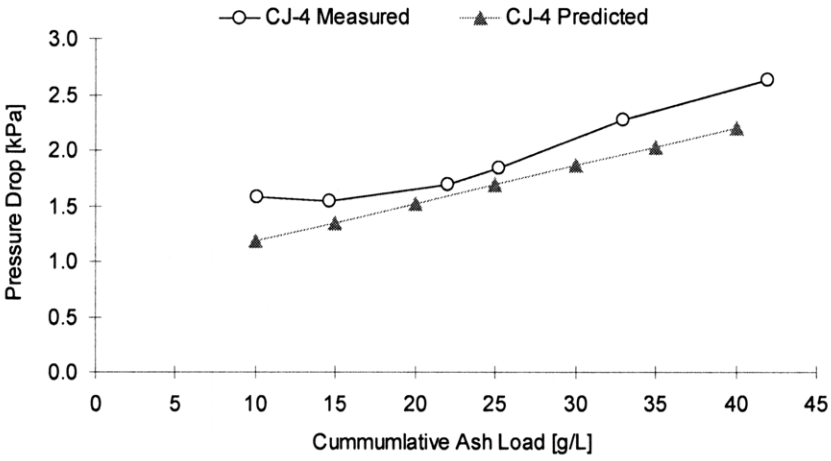

Figure 9.4. Predicted and measured DPF pressure drop. Prediction based on lubricant additive chemistry.

The filter pressure drop predictions presented in Figure 9.4 are based solely on lubricant chemistry for the cake filtration regime. Specifically, the predictions utilized a weighted

average of the CJ-4 oil calcium and zinc content, along with the linear regressions shown in Figure 9.3 to estimate DPF pressure drop based on the lubricant's additive composition. Comparing the measured pressure drop data with the pressure drop estimated based on lubricant chemistry shows this simple lubricant chemistry model under-predicts filter pressure drop by approximately 15% for a CJ-4 oil. Attempts to include additional lubricant additive elements, specifically sulfur and phosphorous levels, in the model resulted in a significant over-estimate of filter pressure drop. The current lubricant chemistry model accounts for only zinc and calcium in the lubricant and fails to include the contribution of magnesium. Magnesium levels in the CJ-4 oil were approximately 25% of the calcium and zinc levels. Inclusion of magnesium may improve the accuracy of these estimates significantly and reduce the 15% error reported above.

9.2 Ash-Properties and Distribution

The DPFs loaded with the three different lubricant formulations were subjected to a post-mortem analysis following the ash loading and performance evaluation testing. The ash generated using the three different lubricants exhibited clear differences in morphology and distribution with the filter channels as well. Figure 9.5 shows select DPF samples containing ash deposits along the channel walls for the CJ-4 oil, predominantly zinc containing oil, and the lubricant containing only the calcium detergent.

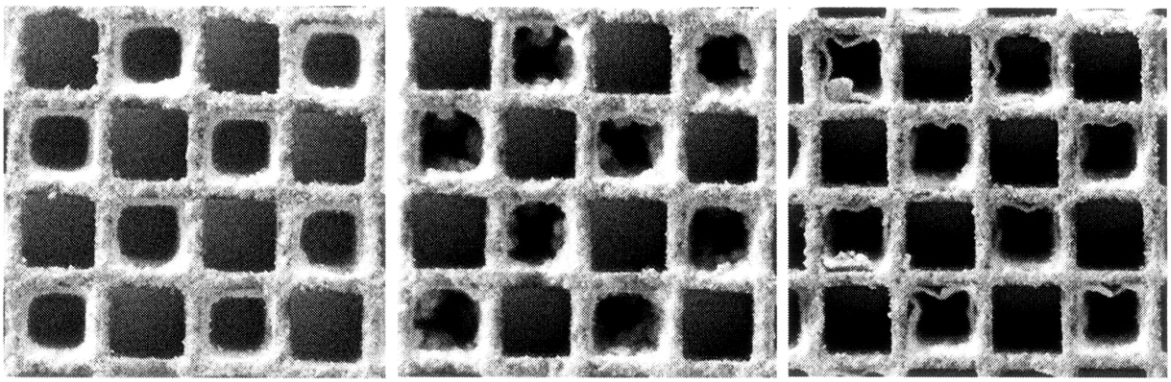

Figure 9.5. Ash adherence to DPF channel walls for ash generated via periodic regeneration in DPFs containing (a) CJ-4 ash, (b) Zn ash, and (c) Ca ash.

The differences in ash morphology and distribution were particularly distinct towards the back of the filter channels but still upstream of the ash plugs. While the CJ-4 ash formed a thin even layer along the walls, the ash generated by the two other lubricant formulations did not. As evident in Figure 9.5, the predominantly zinc-based ash formed deposits in clumps along the side of the channel walls. On the other hand, the calcium-based deposits formed thin, dense layers that appeared to peal away from the channel walls. The irregular shape of the calcium- and zinc-based deposits in this region of the filter complicated measurements of ash layer thickness and volume.

A direct comparison of two filter samples from the same positions within each of the three DPFs is shown in Figure 9.6. The overall distribution of the calcium- and zinc-based ash in the DPF channels was similar to the CJ-4 oil, with the exception of the irregularly shaped deposits found near the back of the filter described above.

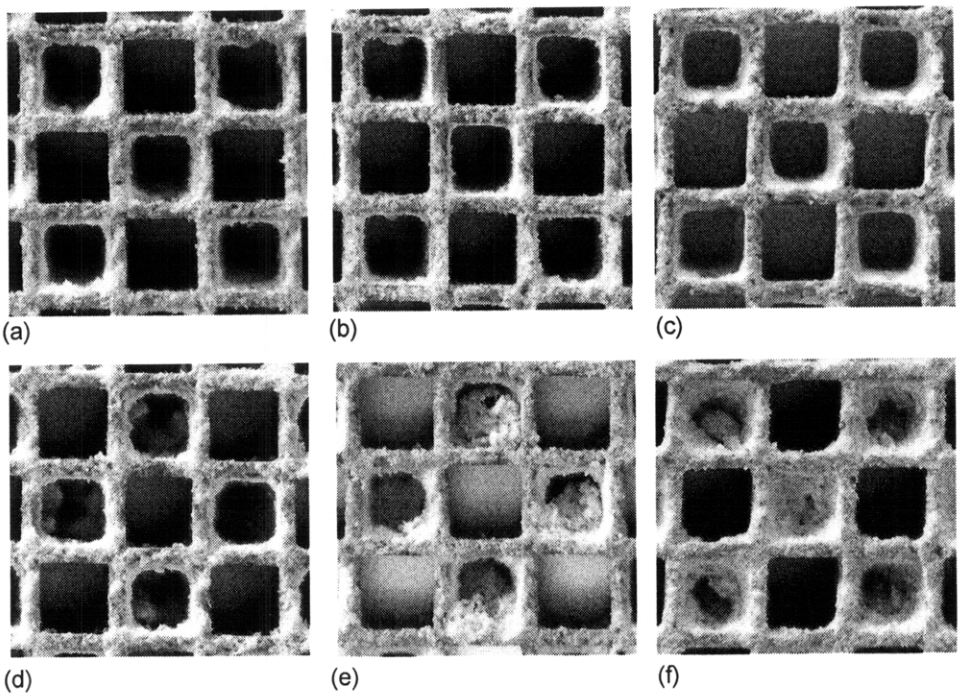

Figure 9.6. Ash accumulation 57 mm from DPF face for (a) DPF containing 28 g/l Zn ash, (b) DPF containing 29 g/l Ca ash, (c) DPF containing 42 g/l CJ-4 ash, and 133 mm from DPF face for (d) DPF containing 28 g/l Zn ash, (e) DPF containing 29 g/l Ca ash, (f) DPF containing 42 g/l CJ-4 ash all generated via periodic regeneration.

The calcium-based ash also seemed to form the "stickiest" deposits. While the CJ-4 and zinc-based ash deposited in plugs toward the back of the channels could easily be tapped out of the DPF, the calcium-based ash could not. In general, the deposits formed by the oil containing only the calcium detergent were the most difficult to remove from the filter samples.

9.2.1 Ash Accumulation and Distribution

The measured ash layer thickness along the DPF centerline is shown in Figure 9.7 for all three of the lubricant formulations tested. The ash layer thickness along the length of the channels varied little between the three cases and ranged from 0.15 mm for the zinc-based ash to 0.18 mm for the calcium-based ash. Due to the low axial resolution of the measurement technique (dependent upon the DPF sample size) the ash layer profiles near the start of the end-plug are not well known.

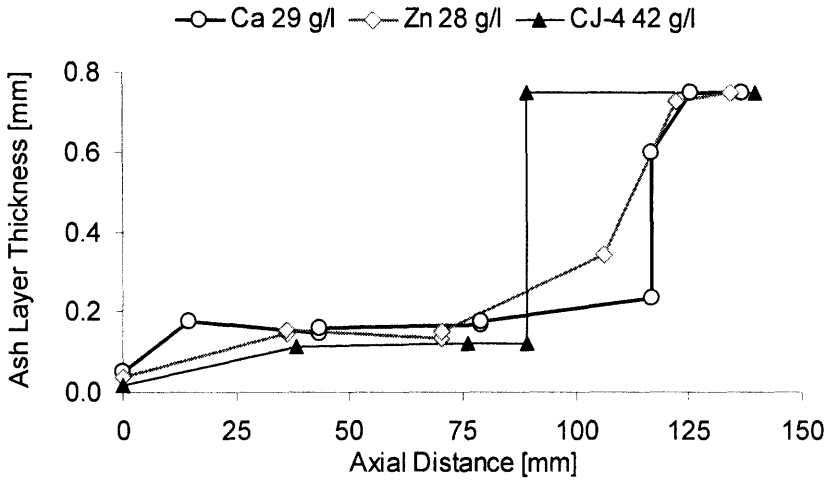

Figure 9.7. Ash layer thickness profiles measured along DPF centerline for DPFs containing ash generated from a fully formulated CJ-4 oil, base oil + Ca detergent, and base oil + ZDDP.

The reader is cautioned when comparing the ash distribution profiles for the CJ-4 ash with the calcium and zinc ash, as the CJ-4 ash-loaded DPF contained 42 g/l ash, whereas the other two filters only contained 28 g/l to 29 g/l ash. Based on this comparison, however, little difference in total ash layer thickness is observed for the three lubricants.

Furthermore, only a small amount of ash was found accumulated in the plugs at the back of the filter for the calcium and zinc cases. Figure 9.8 presents similar ash distribution profiles measured in the radial direction, 36 mm from the DPF centerline for the three cases.

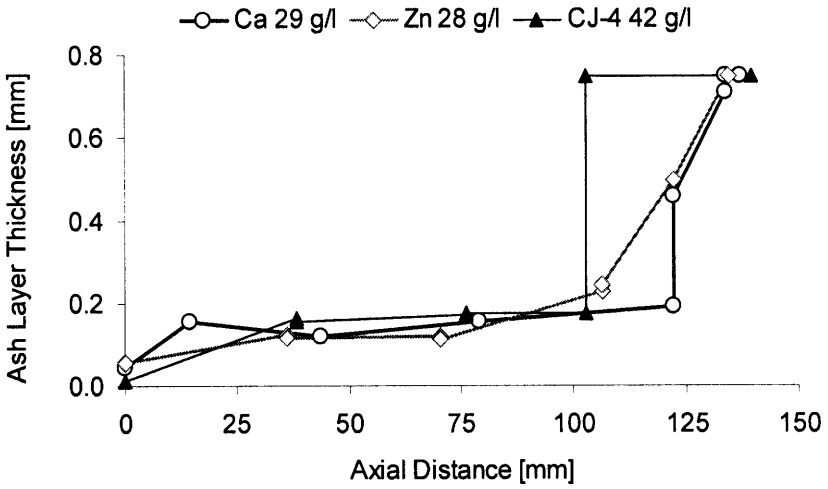

Figure 9.8. Ash layer thickness profiles measured 36mm from DPF centerline for DPFs containing ash generated from a fully formulated CJ-4 oil, base oil + Ca detergent, and base oil + ZDDP.

Figures 9.9 and 9.10 show the full ash distribution profiles for three different radial locations with the zinc- and calcium-based ash, respectively. Ash plug formation was clearly more pronounced in the filter loaded with the oil containing only the calcium detergent. This same filter shows the ash cake layer accumulated along the wall is slightly thicker and more uniform as compared to the ash composed primarily of zinc compounds. As shown in Figure 9.10, the ash layer thickness appears to build-up quite rapidly from the inlet face of the filter (within approximately 15 mm). Due to the larger size of the ash samples in Figure 9.9, the same level of axial resolution was not available for the zinc ash measurements. In both cases however, the ash layer was thickest along the DPF centerline, and the thickness decreased in the radial direction away from the center of the filter. Similarly, the ash end-plugs were also slightly longer in the DPF center.

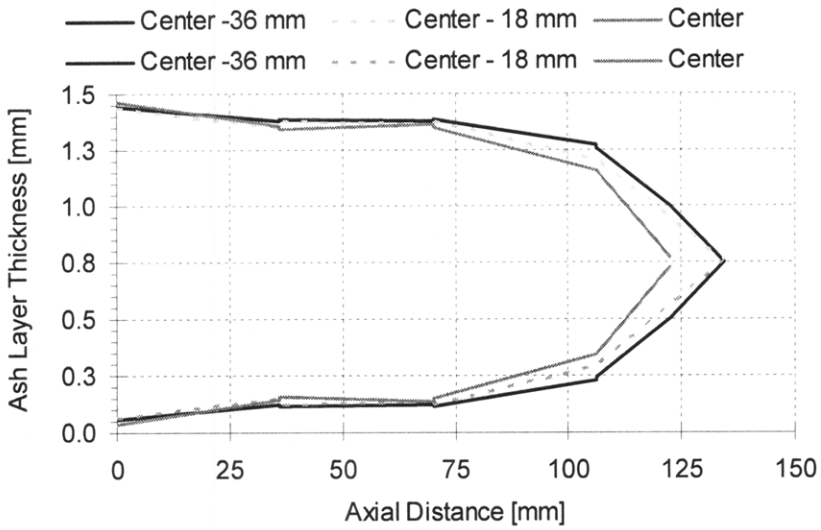

Figure 9.9. Single channel ash distribution profiles for a DPF containing 28 g/l ash generated using a base oil containing only ZDDP in a DPF undergoing periodic regeneration.

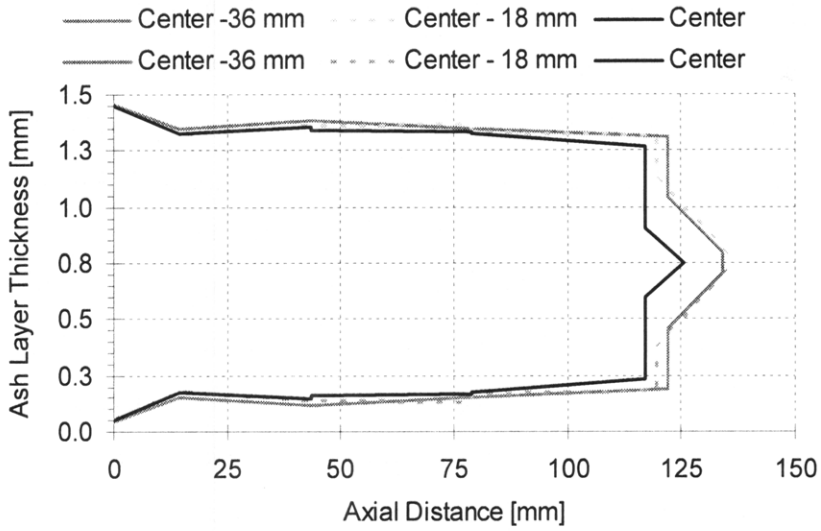

Figure 9.10. Single channel ash distribution profiles for a DPF containing 29 g/l ash generated using a base oil containing only a calcium detergent in a DPF undergoing periodic regeneration.

Figures 9.11 and 9.12 show the channel open area profiles computed from the ash thickness measurements for these three filters. The calcium ash reduced the open channel area along the DPF centerline by approximately 40% on average, whereas the zinc ash

reduced the channel open area in the same region of the filter by only around 35%. Interestingly, the ash distribution and channel open area profiles for the calcium- and zinc-based ash appeared more uniform in the radial direction throughout the filter, whereas a larger difference in ash distribution was observed with the CJ-4 oil.

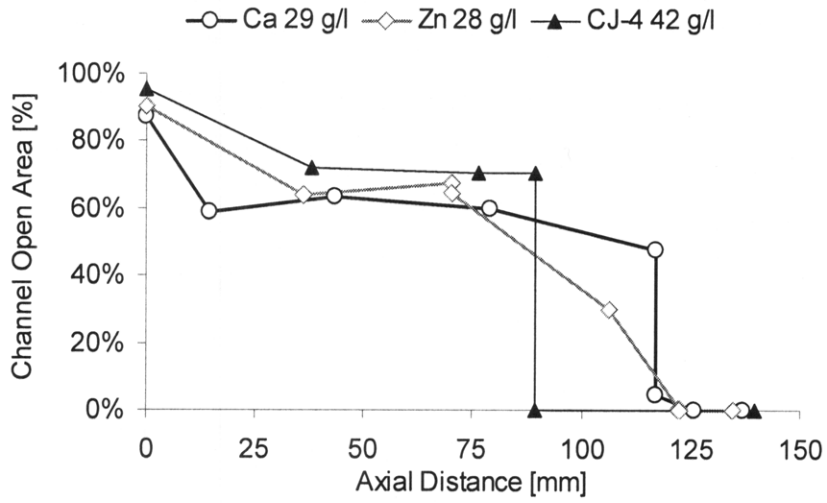

Figure 9.11. Channel open area profiles measured along the DPF centerline for DPFs containing ash generated from a fully formulated CJ-4 oil, base oil + Ca detergent, and base oil + ZDDP.

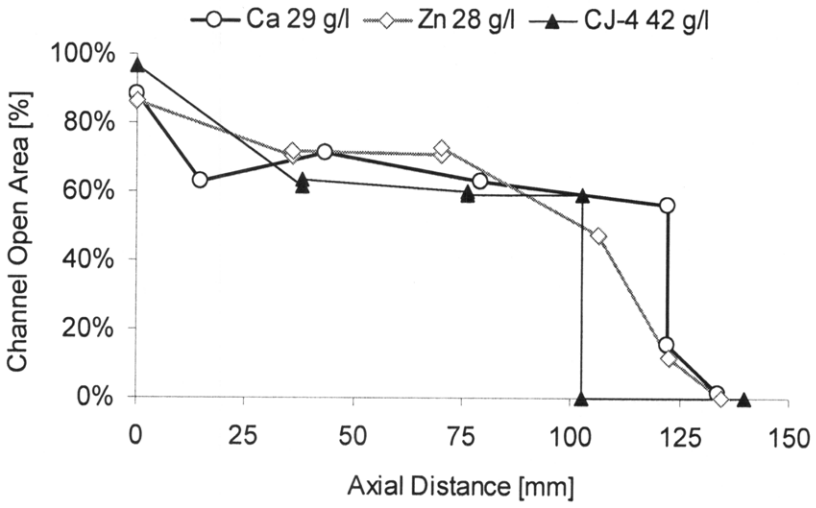

Figure 9.12. Channel open area profiles measured 36 mm from the DPF centerline for DPFs containing ash generated from a fully formulated CJ-4 oil, base oil + Ca detergent, and base oil + ZDDP.

9.2.2 Ash Packing Density and Porosity

Ash packing density measurements were also carried out using the measured ash distribution profiles and known weight of the ash deposits in the filter. The ash packing density profiles for the zinc ash are shown in Figure 9.13, whereas Figure 9.14 shows the ash packing density profiles for the calcium ash. In general, ash packing density in these two filters varied little in the axial direction along the length of the channels. A slight decrease in packing density is observed for the ash accumulated in the plugs at the back of the channel.

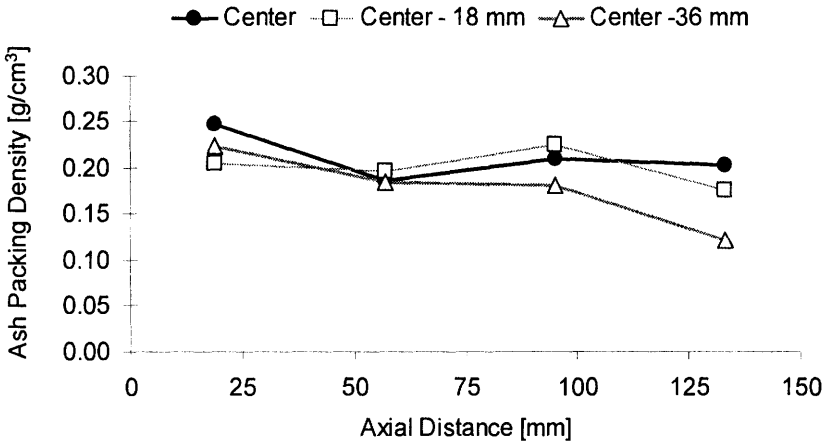

Figure 9.13. Radial ash packing density profiles for a DPF containing 28 g/l ash generated using a base oil containing only ZDDP and periodic regeneration.

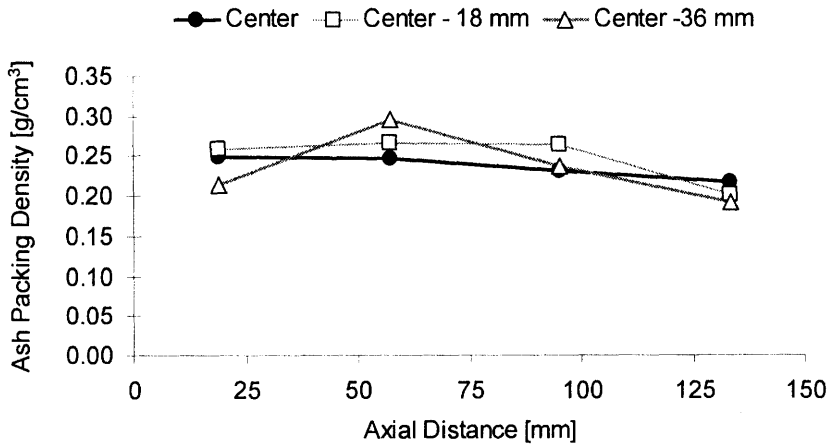

Figure 9.14. Radial ash packing density profiles for a DPF containing 29 g/l ash generated using a base oil containing only a calcium detergent and periodic regeneration.

As noted in Chapter 8, the ash packing density measurements for the sample 57 mm from the front face of the DPF are most representative of the ash packing density for the ash deposited in a layer along the channel walls. Similarly, the ash packing density measurements for the sample 133 mm from the front face of the filter is most representative of the ash accumulated in the end-plugs. Figure 9.15 presents a direct comparison of the ash packing density measurements for these two regions of the filter.

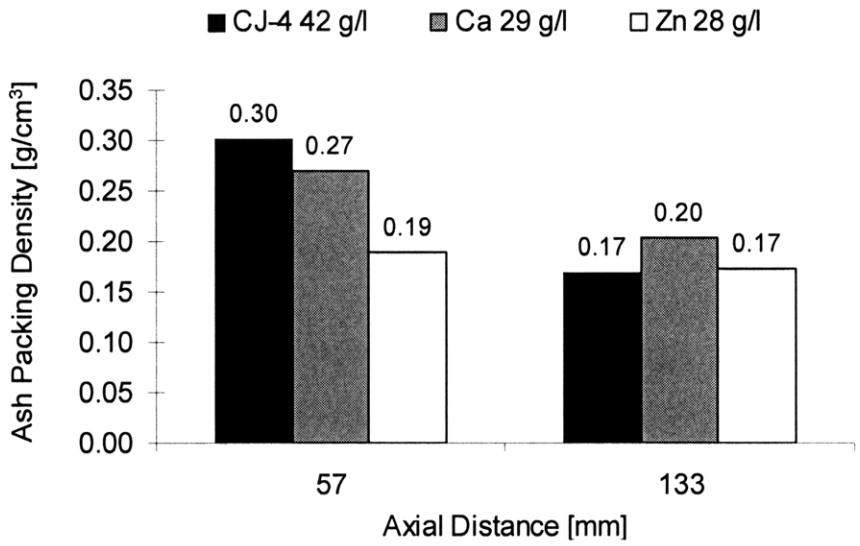

Figure 9.15. Comparison of ash packing density variations axially along the DPF channels with varying lubricant chemistry.

As shown in Figure 9.15, the ash deposited along the channel walls exhibited a higher packing density than the ash accumulated in the plug at the end of the DPF for all cases. This difference in packing density was least pronounced for the ash generated with the zinc-based oil. Furthermore, the CJ-4 oil exhibited the highest packing density for the ash accumulated in a layer along the channel walls. Interestingly, the packing density of the ash accumulated in the end-plugs varied little for the three lubricants. This is further circumstantial evidence that the ash transport and deposition mechanisms play a key role in controlling the packing characteristics of the ash accumulated in the end-plugs. It is expected that the ash deposited in a layer along the channel walls experiences higher filtration velocities, as compared with the ash deposited at the end of the channels. The difference in the local flow conditions may have a large effect on ash packing density.

9.2.3 Ash Composition

The composition of the ash generated from the oils containing only calcium and only zinc additives and accumulated in the DPF following periodic regeneration was analyzed using x-ray diffraction. The spectrum for the zinc-based oil is shown in Figures 9.16. The two predominant ash compounds in the ash generated from the oil containing only ZDDP additives were two forms of zinc phosphate, $Zn_3(PO_4)_2$ and $Zn_2P_2O_7$. The main peaks corresponding to these compounds are also identified in the spectra.

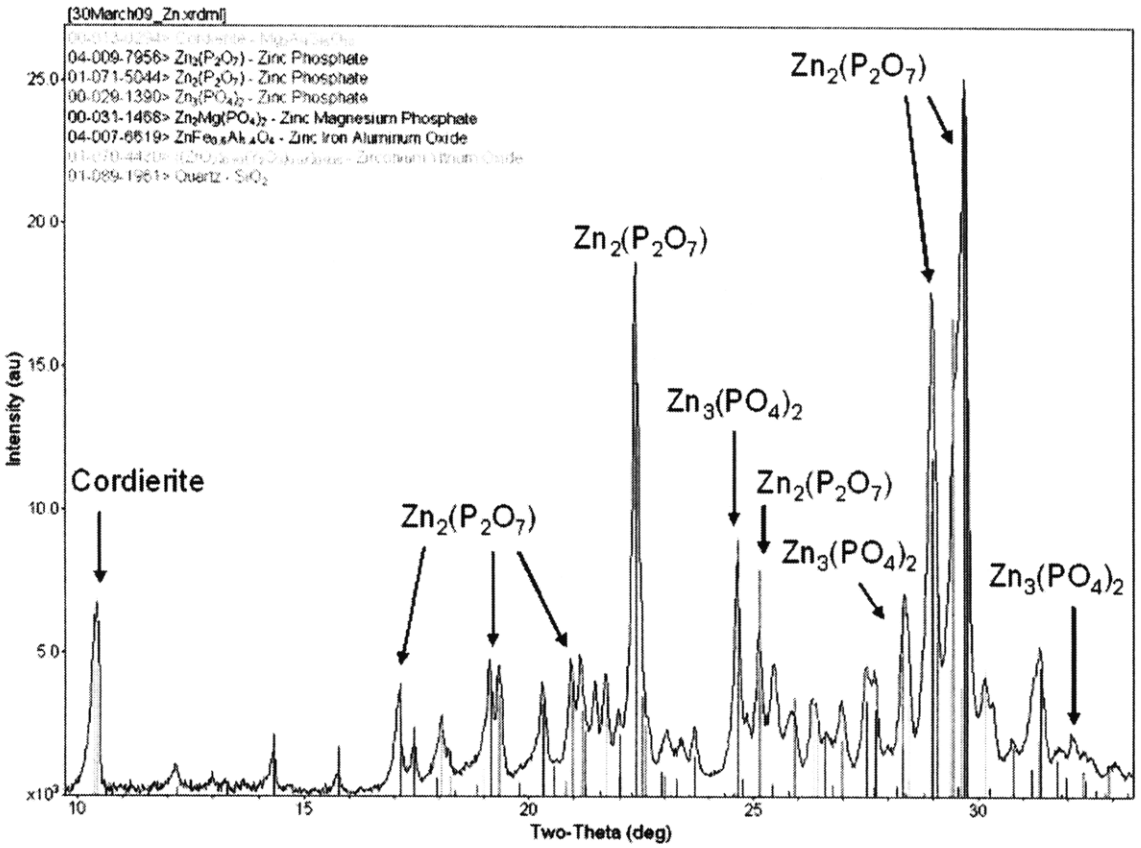

Figure 9.16. Ash compositional analysis via XRD for ash generated from oil containing only ZDDP.

The theoretical density of $Zn_3(PO_4)_2$ is 4.0 g/cm^3, whereas the theoretical density of $Zn_2P_2O_7$ is 3.75 g/cm^3. Assuming the ash consists of equal amounts of these two zinc phosphates, gives a theoretical ash density of approximately 3.875 g/cm^3. Few constituents other than zinc phosphates were found in the ash in any appreciable amounts.

The cordierite peak, identified in the spectra, is due to a small amount of DPF wall material in the ash sample.

Figure 9.17 shows the spectrum for the ash generated from the oil containing only the calcium detergent. Calcium sulfate, $CaSO_4$, was the main ash compound identified in this ash sample. The major peaks are also identified in the spectra. Some amount of calcium carbonate, $CaCO_3$, was also found in the ash along with a small amount of cordierite from the filter wall.

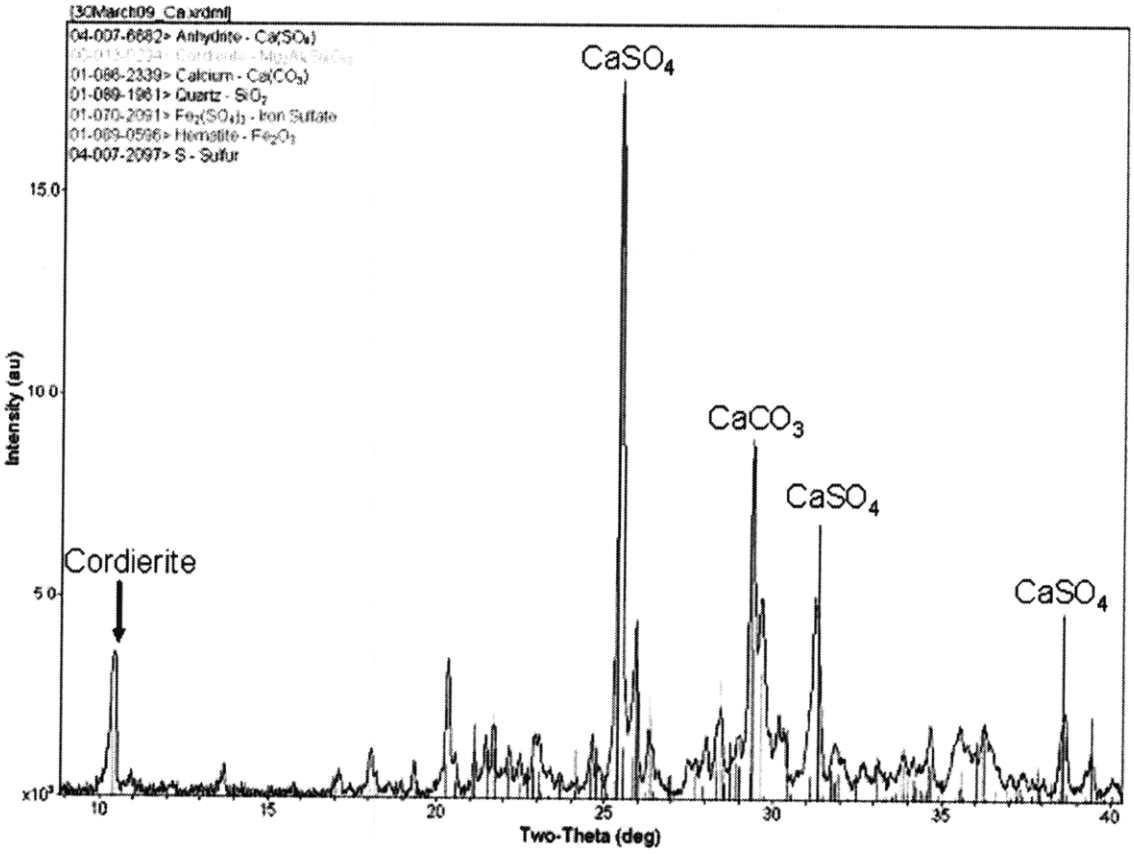

Figure 9.17. Ash compositional analysis via XRD for ash generated from oil containing only calcium detergent.

The theoretical density of calcium sulfate, $CaSO_4$, is 2.96 g/cm^3. Calcium sulfate is assumed to be the primary ash constituent in this sample, giving a theoretical ash density of 2.96 g/cm^3. The theoretical ash density values are useful to compute ash porosity using the measured packing densities from the post-mortem analysis in Section 9.2.2.

9.3 Measured and Computed Ash Properties

A summary of the measured ash properties from the post-mortem analysis is presented in Table 9.1 below. Based on the measured ash packing density values and ash composition determined via XRD, the ash porosities ranged from 91% to 95%, with the calcium-based ash being the least porous. In general, the properties of the CJ-4 ash and calcium-based ash were quite similar, providing further evidence that calcium-based additives exert the greatest influence on controlling ash properties and the resulting pressure drop measured with fully-formulated CJ-4 oils.

Lubricant	Regeneration	Ash	Ash Layer Thickness	Wall Density	Plug Density	Theoretical Density	Ash Porosity
		[g/l]	[cm]	[g/cm^3]	[g/cm^3]	[g/cm^3]	[%]
Base + Zn	Periodic	28.0	0.013	0.19	0.17	3.9	95.1
Base + Ca	Periodic	29.0	0.015	0.27	0.20	3.0	90.9
CJ-4	Periodic	42.0	0.013	0.30	0.17	3.4	91.1

Table 9.1. Summary of measured ash properties for ash generated using the CJ-4 oil and specially formulated oils with periodic regeneration.

Table 9.2 provides additional parameters related to the changes in DPF geometries computed from the ash distribution measurements and properties listed in Table 9.1.

Lubricant	Regeneration	Ash	Channel Filtration Area	Change in Filtration Area	Change in Frontal Area	Change in Length	Ash End Plug Volume Fraction
		[g/l]	[cm^2]	[%]	[%]	[%]	[%]
Base + Zn	Periodic	28.0	5.2	-41.9%	-36.0%	-12.6%	18.9%
Base + Ca	Periodic	29.0	5.6	-37.3%	-40.2%	-22.0%	39.3%
CJ-4	Periodic	42.0	4.7	-47.9%	-27.0%	-40.5%	76.3%

Table 9.2. Summary of calculated ash effects on filter geometry for ash generated using the CJ-4 oil and specially formulated oils with periodic regeneration.

9.4 Ash-Compositional Effects on Pressure Drop

The pressure drop trends for the DPFs loaded with the three different lubricants are shown in Figure 9.18 as a function of space velocity. Figure 9.19 shows the filter pressure drop contribution due to flow through the ash layer and DPF substrate (porous media) as a function of wall velocity for the DPFs loaded with ash from the three different lubricants.

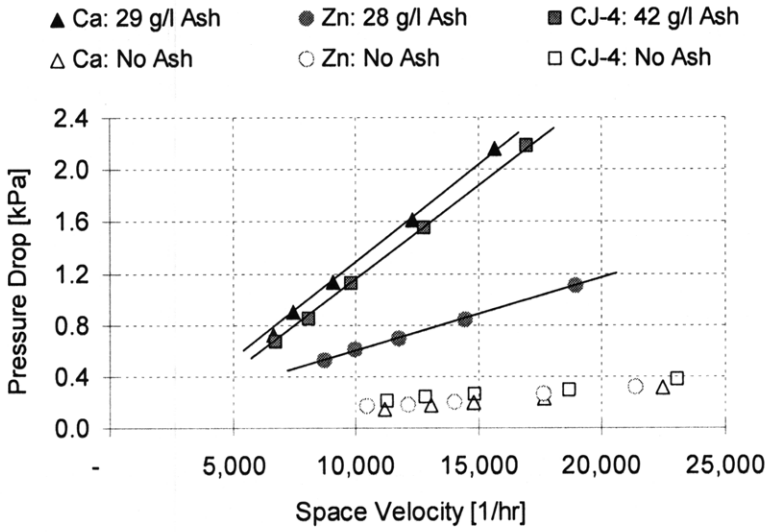

Figure 9.18. Pressure drop as a function of space velocity for clean and ash loaded DPFs with varying lubricant-derived ash chemistries.

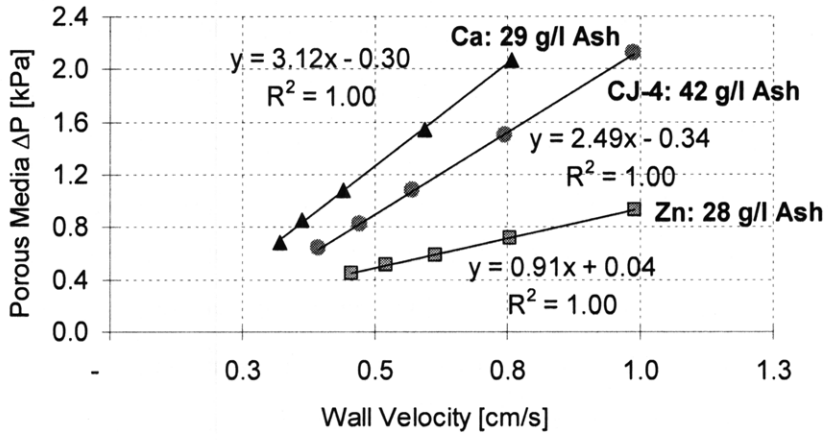

Figure 9.19. Pressure drop through the ash layer and DPF substrate as a function of wall velocity for clean and ash loaded DPFs with varying lubricant-derived ash chemistries.

The ash distribution measurements obtained from the post-mortem filter analysis were also used to compute the average filter wall velocity, which is dependent on the exhaust gas flow rate and available filtration area. The determination of pressure drop due to the flow through the ash layer and substrate (porous media) was described in Section 8.5. Plotting the porous media pressure drop as a function of wall velocity, therefore, accounts for the changes in DPF channel geometry due to ash accumulation. Further, the slopes of the pressure drop curves in Figure 9.19 are directly proportional to the quantity (w/k). This term is related to the flow resistance of the porous media (layer thickness divided by permeability), as all of the test were carried out on the same filter substrate at the same temperature and gas viscosity using the flow bench with air at ambient conditions.

The average ash wall layer thicknesses measured as part of the post mortem analysis for the DPFs containing ash resulting from the three different lubricant formulations were listed in Table 9.1. All of the DPFs exhibited ash layers with similar thicknesses, between 0.13 and 0.15 mm. Due to the large difference in pressure drop slopes for these three cases, shown in Figure 9.19, the ash layer permeabilities must be quite different as well. Relative to the ash generated from the CJ-4 oil, the ratio of the flow resistance terms (w/k) for the DPF containing primarily calcium-based ash is 0.8, whereas the ratio of the flow resistance term for the DPF containing primarily zinc-based ash is 2.7.

The data indicates the ash generated using the base oil containing only ZDDP must be significantly more permeable than the ash generated from the CJ-4 oil or the base oil containing only the calcium detergent. Furthermore, the permeabilities of the ash resulting from the CJ-4 oil and base oil containing only calcium detergents must be quite similar. Ash resulting from calcium-based additives may exert a much larger effect on DPF pressure drop than ash resulting from zinc-based additives and may play a dominant role in influencing total DPF pressure drop when fully-formulated CJ-4 oils are used. The large differences in the measured pressure drop trends, shown in Figure 9.19, are also supported by the observed differences in measured packing density and porosity for ash generated by the three oils, presented in Table 9.1. The results of the modeling

studies presented in Chapter 11, explore these differences in ash layer permeabilities in more detail.

9.5 Combined Ash and Soot Effects on Pressure Drop Sensitivity

Following ash loading and DPF performance characterization with the three different lubricant chemistries, the filters were also loaded with soot on the Cummins ISB. Figure 9.20 shows DPF pressure drop as a function of soot load for the filters pre-loaded with ash. Pressure drop data for a filter containing no ash is also presented in the figure, and all measurements were carried out on a flow bench using air at ambient conditions.

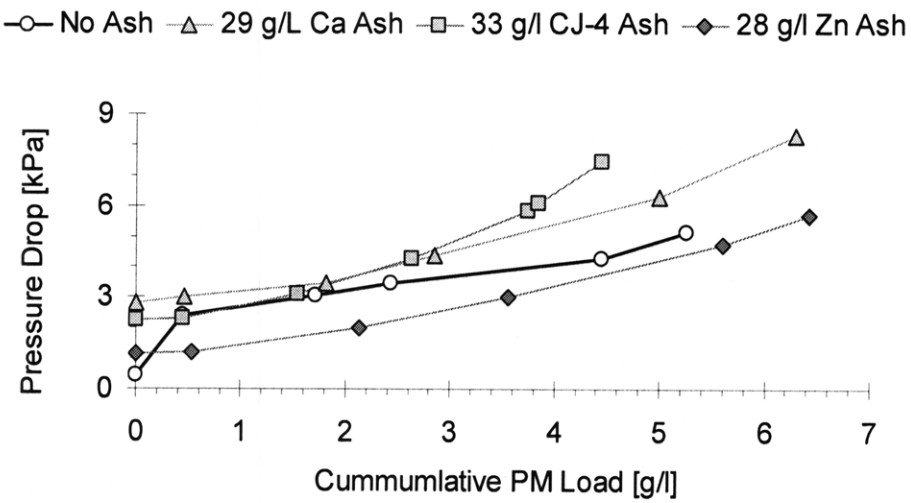

Figure 9.20. Pressure drop as a function of soot accumulation on Pt-catalyzed DPFs preloaded with ash generated via periodic regeneration from the CJ-4 oil and oils containing only Ca or Zn additives at 20,000 hr^{-1} space velocity.

All of the ash pre-loaded DPFs exhibit an increase in pressure drop over the filter containing no ash at 0 g/l soot. This increase in pressure drop is solely due to the ash deposits in the filter. Similar to the CJ-4 ash, the ash layer generated by the lubricants containing only calcium and zinc additives also prevents soot depth filtration, as evident in the pressure drop data. Interestingly, the filter containing 28 g/l of ash generated from the zinc-based oil showed a reduction in pressure drop for all levels of soot loading relative to the filter containing no ash. Additionally, two distinct pressure drop regimes

were observed for each of the filters, and they are clearly labeled and shown in Figure 9.21.

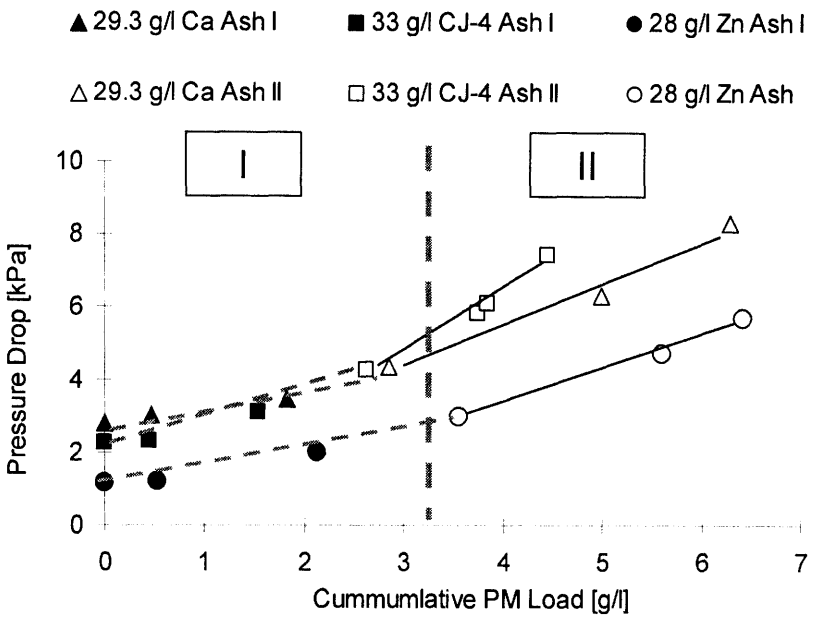

Figure 9.21. Definition of pressure drop regimes (I) and (II) observed with soot accumulation on ash loaded DPFs at 20,000 hr^{-1} space velocity.

Similar to the approach employed in Chapter 8, the pressure drop response within each regime was characterized by a simple linear regression. The slope of the pressure drop curves within each regime represents the pressure drop sensitivity to additional soot accumulation in the DPF, and can be used to compute the relative pressure sensitivity for each filter as defined in Equation 8.1. While the DPF exposed to the calcium-based lubricant exhibited the greatest increase in pressure drop due to the ash accumulation alone, the DPF loaded with the CJ-4 oil exhibited the greatest increase in pressure drop when both ash and soot were accumulated in the filter, as shown in Figure 9.21. It should be noted however, that the DPF loaded with the CJ-4 oil contained approximately 4g/l more ash than the filter loaded with the calcium-based ash.

Figure 9.22 presents a comparison of the relative pressure drop sensitivities within each pressure drop regime for the three lubricant formulations. While the actual pressure drop curves do not physically contain separate discrete pressure drop regimes, defining the

regimes presents a convenient means for comparing the ash effect on pressure drop sensitivity. The pressure drop regimes were defined in Chapter 8. For all of the lubricants tested, ash accumulation in the DPF reduced pressure drop sensitivity quite significantly to low soot loads, below 0.4 g/l (regime I). On the other hand, elevated soot loads, above 2.6 g/l, regime (III), resulted in a significant increase in pressure drop sensitivity in all of the ash loaded filters.

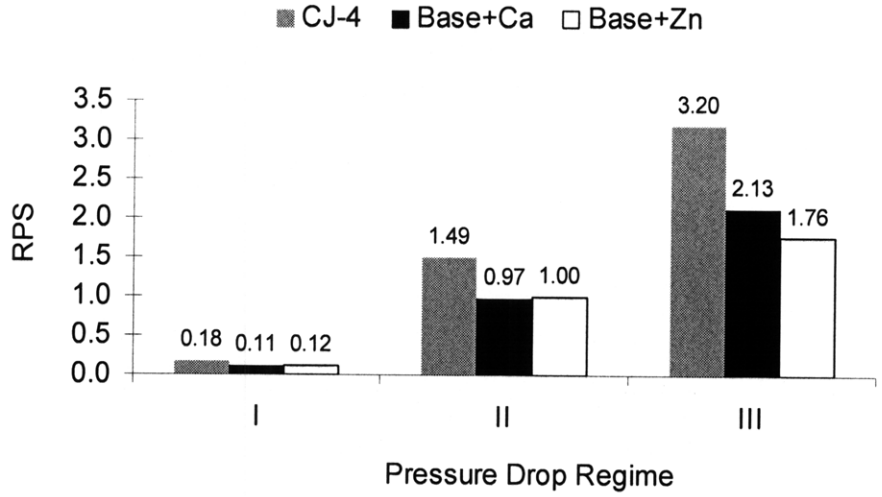

Figure 9.22. Lubricant chemistry effects on ash composition and DPF relative pressure drop sensitivity (RPS) to soot accumulation.

In general, the CJ-4 ash exhibited the largest effect on pressure drop sensitivity to additional soot loading, followed by the calcium- and zinc-based ash. The large effect of the fully-formulated CJ-4 oil on soot pressure drop sensitivity implies that additional parameters or lubricant additives may significantly affect ash morphology, magnesium for example, which were not included in the current experimental test matrix. Furthermore, synergistic effects may also play a role when the various individual additive compounds are combined in the lubricant.

(This page intentionally left blank)

10 EXHAUST CONDITIONAL EFFECTS ON DPF PRESSURE DROP

In addition to investigating the effects of lubricant additive chemistry on ash characteristics and DPF pressure drop, the role of exhaust conditions such as temperature, flow, and the filter thermal history in controlling ash properties and pressure drop was investigated as well. Two primary DPF operating regimes were employed in these investigations: (1) periodic DPF regeneration with soot and ash loading at a filter inlet temperature of 250 °C followed by periodic high temperature regeneration at 600 °C, and (2) continuous filter regeneration with DPF inlet temperatures maintained above 600 °C for the duration of the ash loading procedure. All of the experimental results reported in this section were carried out using the same CJ-4 oils and DPF substrates, and only varying exhaust conditions.

10.1 Ash Accumulation and Impact Over Service Life

Figure 10.1 shows the effect of ash generated via periodic and continuous regeneration on DPF pressure drop. Despite a slightly lower level of accumulated ash, the DPF in which ash was accumulated via continuous regeneration showed a greater increase in pressure drop as compared to the periodically regenerated case. Pressure drop over the clean filters was nearly the same, as shown in Figure 10.1.

It is hypothesized that ash accumulated in DPFs undergoing periodic regeneration forms a thin layer along the channel walls, with significant accumulation in plugs toward the back of the channels. On the other hand, continuously regenerated filters tend to show fairly even distribution of the ash along the channel walls with little plug formation [45]. Images illustrating the differences in ash distribution profiles for periodically and continuously regenerated DPFs were presented in Figure 2.5. These differences in ash distribution may be responsible for the observed differences in the pressure drop trends. The post-mortem analysis conducted following filter ash loading and testing provides additional details regarding ash properties and distribution.

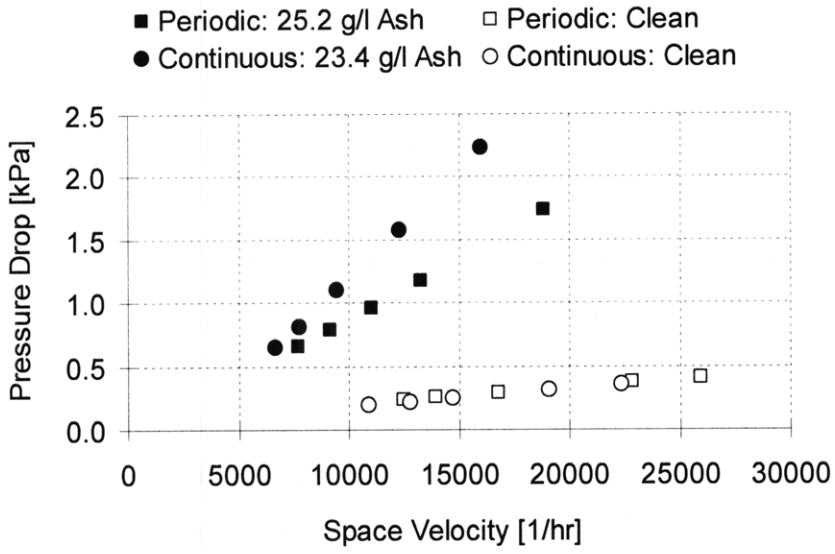

Figure 10.1. Effect of ash generated under periodic and continuous regeneration on pressure drop for the platinum catalyzed DPFs with conventional CJ-4 oil.

Figure 10.2 compares pressure drop characteristics for DPFs subjected to continuous and periodic regeneration as a function of ash load. Once again the pressure drop measurements were conducted on the flow bench following complete filter regeneration.

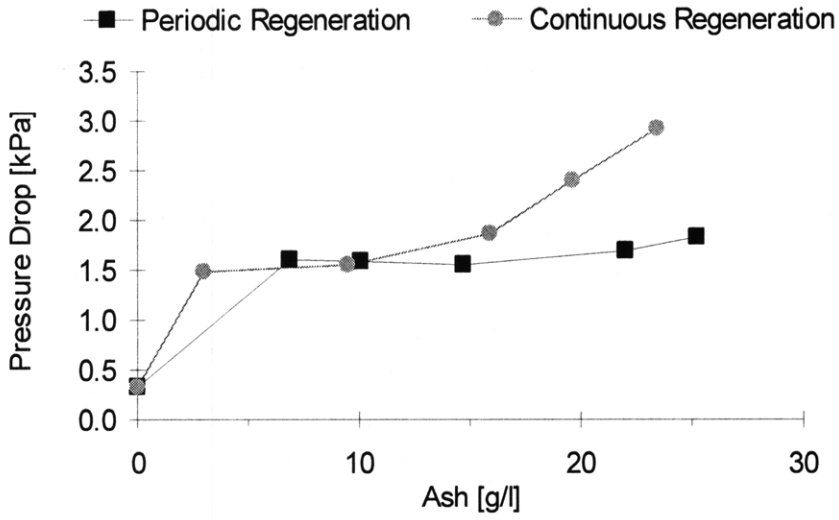

Figure 10.2. Pressure drop as a function of ash load at 20,000 hr^{-1} space velocity for DPFs subject to periodic and continuous regeneration with CJ-4 oil.

The apparent discrepancy in Figure 10.2 between depth filtration levels for the periodic and continuously regenerated cases is due to a lack of data points at low ash loads for the filter with periodic regeneration. Both filters exhibited similar levels of ash depth filtration as shown in Figure 8.1 for the periodically regenerated case and Figure 10.2 for the continuously regenerated filter. For ash loads below 10 g/l both filters show a similar increase in pressure drop. Above 10 g/l ash loading, the pressure drop across the continuously regenerated DPF increases significantly relative to the DPF undergoing periodic regeneration, as shown in Figure 10.2. Some localized ash face plugging was observed in the continuously regenerated DPF at the end of the test, also possibly contributing to the increase in pressure drop.

10.2 Ash-Properties and Distribution

The post-mortem analysis provides additional details regarding ash properties and their effects on the observed differences in DPF pressure drop. Figure 10.3 compares the ash distribution for DPFs subjected to periodic and continuous regeneration.

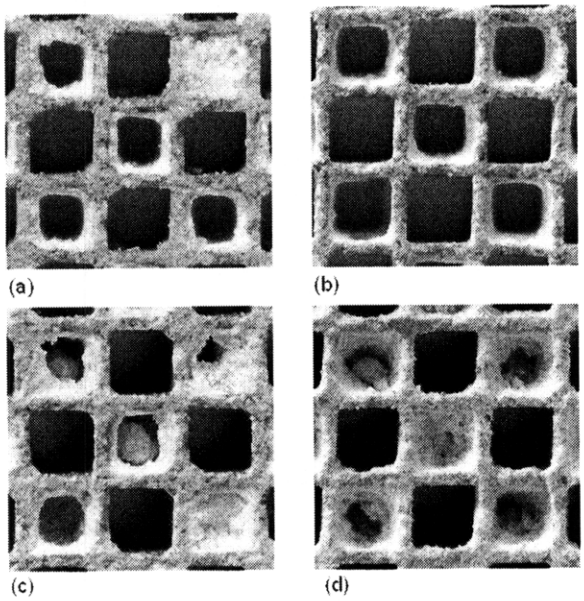

Figure 10.3. Ash accumulation 57 mm from DPF face for (a) continuously regenerated DPF containing 33 g/l ash, (b) a periodically regenerated DPF containing 42 g/l ash, and 133 mm from DPF face for (c) DPF containing 33 g/l ash, (d) DPF containing 42 g/l ash undergoing continuous and periodic regeneration, respectively.

Despite lower levels of ash in the filter, the ash layer formed along the walls of the filter experiencing continuous regeneration appears thicker than the ash layer found along the walls of the periodically regenerated DPF. Furthermore, both filters exhibited considerable ash plug formation near the end of the filter channels, and the ash accumulated in the center of the plugs appeared less densely packed than the ash near the channel walls. Some ash bridging may also be seen in Figure 10.3 (a) for the continuously regenerated DPF. The following sections describe the measurements which serve to quantify the observed differences in ash distribution.

10.2.1 Ash Layer Thickness and End-Plug Formation: Continuous Regeneration

The ash layer distribution profiles are shown in Figure 10.4 for three different radial locations in the continuously regenerated DPF. Average ash layer thicknesses for this filter were measured between 0.25 mm and 0.30 mm near the centerline of the DPF. Ash layers near the DPF centerline were slightly thicker than the ash layers along the channels near the DPF periphery. As substantial ash plug was also formed in these filters, and the plug length is shown in Figure 10.4 as well. The horizontal axis in the figure corresponds to the actual filter length.

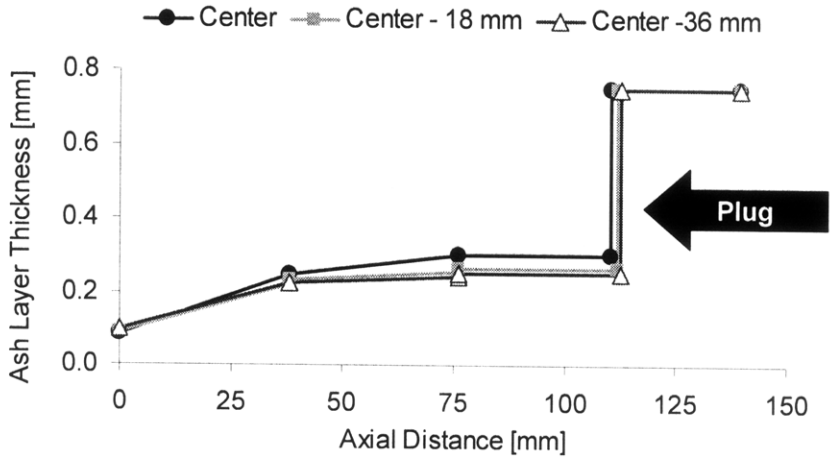

Figure 10.4. Ash layer thickness profiles for a DPF containing 33 g/l ash generated in the laboratory using CJ-4 oil and continuous regeneration.

Figure 10.5 presents the channel open area profiles for the same DPF undergoing continuous regeneration. Channel open area was computed from the measured ash distribution. Due to the relatively large amount of ash accumulated on the channel walls, the channel open area ranged from 80% at the front face of the filter to slightly less than 40% near the middle and back of the channels. Reduction in channel open area below 50% can have a considerable effect on the pressure drop for the exhaust gas flows along the DPF inlet channels.

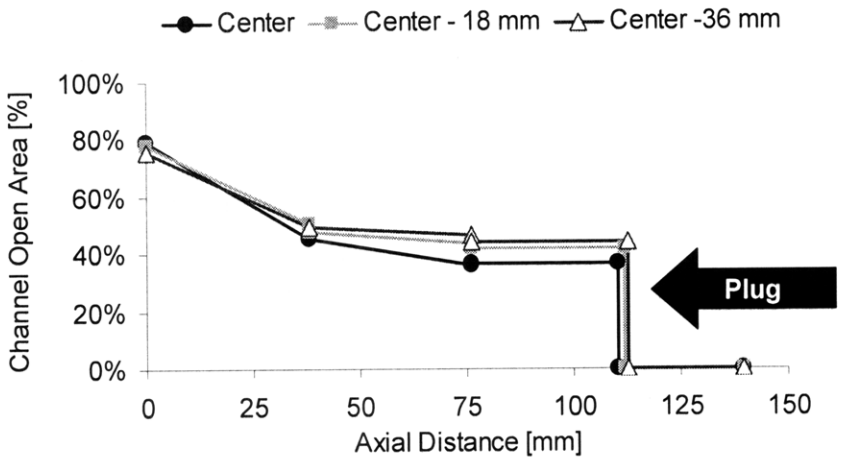

Figure 10.5. Channel open area profiles for a DPF containing 33 g/l ash generated in the laboratory using CJ-4 oil and continuous regeneration.

The ash distribution profiles within the filter channels are shown in Figure 10.6. Due to a lack of measurement resolution in the axial direction, the exact shape of the layer thickness profiles near the DPF inlet and at the start of the ash end-plugs is not well-defined. Despite the lack of axial measurement resolution, a substantial amount of ash was measured immediately at the DPF inlet face.

Similar to the radial variation in ash layer thickness, slightly more material was deposited in the ash plugs formed near the DPF centerline than in the ash plugs found at the filter periphery. Slight differences in ash plug radial distribution have also been reported and in the literature and attributed to exhaust gas flow non-uniformities in the DPF. The flow non-uniformities may be due to the DPF inlet cone design which can result in a greater proportion of the exhaust flowing through the center of the filter.

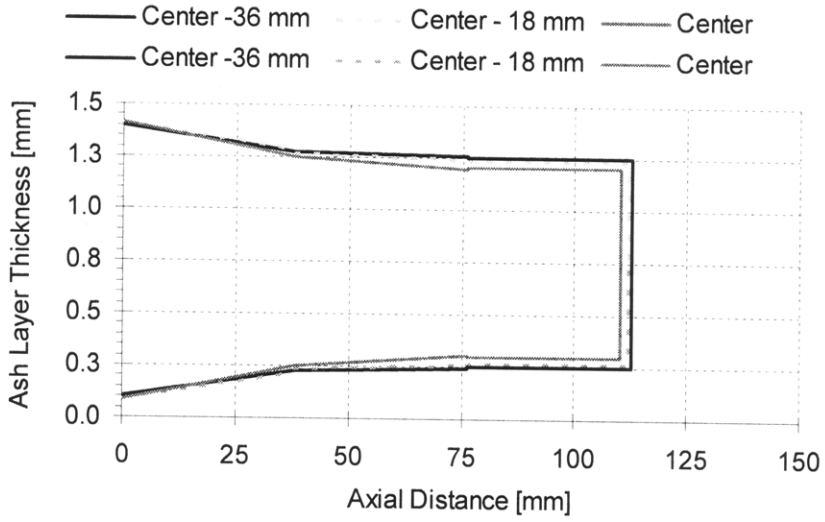

Figure 10.6. Single channel ash distribution profiles for a DPF containing 33 g/l ash generated in the laboratory using CJ-4 oil and continuous regeneration.

10.2.2 Ash Packing Density and Porosity

Ash packing density was determined directly from the measurements of ash distribution (layer thickness and plug formation) in the DPF channels, along with the known ash weight. Figure 10.7 shows the ash packing density profiles for ash samples taken from the continuously regenerated DPF.

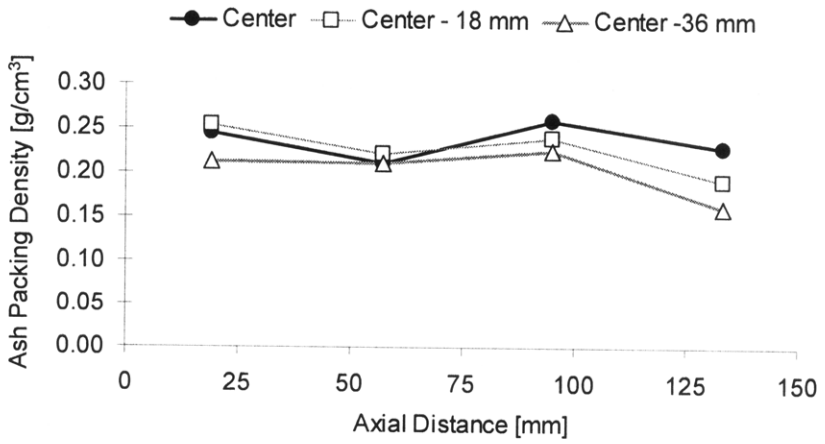

Figure 10.7. Ash packing density profiles for a DPF containing 33 g/l ash generated in the laboratory using CJ-4 oil and continuous regeneration.

Little ash packing density variation in the axial direction was measured for the ash accumulated in a layer along the channel walls. However, a slight decrease in average packing density is observed for the ash accumulated in the plugs near the back of the DPF. Once again, the packing density measurements for the ash samples 57 mm and 133 mm from the front face of the DPF are believed to be most representative of the ash packing density variations between ash deposited in the wall layer and ash accumulated in the end-plugs. A detailed discussion of these differences was presented in Chapter 8.

Figure 10.8 depicts the measured ash packing density variation within the ash plugs. The figure clearly shows that ash deposited near the center of the plug is packed less densely than the ash accumulated in the plug near the filter walls. These measurements are consistent with the images of the ash plugs shown in Figure 10.3 (c) and (d). The density gradients within the ash plug appeared most pronounced for ash accumulated near the DPF periphery, farthest from the filter's centerline.

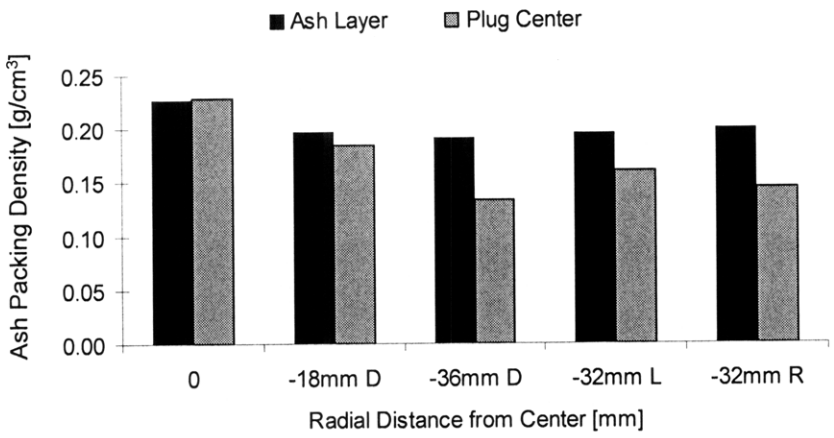

Figure 10.8. Comparison of radial packing density variation within ash end-plugs for a DPF containing 33 g/l ash from a CJ-4 oil undergoing continuous regeneration.

Measurements from post-mortem analysis of the periodically regenerated filters also showed similar variation in ash packing density within the ash plugs. The ash plug packing density variation in the periodically regenerated filters was shown in Figure 8.17. Additional measurements were carried out to better understand the mechanisms responsible for these observed density gradients.

10.2.3 Ash End-Plug Formation

In order to better understand the mechanisms governing ash transport in the DPF and end-plug formation, additional measurements of the continuously regenerated DPF filter samples were carried out. The filter sections containing the ash end-plugs were tapped until no more ash could be removed from the samples. In this manner, the less densely packed ash in the center of the end-plugs was easily removed. Ash deposited in the DPF end-plug but along the channel walls could not be removed by tapping, and remained in the DPF. Following the tapping procedure, the DPF samples were once again imaged, and the thickness of the remaining ash layer measured. Figure 10.9 shows the ash layer thickness profiles over the length of the DPF with the ash removed from the center of the channel end-plugs.

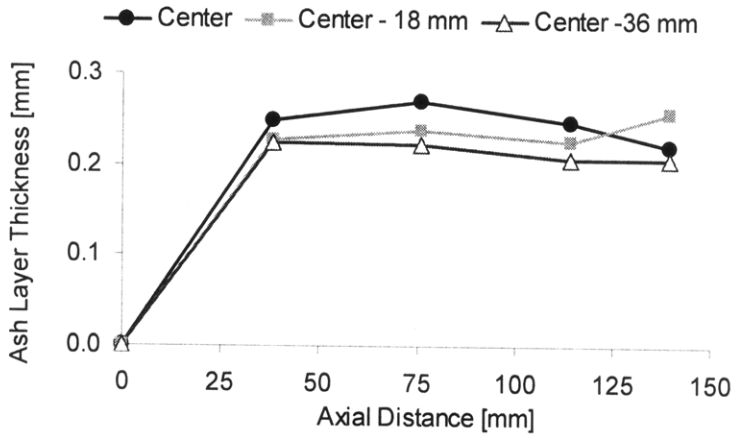

Figure 10.9. Ash wall-layer thickness variation for a DPF containing 33 g/l ash from a CJ-4 oil undergoing continuous regeneration.

Figure 10.9 shows the ash layer thickness is nearly uniform along the length of the DPF. Even the ash layer previously covered by the end-plug exhibits almost the same thickness as the ash deposited along the rest of the channel walls. These measurements were further used to compute the channel open area profiles with the ash removed from the center of the end-plugs as well. The channel open area profiles are shown in Figure 10.10, and appear fairly uniform along the filter length.

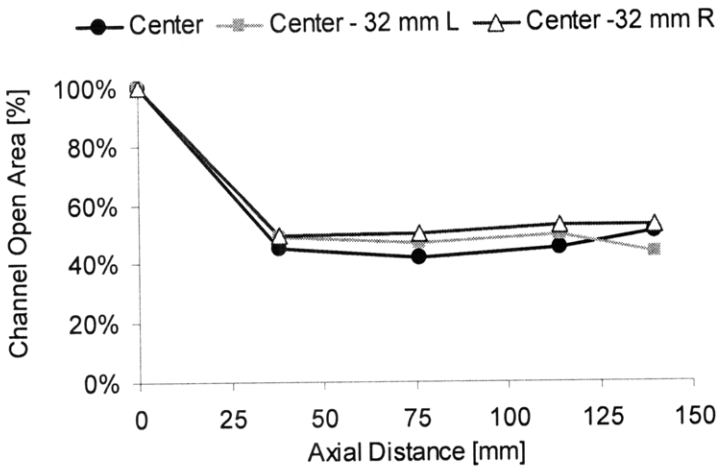

Figure 10.10. Ash wall-layer open area variation for a DPF containing 33 g/l ash from a CJ-4 oil undergoing continuous regeneration.

A direct comparison between the tapped and un-tapped filter samples is shown in Figure 10.11. Tapping the sample removes the ash deposited in the center of the end-plugs, whereas the more densely packed material along the channel walls remains. The area of overlap between the region of the DPF occupied by the end-plug, and the wall layer thickness remaining after the center of the end-plug was removed is clearly visible in the figure.

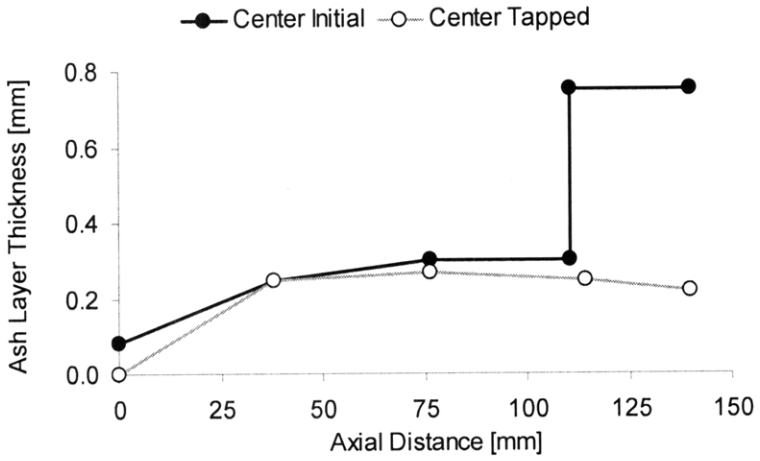

Figure 10.11. Comparison of ash layer thickness profiles for a DPF containing 33 g/l ash from a CJ-4 oil undergoing continuous regeneration before and after ash end-plug removal.

The measurements presented above provide further evidence to indicate the ash wall layer thickness is initially fairly uniform along the length of the DPF channels. As noted in Chapter 8, the results of the post mortem analysis for the DPF containing 12.5 g/l of ash suggest the ash initially accumulates in the DPF pores and in a layer along the channel walls. Only after the ash cake layer reaches sufficient thickness, is material removed from the layer and transported to the back of the DPF, forming the end-plug. Further evidence showing elevated ash packing densities for ash accumulated along the channel walls relative to the ash accumulated in the end-plug supports the proposed ash transport theory. Figure 10.12 presents several images and a schematic depicting the various stages of ash accumulation in the DPF.

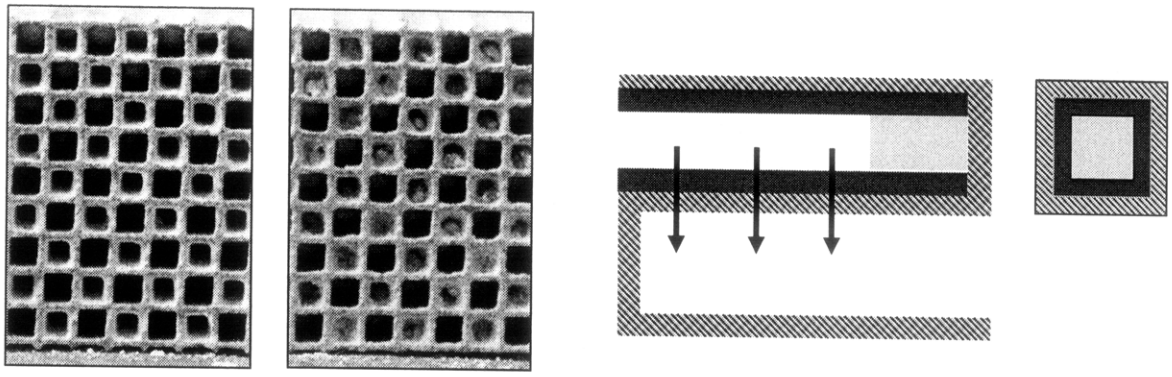

Figure 10.12. DPF images and schematic illustrating ash end-plug formation and resulting ash packing density gradients.

The images in Figure 10.12 show the evolution of ash build-up in the DPF channels. Initial ash deposition along the channel walls, followed by ash accumulation in the center of the channels near the back of the filter, is clearly visible. The ash deposited along the channel walls is subjected to the exhaust gas flows which may significantly affect the morphology of the ash structures. Ash transport from the channel walls to the back of the DPF is believed to be a function of the ash deposit critical shear stress. As more ash is deposited along the channel walls and the cake layer thickness grows, the channel velocities increase as well, thus increasing the shear stress imposed on the ash layer. Upon reaching some critical ash layer thickness, a steady-state equilibrium is reached between the ash deposited along the walls, and the ash removed from the walls, re-entrained in the flow, and deposited in the plugs at the back of the filter. This gives rise

to the constant ash layer thickness observed in the post-mortem analysis. Furthermore, the low exhaust gas velocities near the back of the filter in the region of the ash plug result in a reduction in ash packing density in this region. The difference in packing densities for ash accumulated in the center of the end-plug, and in the plug but closer to the channel walls was noted in Figures 8.17 and 10.8.

10.2.4 Exhaust Conditions and Effects on Ash Properties and Distribution

A direct comparison of the ash distribution profiles between DPFs regenerated continuously and periodically is shown in Figure 10.13. Despite a lower total ash level, the DPF subjected to the high temperature continuous regeneration exhibited a significantly thicker layer of ash along the channel walls, as compared to the periodically regenerated filter. These measurements are consisted with those reported in the literature and the images shown in Figure 2.5.

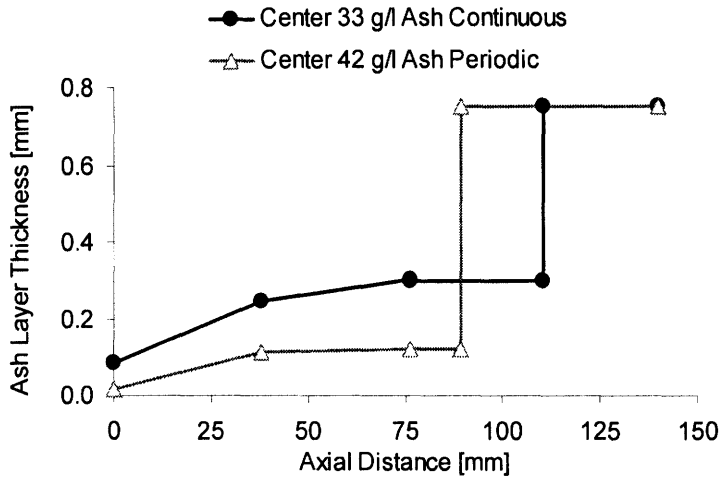

Figure 10.13. Comparison of ash layer thickness profiles along the filter centerline for DPFs containing 33 g/l ash (continuous regeneration) and 42 g/l ash (periodic regeneration) both using CJ-4 oil.

The thicker ash cake layer along the channel walls leads to a significant increase in flow resistance for the exhaust gasses passing through the ash layer. In addition to increasing the flow resistance through the ash layer, the channel open area is also considerably reduced in the case of the continuously regenerated filter. Figure 10.14 presents a direct

comparison between the channel open area profiles for the continuously and periodically regenerated DPFs. The reduction in channel area also contributes to a further increase in pressure drop with the continuously regenerated DPF.

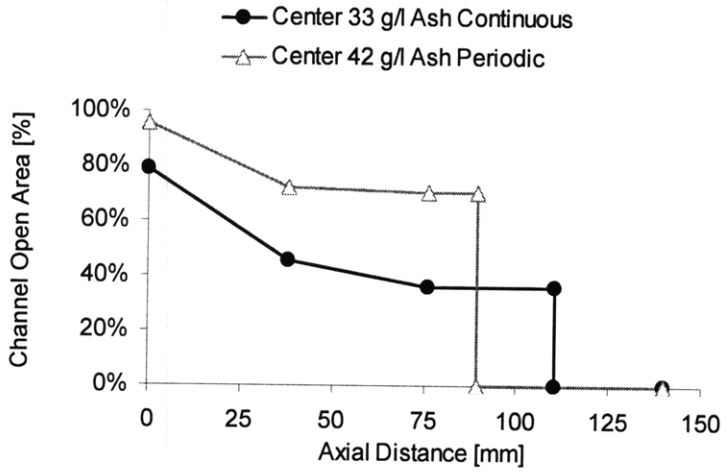

Figure 10.14. Comparison of channel open area profiles along filter centerline for DPFs containing 33 g/l ash (continuous regeneration) and 42 g/l ash (periodic regeneration) both using CJ-4 oil.

Figure 10.15 shows the variation in ash packing density for ash accumulated in a layer along the channel walls (57 mm from the DPF inlet) and accumulated in a plug toward the end of the DPF (133 mm from the DFP inlet) for the periodically and continuously regenerated cases.

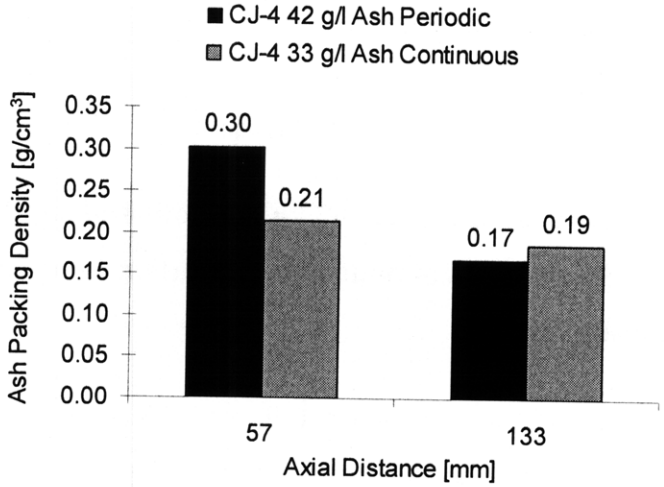

Figure 10.15. Comparison of axial ash packing density variation for ash generated via periodic and continuous regeneration.

Ash accumulated along the DPF channel walls in both filters exhibited an increase in packing density compared to the ash deposited in the channel end-plugs. This difference was much less pronounced in the continuously regenerated filter. Interestingly, despite a large difference in ash wall-layer packing densities, the packing density for the ash accumulated in the channel end-plugs was quite similar for both cases.

Based on the measured ash packing density and distribution profiles, it appears that ash generated under high temperature conditions (continuous regeneration) is less densely packed along the channel walls than ash accumulated under lower temperature conditions. The reduced ash packing density causes the ash to occupy more space in the DPF channels, for a given ash mass, and therefore leads to the increase in measured ash thickness with the continuously regenerated DPF. Furthermore, the sustained high temperatures of the continuous regeneration test cycle, may result in "sticky" ash particles more apt to sinter or fuse together, thereby making removal and transport from the wall layer to the plugs in the back of the DPF less likely. The effect of elevated ash "stickiness" increases the critical shear stress of the ash deposits, thereby allowing for the build-up of thicker ash layers before significant amounts of ash are removed from the layer and transported to the back of the DPF to form the ash end-plugs.

In addition to the direct temperature effect on ash morphology, the different regeneration strategies may also play an important role in controlling the ash deposition and formation processes. During periodic regeneration, ash particles and precursors are deposited and well mixed in the soot cake layer which accumulates along the DPF walls. During DPF regeneration, the soot is oxidized and the ash particles begin to fuse together and agglomerate, leaving the ash structures with large void spaces behind.

Given the low concentration of ash in the soot layer, 0.5% to 1.0% of the soot deposits, the ash particles and structures that remain following DPF regeneration consist primarily of void spaces and are extremely mechanically unstable. The inherent instability of these structures causes them to break down forming an ash layer along the DPF surface. The most densely packed particles remain on the filter surface or existing ash layer, whereas

the loosely held particles are more easily removed and re-entrained in the flow. In this manner periodically regenerated DPFs may be expected to accumulate a densely packed ash layer along the walls, and a large fraction of less densely packed material in the channel end-plugs.

On the other hand, during continuous regeneration conditions, the soot is rapidly oxidized upon entering the DPF and no appreciable soot layer forms in the filter. In this manner only ash is deposited along the filter walls in sufficient amounts. As the ash particles are directly deposited on top of one another, with no significant amount of soot separating the particles, the resulting ash deposits are more mechanically stable than ash deposits formed during periodic filter regeneration. Further, the elevated temperatures in the DPF during continuous regeneration are more conducive to ash particle agglomeration, causing the particles to bond more strongly with the substrate and the surrounding ash. These processes may result in the thicker ash layers observed along the channel walls and less ash accumulated in the end-plugs at the back of the filter.

10.2.5 Ash Composition

The composition of the ash generated from the CJ-4 oil and accumulated in the DPF following continuous regeneration was also analyzed using x-ray diffraction. The spectrum corresponding to the ash composition is shown in Figures 10.16. Similar to the ash composition for the CJ-4 oil with periodic regeneration shown in Figure 8.21, the two predominant ash compounds in this sample were calcium sulfate and zinc magnesium phosphate. The main peaks corresponding to these compounds are also identified in the spectra.

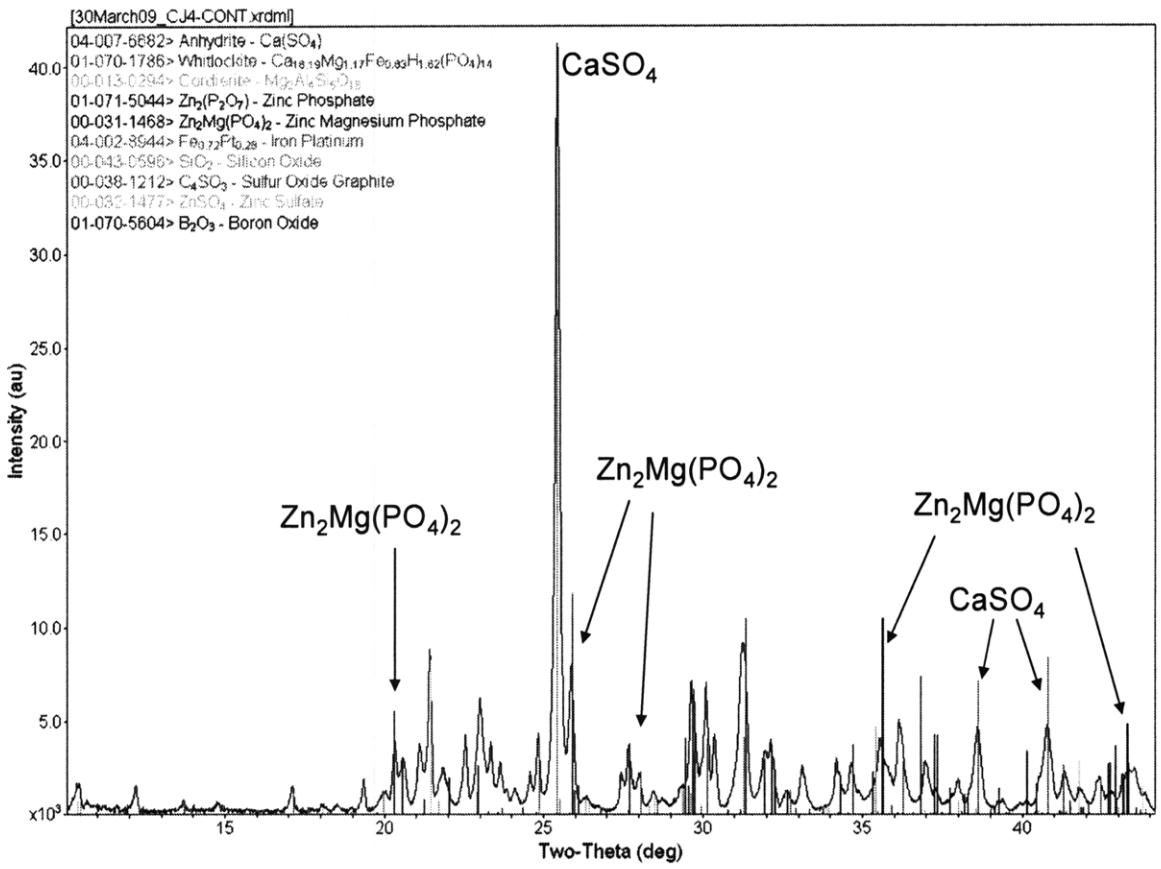

Figure 10.16. Ash compositional analysis via XRD for ash generated from CJ-4 oil and continuous regeneration.

The theoretical density of calcium sulfate, $CaSO_4$, is 2.96 g/cm^3, whereas the theoretical density of zinc magnesium phosphate, $Zn_2Mg(PO_4)_2$ is 3.60 g/cm^3. Assuming an ash composition consisting of calcium sulfate and zinc magnesium phosphate in a ratio of 1:2, respectively, gives a theoretical ash density of approximately 3.4 g/cm^3. Furthermore, the overall ash composition was assumed to be quite similar to the ash generated from the same oil following periodic regenerations, presented in Figure 8.21. The peaks in the spectrum shown in Figure 10.16 are considerably more pronounced than the corresponding peaks in Figure 8.21 due to the extended exposure of the ash to high temperatures during the continuous regeneration tests.

10.3 Measured and Computed Ash Properties

A summary of the measured ash properties from the post-mortem analysis is presented in Table 10.1 below. Based on the measured ash packing density values and ash composition determined via XRD, the ash porosity for the DPF subjected to periodic regeneration was 91.1% and the ash layer generated in the DFP subjected to continuous regeneration was 93.7% porous.

Lubricant	Regeneration	Ash	Ash Layer Thickness	Wall Density	Plug Density	Theoretical Density	Ash Porosity
		[g/l]	[cm]	[g/cm^3]	[g/cm^3]	[g/cm^3]	[%]
CJ-4	Periodic	42.0	0.013	0.30	0.17	3.4	91.1
CJ-4	Continuous	33.0	0.025	0.21	0.19	3.4	93.7

Table 10.1. Summary of measured ash properties for ash generated using CJ-4 oil undergoing continuous and periodic regeneration.

Table 10.2 provides additional parameters related to the changes in DPF geometries computed from the ash distribution measurements and properties listed in Table 10.1 above. The filter containing ash generated via continuous regeneration exhibited almost twice the reduction in channel frontal areas as opposed to the DPF regenerated periodically. Furthermore, the total ash level in the filter subjected to continuous regeneration was significantly lower than the periodically regenerated DPF.

Lubricant	Regeneration	Ash	Channel Filtration Area	Change in Filtration Area	Change in Frontal Area	Change in Length	Ash End Plug Volume Fraction
		[g/l]	[cm^2]	[%]	[%]	[%]	[%]
CJ-4	Periodic	42.0	4.69	-47.9%	-27.0%	-40.5%	76.3%
CJ-4	Continuous	33.0	4.44	-50.7%	-59.9%	-26.7%	37.0%

Table 10.2. Summary of calculated ash effects on filter geometry for ash generated using CJ-4 oil undergoing continuous and periodic regeneration.

10.4 Ash-Distribution Effects on Pressure Drop

The pressure drop trends for the DPFs subjected to periodic and continuous regeneration and loaded with ash using CJ-4 oil are shown in Figure 10.17 as a function of space velocity. The pressure drop characteristics of the clean filters are also provided for comparison. Initially both clean filters exhibited nearly the same pressure drop. Despite the same level of ash loading, the continuously regenerated filter exhibited a larger increase in pressure drop due to ash accumulation.

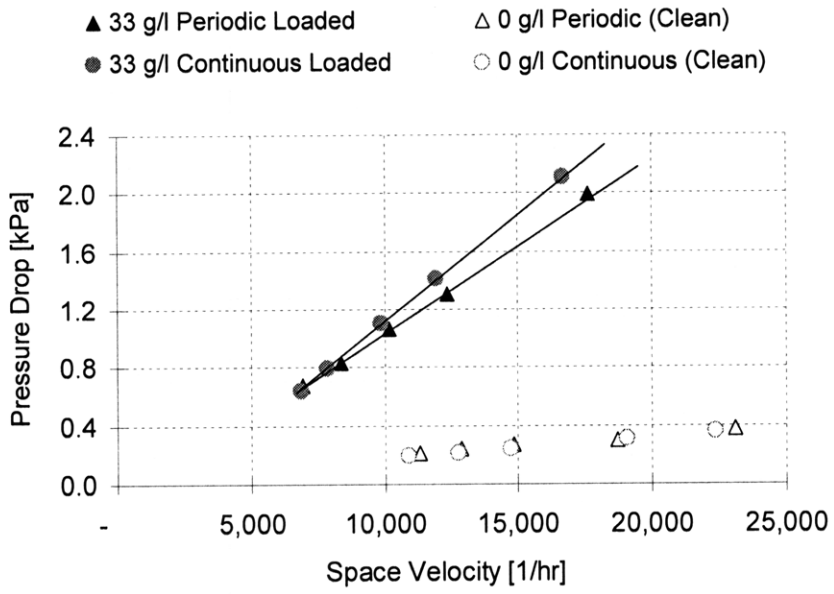

Figure 10.17. Pressure drop as a function of space velocity for clean and ash loaded DPFs subjected to periodic and continuous regeneration.

The ash distribution measurements obtained from the post-mortem filter analysis were used to compute the average filter wall velocity, which is dependent on the exhaust gas flow rate and available filtration area. Figure 10.18 shows the filter pressure drop contribution due to flow through the ash layer and DPF substrate (porous media) as a function of wall velocity for the DPFs containing 33 g/l ash generated via periodic and continuous regeneration.

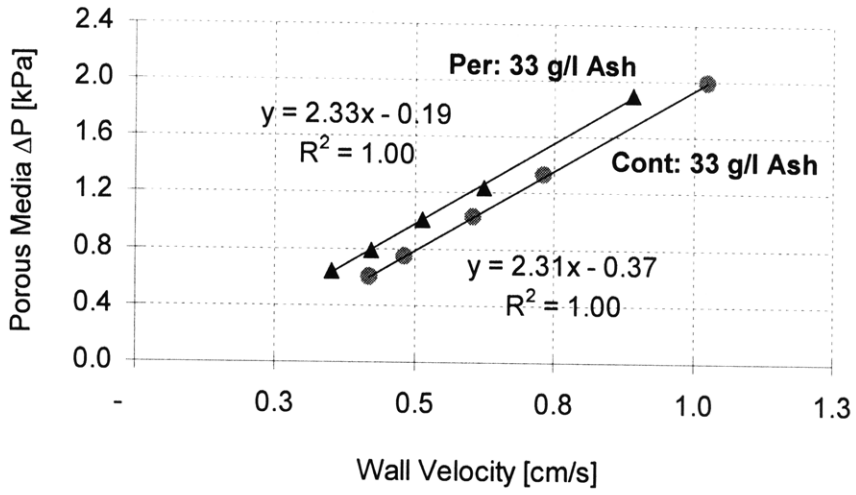

Figure 10.18. Pressure drop through ash layer and DPF substrate as a function of wall velocity for the ash loaded DPFs subjected to periodic and continuous regeneration.

The determination of pressure drop due to the flow through the ash layer and substrate (porous media) was described in Section 8.5. Plotting the porous media pressure drop as a function of wall velocity, therefore, accounts for the changes in DPF channel geometry due to ash accumulation. Further, the slopes of the pressure drop curves in Figure 10.18 are directly proportional to the quantity (w/k). This term is related to the flow resistance of the porous media (layer thickness divided by permeability), as all of the test were carried out on the same filter substrate at the same temperature and gas viscosity using the flow bench with air at ambient conditions.

The slopes shown in Figure 10.18 indicate the flow resistance through the ash layer and DPF substrate for the two filters to be nearly the same. On the other hand, the ash layer thickness measured in the DPF containing ash produced via continuous regeneration was nearly twice as thick as the ash layer generated with periodic regeneration. This large difference in ash layer thickness indicates the ash generated in the continuously regenerated filter to be nearly twice as permeable as the ash generated in the periodically regenerated filter.

For both cases shown in Figure 10.18, the lubricant chemistries were the same (CJ-4 oil), with the only difference being the filter thermal histories. While the post-mortem analysis has shown a significant dependence of the bulk ash distribution (wall layer vs. end-plug) on filter temperature and regenerations strategy, the flow resistance characteristics of the ash, specifically permeability, generated under these varying conditions is also affected. This provided further evidence of the large role exhaust temperatures and DPF thermal history may play in controlling ash properties affecting DPF pressure drop.

10.5 Exhaust Temperature Effects on Ash Properties and Composition

The results presented in the previous sections show a significant effect of exhaust temperature not only on influencing ash distribution and morphology, but also on ash composition. To better understand the effect of exhaust conditions, specifically temperature, on lubricant-derived ash properties and composition, a number of specific, targeted experiments were carried out.

A series of engine tests were performed using full-sized catalyzed and un-catalyzed DPFs mounted in the exhaust system of the Cummins ISB. In order to accommodate the full exhaust flow of the engine, two D7.5" x 12" filters were installed in parallel. The engine tests utilized conventional ultra-low sulfur diesel fuel and a commercial CJ-4 lubricant. The DPFs were subjected to a steady-state soot loading cycle (low speed and load), followed by a high load condition to increase exhaust temperatures for DPF regeneration. Filter regeneration with DPF inlet temperatures in excess of 600 °C was achieved by modifying boost and EGR levels at the high load condition. Figure 10.19 presents the measures SO_2 emissions before and after the DPF during the high temperature regeneration for the catalyzed and un-catalyzed filters.

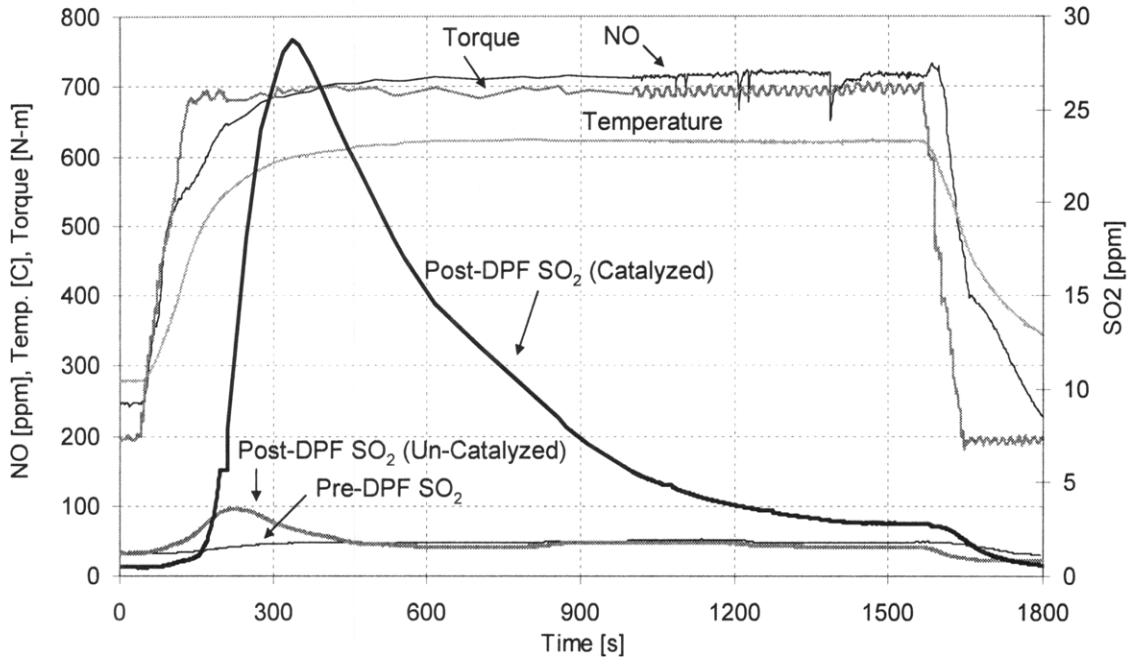

Figure 10.19. DPF desulfation during high temperature regeneration.

Figure 10.19 shows a significant increase in post-DPF SO_2 emissions during the regeneration event. The increase in post-DPF SO_2 emissions was most pronounced with the catalyzed DPF and is attributed to the release of sulfur stored on the platinum catalyst (desulfation). A similar increase in SO_2 emissions was also observed for the un-catalyzed filter, however the amount of SO_2 released was significantly less. The experimental data indicates that sulfates present in the particulate matter as well as in the ash compounds may decompose at high temperatures resulting in the observed increase in SO_2 emissions. Clearly DPF exposure to high temperatures achieved during filter regeneration may alter the composition of sulfate-containing ash compounds.

The pre-DPF SO_2 emissions and NO emissions are also included in Figure 10.19. The SO_2 emissions levels entering the DPF were relatively constant during the regeneration event, indicating that the observed increase in post-DPF SO_2 emissions must be coming from sulfur compounds contained in the filter. While NO emissions can interfere with SO_2 emissions measurements, the NO emissions during the regeneration event were also relatively constant.

As the increase in post-DPF SO_2 emissions during filter regeneration may be attributed to sulfur compounds present in both the particulate matter and ash, additional targeted experiments were conducted to determine the effect of exhaust temperature on sulfate decomposition in the ash alone. In these tests, ash samples from field- and laboratory-aged filters were subjected to TGA with the evolved decomposition products determined by mass spectrometry. The ash in the field-aged filters was accumulated following slightly more than 180,000 miles of on-road use, whereas the ash in the lab-aged filters was generated over an accelerated loading cycle simulating approximately 180,000 miles of on-road use. The results of the analysis are shown in Figure 10.20.

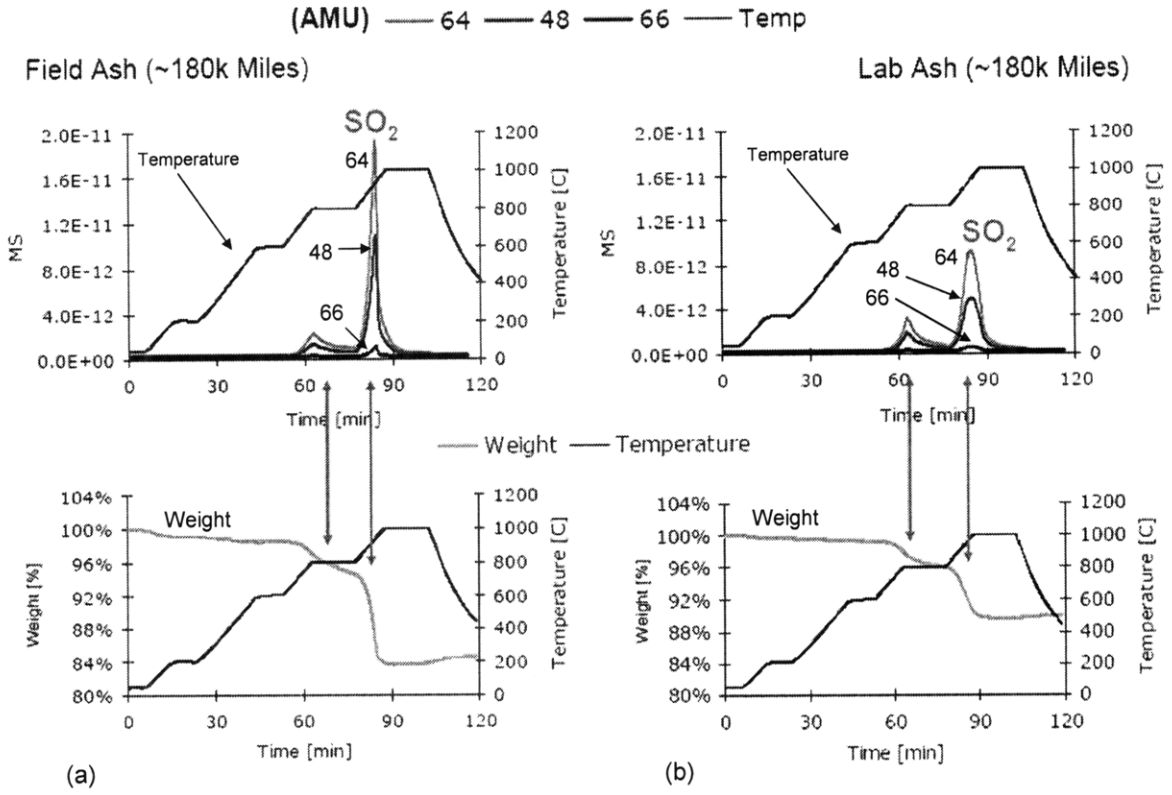

Figure 10.20. Partial ash decomposition at high temperatures observed via TGA-MS for (a) field ash sample and (b) lab ash samples following 180,000 miles of on-road and simulated on-road exposure, respectively.

The TGA analysis of the ash samples showed approximately 20% reduction in ash weight at a temperature of 800 °C. Furthermore, the mass spectrometry analysis showed significant amounts of SO_2 evolved from the samples at this temperature. Two distinct

spikes in SO_2 emissions were observed in the mass spectrometry data presented in Figure 10.20. The first spike in SO_2 emissions occurs between 600 °C and 800 °C, with the second and much larger spike in SO_2 emissions occurring at 800 °C. Furthermore, the large increase SO_2 emissions is directly correlated to the ash weight loss measured via TGA. The results of this analysis clearly show that sulfate compounds present in the ash, primarily calcium sulfates, may decompose at elevated temperatures in the DPF, such as those which may be experienced during high temperature active regenerations.

While the data presented above shows a clear effect of exhaust temperature on ash decomposition, additional investigations focused on understanding how these changes in ash composition may affect ash properties. In these studies, changes in ash weight and volume as a function of temperature were measured using TGA and dilatometry for a representative field ash sample. The results of these measurements were used to compute relative ash density changes over a range of temperatures shown in Figure 10.21. Ash generated in the laboratory shows similar trends.

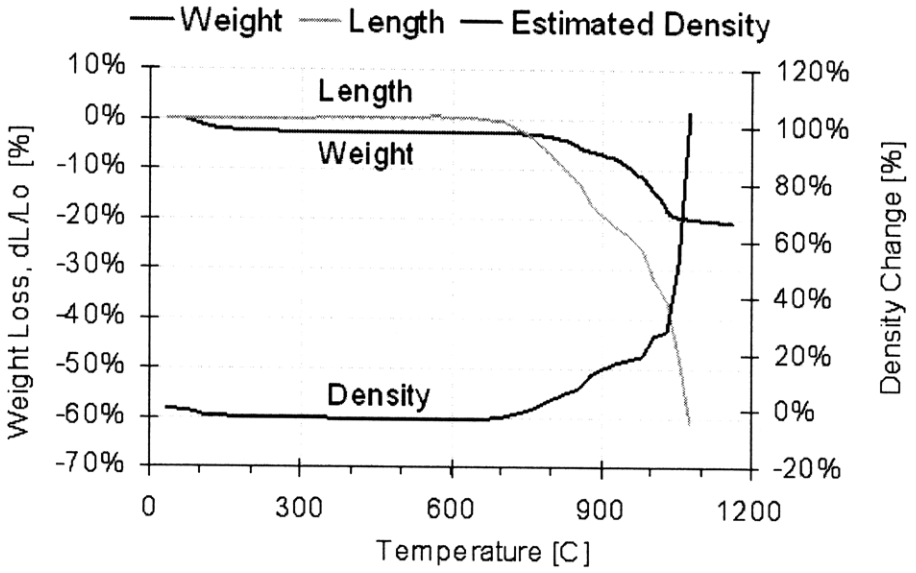

Figure 10.21. Estimated ash density change as a function of temperature computed from measured weight and volume change.

Initially, between 25 °C and 200 °C, 3%-4% weight loss is observed in the ash samples and attributed to moisture content. At elevated temperatures, between 800 °C and 1,150

°C, an additional 18% weight loss is attributed to decomposition of specific ash compounds, as LECO carbon analysis of the ash revealed less than 1% carbon content. Beginning at 750 °C the ash sample begins to shrink, and by 1,100 °C ash shrinkage was measured at over 60%. When DPF internal temperatures exceed 700 °C ash density begins to increase as the ash shrinks, with large density changes at temperatures over 1,000 °C. Temperatures in this range are not uncommon during DPF regeneration and can appreciably affect ash packing density [54].

Figure 10.22 presents images of select ash samples after exposure to elevated temperatures. As evident in the figure, no significant visual changes were observed below 900 °C. At temperatures in excess of 900 °C, ash morphology changes quite rapidly as the particles sinter and fuse together.

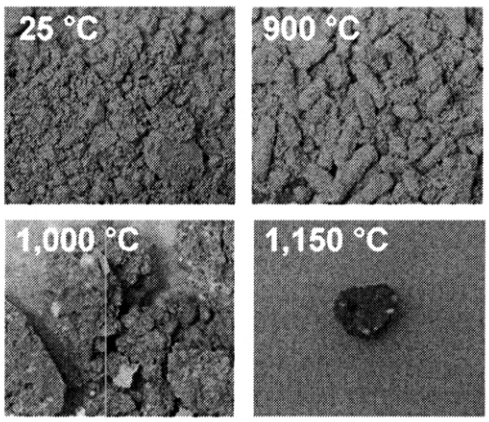

Figure 10.22. Ash samples at various stages of heating from 25 °C to 1,150 °C.

Ash composition at various temperatures was also measured using XRD to better understand the effects of temperature on ash properties. XRD enables the measurement of specific compounds in the ash sample. Figure 10.23 shows only small changes in ash composition below 850 °C. For temperatures above 1,000 °C, many of the Ca, Mg, S, and P compounds undergo phase changes, while the levels of zinc oxide related phases increase significantly. The top spectrum in Figure 10.23 corresponds to the measured sample composition upon cooling back to room temperature. The data presented in

Figure 10.23 are from ash samples obtained from a field-aged DPF which experienced slightly over 180,000 miles of on-road use. The XRD data is consistent with the TGA-mass spectrometry data shown in Figure 10.20, indicating the conversion of metal sulfates to oxides at higher temperatures.

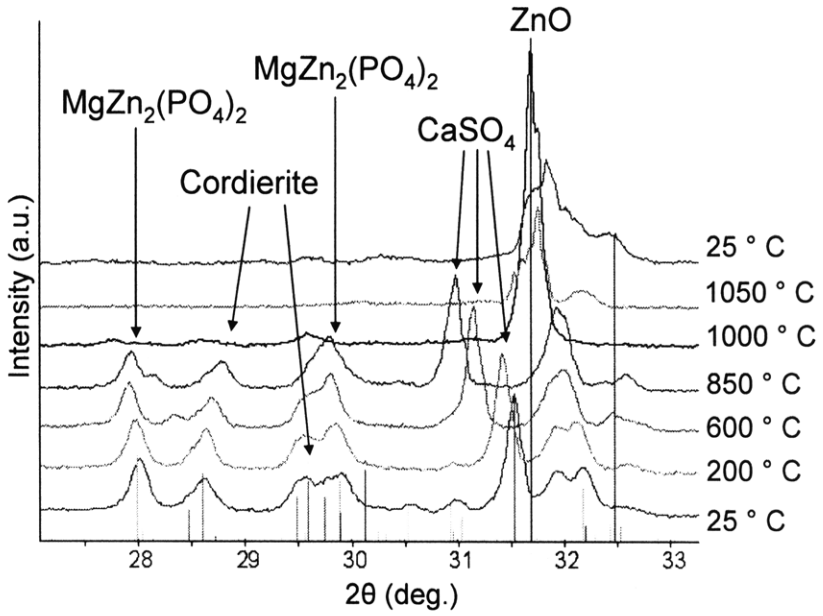

Figure 10.23. Ash compositional changes measured via XRD for field ash samples over a temperature range of 25 °C to 1,050 °C.

Results of the XRD analysis at room temperature for the field generated ash are also listed in Table 10.3. The small amount of cordierite present in the sample was most likely introduced during filter sectioning and sample preparation.

Compound		Field Ash (ACT) [% wt.]
Cordierite	$Mg_2Al_4Si_5O_{18}$	13.0%
Anhydrite, syn	$CaSO_4$	26.3%
Zincite, syn	ZnO	2.8%
Magnesium Zinc Phosphate	$MgZn_2(PO_4)_2$	54.0%
Hexahydrite, syn	$MgSO_4 \cdot 6H_2O$	3.8%

Table 10.3. Ash compounds measured via XRD for a field DPF ash samples.

The results presented in this section show a fairly pronounced effect of exhaust temperature on ash distribution in the filter, ash composition, and packing density. Differences in exhaust temperatures during ash and soot deposition as well as ash agglomerate formation during soot oxidation clearly influence ash properties and the resulting DPF pressure drop performance. It is, therefore, important to consider the DPF thermal history, in addition to lubricant additive chemistry, when evaluating ash effects on DPF pressure drop.

(This page intentionally left blank)

11 DPF ASH PRESSURE DROP MODELS AND THEORY

The ash pressure drop models described in Chapters 3 and 4 were developed in parallel with the experiments. Initially the experimental data was utilized to validate the model output and the results of the DPF post-mortem analysis provided valuable ash properties for the model input. As the models were validated and refined, they were increasingly used to explore specific ash effects and conduct parametric studies. Further, the experimentally validated models provided additional insight into the specific underlying mechanisms controlling the manner in which ash affects DPF performance.

11.1 Model Development and Validation

Initial model calibration was performed using experimental pressure drop and flow data measured for a clean DPF. The DPF geometry used in the model was the same as for the filters utilized in the experiments, D5.66" x 6", 200 cpsi. DPF porosity of 50% was assumed in the model, consistent with data supplied by the manufacturer for this particular filter. The predicted pressure drop (model output) was fit to the experimental data by adjusting the filter permeability. A comparison of predicted and measured pressure drop is shown in Figure 11.1.

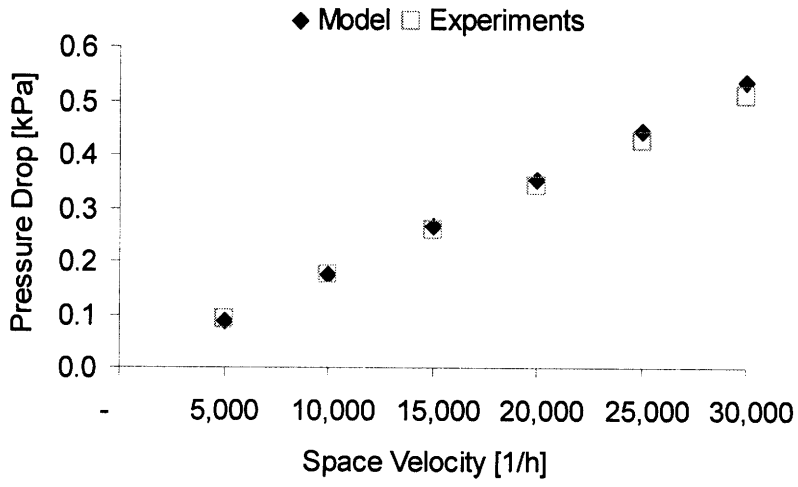

Figure 11.1. Measured and predicted pressure drop behavior for a clean DPF.

The filter permeability determined using the model was $2.2x10^{-13}$ m^2. Clean, uncatalyzed cordierite filters generally exhibit permeabilities around $5x10^{-13}$ m^2, however, as the filters used in this study were coated with a washcoat and catalyst, the permeability is expected to be lower than an uncoated DPF.

A similar procedure was applied to calibrate the model, using experimental pressure drop data for a DPF containing only ash and no soot. The predicted and measured pressure drop values as a function of ash load are shown in Figure 11.2. In this case, the ash layer permeability determined using the model was $2.9x10^{-14}$ m^2. Additional ash input parameters based on measured values from the DPF post-mortem analysis included ash layer packing density of 0.25 g/cm^3, ash plug fraction of 0.5, and ash deep-bed trapped fraction of 0.04.

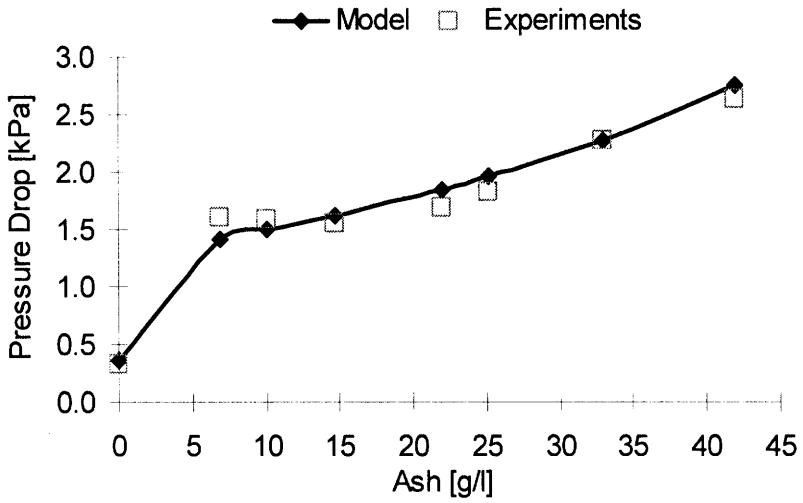

Figure 11.2. Measured and predicted DPF pressure drop as a function of ash load.

Calibration of the model for the case of a DPF containing soot and no ash followed a similar procedure using the experimental pressure drop data. The predicted and measured pressure drop values as a function of soot load are shown in Figure 11.3. In this case, the soot layer permeability determined using the model was $5.0x10^{-15}$ m^2, consistent with values reported in the literature. Additional soot input parameters based on values reported in the literature for similar exhaust flow conditions included soot layer packing density of 0.1 g/cm^3, and soot deep-bed trapped fraction of 0.04. The soot was

assumed to be uniformly distributed along the DPF channels, with no accumulation in channel end-plugs.

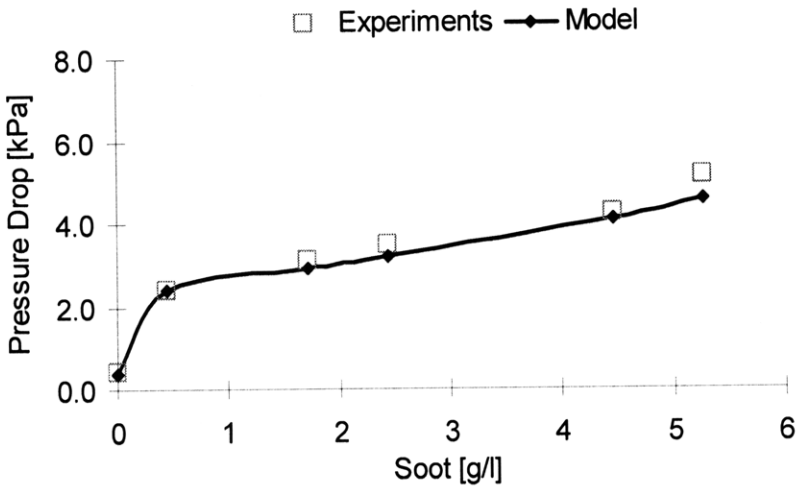

Figure 11.3. Measured and predicted DPF pressure drop as a function of soot load.

Following model calibration with the baseline experimental data, a series of parametric studies were carried out to explore the effect of specific ash properties on DPF pressure drop. Pressure drop for various levels of DPF ash load as a function of ash packing density are shown in Figure 11.4. An increase in ash packing density for a constant value of ash permeability reduces filter pressure drop, as the ash occupies as smaller amount of the channel volume.

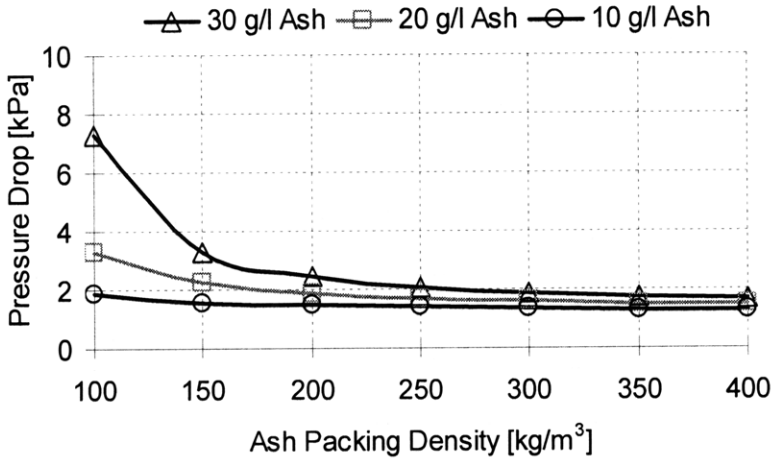

Figure 11.4. Ash packing density effects on total filter pressure drop assuming 50:50 distribution of ash trapped along the channel walls and in the end-plug.

Typical ash packing densities measured as part of the post-mortem analysis in this work, ranged from 0.2 g/cm^3 to 0.3 g/cm^3. The results show a significant increase in pressure drop, as ash packing density is reduced beyond 0.2 g/cm^3. Increasing ash packing density above this level has little effect on pressure drop for constant ash layer permeability. In reality, however, ash packing density is believed to be inversely related to permeability, with an increase in packing density resulting in a decrease in ash layer permeability.

DPF pressure drop trends as a function of ash layer permeability, for constant ash packing density and various levels of DPF ash loads are shown in Figure 11.5. Ash layer permeabilities on the order of $1.0x10^{-14}$ m^2 are reported in the literature, as shown in Table 3.3. Decreasing ash permeability below $1.0x10^{-14}$ m^2 has an appreciable effect on pressure drop, significantly greater than the effect observed in Figure 11.4 for ash packing density variation. Above ash layer permeability values of $1.0x10^{-14}$ m^2, ash permeability has only a small effect on pressure drop. Once again, it is important to note that changes in ash layer density also affect permeability; they are coupled. The following sections describes the specific manner in which these parameters are coupled and the manner in which this variation was accounted for in the models.

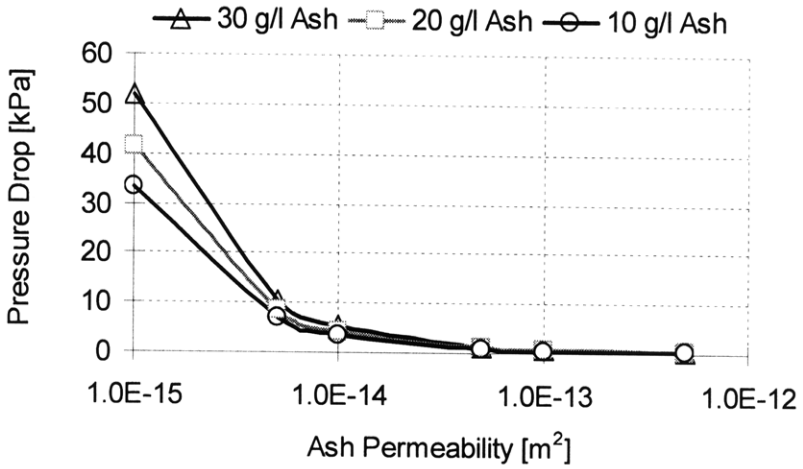

Figure 11.5. Ash permeability effects on total filter pressure drop assuming 50:50 distribution of ash trapped along channel walls and in the channel end-plug.

11.2 Theoretical Estimation of Ash Layer Properties

The permeability and porosity of porous materials is closely coupled. Furthermore, porosity is a direct function of material packing density, which was measured in this study. The two methods commonly cited in the literature for relating permeability and porosity, are the relations proposed by Rumpf and Gupte (Equation 4.7) and Carman-Kozeny (Equation 4.8). These methods relate material porosity and mean pore size to permeability [49]. While the porosity can often be directly measured, mean pore size is much more difficult to estimate. The empirical relationship proposed by Rumpf and Gupte is generally accepted to be valid for material porosities ranging from 30% to 70%, whereas the Carman-Kozeny relationship is applied to cases in which the porosity exceeds 80%. However, this relationship may not hold true for materials exhibiting extremely high porosity. Figure 11.6 shows the relationship between porosity and permeability for both the Rumpf and Gupte and Carman-Kozeny methods. The pore size value used in these calculations was 20 μm, consistent with the average pore diameter of a typical DPF substrate.

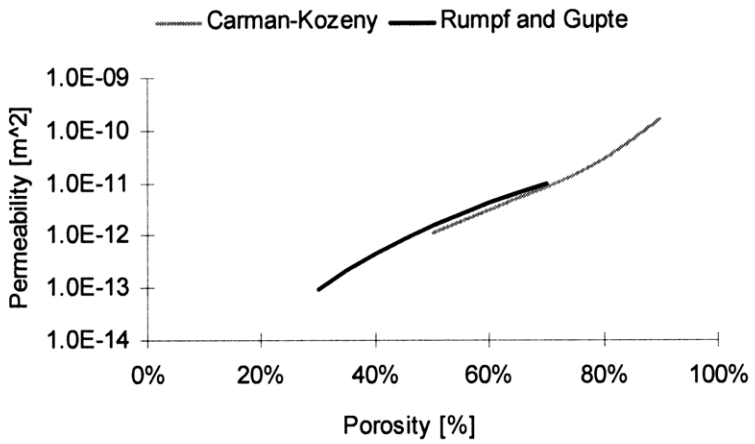

Figure 11.6. Variation of permeability with porosity according to Rumpf and Gupte and Carman-Kozeny for a typical DPF substrate.

Figure 11.7 presents similar results, showing the relationship between permeability and mean pore size predicted by the Rumpf and Gupte and Carman-Kozeny methods. The porosity value used in these calculations was 50%, consistent with the porosity of a typical cordierite DPF.

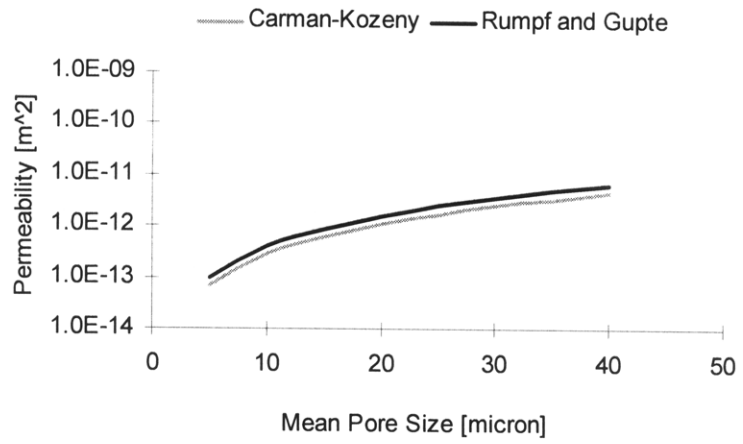

Figure 11.7. Variation of permeability with mean pore size according to Rumpf and Gupte and Carman-Kozeny for a typical DPF substrate.

Based on the high soot layer porosity values reported in the literature, and shown in Figure 3.4, the Carman-Kozeny relationship was used to model soot layer permeability in this study. Figure 11.8 shows soot layer permeability variation as a function of porosity. The mean pore size used in the calculations was 100 nm, consistent with the average diameter of a soot agglomerate. Compared with soot layer permeability values reported in the literature, Figure 3.4, the Carman-Kozeny relationship predicts soot permeability quite well for the range of typical soot porosities. In this model, an average soot layer porosity of 90% was assumed, based on the measured DPF flow conditions.

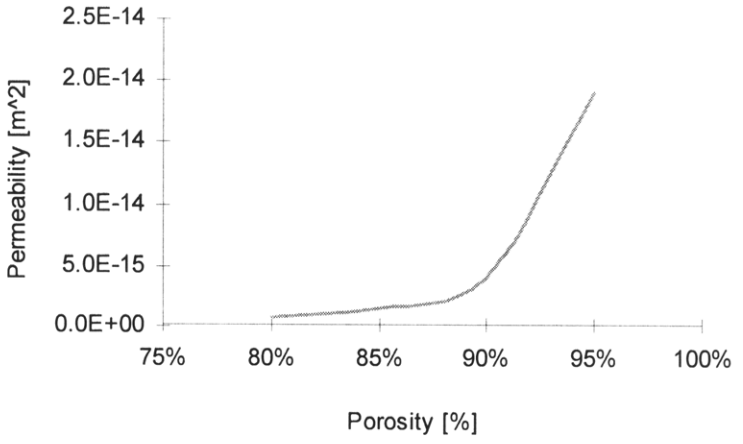

Figure 11.8. Variation of permeability with porosity modeled with Carman-Kozeny relationship for a typical soot layer.

Similarly, the Carman-Kozeny relationship was also used to model ash layer permeability due to the high ash porosity values measured as part of the post-mortem analysis. Figure 11.9 shows ash layer permeability variation as a function of porosity. The mean pore size used in the calculations was 1 μm, consistent with the average diameter of an agglomerated ash particle. Compared with ash layer permeability values reported in the literature, Table 3.4, the Carman-Kozeny relationship appears to slightly under-predict ash permeability, given the pore size assumption listed above. Figure 11.10 shows the variation in predicted ash layer permeability as a function of mean pore size, assuming a porosity of 90%.

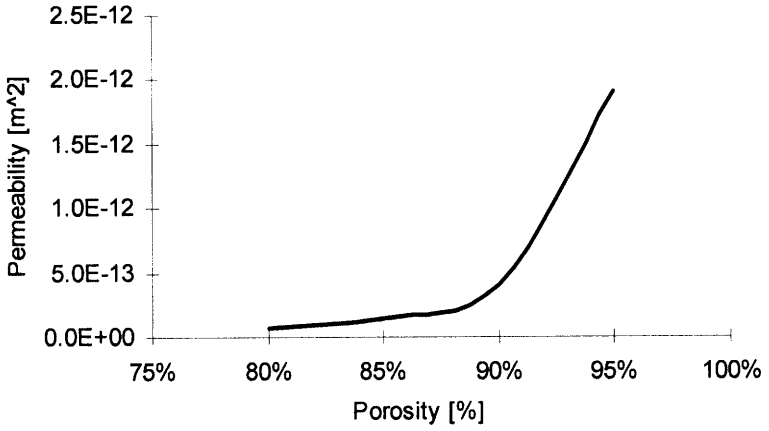

Figure 11.9. Variation of permeability with porosity modeled with Carman-Kozeny relationship for a typical ash layer assuming 1 μm pore size.

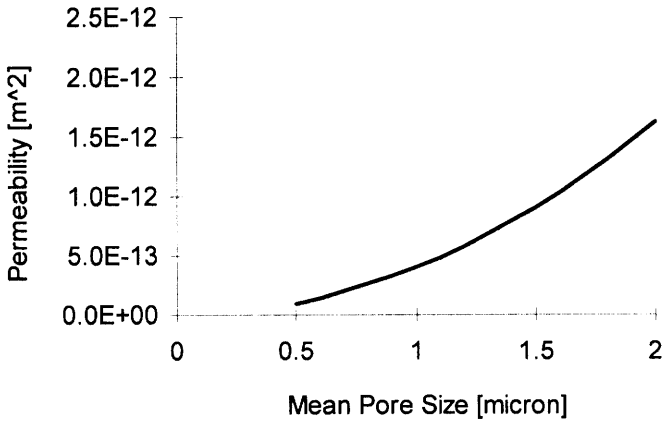

Figure 11.10. Variation of permeability with mean pore size modeled with Carman-Kozeny relationship for a typical ash layer assuming porosity of 90%.

A direct comparison of the predicted ash and soot layer permeabilities is presented in Figure 11.11. Similar to the permeability values presented in the literature, the ash layer is approximately ten times more permeable than the soot layer.

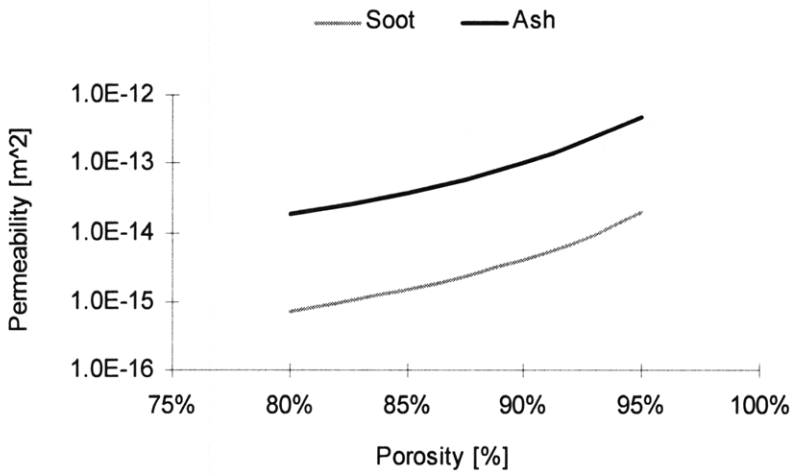

Figure 11.11. Comparison of soot and ash layer permeability as a function of porosity modeled with Carman-Kozeny relationship.

Based on the ash permeability computed using the experimental data and the ash pressure drop model, the Carman-Kozeny relationship was also utilized to predict ash layer mean pore size as a function of ash porosity. The results of these calculations are shown in Figure 11.12, and indicate ash layer pore sizes on the order of typical ash particle sizes reported in the literature.

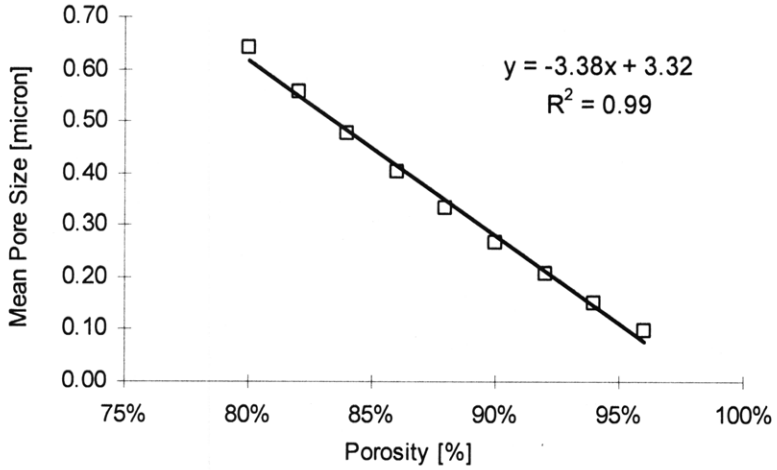

Figure 11.12. Estimation of ash layer pore size as a function of porosity using the Carman-Kozeny relationship.

The Carman-Kozeny relationship was also applied to compute the mean pore sizes for the DPF substrate, soot layer, and ash layer based on measured porosity values for these different materials. The permeability values were computed using the DPF pressure drop model and experimental pressure drop data. The results of the mean pores size calculations and inputs are summarized in Table 11.1.

Material	Packing Density	Permeability	Mean Pore Size	Porosity
	[g/cm^3]	[m^2]	[μm]	[%]
DPF Substrate	--	2.20E-13	8.90	50%
Ash Layer	0.25	2.90E-14	0.21	92%
Soot Layer	0.10	5.00E-15	0.05	95%

Table 11.1. DPF, ash, and soot layer properties determined using DPF performance model and Carman-Kozeny relationship.

In general, cordierite DPFs exhibit a pore size distribution with pore sizes varying from 10 μm to 30 μm. The DPF mean pore size predicted from the Carman-Kozeny relationship is 8.9 μm, slightly less than expected, however the relationship is generally valid for porosities in excess of 80%, whereas typical DPF porosities are around 50%. Furthermore, the mean pores sizes calculated for the ash and soot particle layers were slightly smaller than the typical particle agglomerate sizes.

11.3 Ash Distribution Effects on DPF Pressure Drop

Following model calibration and validation with the experimental data, a series of studies were performed to investigate the effect of ash distribution on pressure drop. The experimental results presented in Chapter 10 show exhaust temperature and regeneration strategy (periodic vs. continuous) can affect the ash distribution within the DPF channels. Periodically regenerated filters typically exhibit more ash deposition towards the back of the channel in end-plugs (up to 75% of the total ash volume in some cases), whereas continuous regeneration showed more ash accumulation in a fairly even layer along the channel walls. Figure 11.13 presents predicted DPF pressure drop for cases in which 100% of the ash is accumulated along the channel walls, 100% of the ash is accumulated

at the back of the channel in the end-plug, and 50% of the ash is accumulated along the walls with the remainder accumulated in the end-plug.

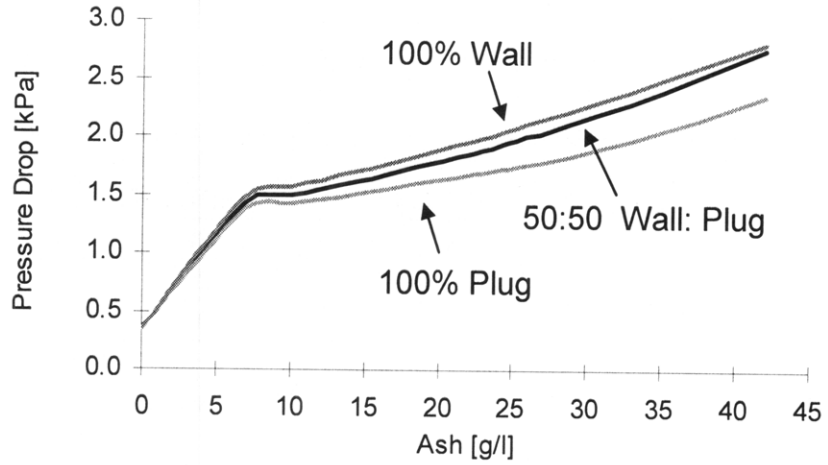

Figure 11.13. Effect of ash distribution on total predicted DPF pressure drop.

The model results presented in Figure 11.13, show some benefit to packing all of the ash at the back of the channel in end-plugs to minimize the total DPF pressure drop due to ash accumulation alone. Interestingly, depositing half of the ash along the channels and the other half of the ash in the end-plug resulted in little overall benefit to reduce filter pressure drop compared to the case in which all of the ash is deposited along the channel walls. This non-linear effect is clearly visible in Figure 11.13. Furthermore, for high levels of DPF ash loading, above 40 g/l, the DPF in which all of the ash is deposited along the channel walls exhibits nearly the same pressure drop as the filter in which only 50% of the ash is deposited along the walls.

In order to explore the effect of ash distribution on ash-related pressure drop in more detail, the contribution of individual parameters (Equation 3.1) to the total DPF pressure drop was explored in more detail, for three different ash distribution scenarios. Figure 11.14 presents the pressure drop due to exhaust flow through the DPF channels as a function of ash load.

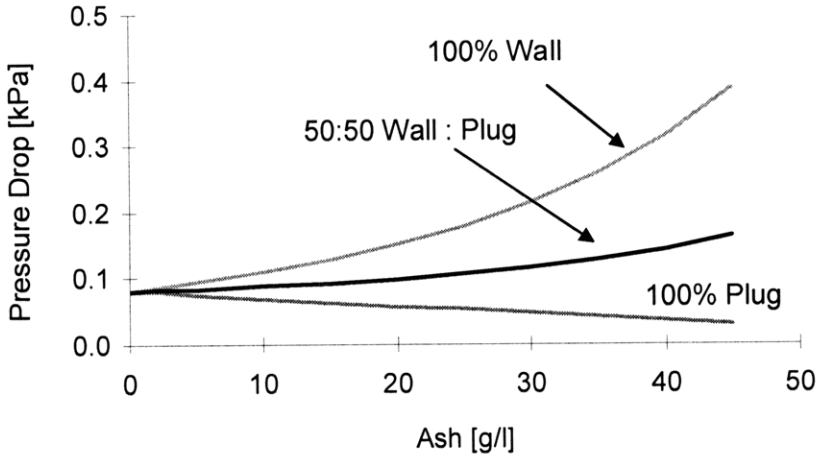

Figure 11.14. Effect of ash distribution on predicted DPF channel pressure drop.

For the case in which all of the ash is accumulated toward the back of the channel in the end-plug, the channel pressure drop decreases as the ash end-plug reduces the overall channel length. On the other hand, for the case in which 100% of the ash is accumulated along the channel walls, the channel pressure drop increases significantly as the channel hydraulic diameter is reduced. A similar, but smaller, increase in pressure drop is observed for the case in which half of the ash is accumulated along the channel walls, with the other half deposited in the end-plug.

The effect of ash distribution on pressure drop through the DPF substrate wall is shown in Figure 11.15. Pressure drop through the wall increases for all of the ash distribution scenarios. When all of the ash is accumulated along the channel walls, the pressure drop through the wall increases only slightly due to the small increase in wall velocity, a result of a reduction in the channel hydraulic diameter and total filtration area. This effect is much more pronounced for the case in which all of the ash is deposited in the channel end-plug. As the channel eng-plug grows, the channel length is reduced, resulting in a significant decrease in filtration area and associated increase in channel wall velocities.

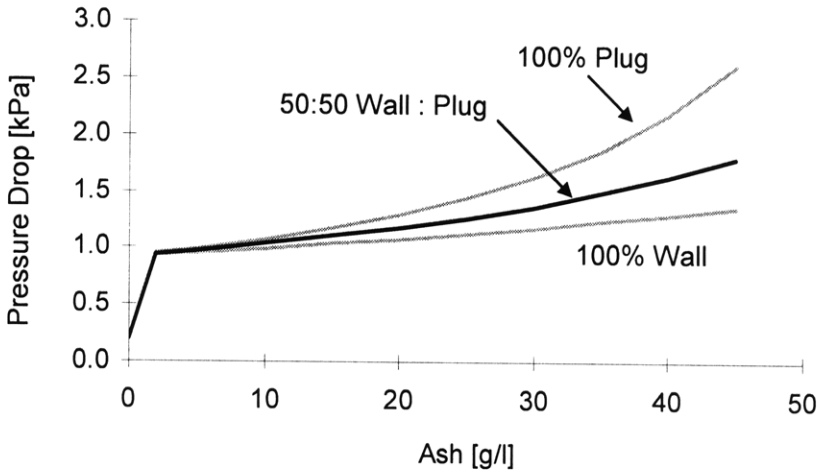

Figure 11.15. Effect of ash distribution on predicted pressure drop through the DPF wall.

For both cases (100% wall deposition and 100% end-plug deposition) the total volume of ash deposited in the filter is the same. However for the case in which all of the ash is distributed along the channel walls, while the filtration area is decreased slightly, exhaust still flows through the entire length of the DPF channel. On the other hand, when all of the ash is deposited in the channel end-plug, the ash plug is impervious to the exhaust flow and significantly reduces the channel length.

Figure 11.16 shows the effect of ash distribution on pressure drop through the ash layer deposited along the channel walls. For the case in which all of the ash is deposited along the wall, pressure drop scales linearly with the amount of ash accumulated in the filter (i.e. ash layer thickness). Conversely, when all of the ash is deposited in the end-plug, an ash layer along the channel walls does not exist. Interestingly, when half of the ash is deposited along the channel walls and the other half of the ash is deposited in the end-plug, the pressure drop through the ash layer is not very different from the case in which all of the ash is deposited along the channel walls. In this case, although the ash layer thickness is reduced, as only half of the ash is accumulated along the channel walls, the wall velocities are increased due to the ash plug, contributing to the relatively large increase in pressure drop through the ash layer. It is this effect, which is believed to

dominate and is responsible for small difference in the total DPF pressure drop observed in Figure 11.13.

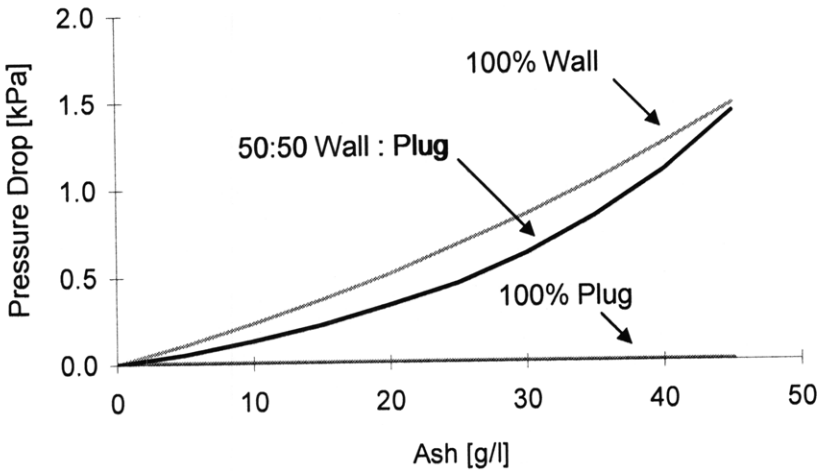

Figure 11.16. Effect of ash distribution on predicted pressure drop through the DPF ash layer.

Lastly, for the sake of completeness, the effect of ash distribution on DPF pressure drop due to channel inlet and outlet losses was investigated as well, and the results are shown in Figure 11.17.

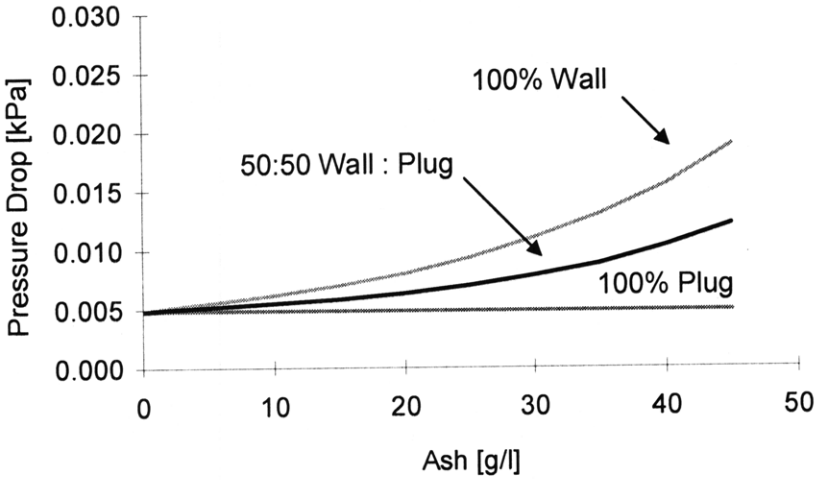

Figure 11.17. Effect of ash distribution on predicted pressure drop due to inlet DPF channel contraction.

The DPF inlet and outlet losses are a small contribution to the total filter pressure drop. When all of the ash is accumulated along the channel walls, the inlet losses increase significantly due to the reduction in channel diameter. On the other hand, no difference in inlet losses is observed when all of the ash is deposited in the channel end-plug, as the channel diameter remains fixed at the initial clean value

The analysis of the individual pressure drop contributions presented above showed the relative distribution of ash in the DPF channels between the wall layer and end-plug significantly affects ash layer thickness and DPF filtration velocities. While depositing more ash toward the back of the channel in the end-plug results in a decrease in ash layer thickness along the filter walls, end-plug growth reduces the effective channel length with an associate increase in wall velocity.

While the analysis of the individual parameters affecting DPF pressure drop aid in understanding the manner in which ash distribution affects total filter pressure drop, it provides little insight into the optimum ash distribution to reduce filter pressure drop. A series of parametric studies was conducted to investigate the effects of varying ash distribution (end-plug vs. wall layer) on the total filter pressure drop for varying levels of DPF ash loading. The results of this analysis, for a DPF containing only ash, are shown in Figure 11.18. An ash end-plug fraction of 0 indicates all of the ash is accumulated along the channel walls, and an ash end-plug fraction of 1 indicates all of the ash is accumulated in the end-plug.

For typical DPF ash loading levels, below 40 g/l, the total DPF ash-related pressure drop decreases slightly with increasing ash end-plug fraction. This beneficial effect is most pronounced at high values of the plug fraction, above 70%. For most of the ash distribution profiles measured in this study, the ash plug fraction varied from 0.5 to 0.7. Within this range, and for typical ash loading levels, there is only a marginal effect of ash distribution on filter pressure drop.

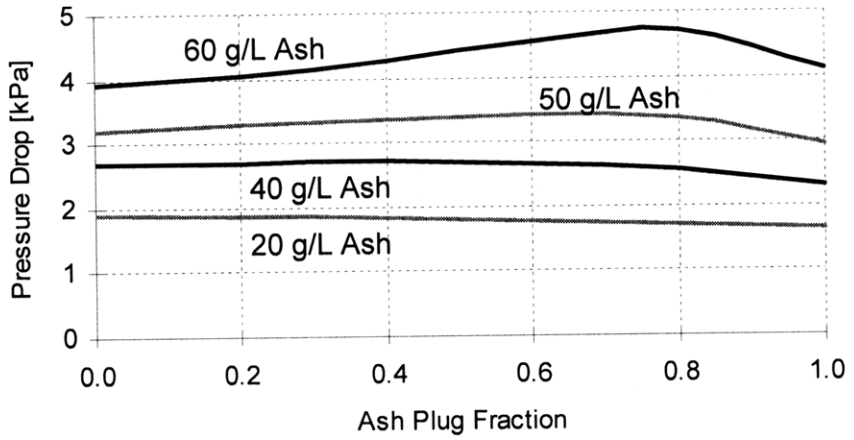

Figure 11.18. Effect of ash distribution on DPF pressure drop.

Interestingly, for high ash levels, 50 g/l to 60 g/l, not generally observed in DPFs in the field, the effect of varying ash distribution on filter pressure drop is not straightforward. Initially as the ash plug fraction is increased from 0 to 0.7 or 0.8, the total DPF pressure drop increases. This is due to the significant ash layer thicknesses at these high ash loading conditions, and the effect of ash end-plug formation on increasing filter wall velocities. In other words, as ash is removed from the walls and re-deposited at the back of the DPF, although the ash layer thickness decreases, the newly-formed end-plug serves to increase filtration velocities as well. It is not until fairly high end-plug fractions are achieved, above 0.8, that pressure drop starts to decrease as the ash layer thickness is significantly reduced. Furthermore, for DPFs containing very high ash loads, around 60 g/l, there is little noticeable difference in pressure drop between the case in which 100% of the ash is deposited along the wall and 100% of the ash is deposited in the end-plug.

Similar studies were repeated to investigate the effect of ash distribution on DPF pressure drop for a DPF containing both soot and ash. A soot level of 6 g/l was used in the calculations, as 6 g/l is near the maximum level of soot loading in cordierite DPFs, before the filters are regenerated. Figure 11.19 presents the predicted filter pressure drop as a function of ash distribution for three different DPF ash levels.

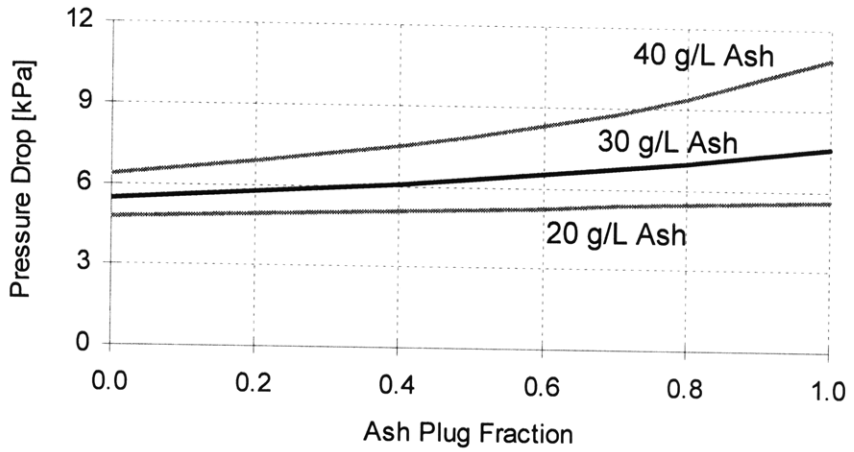

Figure 11.19. Effect of ash distribution on DPF pressure drop with 6 g/l soot load.

For all of the cases presented in Figure 11.19, increasing ash end-plug fraction results in an increase in the total filter pressure drop for a DPF containing ash and 6 g/l soot. Ash deposition along the channel was observed to prevent soot depth filtration. As the amount of ash deposited in the end-plug increases, the effective channel length is reduced, resulting in an increase in DPF wall velocities. For DPFs containing both soot and ash, the low packing density of the soot results in a much thicker soot layer compared to the same amount of ash. Furthermore, the lower permeability of the soot, approximately an order of magnitude less permeable than the ash, results in a significant increase in pressure drop as the DPF wall velocities increase with increasing ash plug fraction. Based on the results of this analysis, preferentially depositing ash in plugs at the end of the channels results in a slight reduction in pressure drop compared to depositing the ash along the channel walls, when only ash accumulation in the DPF is considered. However, this effect is reversed for DPFs containing both soot and ash, where preferentially depositing all of the ash in an even layer along the channel walls results in the lowest total filter pressure drop.

11.4 Lubricant Chemistry Effects on Ash Properties

In addition to applying the DPF ash models to investigate the effects of ash distribution on filter pressure drop, the same models were applied to evaluate the effect of varying

lubricant chemistry and ash properties on pressure drop as well. Figures 11.20 and 11.21 present the measured and predicted DPF pressure drop curves for ash generated from a lubricant containing only ZDDP and another lubricant containing only calcium detergent.

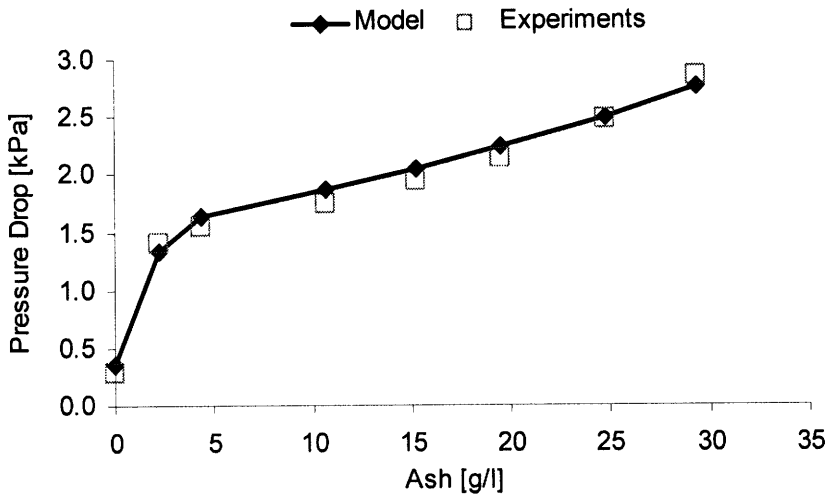

Figure 11.20. Measured and predicted filter pressure drop for a DPF containing ash generated from a lubricant containing only a calcium detergent.

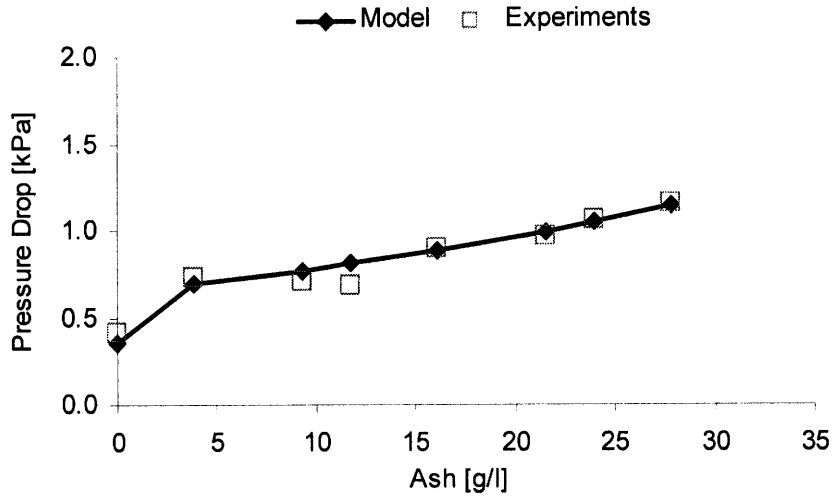

Figure 11.21. Measured and predicted filter pressure drop for a DPF containing ash generated from a lubricant containing only ZDDP.

Using measured values for the ash porosity, packing density, and distribution from the post-mortem analysis, the ash pressure drop model was applied to compute ash layer permeability for the ash generated from the oils containing only ZDDP and only calcium-

based detergents. The ash layer permeability was determined by fitting the models to the experimental data, using the measured ash properties. The results of these calculations are shown in Table 11.2.

Material	Packing Density	Permeability	Mean Pore Size	Porosity
	[g/cm^3]	[m^2]	[μm]	[%]
DPF Substrate	--	2.20E-13	8.90	50%
CJ-4 Ash	0.25	2.90E-14	0.21	92%
Ca Ash	0.24	2.30E-14	0.18	92%
Zn Ash	0.18	9.00E-14	0.20	95%

Table 11.2. DPF and ash layer properties determined using DPF performance model and Carman-Kozeny relationship.

Based on the model, the permeability of the zinc-based ash was computed to be approximately $9.0x10^{-14}$ m^2 whereas the permeability for the calcium-based ash was estimated at $2.3x10^{-14}$ m^2. The DPF loaded with the zinc-based ash also exhibited the lowest pressure drop for the same level of ash loading when compared with the ash generated from the CJ-4 and calcium-based lubricants. Furthermore, the permeability of the calcium-based ash was quite similar to that of the CJ-4 ash, ash shown in Table 11.2. Permeability values for the clean DPF substrate are also included in Table 11.2 for comparison.

Applying the Carman-Kozeny relationship and using the experimentally measured ash properties and permeability values computed using the pressure drop model, mean pore sizes for the various ash layers were computed as well. The mean pore sizes were nearly the same for all of the ash layers generated using the various lubricants and ranged from 0.18 μm to 0.21 μm, with the calcium-based ash exhibiting the smallest mean pore size. The mean pore sizes computed for all of the ash layers and the clean filter are presented in Table 11.2.

11.5 Ash Influences on DPF Soot Pressure Drop Sensitivity

The experimental results presented in Chapters 8 an 9 show a significant effect of ash loading on the DPF pressure drop sensitivity to additional soot accumulation. For low soot loads, below 0.4 g/l, ash was observed to decrease the pressure drop sensitivity, whereas for soot loads above 3 g/l, the presence of ash in the filter increased the pressure drop sensitivity quite significantly. It was further shown that this effect could be partially accounted for through the reduction in available filtration volume, as a result of ash accumulation in the filter. Ash deposited along the channel walls and in the channel end-plug effectively reduces the size of the filter, displaces the soot, and results in higher local soot loadings toward the front of the filter. The specific soot loading (soot mass per filter volume) data presented in this section has been adjusted to account for the reduction in filter volume due to ash accumulation.

However, even when the reduction in filter volume due to ash accumulation was accounted for, this effect alone could not fully explain the observed changes in pressure drop sensitivity. The ash pressure drop models were applied to better understand the underlying processes responsible for controlling filter pressure drop sensitivity due to ash accumulation, not readily transparent from the experiments. The models developed to further explore these effects utilized the following experimentally determined input parameters:

- Ash distribution: 50% along channel walls, 50% in end-plug (by volume)
- Ash packing density: 0.235 g/cm^3
- Ash permeability: 3.0×10^{-14} m^2
- DPF permeability: 2.2×10^{-13} m^2
- Deep-bed trapped fraction: 0.04

The model was initially calibrated assuming a constant soot packing density and permeability. The experimental data used for comparison was for the case of a DPF containing 33 g/l of ash generated using a commercial CJ-4 oil and periodic regeneration. This level of ash accumulation in the DPF was estimated to correspond to slightly more

than 180,000 miles of on-road use. The values of the soot properties assumed constant were: packing density of 0.1 g/cm^3, true density of 2g/cm^3 (carbon), and permeability of $5.0x10^{-15}$ m^2. Figure 11.22 presents a comparison of the measured and predicted DPF pressure drop profiles for a DPF pre-loaded with 33 g/l ash as a function of soot load.

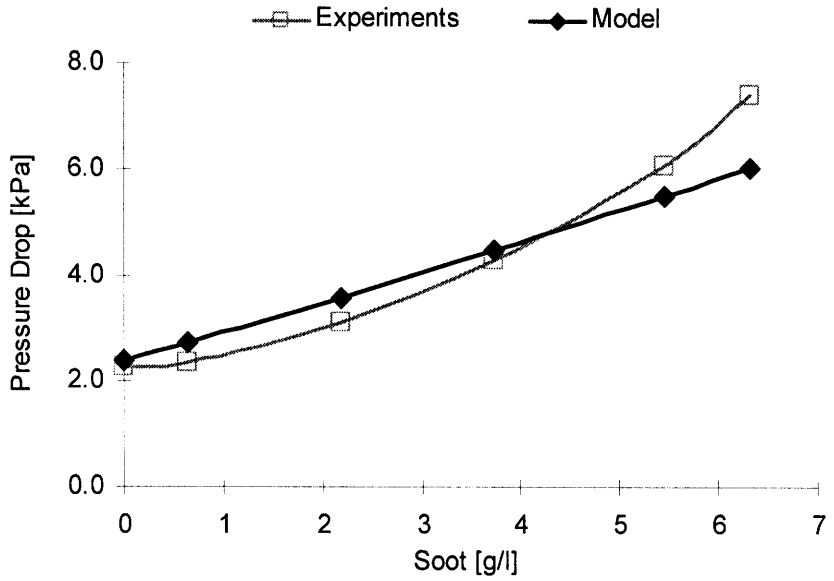

Figure 11.22. Comparison of predicted pressure drop performance with experimental data for a DPF containing 33 g/l ash and 6 g/l soot, assuming constant soot permeability and packing density.

From Figure 11.22, it is clear that the assumption of constant soot packing density and permeability fails to capture the observed changes in DPF pressure drop sensitivity, and results in a linear increase in pressure drop with soot load. The specific soot load values listed on the horizontal axis of Figure 11.22 have been adjusted to account for the reduction in filter volume due to ash accumulation.

The simulations described above were repeated, however in this case, soot permeability was allowed to decrease with increasing soot levels. A comparison of the measured and predicted DPF pressure drop trends is shown in Figure 11.23. By allowing soot permeability to vary with increasing soot load, the predicted pressure drop was able to fit the experimental values almost exactly. These results provide evidence that ash

accumulation in the DPF affects not only the filter geometry and reduces the filter volume, but may also influence the properties of the soot deposited on the ash layer.

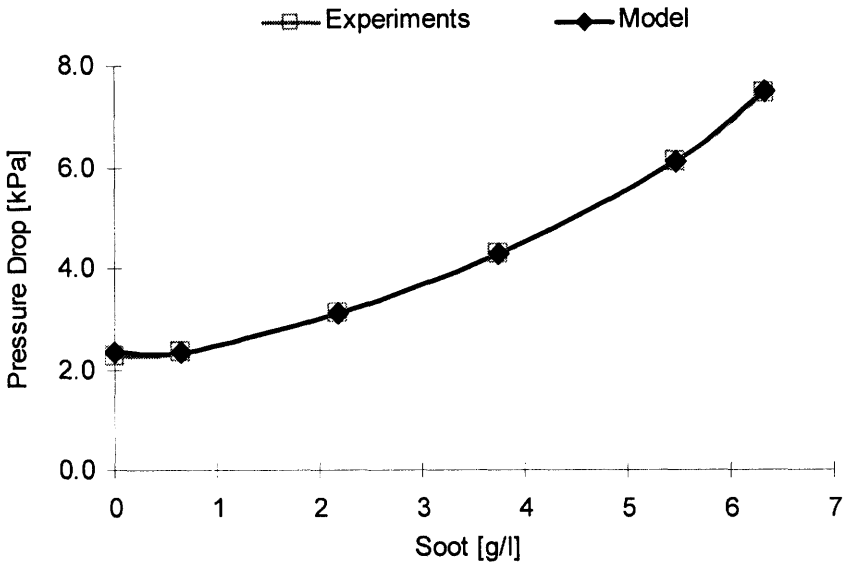

Figure 11.23. Comparison of predicted pressure drop performance with experimental data for a DPF containing 33 g/l ash and 6 g/l soot, assuming decreasing soot packing density.

As ash is deposited in the filter, it reduces the available filter volume. The reduction in filter volume not only increases local soot loading toward the front of the filter, but also increases the filter wall velocities. Soot packing density and permeability are strong functions of the filter wall velocity as shown in Figure 3.5. The results shown in Table 11.3, clearly illustrate the manner in which ash accumulation at 33 g/l affects local soot loads and wall velocities in the DPF, relative to a DPF that contains no ash.

DPF @ 33 g/l Ash			
Nominal Soot Load	**Soot thickness** relative to no-ash DPF	**Wall velocity** relative to clean no-ash DPF	Actual local soot load
2 g/l	+27%	+40%	2.7 g/l
6 g/l	+31%	+46%	8.0 g/l

Table 11.3. Ash effect on local soot load and DPF wall velocities.

Figure 11.24 presents additional experimental data from a 2006 study by Koltsakis et al. showing the effects of filtration velocity and soot levels on soot packing density. The same study investigated similar effects on soot permeability and the detailed results are shown in Table A-1 of the Appendix. As shown in Table 11.3, ash accumulation in the filter increases local soot loads and results in increased filtration velocities, which may result in increased soot packing density, as shown by the experimental data presented in Figure 11.24. Furthermore, the wall velocities in the filters used in the experiments reported in this work ranged from 1 cm/s to 2 cm/s, corresponding to the shaded area of Figure 11.24 in which large changes in soot packing density are observed.

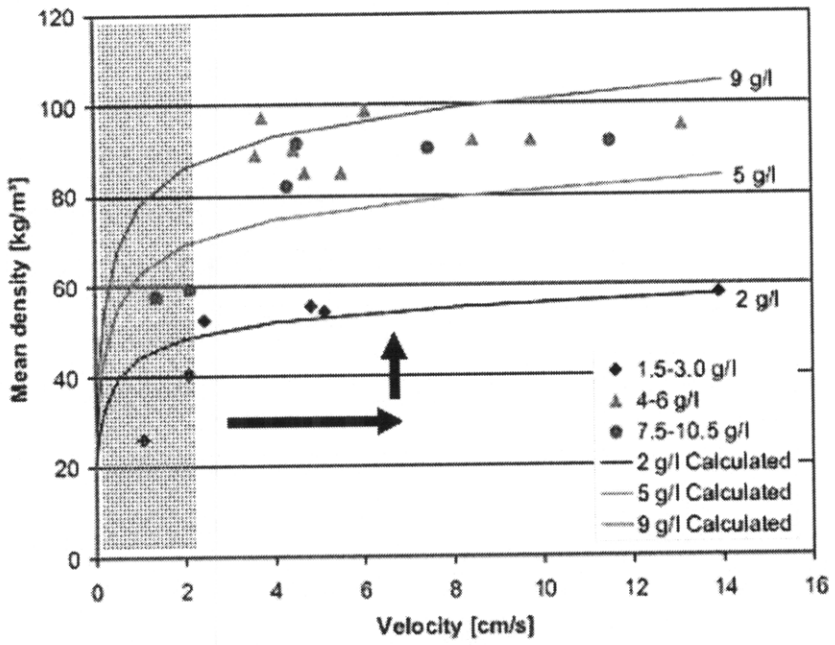

Figure 11.24. Soot layer packing density as a function of filtration velocity for three levels of DPF soot loading. Adapted from [64].

In order to explore the effects of ash accumulation on the parameters and soot properties influencing soot layer permeability, soot permeability was modeled using the Carman-Kozeny relationship. Following this approach, soot permeability is a function of the mean pore size and layer porosity. The layer porosity is controlled by the soot packing density. By incorporating the Carman-Kozeny relationship into the DPF pressure drop model, soot packing density and mean pore sizes were adjusted to compute soot

permeability and calibrate the model to the experimental data. The comparison between the predicted and measured pressure drop values was shown in Figure 11.23.

Using the pressure drop model and the Carman-Kozeny relationship, the effect of soot layer porosity and soot layer mean pores size on soot permeability and filter pressure drop were explored. The results are shown in Figures 11.25 and 11.26.

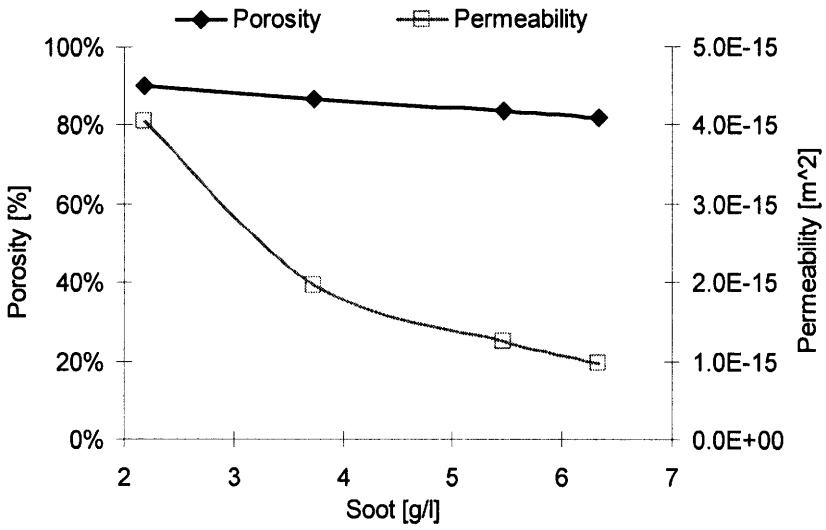

Figure 11.25. Predicted soot layer porosity and permeability variation as a function of soot load for soot deposited in a DPF pre-loaded with 33 g/l ash.

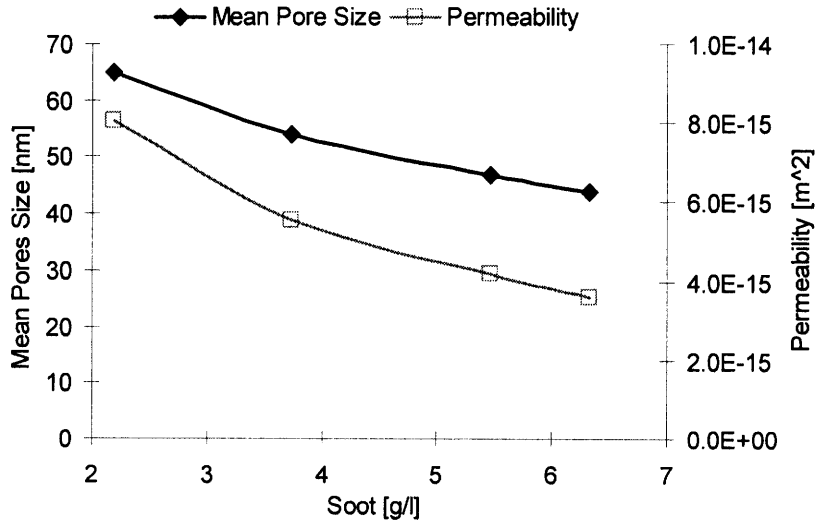

Figure 11.26. Predicted soot layer mean pores size and permeability variation as a function of soot load for soot deposited in a DPF pre-loaded with 33 g/l ash.

The results presented in Figure 11.25 show the variation in soot layer porosity and permeability required to account for the increase in DPF pressure drop sensitivity observed in the experiments. In these simulations, the soot layer mean pore size was assumed constant at a value of 100 nm, similar to the size of the individual soot agglomerates. The simulations show only small changes in soot layer porosity from 90% to 82% resulting in a significant decrease in soot layer permeability by almost a factor of four. Figure 11.27 presents additional experimental results from the literature showing soot layer permeability and porosity variation with DPF soot load for DPF filtration velocities ranging from 1 cm/s to 4 cm/s. While a number of parameters affect soot properties, the manner in which each of these parameters (soot load, wall velocity, pressure drop) affect soot packing density and permeability is still unclear. However, the trends in the experimental data presented in the literature and shown in Figure 11.27 are quite similar to the soot property data obtained using the ash model developed in this study and shown Figure 11.25.

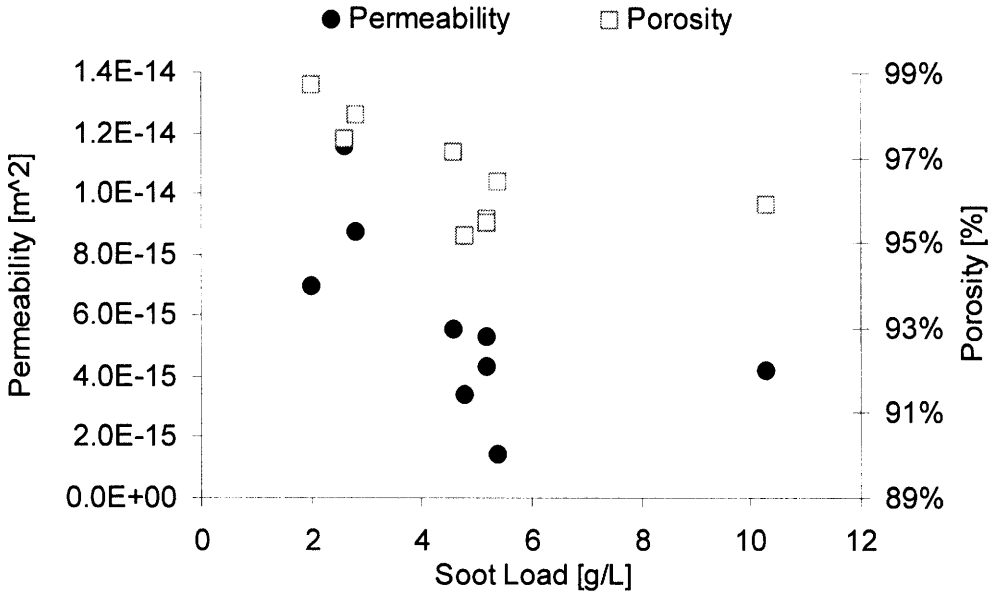

Figure 11.27. Experimentally determined soot layer permeability and porosity values as function of soot load for DPF wall velocities from 1.1 to 4.4 cm/s. Adapted from data presented in [64].

Similarly, the results presented in Figure 11.26 show the changes in soot layer mean pore size and permeability required to account for the change in DPF pressure drop sensitivity observed in the experimental results. In these simulations, the soot layer porosity was assumed constant at a value of 95%, within the range of typical values reported in the literature. The simulations show a reduction in soot layer mean pore size from 65 nm to 44 nm resulting in a decrease in soot layer permeability by a factor of two.

In addition to the comparison of the experimental and computational results with the soot properties data reported in the literature and presented in Figure 11.27, a considerable knowledge-base has been developed relating soot properties to the Peclet number. The variation of the Peclet number with DPF ash load is shown in Figure 11.28 for the exhaust flow conditions measured in the experiments. The Peclet number is a strong function of the soot primary particle diameter, and results for two soot primary particle diameters are presented in Figure 11.28.

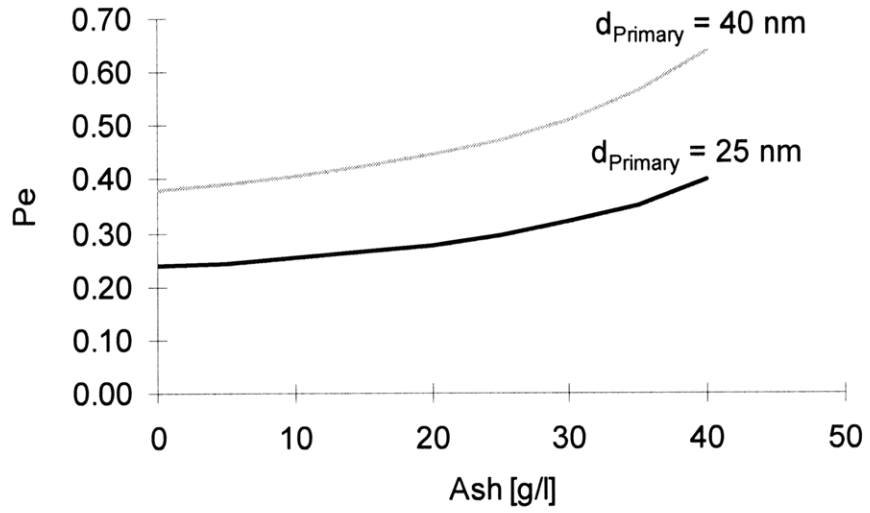

Figure 11.28. Variation of Peclet number with DPF ash load.

Ash accumulation in the DPF, particularly the ash deposited in the channel end-plug, increases the filter wall velocities, giving rise to the increase in Peclet number observed in Figure 11.28. Further, accurate knowledge of the soot particle sizes (primary particle and agglomerate) is critical for accurate determination of the Pe number. A comparison

of the increase in Peclet number for a DPF containing 33 g/l ash with a DPF containing no ash is shown in Figure 11.29.

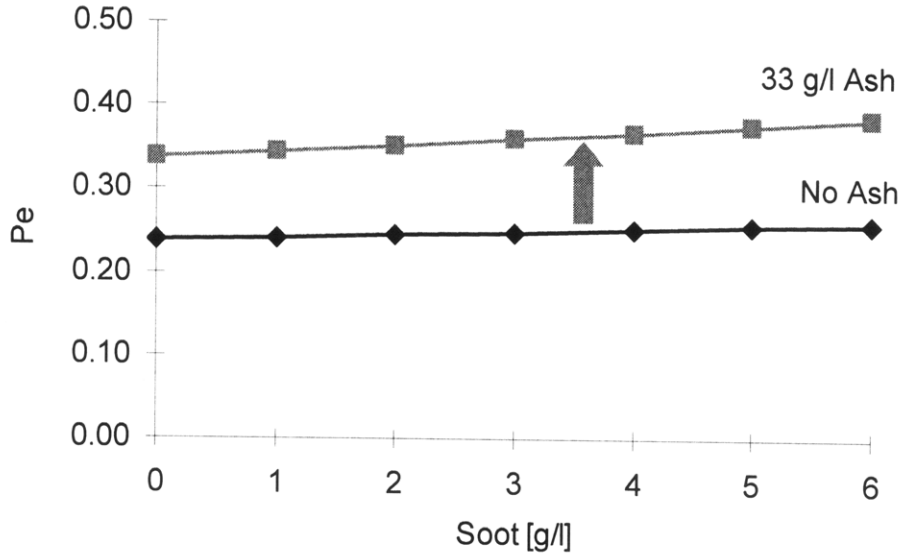

Figure 11.29. Comparison of Peclet number for a DPF containing 33 g/l ash with a DPF containing no ash as a function of soot load.

The data presented in Figure 11.29 assumes an average soot primary particle size of 25 nm and an agglomerate size of 100 nm. Compared to a DPF containing no ash, ash accumulated at a level of 33 g/l in the DPF increases the Pe number by approximately 40%. This increase in the Peclet number due to ash accumulation has a significant effect on porosity and permeability of the soot cake layer formed in a DPF containing ash.

Figures 11.30 and 11.31 show the variation of soot layer permeability and porosity as a function of the Pe number reported in the literature [60]. The outlined areas of the figures correspond to the range of Peclet numbers for the experiments conducted in this study. Within this range of Pe numbers, increasing the Peclet number, even slightly, results in a significant decrease in soot layer permeability and porosity.

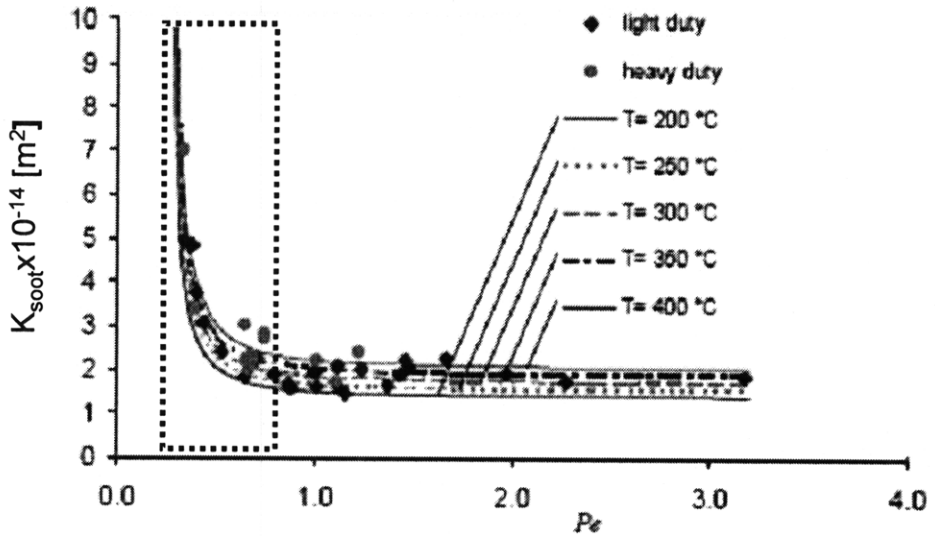

Figure 11.30. Variation of soot permeability with Peclet number. Outlined area corresponds to range of Peclet numbers from the experiments. Adapted from [60].

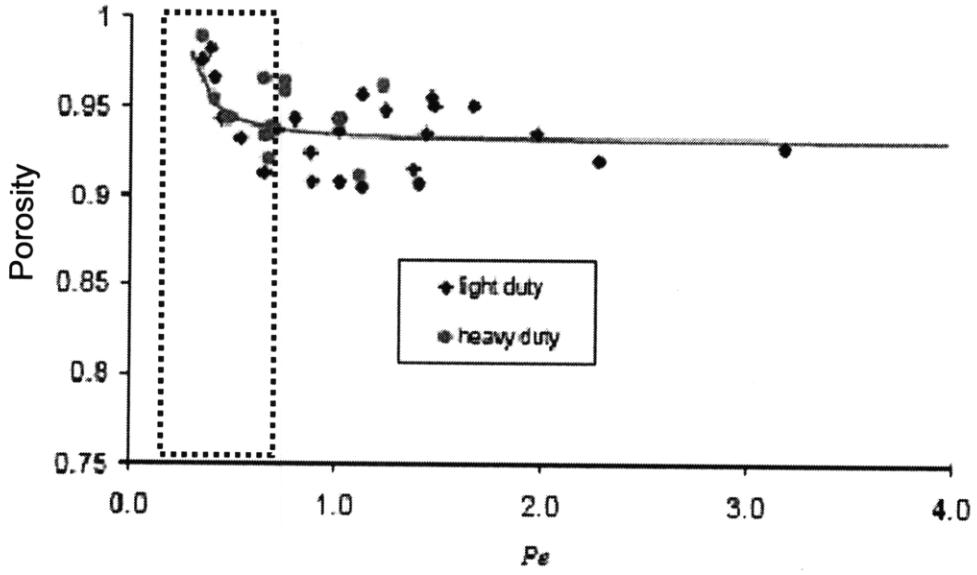

Figure 11.31. Variation of soot porosity with Peclet number. Outlined area corresponds to range of Peclet numbers from the experiments. Adapted from [60].

In reality, changes in DPF flow conditions and local soot distribution due to ash accumulation are expected to affect soot layer packing density, mean pore size, and permeability. The experimental and modeling efforts outlined above highlight the effects

of these parameters on DPF pressure drop sensitivity. More importantly, the results demonstrate that these parameters can account for the observed changes in pressure drop sensitivity, however understanding the specific manner in which these parameters are coupled, requires additional investigation.

12 CONCLUSIONS

The results presented in this work, among few fundamental data of its kind, highlight the underlying mechanisms responsible for the manner in which ash accumulation in diesel particulate filters affects the filter's pressure drop performance. After only 35,000 miles of on road use, ash comprises nearly 50% of the material accumulated in diesel particulate filters, highlighting the need to understand ash effects on DPF performance over the filter's 150,000 mile minimum service life. Targeted experiments carried out with carefully-controlled exhaust conditions provide insight into exhaust ash transport to the DPF, ash accumulation in the DPF, and the specific parameters controlling ash deposit formation and the resulting ash properties. Modeling efforts complemented the experimental work and served to advance the theoretical understanding. Lubricant chemistry and exhaust conditions were observed to play a significant role in influencing the magnitude in which ash affects filter pressure drop. Furthermore, the results of this study provide practical information to aid engine and aftertreatment designers as well as lubricant formulators to mitigate the deleterious effects of ash accumulation on diesel particulate filter performance.

12.1 Ash Transport and Deposition in Diesel Particulate Filters

Studies of engine-out soot and ash emissions revealed lubricant-derived ash related species to comprise between 0.5% and 1.0% of the total particulate matter emitted by the engine. Microscopy analysis of individual soot particles showed lubricant-derived ash precursors (Ca, Mg, Zn, S, and P compounds) to be intimately bound to the carbonaceous particulate matter. While individual wear metal and corrosion particles were found in the exhaust, no lubricant derived ash-related material was found to exist as distinctly separate particles. These observations provide circumstantial evidence that not only are the lubricant-derived ash compounds transported to the exhaust bound to the particulate matter, but the size of the ash particles embedded in the particulate matter are no larger than the soot agglomerates themselves.

These experimental observations indicate that sub-micron-sized ash precursors, transported to the DPF bound to the soot particles, are fairly well-mixed in the accumulated soot layer. Upon filter regeneration and soot oxidation, the soot is removed leaving a loose network of agglomerated ash particles and structures. These structures and particles were observed in the electron micrographs. Over time, and following repeated regeneration events, the ash particles agglomerate and grow to the micron-sized particles observed in the resulting ash layer. Exhaust conditions affect the ash deposition and formation processes, and the lubricant chemistry plays a role in defining the resulting ash composition and properties. Furthermore, the local ash critical shear stress controls the resulting thickness of the ash layer, and ash particle re-entrainment in the exhaust gasses and transport to the back of the filter channels resulting in end-plug formation.

Measurements of pre- and post-DPF elemental ash emission rates further showed that nearly all metallic lubricant-derived elements (Ca, Mg, Zn) are trapped in the DPF at a high rate, in excess of 98%. On the other hand, trapping efficiencies for sulfur and phosphorous compounds were somewhat lower and ranged from 65% to 85%, respectively. Sulfur compounds may exist as particle-phase sulfates and in the gaseous phase as SO_2, and may thus more readily pass through the filter. Furthermore, decomposition of lubricant-derived sulfate compounds at high temperatures, and sulfate production over the platinum catalyst may also contribute to the reduced sulfur trapping efficiencies.

12.2 Ash Effects on DPF Pressure Drop

Studies of ash effects on DPF pressure drop utilizing a fully-formulated CJ-4 oil and a base oil containing no additional additives defined an upper- and lower- bound for the increase in pressure drop due to lubricant-derived ash accumulation. Experiments using the ashless base oil showed no detectable increase in filter pressure drop over the accelerated ash loading cycle simulating 180,000 miles of on-road use. Furthermore, no ash deposits were observed in this DPF. On the other hand, 33 g/l of ash was accumulated in the filter with the CJ-4 oil, over the same simulated driving distance.

This level of ash accumulation led to an increase in DPF pressure drop by a factor of 1.8 to 1.9 times greater than the pressure drop in a clean filter.

Ash accumulation in a clean DPF first deposit in the DPF pores close to the filter surface. While only a small fraction of the ash is deposited in the DPF pores, it accounts for a significant fraction of the total ash-related pressure drop. Over a simulated driving distance of 180,000 miles, approximately 5% of the total ash was accumulated in the DPF pores, however it accounted for almost 60% of the total ash-related filter pressure drop. In general, around 2 g/l of ash was estimated to accumulate in the DPF pores with the D5.66" x 6" particulate filters used in this study.

Ash distribution in the DPF is a dynamic process with the amount of ash deposited along the filter wall and in the end-plug at the back of the DPF changing as the filter is loaded with ash. Following initial ash depth filtration, ash accumulates on top of the filter wall in a cake layer. The cake layer grows as additional ash and soot is deposited in the filter. Initial stages of ash accumulation find the ash predominately accumulated along the filter walls in the cake layer, with little ash deposition at the back of the channel in end-plugs. However, as ash continues to accumulate in the filter, at levels in excess of 12.5 g/l, the relative proportion of ash deposited in the end-plug increases. That is, the ash distribution shifts to deposit more material at the back of the channels as opposed to along the channel walls. The critical shear stress of the ash deposits is believed to govern the transport of ash from the cake layer to the channel end-plugs.

Analysis of the DPF pressure drop data for filters with varying levels of ash generated from CJ-4 oils showed the ash layer permeabilities to be quite similar for ash generated from the same oils under the same conditions in the DPF. The primary difference in the flow resistance parameter (w/k) was attributed to the difference in ash layer thickness. The DPF models further show filter wall velocities increase as the filtration area is reduced with ash accumulation in the DPF. The increasing wall velocities may result in a settling effect of the ash particles in the cake layer which would also affect layer permeability. Measurements of ash packing density, showing a slight increase in packing

density from 0.18 g/cm^3 to 0.30 g/cm^3 with an increase in DPF ash loading from 12.5 g/l to 42 g/l are consistent with the experimental observations and established cake filtration theory.

12.3 Lubricant Chemistry Effects on DPF Pressure Drop

Studies varying lubricant chemistry showed that ash containing predominantly calcium compounds exhibits a much greater increase in DPF pressure drop than fully-formulated CJ-4 oils for the same level of DPF ash loading. Furthermore, ash composed primarily of zinc-based compounds exhibited the lowest increase in pressure drop of all the lubricants tested. Measurements of ash composition via x-ray diffraction showed the ash generated from the oil containing only a calcium-based detergent to consist primarily of $CaSO_4$. The oil containing only the ZDDP additive produced ash composed primarily of $Zn_3(PO_4)_2$ and $Zn_2P_2O_7$. The composition of the ash generated from the fully-formulated CJ-4 was considerably more complex, with $CaSO_4$ and $MgZn_2(PO4)_2$ being the primary constituents.

Application of the DPF ash model and Carman-Kozeny relationship in conjunction with the experimental pressure drop data and measured ash properties allowed for the determination of ash layer permeability, porosity, and mean pore size. The ash porosities measured for the ash generated by the three diffident lubricant additives (CJ-4 package, Ca, and ZDDP) ranged from 92% to 95%. However, it should be noted that the results of the microscopy analysis conducted as part of this work, and data published in the literature, indicate that some of the individual ash particles themselves may be hollow structures with a void inner core. The morphology of the individual ash particles will result in a lower porosity structure encountered by the exhaust gasses. Application of the Carman-Kozeny relationship to the experimental data showed mean pore sizes for the ash layers ranging from 0.18 μm to 0.21 μm, with the calcium-based ash exhibiting the smallest mean pore size.

Determination of ash layer permeabilities using the pressure drop model resulted in permeabilities of $2.3x10^{-14}$ m^2 for ash generated from the oil containing only the calcium detergent and $2.9x10^{-14}$ m^2 for the ash generated from the CJ-4 oil. The permeability of the ash containing predominantly zinc phosphates was $9.0x10^{-14}$ m^2, significantly greater than the ash generated from the CJ-4 and calcium-based oils. The measured and computed ash properties were consistent with the experimentally-determined pressure drop trends. Based on the measured pressure drop and ash properties, calcium-based lubricant additives appear to generate ash layers exhibiting a greater flow resistance and elevated pressure drop as opposed to zinc-based additives. Furthermore, high levels of $CaSO_4$ were also found in the ash generated with the CJ-4 oils. Similarities between the DPF pressure drop performance for the filters exposed to the calcium-based oil and fully-formulated CJ-4 oil, indicate calcium additives to be one of the largest contributors to DPF pressure drop increase due to ash accumulation.

12.4 Exhaust Temperature Effects on DPF Pressure Drop

Investigations of exhaust temperature and DPF regeneration condition effects on ash properties and DPF pressure drop showed 25% of the ash generated via periodic regeneration distributed along the channel walls and 75% accumulated in the channel end-plug by volume, for a DPF containing 42 g/l ash. On the other hand, ash generated via continuous regeneration tended to preferentially accumulate along the channel walls. Regardless of regeneration method, initial stages of ash accumulation in the DPF, up to 10 g/l, showed no significant differences in filter pressure drop between the periodic and continuously regenerated cases. Furthermore, results of the post-mortem analysis showed ash primarily deposited in the DPF pores and along the channel walls during initial stage of ash accumulation (less than 10 g/l ash). The differences in pressure drop became much more pronounced at elevated ash loading levels, with the continuously regenerated filter exhibiting a greater increase in pressure drop for the same level of ash loading.

Results obtained from the DPF ash pressure drop models provide additional insight into the effect of ash distribution (end-plug vs. wall layer) on filter pressure drop. Ash

primarily accumulated in the end-plug reduces the overall channel length leading to a decrease in the channel pressure drop. However, the reduction in channel length also increases the exhaust gas wall velocities increasing the pressure drop through the DPF walls. On the other hand, ash primarily accumulated along the channel walls decreases the hydraulic diameter of the channels resulting in an increase in the channel pressure drop. Furthermore, increasing ash layer thickness also increases the pressure drop through the ash layer. In general, for ash loads below 40 g/l, which are typical in most DPF applications, packing the ash in the end-plugs at the back of the channels results in a lower pressure drop as opposed to ash deposition along the channel walls, when only ash effects are considered.

Extension of the DPF pressure drop models to include both ash and soot effects, showed the opposite behavior. When soot is deposited in a DPF containing moderate ash loads, above 10 g/l, the lowest pressure drop is achieved when all of the ash is deposited along the channel walls and no ash is deposited in the end-plug. As noted above, ash deposition in the end-plug reduces the effective channel length, driving up the wall velocities. The increased wall velocities, combined with the low permeability of the soot layer, lead to an increase in pressure drop for the case in which ash is deposited in the end-plug. The experimental data further showed a beneficial effect of the ash layer to inhibit soot depth filtration and is consistent with the filter pressure drop performance predicted in the model.

Detailed investigations of exhaust temperature effects on ash composition and ash layer properties showed elevated temperatures, above 700 °C, resulting in ash decomposition. The ash decomposition was primarily attributed to the decomposition of sulfate compounds, as observed by measurements of SO_2 evolved from the ash samples at these elevated temperatures. X-ray diffraction analysis further revealed the formation of metal oxide compounds at elevated temperatures as well. While some ash decomposition at temperatures in excess of 700 °C was observed, the primary effect of the high temperatures was to increase ash packing density, and ash sintering was clearly observed after ash exposure to temperatures above 900 °C.

12.5 Combined Ash and Soot Effects on DPF Pressure Drop

Ash significantly affects the DPF pressure drop sensitivity to soot accumulation. Ash deposited along the DPF channels forms a physical barrier or membrane preventing soot depth filtration. For low ash loads, below 12.5 g/l, with conventional CJ-4 oil, the ash layer was shown to have a beneficial effect in reducing DPF pressure drop due to soot accumulation relative to the filter with the same level of soot loading but no ash. Interestingly, these same beneficial effects were also noted with the zinc-based ash, but at much higher ash levels of 28 g/l. The reduction in pressure drop is attributed to the elimination of soot depth filtration by the ash layer.

The prevention of soot depth filtration by the ash layer, results in a marked decrease in DPF pressure drop sensitivity to additional soot accumulation for low soot loads, below 0.4 g/l. At moderate soot loads (0.4 g/l to 3 g/l), little difference in pressure drop sensitivity is observed between the DPFs with and without ash. However, at elevated soot loads above 3 g/l, pressure drop sensitivity increases much more rapidly in DPFs containing ash than in filters with no ash. Depending on ash levels, this increase in pressure drop sensitivity may range from 1.4 to 4.4 times greater than in a filter without ash, and increases with the level of ash loading.

The increase in pressure drop sensitivity observed in the ash loaded DPFs with elevated soot loading levels was primarily attributed to the reduction in available filter volume due to the ash. Ash accumulation in the DPF reduces the volume available for soot deposition, thereby increasing the local soot loading. Although the absolute mass of soot stored in the filter is the same for a clean and ash loaded DPF, the filter containing ash exhibits higher local soot levels, as much of the filter volume is already occupied by ash. Second order effects also contributing to the observed increase in pressure drop sensitivity include an increase in channel wall velocities with ash loading, and a reduction in the channel hydraulic diameter.

The DPF pressure drop model was also applied to investigate the second order effects (soot property variation) due to ash loading. The models showed a decrease in soot layer

permeability due to decreasing layer porosity and mean pore size with additional soot accumulation in a DPF containing ash. The elevated filter wall velocities, due to the ash accumulation, may result in more densely packed soot structures and/or cause soot re-ordering whereby small soot particles partially block the pores, resulting in a reduction in the mean pore size. The specific manner in which these parameters are coupled, requires further investigation. Increasing channel wall velocities has also been shown in the literature to result in slightly denser and less permeable soot layers, and the trends observed with the DPF model (decreasing soot layer permeability and increasing packing density) were consistent with the general trends reported in the literature as well.

12.6 Practical Applications

In practical applications, all DPFs contain some level of ash and soot loading. Estimates based on the results presented in this work show approximately 1.75 g/l ash accumulation per 10,000 miles. At this rate of ash accumulation, the DPF contains 6 g/l of ash after only 35,000 miles. Typically, cordierite DPFs are regenerated at soot loading levels of 6 g/l. Therefore, after only 35,000 miles of on road use, the ash fraction of the accumulated material in the DPF (ash and soot) exceeds 50%. Typical on-highway heavy-duty trucks average 150,000 miles per year, which coincidentally is equal to the EPA's minimum DPF ash cleaning interval. Following the same logic, at 150,000 miles, the DPF can be expected to contain 26 g/l ash, slightly more than 80% of the accumulated material, if the filter is regenerated at a maximum soot load of 6 g/l. Despite the relatively high amount of ash accumulated in particulate filters, few studies in the literature consider ash effects when evaluating DPF performance.

Ash accumulation in the DPF significantly affects the filter's pressure drop sensitivity to soot accumulation, which is of great practical importance for pressure-based methods used to determine DPF soot loading. At low soot loads, ash reduces the pressure drop sensitivity to soot accumulation resulting in an underestimate of soot loading. On the other hand, at elevated soot loads, ash increases the DPF pressure drop sensitivity to soot accumulation resulting in an overestimate of soot levels. If ash effects are not accounted

for, the DPF may be regenerated more often than necessary resulting in additional fuel economy penalties, particularly at high ash loads.

Ash accumulated in end-plugs at the back of the DPF channels also reduces the channel length, shifting soot distribution in the filter, resulting in higher local soot loads towards the front of the filter. Results of experiments conducted in this study show between 50% and 75% (by volume) of the ash accumulated in end-plugs at the back of the filter after a simulated driving distance of 180,000 miles with a conventional CJ-4 oil and periodic regeneration. These results further show that ash levels of 33 g/l and a nominal DPF soot load of 6 g/l, corresponds approximately to 8 g/l of soot locally. Higher local soot loads result in elevated local temperatures during active DPF regeneration which may affect DPF service life.

Exhaust temperatures and regeneration strategy also affect ash deposition and distribution within the DPF. Ash accumulated in a filter regenerated periodically leads to increased ash plug formation at the back of the channels. On the other hand, ash accumulation in a filter regenerated continuously results in a larger proportion of the ash deposited in a layer along the channel walls. Packing the ash in end-plugs toward the back of the DPF channels is preferred to reduce filter pressure drop associated with ash accumulation. However when both soot and ash accumulation is considered, evenly distributing all of the ash along the channel walls, with no end-plug formation, is preferred to reduce the total filter pressure drop. Modifying DPF regeneration strategy and DPF regeneration temperatures may provide some control of ash distribution and the resulting magnitude of the ash effect on DPF pressure drop.

Low levels of ash accumulation in the DPF, below 12.5 g/l, show a beneficial effect on reducing filter pressure drop with soot accumulation, as the ash layer forms a membrane covering the DPF surface pores, preventing soot depth filtration. Based on the results presented in this study, ash levels of 12.5 g/l in the DPF correspond to slightly more than 70,000 miles. Conversely, elevated ash levels in the filter increase DPF pressure drop sensitivity to soot accumulation and significantly increase total filter pressure drop with

soot loads greater than 3 g/l. Increasing filter ash cleaning frequency, or better yet, leaving a thin ash layer in the filters following DPF ash cleaning, if possible, may provide additional means for reducing DPF pressure drop. Accurate knowledge of both soot and ash levels in the filter is required to optimize filter regeneration strategy and cleaning intervals to minimize DPF pressure drop.

Investigations of individual lubricant additive effects on DPF pressure drop, showed ash primarily composed of calcium compounds to result in a much larger increase in filter pressure drop as opposed to ash composed primarily of zinc-based compounds. Furthermore, even at ash levels of 28 g/l, the DPF containing zinc-based ash showed a reduction in total pressure drop, compared with a filter containing no ash, at the same level of soot loading. This information may prove useful to lubricant and additive formulators to design lubricants for reduced impact on aftertreatment systems, while maintaining adequate engine protection.

12.7 Practical Considerations and Opportunities for Future Work

The results of the study presented in this work should be interpreted within the context of the experimental procedures and the manner in which they were obtained. The accelerated ash loading system utilized to load the DPFs with ash was designed to generate ash and soot as realistically as possible. Detailed studies of the ash and soot properties generated by the accelerated ash loading system showed overall ash and soot morphology, composition, and properties to be quite similar to engine-out ash and soot; the one exception being the significantly higher levels of ash in the exhaust with the accelerated loading system. Furthermore, analysis of ash deposits from field-aged filters subjected to 180,000 miles of on-road use were quite similar to the ash deposits found in the filters loaded with ash in the laboratory over a test cycle simulating 180,000 miles of on-road use. In particular, ash distribution (end-plug vs. wall layer), ash composition, ash packing densities, and ash particle sizes were all quite similar for the field- and laboratory-generated ash.

Despite the considerable similarities between the procedure developed and utilized in this work and engine-out exhaust conditions, the following key differences between the laboratory procedures and processes occurring in an engine remain:

- Lubricant consumption and transport to the exhaust in a diesel engine can occur via the following three paths: (1) combustion of the lubricant in the power cylinder, (2) volatilization and vapor-phase losses at high temperatures, and (3) liquid losses via valve and turbocharger seal leakage. The first two mechanisms are generally responsible for the majority of lubricant consumption in an engine. The design of the accelerated ash loading system utilized a diesel burner to combust lubricant injected into the combustion chamber via a secondary oil injector. The combustion products resulting from this system are primarily composed of combusted and vaporized lubricant constituents, as well as soot generated by the burner. Lubricant losses to the exhaust in liquid form were not simulated, as they are believed to be small relative to the other mechanisms.
- Due to differences in the volatility of specific lubricant additives, and the deposition of additives within the engine, such as through formation of anti-wear films, not all lubricant additives are consumed at the same rate during engine operation. The experiments conducted in this work consumed the fully-formulated lubricant in the diesel combustor, and all of the lubricant additives were consumed at the same rate.
- Hardware limitations due to the exhaust backpressure sensitivity of the diesel burner and centrifugal blower used control the exhaust flow rate through the DPF placed a limit on the maximum exhaust space velocity of 30,000 hr^{-1}. While space velocities in the range of 20,000 hr^{-1} to 30,000 hr^{-1} may be achieved during normal engine operation, in many practical applications, the space velocities may be higher.

While the system limitations described above are not expected to significantly affect the results and conclusions developed from this work, it is important to understand the key differences between the accelerated ash loading system employed in the laboratory and

actual engine-out exhaust conditions. Furthermore, opportunities for future work may address some of these limitations and may also expand upon the following key areas indentified in this study:

- Extend system operating range to explore the effect of varying DPF wall velocity on the properties of the ash and soot accumulated in the DPF. Filter space velocity was maintained relatively constant in this study.
- Utilize specially formulated lubricants with additive levels corresponding to the actual engine-out additive emissions rates. Tailoring lubricant composition in this manner will result in the same relative proportion of lubricant additives accumulated in the DPF as observed in field-aged filters.
- Investigate the effect of lubricant additive forms in the exhaust (solid-, liquid-, vapor-phase), on the resulting ash properties and DPF pressure drop. The design of the current accelerated ash loading system allows for liquid- and vapor-phase components to be introduced directly into the exhaust stream.
- Expand the lubricant test matrix to evaluate the synergistic effects of specific lubricants on ash composition and properties affecting DPF pressure drop. Only fully-formulated CJ-4 oils and lubricants containing individual additives were utilized in this study. Analysis of the DPF ash suggests that individual additives, particularly zinc and magnesium, may form complexes with sulfur and phosphorous compounds.
- Perform targeted studies to better understand the parameters controlling ash transport within the DPF from the filter walls to the end-plugs at the back of the filter. While the local critical shear stress of the ash is believed to control these transport processes, little is known about the ash properties and exhaust parameters that affect the critical shear stress.
- Expand the DPF ash pressure drop models to more accurately account for the coupling between ash and soot layer porosity, mean pore size, and permeability. These parameters significantly influence pressure drop in diesel

particulate filters containing both soot and ash, and require additional investigation.

- While the present study examined the effects of lubricant-derived ash on DPF pressure drop, ash may also originate from a number of other sources. Typically, additives present in diesel engine lubricants contribute to the majority of the ash accumulated in DPFs. In some cases, particularly when fuel-borne additives are used, the fuel contribution to the DPF ash increases as well. Further, due to the much higher rate of fuel consumption relative to oil consumption, small amounts of trace elements in the fuels can contribute significantly to ash accumulation in the DPF. Recent studies have noted that approximately 1 ppm of trace elements in the fuel are equivalent to approximately 1,000 ppm of the same element in the oil, due to the much greater fuel consumption rate [85]. Additional studies may focus on the contribution of trace elements in fuels to ash accumulation in DPFs as well.

The results obtained in this study provide considerable insight into the underlying mechanisms and parameters controlling key ash properties, which in turn influence the magnitude of the ash effect on DPF pressure drop. While considerable progress has been made, much additional work remains. Nonetheless, this work has served to advance not only the theoretical understanding, but also identified opportunities useful in practical applications to aid engine and aftertreatment designers as well as lubricant formulators in reducing the overall impact of ash accumulation on diesel aftertreatment system performance.

(This page intentionally left blank)

13 REFERENCES

[1] Heywood, J. B., Internal Combustion Engine Fundamentals, McGraw-Hill, Inc., New York, 1988.

[2] Adler, U., Editor-in-Chief, Bosch Automotive Handbook, 2nd Edition, Robert Bosch GmbH, Stuttgart, 1986.

[3] DieselNet Technology Guide, <http://www.dieselnet.com/tg.html/>, 2005.

[4] Diesel Technology Forum, "Where is Diesel: Cars, Trucks, and SUVs," <http://www.dieselforum.org/where-is-diesel/cars-trucks-suvs/>, 2005.

[5] Energy Information Administration, Doc. No. DOE/EIA-X063, "Diesel Fuel Prices, What Consumers Should Know" United States Department of Energy, 2007.

[6] Charles River Associates, "Diesel Technology and the American Economy," Diesel Technology Forum Report no. D02378-00, 2000.

[7] European Automobile Manufacturer's Association, "Automobile Production Expanded by 5.3% in 2007, Trend Toward Diesel Remains,". <http://www.acea.be/index.php/news/news_detail/automobile_production_expanded_by_53_in_2007>, February 20, 2008.

[8] Sappok, A., and Wong, V.W., "Comparative Particulate Trap Performance using Fischer-Tropsch and Conventional Diesel Fuels in a Modern CI Engine," ASME paper ICES2006-1345, 2006.

[9] Swiss Agency for the Environment, Forests and Landscape,"Vert-Filterliste: Gepruefte und Erprobte Partikelfilter-Systeme fuer die Nachruestung von Dieselmotoren", Bern, Switzerland, 2005.

[10] United States Environmental Protection Agency, <http://www.epa.gov/air/oaqps/greenbk/>, 2009.

[11] Office of Transportation and Air Quality, "Heavy Duty Engine and Vehicle Standards and Highway Diesel Fuel Sulfur Requirements," US Environmental Protection Agency (EPA)< http://www.epa.gov/otaq/regs/hd2007/frm/f00057.pdf>, 2000.

[12] EPA Office of Transportation and Air Quality, "Mobile Source Black Carbon Emissions," Black Carbon Emissions and Climate Change: A Technical Workshop, San Diego, <http://www.nrel.gov/vehiclesandfuels/nfti/pdfs/bc12_j_somers.pdf>, 2004.

[13] Klanner, W., "Car Emissions and Euro 5 Consumers View," ADAC Workshop, Brussels, <http://www.fiafoundation.com/>, 2005.

[14] Charlton, S., "Clean and Efficient Diesel Engines – Design for the Customer," Diesel Engine Efficiency and Emissions Research Conference, Detroit, MI, 2008.

[15] Johnson, J.H., Bagley, S.T., Gratz, L.D., and Leddy, D.G., "A Review of Diesel Particulate Control Technology and Emissions Effects," SAE 940233, 1994.

[16] Schweizerischen Krebsliga "Dieselpartikel Luftschadstoff Nr. 1: Wirkungen auf den menshclichen Organismus und technische Loesungen zur Eliminierung dieses Schadstoffs," 2004.

[17] Green Car Congress, "Study: Black Carbon Pollution Major Factor in Global Warming," <http://www.greencarcongress.com/2008/03/study-black-car.html>, 2008.

[18] Ramanathan, V., and Carmichael, G., "Global and Regional Climate Changes Due to Black Carbon," Nature Geosciences, vol. 1, April 2008. <www.nature.com/ngeo/journal/v1/n4/pdf/ngeo156.pdf>

[19] Salvat O., P. Marez and G. Belot, 2000. "Passenger Car Serial Application of a Particulate Filter System on a Common Rail Direct Injection Diesel Engine", SAE 2000-01-0473, 2000.

[20] Mogaka, Z.N., Wong, V.W., and Shahed, S.M., "Performance and Regeneration Characteristics of a Cellular Ceramic Diesel Particulate Trap," SAE 820272, 1982.

[21] Cheng, S.S., "Rolling Regeneration Trap for Diesel Particulate Control," SAE 2003-01-3178, 2003.

[22] Manufacturers of Emission Controls Association (MECA): "Diesel Particulate Filter Maintenance: Current Practices and Experience," Washington D.C., 2005.

[23] Aravelli, K., Jamison, J., Robbinson, K., Gunasekaran, N., and Heibel, A., "Improved Lifetime Pressure Drop Management for DuraTrap RC Filters with Asymmetric Cell Technology (ACT)," Diesel Engine Efficiency and Emissions Reduction Conference, Detroit, MI, 2006.

[24] McGeehan, J., Yeh, S., Couch, M., Hinz, A., Otterholm, B., Walker, A., and Blakeman, P., "On the Road to 2010 Emissions: Field Test Results and Analysis with DPF-SCR System and Ultra-Low-Sulfur Diesel Fuel", SAE 2005-01-3716, 2005.

[25] Bodek, B., and Wong, V., "The Effects of Sulfated Ash, Phosphorous and Sulfur on Diesel Aftertreatment Systems – A Review", SAE 2007-01-1922, 2007.

[26] Kimura, K., Lynskey, M., Corrigan, E., Hickman, D., Wang, J., Fang, H., and Chatterjee, S., "Real World Study of Diesel Particulate Filter Ash Accumulation in Heavy-Duty Diesel Trucks", SAE 2006-01-3257, 2006.

[27] Jääskeläinen, H., and Majewski, A.: "Diesel Engine Lubricants," <www.DieselNet.com>, 2006.

[28] Givens, W., Buck, W., Jackson, A., Klador, A., Hertzberg, A., ,Moehrmann, W., Mueller-Lunz, S., Pelz, N., and Wenniger, G., "Lube Formulation Effects on Transfer of Elements to Exhaust After-Treatment System Components", SAE 2003-01-3109, 2003.

[29] Bardasz, E., Cowling, S., Panesar, A., Durham, J., and Tadrous, T., "Effects of Lubricant Derived Chemistries on Performance of the Catalyzed Diesel Particulate Filters", SAE 2005-01-2168, 2005.

[30] Mc Geehan, J., "API CJ-4: Diesel Oil Category for Both Legacy Engines and Low Emission Engines Using Diesel Particulate Filters", SAE 2006-01-3439, 2006.

[31] ASTM International. "D 874-06: Standard Test Method for Sulfated Ash from Lubricating Oils and Additives."

[32] Haycock, R., Caines, A., and Hiller, J., Automotive Lubricants Reference Book, Society of Automotive Engineers, 1996.

[33] Totten, G., Handbook of Lubrication and Tribology: Applications and Maintenance, Taylor and Francis, 2006.

[34] Advanced Petroleum Based Fuels – Diesel Emission Control (APBF-DEC), Lubricants Project, Phase I Report, 2004.

[35] Britton, N., Sutton, M., Otterholm, B., Tengstrom, P., Frennfelt, C., Walker, A., and Murray, I., "Investigations into Lubricant Blocking of Diesel Particulate Filters", SAE 2004-01-3013, 2004.

[36] Bardasz, E., Cowling, S., Panesar, A., Durham, J., and Tadrous, T., "Effects of Lubricant Derived Chemistries on Performance of the Catalyzed Diesel Particulate Filters", SAE 2005-01-2168, 2005.

[37] Warner, J., Johnson, J., Bagley, S., and Huynh, C., "Effects of Catalyzed Particulate Filter on Emissions from a Diesel Engine: Chemical Characterization Data and Particulate Emissions Measured with Thermal Optical and Gravimetric Methods", SAE 2003-01-0049, 2003.

[38] Manni, M., Pedicillo, A., and Bazzano, F., "A Study of Lubricating Oil Impact on Diesel Particulate Filters by Means of Accelerated Engine Tests", SAE 2006-01-3416, 2006.

[39] Aravelli, K., and Heibel, A., "Improved Lifetime Pressure Drop Management for Robust Cordierite (RC) Filters with Asymmetric Cell Technology (ACT)", SAE 2007-01-0920, 2007.

[40] Allansson, R., Blakeman, P., Cooper, B., Phillips, P., Thoss, J., and Walker, A., "The Use of Continuously Regenerating Trap (CRTTM) to Control Particulate Emissions: Minimizing the Impact of Sulfur Poisoning", SAE 2002-01-1271, 2002.

[41] Nemoto, S., Kishi, Y., Matsuura, K., Miura, M., Togawaw, S., Ishikawa, T., Hashimoto, T., and Yamazaki, T.,. "Impact of Oil-Derived Ash on Continuous Regeneration-Type Diesel Particulate Filter-JCAPII Oil WG Report", SAE 2004-01-1887, 2004.

[42] Bunting, B., More, K., Lewis, S., and Toops, T., "Phosphorous Poisoning and Phosphorous Exhaust Chemistry with Diesel Oxidation Catalysts", SAE 2005-01-1758, 2005.

[43] Bardasz, E., Antoon, F., Schiferl, E., Wang, J., and Totten, W., "The Impact of Lubricant Derived Sulfur Species on Efficiency and Durability of Diesel NOx Adsorbers", SAE 2004-01-3011, 2004.

[44] Gaiser, G., and Mucha, P., "Prediction of Pressure Drop in Diesel Particulate Filters Considering Ash Deposition and Partial Regenerations", SAE 2004-01-0158, 2004.

[45] Piesche, M., Bargende, M., Deuschle, T., Hitzler, G., Janoske. U., and Weitk, W., "Lanzeitstabilität von Partikelfiltern in Dieselmotoren", FVV Heft R521, Informatsionstagung Motoren, FVV Frankfurt, 2003.

[46] Takeuchi, Y., Hirano, S., Kanauchi, M., Ohkubo, H., Nakazato, M., Sutherland, M., and van Dam, W., „The Impact of Diesel Engine Lubricants on Deposit Formation in Diesel Particulate Filters," SAE 2003-01-1870, 2003.

[47] Barris, M.A., Reinhart, S.B., and Wahlquist, F.H., "The influence of Lubricating Oil and Diesel Fuel on Ash Accumulation in an Exhaust Particulate Trap." SAE 910131, 1991.

[48] Bardasz, E., Mackne, D., Britton, N., Kleinschek, G., Olofsson, K., Murray, I., and Walker, A., "Investigations of the Interactions between Lubricant-Derived Species and Aftertreatment Systems on a State-of-the-Art Heavy Duty Diesel Engine", SAE 2003-01-1963, 2003.

[49] Opris, C., and Johnson, J., "A 2-D Computational Model Describing the Flow and Filtration Characteristics of a Ceramic Diesel Particulate Trap," SAE 980545, 1998.

[50] Karin, P., Cui, L., Rubio, P., Tsuruta, T., and Hanamura, K., "Microscopic Visualization of PM Trapping and Regeneration in Micro-Structural Pores of a DPF Wall," SAE 2009-01-1476, 2009.

[51] DieselNet Technology Guide, "Cellular Monolith Substrates", Revision 1998-08c, DieselNet. <http://www.dieselnet.com/tech/cat_substrate.html#pressure>, 1998.

[52] DieselNet Technology Guide, "Wall-Flow Monoliths", Revision 2005-09a, DieselNet. <http://www.dieselnet.com/tech/dpf_wall-flow.html>, 2005.

[53] Fay, J., Introduction to Fluid Mechanics, MIT Press, Cambridge, MA, 1994.

[54] Merkel, G., Vernacotola, M., Beall, D., and Hickman, D., "Effects of Microstructure and Cell Geometry on Performance of Cordierite Diesel Particulate Filters," SAE 2001-01-0193, 2001.

[55] Merkel, A., Cutter, W., and Warren, C., "Thermal Durability of Wall-Flow Ceramic Diesel Particulate Filters", SAE 2001-01-0190, 2001.

[56] Young, D., Hickman, D., Bhatia, G., and Gunasekaran, N., "Ash Storage Concept for Diesel Particulate Filters", SAE 2004-01-0948, 2004.

[57] Harle, V., Pitois, C., Rocher, L., and Garcia, F., "Latest Development and Registration of Fuel-Borne Catalyst for DPF Regeneration", SAE 2008-01-0331, 2008.

[58] Konstandopoulos, A., Kostoglou, M., Skaperdas, E., Papaioannou, E., Zarvalis, D., and Klaopoulou, E., "Fundamental Studies of Diesel Particulate Filters: Transient Loading, Regeneration and Aging", SAE 2000-01-1016, 2000.

[59] Konstandopoulos, A., Zarvalis, D., Kladopoulou, E., and Dolios, I.,. "A Multi-Reactor Assembly for Screening Diesel Particulate Filters", SAE 2006-01-0874, 2006.

[60] Konstandopoulos, A., Skaperdas, E., and Masoudi, M., "Microstructural Properties of Soot Deposit in Diesel Particulate Traps," SAE 2002-01-1015, 2002.

[61] Kladoppoulou, E., Yang, S., Johnson, J., Parker, G., and Konstandopoulos, A., "A Study Describing the Performance of Diesel Particulate Filters During Loading and Regeneration ~ A Lumped Parameter Model for Control Applications", 2003-01-0842, 2003.

[62] Lee, K., Zhu, J., Ciatti, S., Yozgatligil, A., and Choi, M., "Sizes, Graphitic Structures and Fractal Geometry of Light-Duty Diesel Engine Particulates", SAE 2003-01-3169, 2003.

[63] Lee, K., and Zhu, J., "Effects of Exhaust System Components on Particulate Morphology in a Light-Duty Diesel Engine", SAE 2005-01-0184, 2005.

[64] Koltsakis, G., Konstantinou, A., Haralampous, O., and Samaras, Z., "Measurement and Intra-Layer Modeling of Soot Density and Permeability in Wall-Flow Filters," SAE 2006-01-0261, 2006.

[65] Sappok, A., and Wong, V., "Detailed Chemical and Physical Characterization of Ash Species in Diesel Exhaust Entering Aftertreatment Systems," SAE 2007-01-0318, 2007.

[66] Houi, D, and Lenormand, R., "Particle Deposition on a Filter Medium," Kinetics of Aggregation and Gelation, Elsevier Science Publishers, B.V., 1984.

[67] Tassopoulos, M., O'Brien, J., and Rosner, D., "Simulation of Microstructure/Mechanism Relationships in Particle Deposition." AIChe Journal, Vol. 35, No. 6, June 1989.

[68] Tassopoulos, M., "Relationships Between Particle Deposition Mechanism, Deposit Microstructure and Effective Transport Properties," PhD Dissertation, Yale University, 1991.

[69] Konstandopoulos, A., and Johnson, J., "Wall-Flow Diesel Particulate Filters – Their Pressure Drop and Collection Efficiency," SAE 890405, 1989.

[70] Suresh, A., Khan, A., and Johnson, J., "An Experimental and Modeling Study of Cordierite Traps – Pressure Drop and Permeability of Clean and Particulate Loaded Traps," SAE 2000-01-0476, 2000.

[71] Konstandopoulos, A., "Flow Resistance Descriptors for Diesel Particulate Filters: Definitions, Measurements and Testing," SAE 2003-01-0846, 2003.

[72] Konstandopoulos, A., Kostoglou, M., Housiad, P., Vlachos, N., and Zarvalis, D., "Multichannel Simulation of Soot Oxidation in Diesel Particulate Filters," SAE 2003-01-0839. 2003.

[73] Konstandopoulos, A., and Kladapoulou, E., "The Optimum Cell Density for Wall-Flow Monolithic Filters: Effects of Filter Permeability, Soot Cake Structure and Ash Loading," SAE 2004-01-1133, 2004.

[74] Dullien, F., Porous Media – Fluid Transport and Pore Structure, Academic Press, New York, NY, 1979.

[75] Sachdev, R., Wong, V.W., Shahed, S., "Effect of Ash Accumulation on the Performance of Diesel Exhaust Particulate Traps," SAE 830182, 1983.

[76] Manni, M., Pedicillo, A., Del Piero, G., Massara, E., "An Experimental Evaluation of the Impact of Lubricating Oils and Fuels on Diesel Particulate Filters", SAE 2007-01-1925, 2007.

[77] Pueffel, P., Thiel, W., and Boesl, U., "Application of a New Method for On-Line Oil Consumption Measurement", SAE 1999-01-3460, 1999.

[78] Fukushima, H., Adachi, M., Nakamura, S., and Hill, L. "Particulate Measurements by a New Analyzing Technique for Duper-Low Mass PM," SAE 2002-30-039, 2002.

[79] Sappok, A., Beauboeuf, D., and Wong, V., "A Novel Accelerated Aging System to Study Lubricant Additive Effects on Diesel Aftertreatment System Degradation," SAE 2008-01-1549, 2008.

[80] Sappok, A., "Emissions and In-Cylinder Combustion Characteristics of Fischer-Tropsch and Conventional Diesel Fuels in a Modern CI Engine," S.M. Thesis, MIT, 2006.

[81] Michigan State University. <http://www.cem.msu.edu/~reusch/VirtualText/Spectrpy/MassSpec/masspec1.htm> 2009.

[82] Netzsch Thermal Analysis. <http://www.dilatometers.com/dil402c/dil402c_09_lit.htm>, 2009.

[83] Virginia Polytechnic Institute and State University, <http://www.cee.vt.edu/ewr/environmental/teach/smprimer/icp/icp.html>, 2009.

[84] University of California, Santa Barbara, <http://www.mrl.ucsb.edu/mrl/centralfacilities/xray/xray-basics/index.html>, 2009.

[85] Sappok, A., and Wong, V., "Impact of Biodiesel on Ash Emissions and Lubricant Properties Affecting Fuel Economy and Engine Wear: Comparison with Conventional Diesel Fuel", SAE 2008-01-1395, 2008.

[86] Froelund, K., and Ross, G., "Laboratory Benchmarking of Seven Model Year 2003-2004 Heavy-Duty Diesel Engines Using CI-4 Lubricant," SAE 2005-01-03715, 2005.

[87] Konstandopoulos, A., "Deposit Growth Dynamics: Particle Sticking and Scattering Phenomena," Powder Technology 109, 262-277, 2000.

14 APPENDIX

Test #	Average wall flow velocity (cm/s)	Final soot loading (g/l)	Final pressure drop (mbar)	Average density (range) (kg/m^3)	$\rho \times k_{p,0}$ (kg/m)
1	4.4	5.2	297	91 (84-100)	4.8
2	4.5	7.6	416	92 (87-100)	4.2
3	2.1	2.8	70	40 (37-42)	3.5
4	6.1	5.8	314	99 (93-101)	5.0
5	4.3	10.3	423	82 (75-90)	3.4
6	4.7	5.8	260	85 (79-94)	3.0
7	7.5	9.1	206	90 (86-107)	7.5
8	5.5	5.9	259	85 (80-88)	4.8
9	3.8	4.8	169	97 (89-102)	3.3
10	4.5	4.2	197	90 (81-101)	4.4
11	3.6	5.2	161	89 (87-91)	3.8
12	2.3	24.7	301	97 (92-100)	4.0
13	2.1	8.4	160	59 (55-66)	2.5
14	8.5	3.3	203	92 (88-97)	5.6
15	9.8	4.5	245	92 (83-100)	4.8
16	6.2	3.4	98	76 (71-84)	6.0
17	13.1	5.4	354	95 (89-105)	7.7
18	1.1	2.0	33.5	26 (21-29)	1.8
19	11.5	9.7	341	92 (87-95)	6.8
20	1.4	4.6	55	58 (54-63)	3.2
21	1.4	8.2	49	58 (54-61)	4.5
22	2.4	2.6	40	52 (47-58)	6.0
23	4.8	1.4	75	55 (43-69)	6.0
24	5.3	3.1	161	79 (69-86)	4.3
25	5.1	2.5	80	54 (50-60)	7.0
26	2.6	5.4	47	72 (69-73)	1.0
27	8.5	2.6	171	65 (60-70)	6.7

Table A-1. Soot permeability and packing density values for a range of exhaust conditions and DPF soot loads [64].

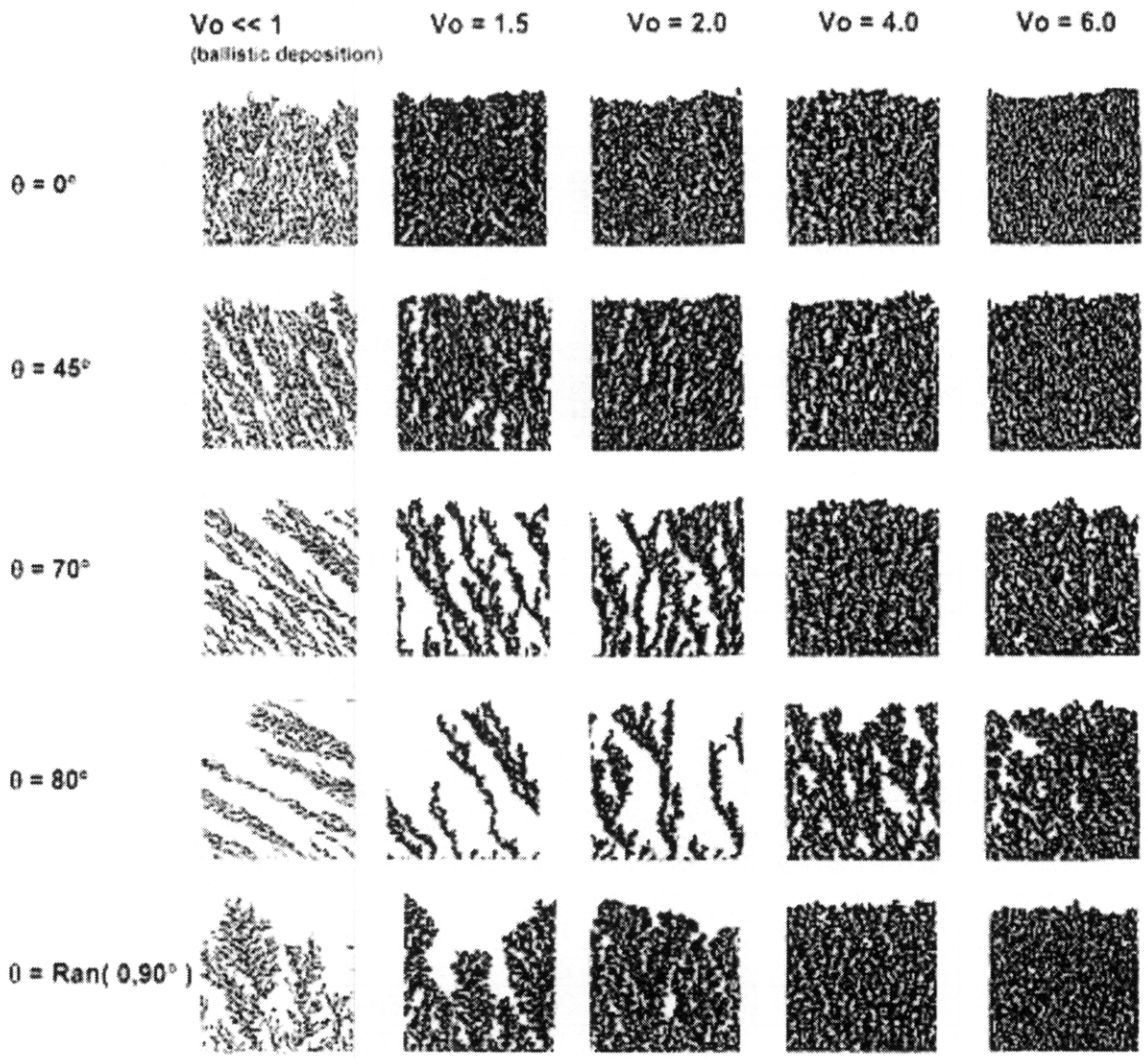

Figure A-1. Particle deposit morphology variation with particle impact velocity and incident angle [87].

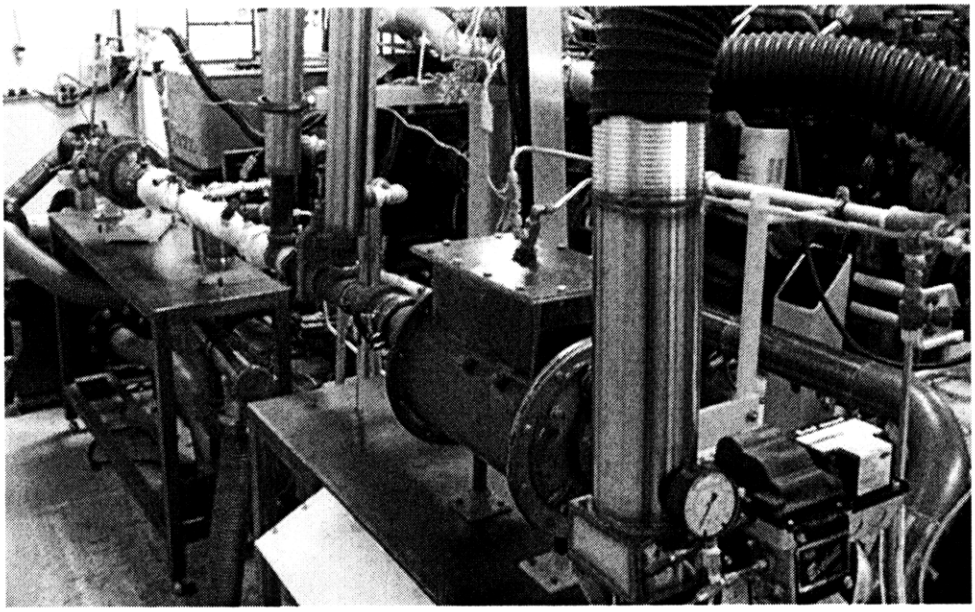

Figure A-2. Experimental set-up showing accelerated ash loading system mounted beside Cummins ISB test bed.

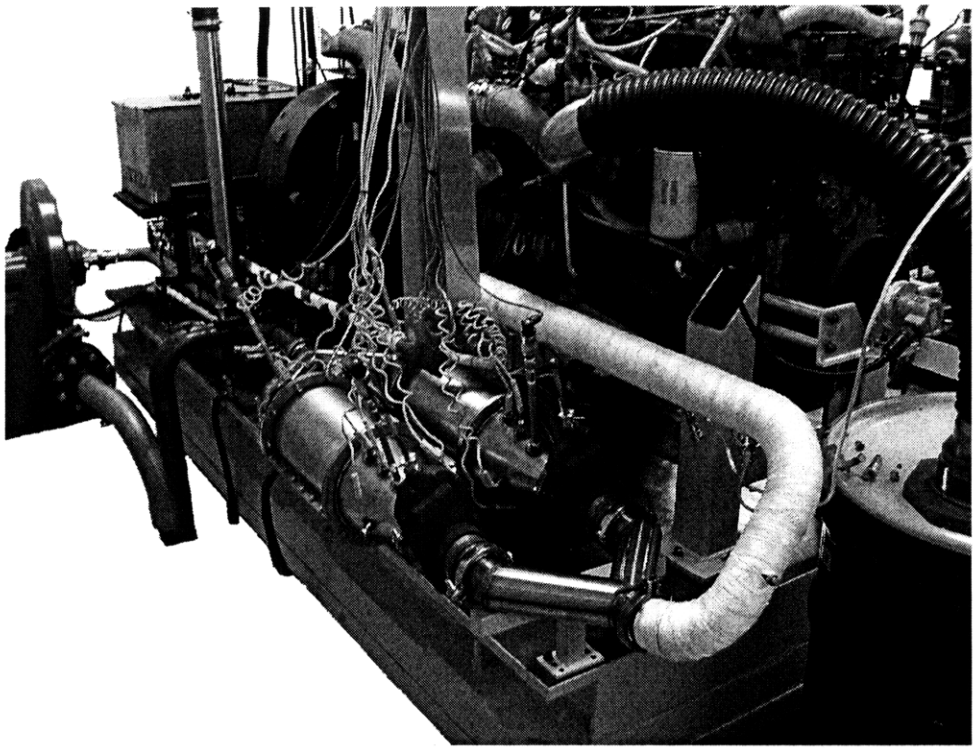

Figure A-3. Fully-instrumented DPF system installed on the test bed.

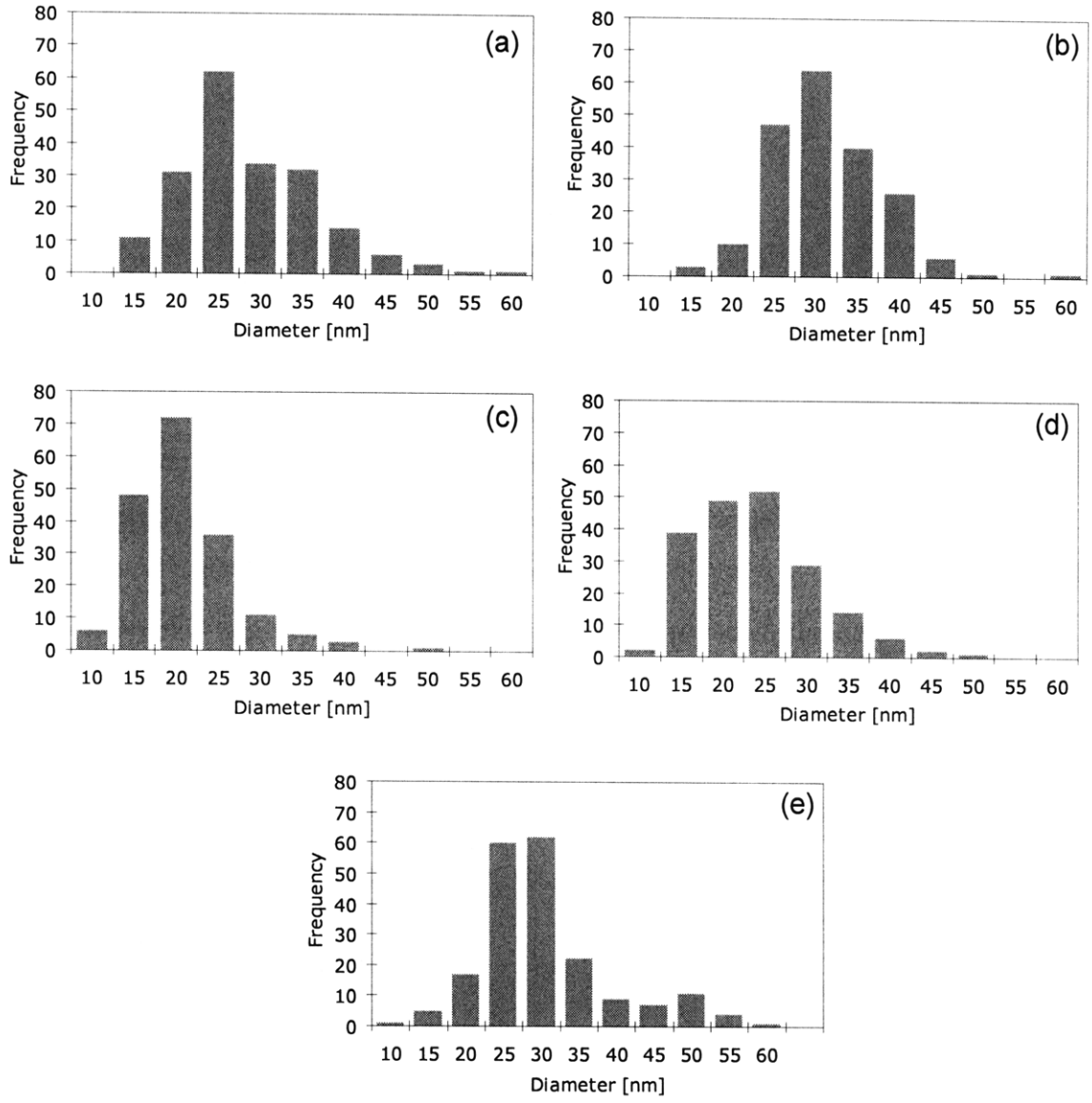

Figure A-4. PM primary particle diameters measured via TEM for: Cummins ISB at (a) 1682 rpm, 25% rated load and (b) 1682 rpm, 75% rated load, and the accelerated ash loading system with (c) oil injection (d) oil doped in the fuel, and (e) no oil addition.

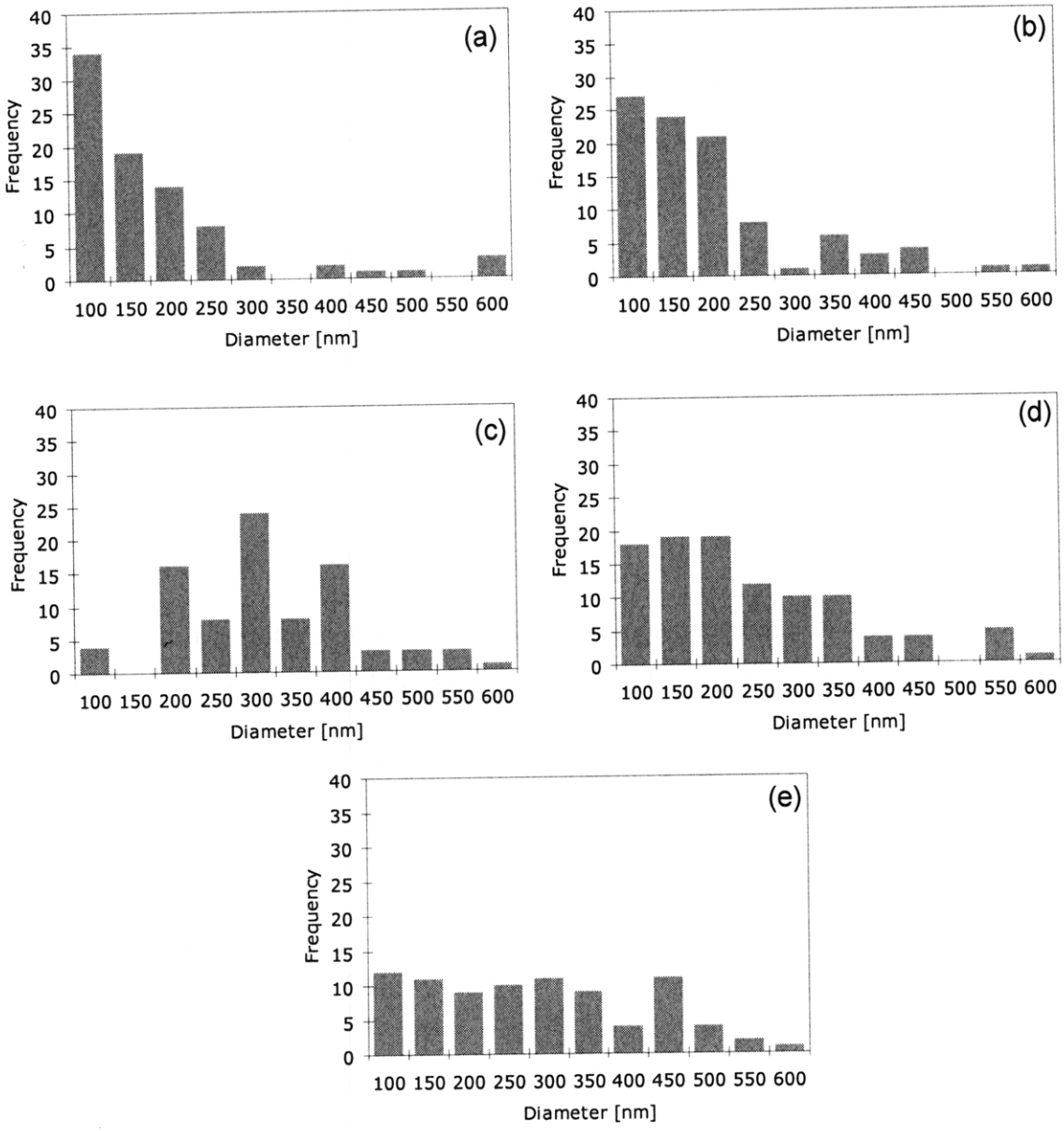

Figure A-5. PM agglomerate diameters measured via TEM for: Cummins ISB at (a) 1682 rpm, 25% rated load and (b) 1682 rpm, 75% rated load, and the accelerated ash loading system with (c) oil injection (d) oil doped in the fuel, and (e) no oil addition. Note that particles and agglomerates smaller than 50 nm in diameter are not included in the size distributions shown above.

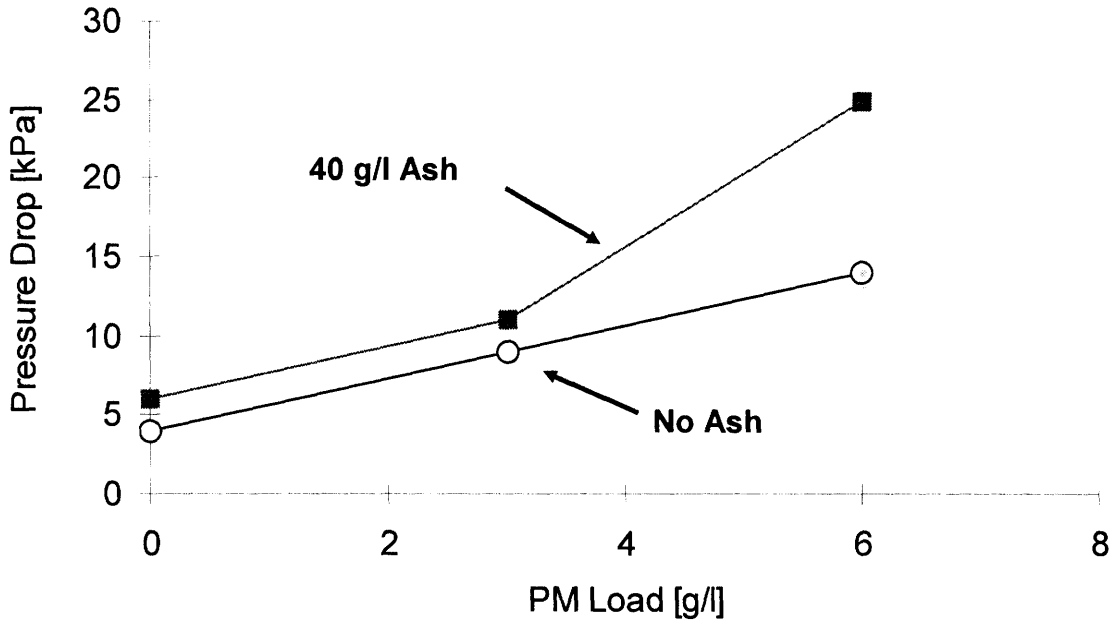

Figure A-6. Effect of ash accumulation on DPF pressure drop as a function of soot load. Adapted from experimental data presented in [23].

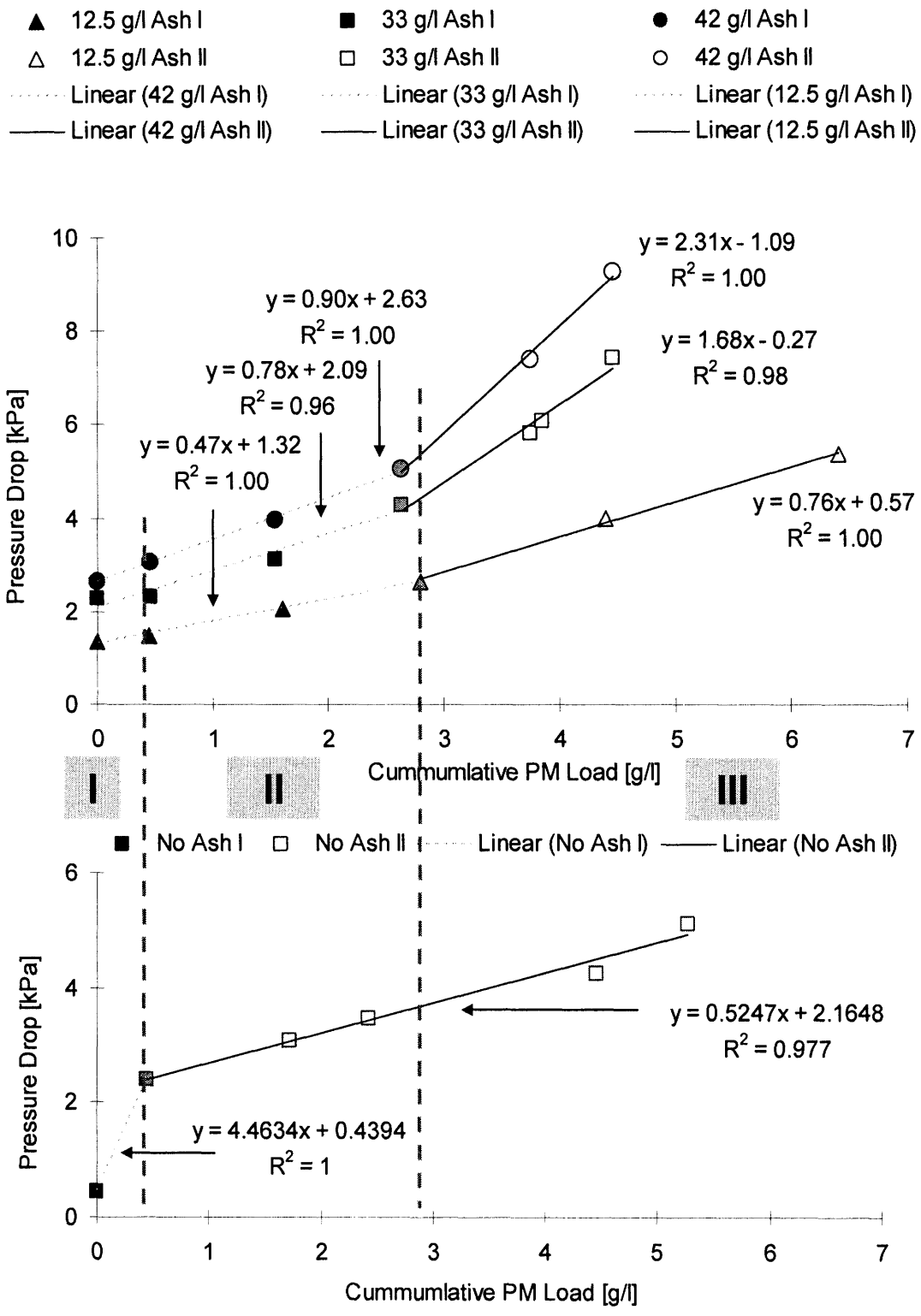

Figure A-7. Definition of pressure drop regimes and linear fit for ash and soot loaded diesel particulate filters from experimental data at 25 °C and 20,000 GHSV.

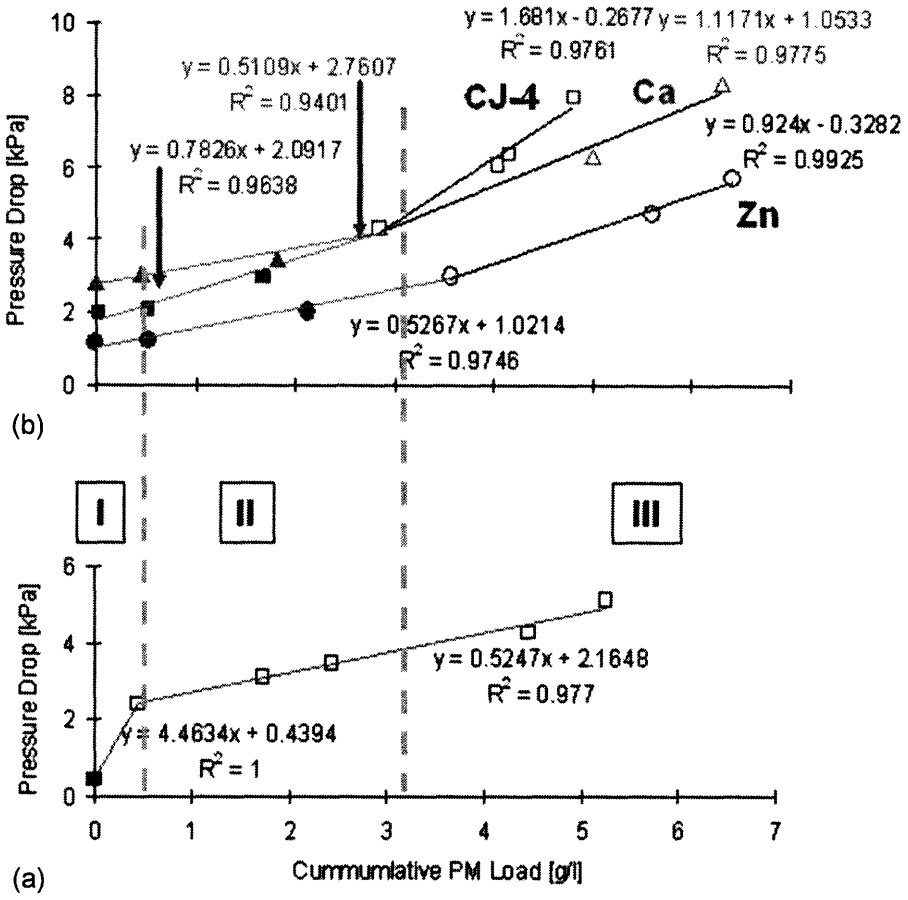

Figure A-8. Definition of pressure drop regimes and linear fit for ash and soot loaded diesel particulate filters from experimental data at 25 °C and 20,000 GHSV.

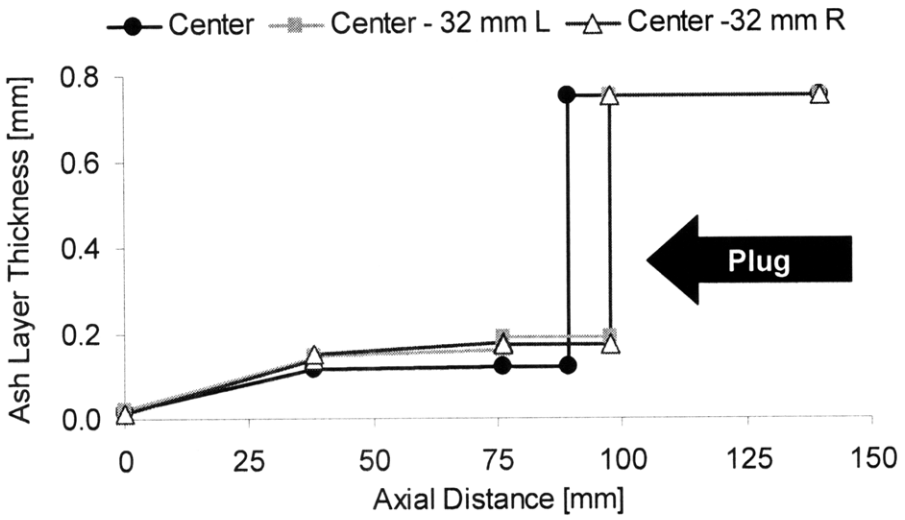

Figure A-9. Ash layer thickness profiles for a DPF containing 42 g/l ash generated in the laboratory using CJ-4 oil and periodic regeneration.

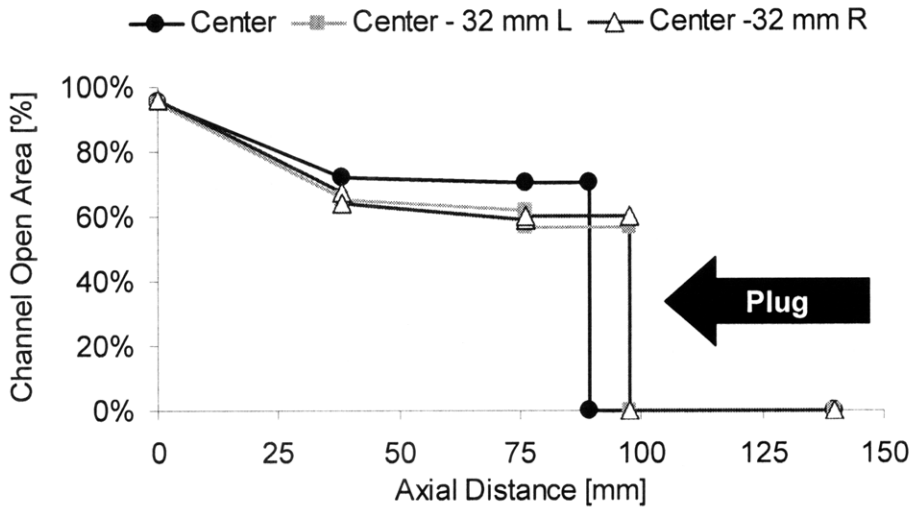

Figure A-10. Channel open area profiles for a DPF containing 42 g/l ash generated in the laboratory using CJ-4 oil and periodic regeneration.

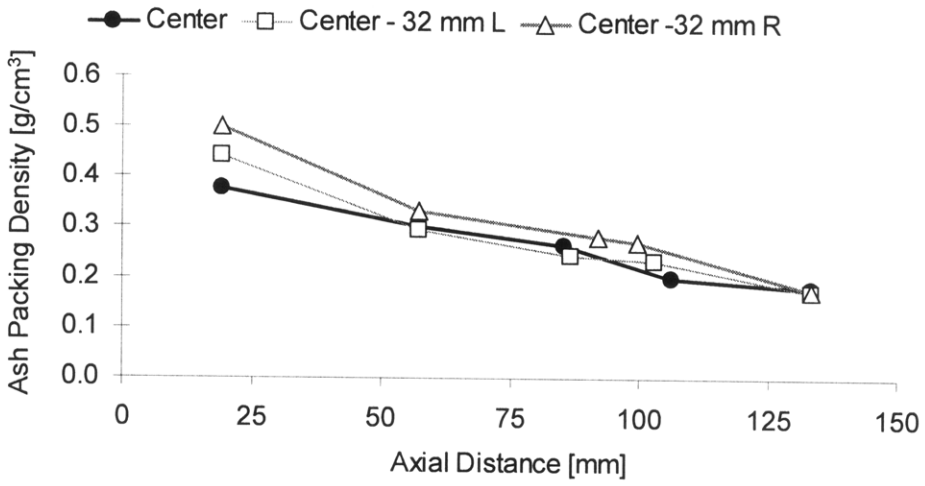

Figure A-11. Ash packing density profiles for a DPF containing 42 g/l ash generated in the laboratory using CJ-4 oil and periodic regeneration.

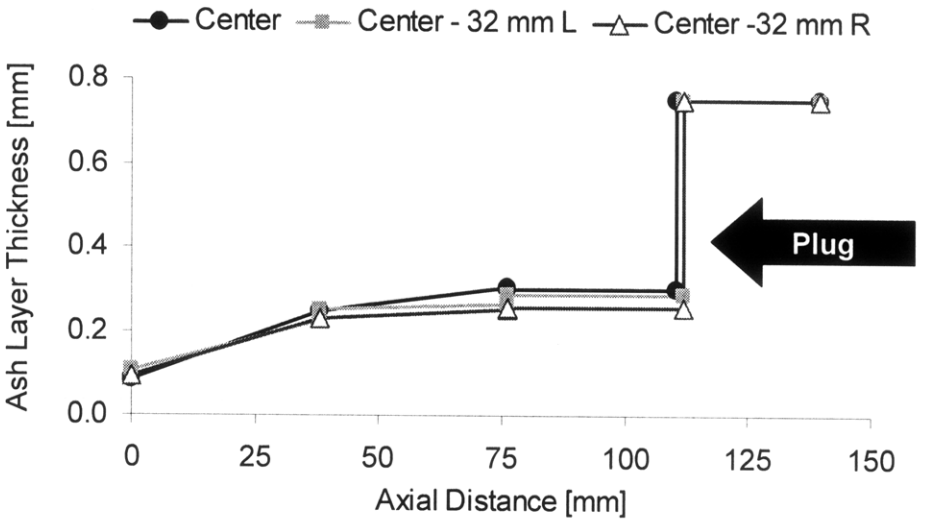

Figure A-12. Ash layer thickness profiles for a DPF containing 33 g/l ash generated in the laboratory using CJ-4 oil and continuous regeneration.

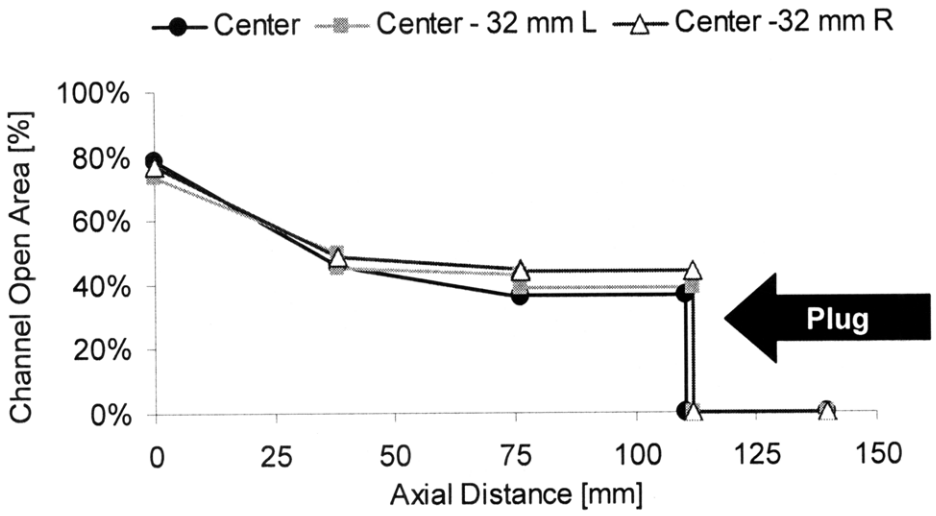

Figure A-13. Channel open area profiles for a DPF containing 33 g/l ash generated in the laboratory using CJ-4 oil and continuous regeneration.

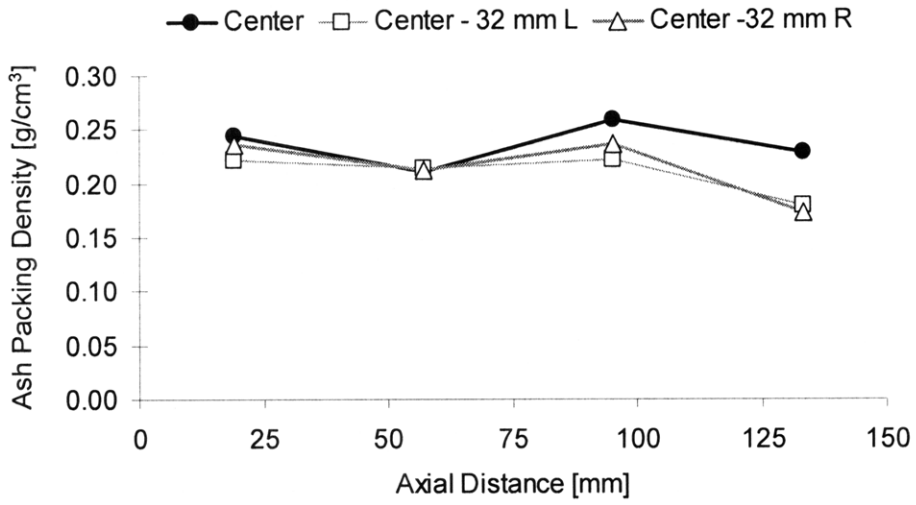

Figure A-14. Ash packing density profiles for a DPF containing 33 g/l ash generated in the laboratory using CJ-4 oil and continuous regeneration.

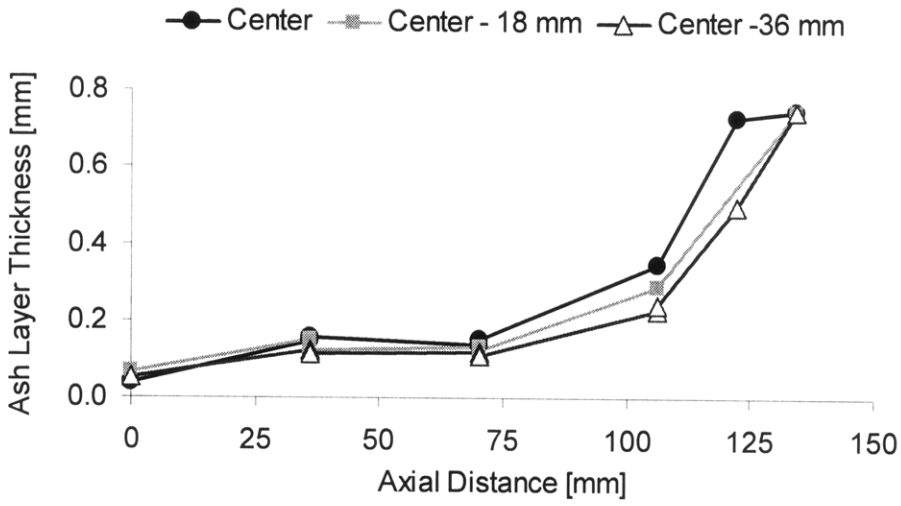

Figure A-15. Ash distribution profiles for a DPF containing 28 g/l ash generated using a base oil containing only ZDDP and periodic regeneration.

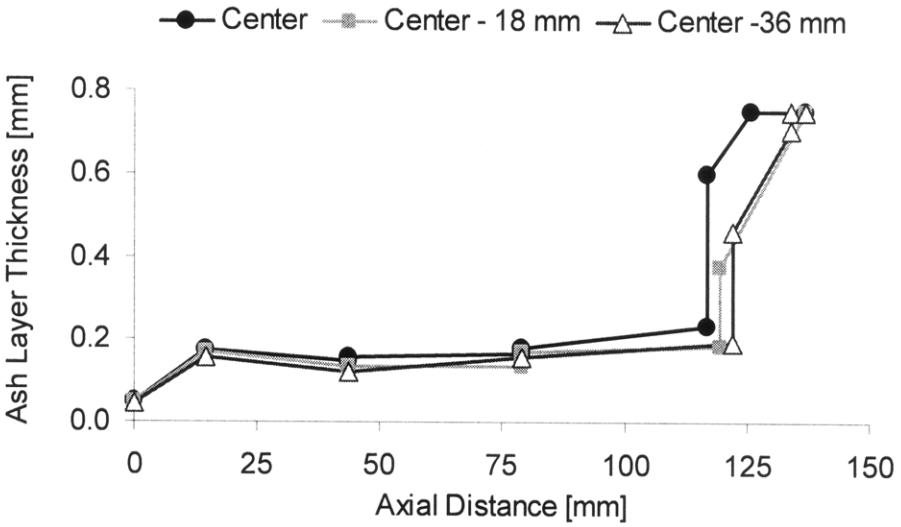

Figure A-16. Ash distribution profiles for a DPF containing 29 g/l ash generated using a base oil containing only calcium detergent and periodic regeneration.

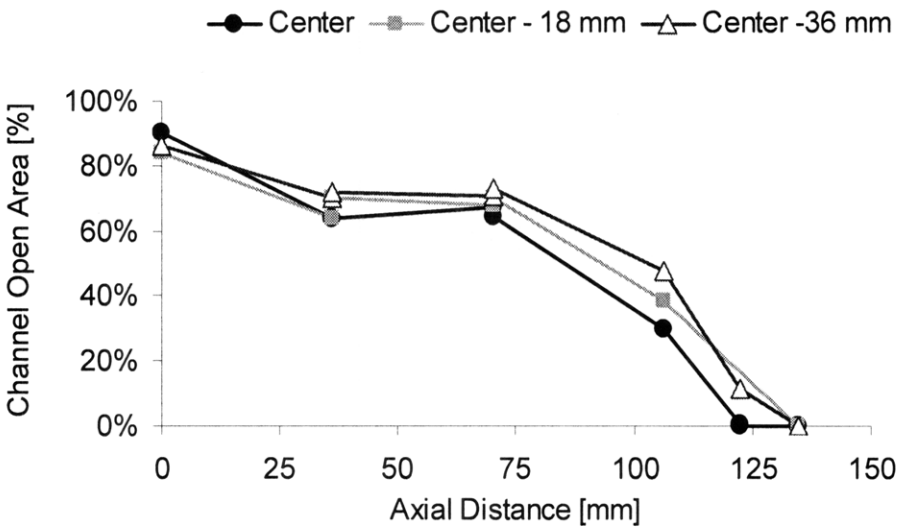

Figure A-17. Channel open area profiles for a DPF containing 28 g/l ash generated using a base oil containing only ZDDP and periodic regeneration.

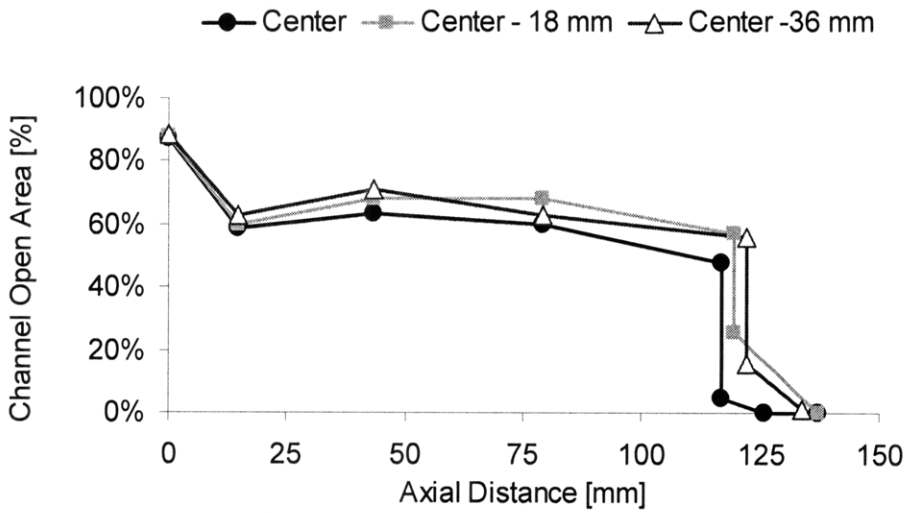

Figure A-18. Channel open area profiles for a DPF containing 29 g/l ash generated using a base oil containing only calcium detergent and periodic regeneration.

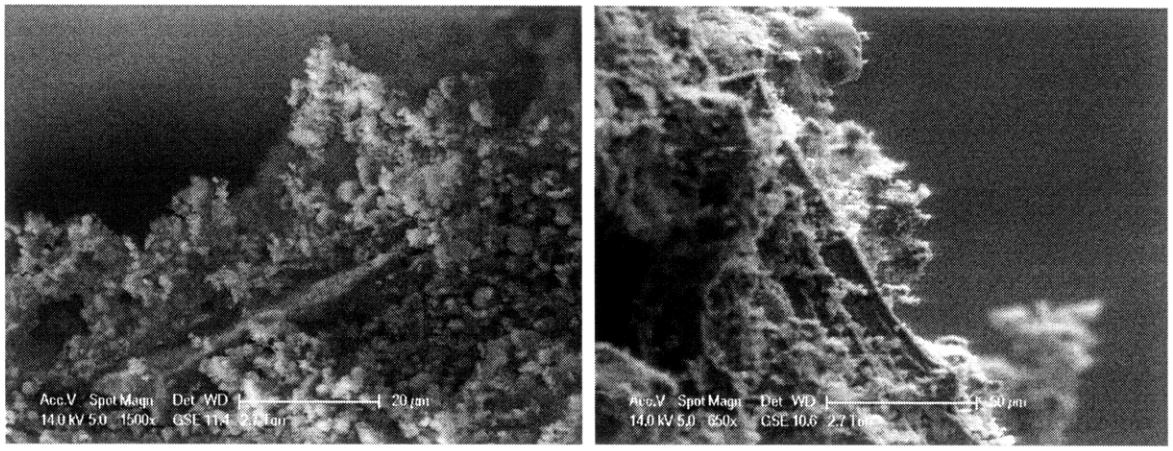

Figure A-19. SEM images showing ash structure formation on DPF walls.

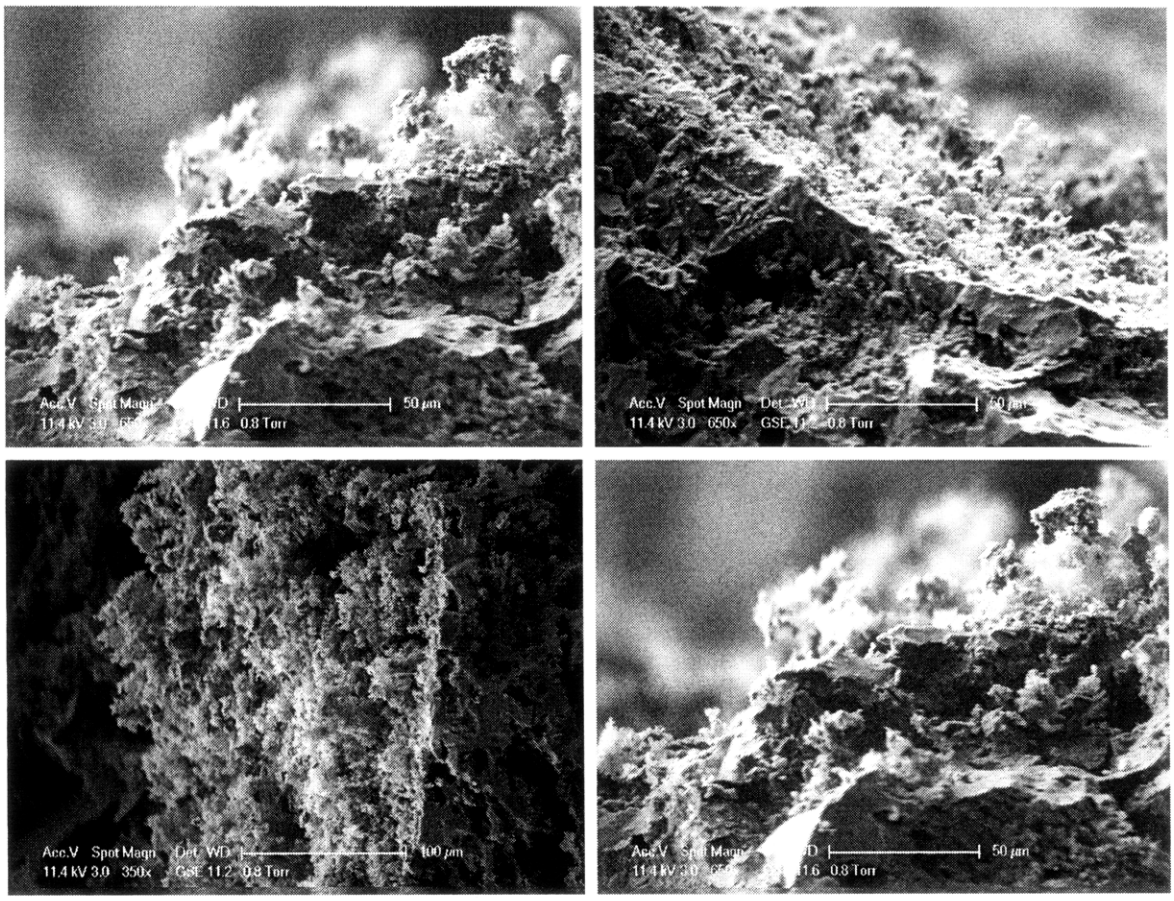

Figure A-20. SEM images showing ash layer formed along DPF walls. Ash does not penetrate deep into the DPF pores.